



ABSTRACT BOOK OF THE INTERNATIONAL CONFERENCE

MODERN PROBLEMS OF SOLID-STATE PHYSICS AND MAGNETISM



in memory of Academician Viktor G. Baryakhtar

September 24-26, 2025. Kyiv, Ukraine





NATIONAL ACADEMY OF SCIENCES OF UKRAINE V. G. BARYAKHTAR INSTITUTE OF MAGNETISM OF THE NATIONAL ACADEMY OF SCIENCES OF UKRAINE

ABSTRACT BOOK OF THE INTERNATIONAL CONFERENCE

MODERN PROBLEMS OF SOLID-STATE PHYSICS AND MAGNETISM

in memory of Academician Viktor G. Baryakhtar

September 24-26, 2025. Kyiv, Ukraine

УДК 538.9, 537.6/.8

Матеріали міжнародної конференції «Сучасні проблеми фізики твердого тіла та магнетизму», присвяченої пам'яті академіка НАН України Віктора Григоровича Бар`яхтара. Україна. – Київ, 2025, - 200 стор.

Збірник тез конференції містить результати роботи дослідників України та іноземних вчених з фізики твердого тіла та магнетизму. Збірник розрахований на наукових працівників, аспірантів та студентів.

За достовірність викладу даних та текст тез несуть відповідальність автори.

[©] Інститут магнетизму імені В.Г. Бар'яхтара НАН України, 2025 р.

Head of conference

Prof. **Oleksandr Tovstolytkin**, Corresponding Member of the NAS of Ukraine, V. G. Barvakhtar Institute of Magnetism of the NAS of Ukraine

Program Committee

Program Committee Chairman – Prof. **Boris Ivanov**, Corresponding Member of the NAS of Ukraine, V. G. Baryakhtar Institute of Magnetism of the NAS of Ukraine

Dr. **Yaroslaw Bazaliy**, University of South Carolina (USA).

Prof. Mykhailo Bezuglyi, Igor Sikorsky Kyiv Polytechnic Institute (Ukraine)

Academician **Mykhailo Bondar**, Institute of Physics of the NAS of Ukraine (Ukraine)

Prof. Andrii Chumak, University of Vienna (Austria)

Dr. **Volodymyr Golub**, V. G. Baryakhtar Institute of Magnetism of the NAS of Ukraine (Ukraine)

Academician **Yurij Holovatch**, Yukhnovskii Institute for Condensed Matter Physics of the NAS of Ukraine (Ukraine)

Dr. **Gleb Kakazei**, University of Porto (Portugal)

Prof. Jarosław Kłos, Adam Mickiewicz University (Poland)

Prof. Oleksiy Kolezhuk, Corresponding Member of the NAS of Ukraine, V. G.

Baryakhtar Institute of Magnetism of the NAS of Ukraine (Ukraine)

Prof. Vladislav Korenivski, Royal Institute of Technology (Sweden)

Academician Oleksandr Kordyuk, Kyiv Academic University (Ukraine)

Prof. **Volodymyr Krivoruchko**, Donetsk Institute of Physics and Engineering named after O. O. Galkin (Ukraine)

Academician **Vadym Loktev**, Academic Secretary of the Physics and Astronomy Division of the NAS of Ukraine (Ukraine)

Dr. Denys Makarov, Helmholtz-Zentrum Dresden-Rossendorf (Germany)

Prof. **Viktor Melnyk**, V. Ye. Lashkaryov Institute of Semiconductor Physics of the NAS of Ukraine (Ukraine)

Dr. habil. **Oleksandr Serga**, University of Kaiserslautern-Landau (Germany)

Prof. Denys Sheka, Taras Shevchenko National University of Kyiv (Ukraine)

Dr. Gurmeet Singh, Indiana University–Purdue University Indianapolis (USA)

Prof. **Andrei Slavin**, Oakland University (USA)

Academician **Valentyn Tatarenko**, G. V. Kurdiumov Institute for Metal Physics of the NAS of Ukraine (Ukraine)

Organization Committee

Roman Verba (chair) Iryna Sharai Vladyslav Borynskyi Olga Saliuk Sergiy Reshetnyak Oleksandra Ostapenko

Serhii Mamilov Dariya Savchenko Lidiia Ushii

TABLE OF CONTENTS

Section I. Nanomaterials and nanotechnologies

Yu. S. Doronin, A.A. Tkachenko, V. L. Vakula, G. V. Kamarchuk.	
Electron-Induced Processes in a Clustered Supersonic Argon Jet.	10
V. V. Lizunov, T. P. Vladimirova, S. V. Lizunova, O. S. Skakunova.	
Diagnostics of Nanoscale Defects in Garnet Crystals by High-Resolution	
Dynamical Diffractometry.	13
Gurmeet Singh Lotey, Sanjeev Kumar. Green Strategy for Environmental	
Remediation and Pathogen Control. (Invited)	14
L. O. Abramenko, A. V. Korotun, V. M. Matiushyn. Ordered MNG-	
Composite Based on a Cubic Lattice Of Metal Nanocylinder Dimers.	15
V. K. Nosenko, O. P. Fedorov, T. V. Pryadko, V. A. Dekhtyarenko, T. P.	
Vladimirova, O. M. Semyrga, I. V. Zagorulko. Formation of Nano-Sized	
Solidification Structure and Specific Segregation of Components in	
Medium-Entropic Co-Ni-Cr Alloys.	19
O. V. Bereznykov, O. S. Pylypchuk, V. V. Vainberg, V. N. Poroshin,	15
O.V. Leshchenko, V. N. Pavlikov, E. A. Eliseev, A. N. Morozovska.	
Dielectric Response of $Hf_xZr_{1-x}O_2$ Nanoparticles and Nanocomposites.	23
	23
Yu. Yu. Shlapa, K. Siposova, A. G. Belous. Inorganic Oxide	
Nanocomposites With Pronounced Bioactivity for Biomedical Application.	27
(Invited)	27
M. V. Los, I. Yu. Sahalianov, T. M. Radchenko, V. A. Tatarenko. On the	
(Non)Monotonic Strain Dependence of The Energy Gap in the Band	20
Structure of Phosphorene.	29
A. V. Bodnaruk, A. N. Morozovska, Yu. O. Zagorodniy, V. N. Pavlikov,	
O. V. Leshchenko, M. V. Karpets, E.A. Eliseev. Room Temperature	
Multiferroics on the Base of Single-Phase Perovskites PFN and PFT Doped	
with Mn Ions.	32
Ya. P. Lazorenko, V. P. Mitsai. Optical and Sensory Propeties of 2,4-	
Dinitrophenylhydrazine-Doped Fumed Silica Films.	34
O. P. Ponomarov, S. O. Ponomarova, Yu. M. Koval'. Graphene	
Vibrational Thermodynamics.	37
O. P. Ponomarov, S. O. Ponomarova, Yu. M. Koval`. Machine Learning	
Approach To Predict Curie Temperature In Binary Alloys.	37
Section II. Physics of condensed matter and phase transforma	tions
•	
A.V. Uriadov, I.V. Ivanchenko, E.N. Kalabukhova, <u>D.V. Savchenko</u> .	
Temperature-Dependent EPR Study of Iron-Doped Cadium Manganese	
Telluride Crystals.	40
M. Yu. Kovalevsky. Spiral Ordering in Spin 3/2 Magnets.	43
S. Sologub, J. Koch, C. Ghosal, M. Gruschwitz, C. Tegenkamp. Structure	
And Electronic Magneto-Transport of Epitaxial Graphene Proximized By	
Adsorbed And Intercalated Atomic Layers.	45
· ·	

Table of contents	5
Table of Collicius	•

<u>I. V. Plyushchay</u> , O. I. Plyushchay, V. B. Shevchenko. First-Principles	
Modeling of the Electronic Structure Peculiarities in High-Entropy	
Transition Metal Carbides.	49
A.P. Bukivskii, Yu.P. Gnatenko, A.S. Opanasyuk, P.M. Bukivskij,	
S.A. Iliash, M.S. Furier. Impact of Dysprosium Doping on the Microstructure, Impurity Content, and Excitonic Properties of CdS Thin	
Films.	52
P.M. Bukivskij, Yu.P. Gnatenko, A.P. Bukivskii. Low-Temperature Study	52
of the Magnetic Polaron Effect in Cd _{1-x} Dy _x Te Diluted Magnetic	
Semiconductors.	56
X. Moya. Barocaloric Materials For Heating And Cooling (<i>Invited</i>)	59
J. J. Ruiz-Lorenzo, M. Dudka, M. Krasnytska, <u>Yu. Holovatch.</u> Effective	33
and Asymptotic Criticality of Structurally Disordered Magnets. (<i>Invited</i>)	60
V. V. Chabanenko, E. E. Zubov, A. Nabiałek. Aspects Of Electro-	00
Magnetic Properties Of Manganites And Polaron Excitation.	62
V. A. L'vov, O. Salyuk, A. Kosogor. Magnetic And Magnetocaloric	
Properties Of Ferromagnets Undergoing Structural Phase Transitions.	
(Invited)	65
Yu. V. Horbatenko, V.V. Sagan, A. I. Krivchikov, O. A. Korolyuk,	
O. O. Romantsova, D. Szewczyk. Low-Temperature Studies of Thermal	
Conductivity of Carbon Materials.	69
A. S. Nuradinov, K. A. Sirenko, I. A. Nuradinov, O. V. Chystiakov,	
<u>D. O. Derecha</u> The Influence of Scale Factors on Nucleation and	
Crystallization.	70
M. Dudka, D. Shapoval, Yu. Holovatch. Critical Properties of Structurally	
Disordered Magnets With Long-Range Interactions.	72
S. O. Reshetniak, G.Yu. Lavanov, V. M. Kalita. Influence of non-	
Heisenberg exchange on the entropy of an isotropic ferromagnet.	74
V. Ivanov Altermagnetism: New Concept or Well-Forgotten Old. (Invited)	77
V. P. Mitsai, Ya. P. Lazorenko. Fluorescent Response of Hybrid Films	70
With a Coumarine7/Fluorescein Dye System to Gaseous Ammonia.	79
D. A. Kukusta, V. N. Antonov, L. V. Bekenov. Energy Band Structure and Resonant Inelastic X-Ray Scattering in Some Iridates.	0.2
R. Y. Umetsu. Electronic State and Magnetic Properies of Half-Metal Type	83
Heusler Alloys. (Invited)	85
	05
Y. I. Mazur, M. P. Semenko, R. V. Ostapenko. Magnetic Interactions In High-Entropy Oxides And Their Correlation With Atomic Structure	
Parameters.	87
i municula,	U/

Section III. Thin films and coatings

R. Pedan, <u>I. Vladymyrskyi.</u> Tailoring Structural and Magnetic Properties of CO/PT Films Via Stacking Engineering, Annealing, and Ion Irradiation. *(Invited)*

6 Modern problems of solid state physics & magnetism	
A. Vovk, D. Popadiuk, B. Postolnyi, S. Bunyaev, P. Strichovanec, J. A. Pardo, P. A. Algarabel, O. Salyuk, V. Korenivski, G. N. Kakazei, V. O. Golub, and J. P. Araujo. Structural and Magnetic Properties of Epitaxial Co ₂ FeGe Films: Effect of Thermal Processing. (<i>Invited</i>) R. A. Osypova, S. I. Bogatyrenko, A. P. Kryshtal. Influence of Atomic Surface Diffusion on The Structure And Morphology of Deposited Tantalum Thin Films.	93 95
Section IV. Superconductivity	
•	
 V. N. Krivoruchko, V. Yu. Tarenkov. Magnetism and Superconductivity: Local Spin-Triplet Pairs In Half-Metallic Manganites - a Base Platform For Quantum Materials With Unique Superconducting Characteristics. D. Menesenko², V. Tarenkov, V. Krivoruchko, A. Shapovalov, V. Shamaev Edge Inhomogeneities and Diode-Like Current-Voltage 	99
Characteristics of Superconducting More Films. J. Kharlan, G. Centała, K. Szulc, K. Sobucki, S. Memarzadeh, K. Guslienko, V. O. Golub, <u>J. W. Kłos.</u> Ferromagnetic-Superconducting	102
Hybrids For Local Control of Magnetization Configuration And Dynamics. <i>(Invited)</i>	104
Section V. Spintronics, magnonics and microwave magnetism	
V. N. Krivoruchko. Quantum Topological Phase and Electric Field Control	
Of Spin-Waves' Dynamics in Magnetic Insulators. <i>(Invited)</i> D.V Slobodianiuk, R. V. Verba. Probalistic Computing With Josephson-	107
Like Antiferromagnetic Spin Hall Oscillator.	110
A. M. Korostil, M. M. Krupa. On Magneto-Controlled Electric Capacitance in Magnetic Junctions.	112
O.L. Andrieieva, A.V. Hlushchenko, O.V. Chechkin. Stochastic Domain Wall and Skyrmion Motion on the Randomly Inhomogeneous Racetrack Memory.	114
A.V. Hlushchenko, M.I. Bratchenko, O.V. Chechkin. Thermal and Spin	114
Current Noise in The Racetrack Memory With Domain Walls and Skyrmions.	116
<u>J. Kharlan</u> , J. Holobradek , M. Urbanek , J. Klos , V.O. Golub . Excitation of High Frequency Spin Waves in Low External Field in Hybrid	
Ferromagnetic-Metallic Systems.	118
O. Yu. Gorobets, V. V. Kulish, S. I. Yeromin. Surface Magnon-Plasmon Hybrid Modes in Metal-AFM-Metal Waveguides.	120
I. Yastremsky, A. Yakimkin. Bloch Point Structure And Relaxation at	120
Finite Temperatures.	122
O. V. Shtanko, O. V. Prokopenko. Dual-antiferromagnetic-Layer Spin Hall Oscillator.	124
<u>D. D. Sheka.</u> Geomerty-governed Chiral Effects in Curvilinear Magnetism. (<i>Invited</i>)	126
	_

<u>D. Makarov</u> Curvilinear Magnetism: Fundamentals And Applications. <i>(Invited)</i>	127
O. Busel, D. Polishchuk, A. Kravets, V.Korenivski. Spin dynamics in	12/
ferro-/antiferromagnetic multilayers. (<i>Invited</i>) R. R. Teslia, O. K. Kolezhuk Current-Driven Dynamics Of Chiral Domain	129
Walls In A Quasi-One-Dimensional Helimagnet.	133
I. O. Sotnyk, O. V. Prokopenko. Programmable Artificial "Neuron" Based on Antiferromagnetic Spin Hall Oscillator.	135
D. Karakuts, K. V. Yershov, D. D. Sheka. Domain Wall Diode and Trap By Cross Section Tailoring in Ferromagnetic Nanostripes.	139
O. V. Prokopenko. Antiferromagnetic Spintronic Oscillators and Signal Detectors. <i>(Invited)</i>	140
I. Fantych, O. V. Prokopenko L1 ₀ -Based Spin Diodes as Non-Resonant	140
Signal Detectors and Energy Harvesters. O. Kozlov, S.Reshetniak, A.Kravets, V. Korenivski, V. Kalita. Current-	142
Induced Switching Of Interlayer Exchange In Spin Valves At Room Temperature.	145
V. S. Gerasimchuk, <u>I. V. Gerasimchuk.</u> Eigenoscillations of the Non-Uniform Spin Texture in a Two-Sublattice Antiferromagnet with the	
Dzyaloshinskii-Moriya Interaction.	147
M. Moalic, R.V. Verba, S.A. Bunyaev, K.Y. Guslienko, M. Krawczyk, G.N.Kakazei. Radial Magnetic Vortices in Multilayered Nanopillars.	
(Invited)	150
O. V. Malyshev, V. Y. Malyshev, O. V. Prokopenko, G. A. Melkov.	450
Hybridized Excitations in a Ferromagnetic Wire.	152
A. V. Chumak. Quantum Magnonics With Propagating Magnons. (Invited) S. A. Majetich. Magnetic Tunnel Junctions: Ferromagnetic,	156
Superparamagnetic, And Antiferromagnetic. (Invited)	158
Section VI. Functional magnetic materials	
V. Borynskyi, D. Popadiuk, A. Kravets, Y. Shlapa, S. Solopan,	
V. Korenivski, A. Belous, A. Tovstolytkin. Magnetic Anisotropy and	
Temperature-Dependent Properties of Al-Doped YIG Ceramics.	161
O. Kapush, B. Shanina, A. Konchits, N. Mazur, V. Dzhagan, I. Vorona,	
L. Mikoliunaite, G. Zambzickaite, M. Talaikis, M. Skoryk,	
Yukhymchuk V. Controllable Synthesis and Characterization of Fe ₃ O ₄ /Au	
Composites for Magneto-Plasmonic Applications.	163
B. S. Baitaliuk, I. K. Yevlash, A. V. Nosenko, O. M. Semyrga, V. K.	
Nosenko. Novel Press-Free Nanocrystalline Soft Magnetic Composites With	40-
a Portland Cement Binder for High-Temperature Applications	167
V. K. Nosenko, A. V. Nosenko, V. V. Kyrylchuk, O. I. Boshko, I. V.	
Zagorulko. Magnetic Behavior and Structural Relaxation of CO-SI-B	171
Amorphous Alloys Doped by Fe and Cr.	171

8 Modern problems of solid state physics & magnetism	
 J. Kharlan, O. Salyuk, <u>H. Marinchenko</u>, V. Golub Tensile Stresses in Nimnga Laminate Composite Framed by Soft Magnetic Foils. O. V. Nogovitsyn, <u>V. O. Seredenko</u>, O. V. Seredenko, D. O. Derecha. 	173
Influence of a Constant Magnetic Field on the Structure Formation of a Cu- Fe Alloy in Its Casting And Solidifying.	175
M. Guo, V. Farenkov, X. Chen, A. Mohanathan, A. Z. K. Goh, Y. Tang, J. Zhang, M. Vickers, S. M. Fairclough, C. Ducati, X. Moya, S. Hirose, N. D. Mathur. Modifying MLCS of PST for improved performance.	
(Invited)	177
O. L. Fertman, O. V. Fedorchenko, D. D. Khalyavin, E. Cižmár, A. N. Salak High-Pressure Stabilized Bi(FeSc)O ₃ Multiferroics: Magnetic	
Behaviour. (<i>Invited</i>)	178
Section VII. Interdisciplinary research	
O. O. Kryvchikov, D. V. Laptev, V. V. Slavin. Graph Neural Networks for	
Predicting Properties of Quasi-One-Dimensional Ising Systems.	181
O. S. Ostapenko, S. O. Mamilov, V. B. Orel, V. E. Orel, O I.	
Tovstolytkin Halbach Matrix Approach as a Promising Method to Advance	100
Magnetomechanical Action On Biological Tissues. O. Yu. Salyuk, O. S. Ostapenko, Yu.B. Skirta, D.V. Velyhotskyi, S. O.	183
Mamilov. Effect of a Constant Mangitic Field on the Magnitude of Laser	
Photodissociation of Oxyhemoglobin in Arterial Blood.	186
V. B. Orel, O. Y. Dasyukevich, O. Yu. Rykhalskyi, A. G. Diedkov,	100
S. O. Mamilov, O. S. Ostapenko, Yu. A. Kurapov, S. Ye. Lytvyn, V. E.	
Orel, A. I. Tovstolytkin. Application of Magnetic Nanocomposite for	
Cancer Imaging and Treatment in an Experimental Tumor Model. (Invited)	189
<u>K. E. Schalm.</u> Electronic Hydrodynamics in Graphene, Incoherent Metals	
and Other Strongly Correlated Systems. (Invited)	191
S. Gorobets, O.Gorobets, <u>D.Sverdlichenko</u> . Magnetic Field Influence on	404
in Intracellular Ca ²⁺ Dynamics.	191
<u>Ye.A. Salatskiy</u> , S.V. Gorobets. Magnetic Field Control of Calcium Signal in Cancer Cells.	195
Post-Deadline contributions	
A. A. Serga. Spontaneous Emergence Of Phase Coherence In A Room-Temperature Magnon Bose–Einstein Condensate	200

SECTION I. NANOMATERIALS AND NANOTECHNOLOGIES

ELECTRON-INDUCED PROCESSES IN A CLUSTERED SUPERSONIC ARGON JET

Yu. S. Doronin, A.A. Tkachenko, V. L. Vakula,

G. V. Kamarchuk.

B. Verkin Institute for Low-Temperature Physics and Engineering of the National Academy of Sciences of Ukraine, Kharkiv 61103, Ukraine

Supersonic jets of rare and molecular gases are widely utilised in various scientific and technological applications [1, 2]. To fully utilise the potential of supersonic jets, several key parameters must be known. These include the nature of the jet flow and the density or concentration of atoms, the ratio of monomers to clusters in the presence of condensation in the jet, the mass fraction of condensate, and the average cluster size. In this work, we propose a novel method based on probing supersonic jets with electrons to determine several specified parameters. The interaction of incident electrons with atoms and clusters in the jet leads to their excitation and ionisation. The subsequent sequence of processes involving atomic and molecular ions, atoms in ground and excited states, as well as excited and ionised clusters, can be studied using luminescence spectroscopy.

The research was done on a supersonic argon jet in atomic and cluster modes. The supersonic argon jet crossed an electron beam at a distance of 30 mm from the nozzle outlet where the clustering process is practically complete and the contribution of secondary processes to the intensity of the observed emissions is significantly suppressed. The electron energy was 1 keV, and the electron beam current was 20 mA. In the atomic mode of a supersonic argon jet, VUV radiation is mainly generated by resonance transitions between the ground and excited states of atoms and ions. In the cluster mode, as the number and size of clusters in the jet increase, the total VUV radiation flux is dominated by continua emitted by neutral and charged excimer complexes formed in the clusters. Figure 1 shows the emission spectrum of a supersonic argon jet in the wavelength range 90-150 nm at gas pressure at the nozzle inlet $P_0 = 0.1$ MPa and temperature $T_0 = 300$ K. The spectrum contains resonance lines emitted by argon ions Ar II (λ =92.0 nm, λ =93.2 nm) and atoms Ar I (λ =104.8 nm, λ =106.7 nm), as well as cluster continuum with maxima λ =109 nm (W) emitted by excimers from partially vibrationally relaxed states and continua emitted by neutral $(Ar_2)^*$ $\lambda=127$ and charged excimer complexes $(Ar_4^+)^* \lambda = 137$ nm in the vibrationally relaxed state [3].

By a specially developed method, we measured the integral radiation flux in absolute units and determined the distribution of the radiation flux density from the

electron-excited supersonic argon jet across the entire wavelength range under investigation.

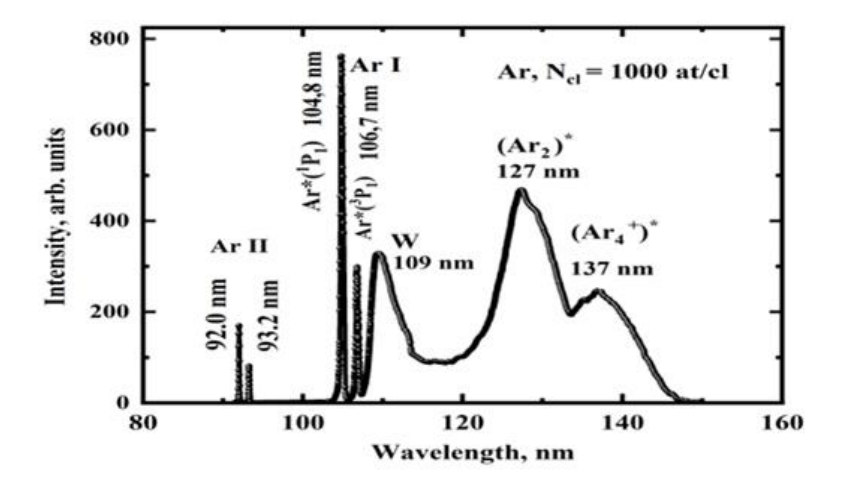


Fig. 1. Spectrum of radiation from a supersonic argon jet, electron energy 1 keV, electron beam current 20 mA, gas pressure and temperature at the nozzle inlet P_0 = 0.1 MPa and T_0 = 300 K

Since the contribution of cascade processes, self-absorption and desorption to the intensity of the λ = 92.0 nm line does not exceed 5%, we used the measured intensity of this line to determine the concentration of argon atoms in the investigated jet region. In the absence of clustering, in atomic jet flow mode, at T₀ = 400 K, the intensity of the 92.0 nm ion line was 3.2×10^{11} photons/s. By measuring the dependence of the intensity of the Ar II line (92.0 nm) on the temperature T₀ of argon at the nozzle inlet in the range from 150 to 400 K, we determined how the density of the atomic component changes in a supersonic argon jet flow and, accordingly, were able to determine the condensation fraction and the number of atoms participating in the clustering process over the entire temperature range studied. Having determined the condensate fraction and the average cluster size, which were experimentally determined in our laboratory under similar jet parameters [4,5], we estimated the cluster concentration in the investigated region of the supersonic Ar jet under various jet parameters. We found a non-monotonic relationship between cluster density and average cluster size, which is typical for systems where cluster formation goes from processes

dominated by condensation nucleus nucleation to processes where clusters grow through coalescence. At the initial stage of the clustering process, the cluster density increases rapidly with the growth of the number of condensation nuclei and reaches a maximum at $N_{cl} \approx 150$ at/cl. Starting from $N_{cl} \approx 400$ at/cl, the coalescence process becomes predominant, increasing the average size of clusters and decreasing their number.

We also estimated the emission cross sections for the ArI resonance lines (λ =104.8 nm, λ =106.7 nm, as well as at the maximum (λ =127 nm) of the so-called second excimer continuum. It was found that the cross sections for the resonance lines σ (104.8 nm) = 10×10^{-18} cm² and σ (106.7 nm) = 5.9×10^{-18} cm² significantly exceed the previously measured emission cross sections for argon atoms in gas [6], which can be explained by the contribution of metastable states to the intensity of the resonance lines. The value of this contribution is higher for the less energetic line λ =106,7 nm. In addition, we obtained a relatively high emission cross section for the second excimer continuum at λ = 127 nm, emitted by clusters with an average size of 1000 at/cl, σ = 2.1×10^{-16} cm², which indicates an efficient conversion of electron beam energy into radiation of this continuum.

The original method presented in the report for determining the condensate fraction and cluster density in a supersonic argon jet flow allows the clustering process to be controlled under various jet flow parameters. The principles of the method make it sufficiently versatile for other gases, which improves understanding of condensation processes in a broader range of applications, including aerospace engineering and environmental science.

- [1] G. Sanzone, J. Yin, Front. Chem. Sci. Eng. 15, 1360 (2021).
- [2] M. Patel, B. R. Geethika, J. Thomas and H. Joshi, Scientific Reports 13, 6338 (2023).
- [3] E. T. Verkhovtseva, E. A. Bondarenko, Yu. S. Doronin, Low Temp. Phys. 30, (2004).
- [4] E. T. Verkhovtseva, S. I. Kovalenko, D. D. Solnyshkin, E. A. Bondarenko, Low Temp. Phys. 23, 140 (1997).
- [5] O. G. Danylchenko, S. I. Kovalenko, V. N. Samovarov, Low Temp. Phys. **34**, 966 (2008).
- [6] J. M. Ajello, G. K. James, B. Franklin and S. Howell, J. Phys. B: At. Mol. Opt. Phys. 23, 4355 (1990).

DIAGNOSTICS OF NANOSCALE DEFECTS IN GARNET CRYSTALS BY HIGH-RESOLUTION DYNAMICAL DIFFRACTOMETRY

<u>V. V. Lizunov</u>¹, T. P. Vladimirova¹, S. V. Lizunova¹, O. S. Skakunova¹

¹G. V. Kurdyumov Institute for Metal Physics, NAS of Ukraine, Kyiv, 03142, Ukraine

Garnet single-crystal systems are of great interest both for fundamental scientific research and for various practical applications, in particular, in magnetic and magneto-optical devices due to the wide range of variations in their crystal structure and the associated physical properties. A convenient way to form the physical properties of garnets is the ion implantation, which to allowing purposefully change the bulk structure of single crystals or their near-surface layers. This method provides, using certain types of ions and high ion energies, the ability to tailor the magneto-optical, magnetic and electrical properties of multilayer structures and magnetic films.

The nondestructive X-ray diffraction methods are widely applied to determine characteristics of structural defects, chemical compositions, and strain distributions in various materials. The objects of such investigations are both the traditional as-grown and/or modified single-crystalline structures, as well as newly developed thin films, multilayer systems, superlattices. The effectiveness of this diffractometric method is largely determined by its high sensitivity to defects with small (nanoscale) radii and even point defects.

In this work, a high-resolution dynamical diffractometry method for non-destructive determination of microdefect characteristics and macrostrain profiles in multilayer single-crystal garnet structures after ion implantation was developed. The developed theoretical model was used to simulate a reciprocal space maps for the imperfect epitaxial yttrium iron garnet film on a gadolinium gallium garnet substrate implanted with fluorine ions. The analytical derivation of the recurrence relations for coherent amplitude reflection and transmission coefficients of such multilayer systems is based on the Ewald–Bethe–Laue consideration of the dynamical wave field in crystal structures with rigorous accounting for boundary conditions at layer interfaces. These relations and the analytical expressions obtained for diffuse components of reflection coefficients are immediately connected with statistical characteristics of defects in each layer due to using the Krivoglaz method of fluctuating waves of defect concentration. Therefore, this diffraction model provides the clear connections between defect characteristics and diffraction parameters. Characteristics of randomly distributed clusters and

dislocation loops in film and substrate, and strain at the cluster boundary, as well as corresponding diffraction parameters were determined.

Thus, the possibility is provided for the self-consistent dynamical description of coherent and diffuse components of the reciprocal space maps, which are measured by the high-resolution triple-crystal diffractometers from imperfect multilayer crystal structures, respectively. Consequently, the way is opened to significantly increasing the physical value of quantitative characterization results, which are obtained for structural imperfections in imperfect multilayers and single crystalline structures with inhomogeneous strain fields by using the most informative and sensitive X-ray diffraction techniques.

GREEN STRATEGY FOR ENVIRONMENTAL REMEDIATION AND PATHOGEN CONTROL (INVITED)

Gurmeet Singh Lotey¹, Sanjeev Kumar²

1Department of Physics, Indiana University Purdue University Indianapolis (IUPUI), Indianapolis, IN, 46202, USA

2Department of Physics, Chandigarh University, Gharuan Mohali, 140413, India

The growing challenges of water pollution and microbial contamination demand innovative and sustainable treatment strategies. In this study, zinc oxide nanoparticles (ZnO NPs) were synthesized using a combined precipitationhydrothermal method assisted by CTAB, leading to the formation of highly crystalline, multi-structured particles with an average size of 40 nm and a narrow band gap of 2.82 eV. These structural features enhanced light absorption and contributed to remarkable photocatalytic activity. The developed CTAB/ZnO nanostructures degraded 91.75% of Reactive Blue-81 dye within 105 minutes under UV light, while demonstrating excellent efficiency across key performance indicators such as quantum yield, space-time yield, and energy consumption. Importantly, the process required comparatively low energy, making it a costeffective option. Beyond pollutant degradation, the nanoparticles also showed strong antibacterial activity against Staphylococcus aureus and Pseudomonas aeruginosa. The combined photocatalytic and antimicrobial performance highlights the potential of CTAB-modified ZnO nanostructures as a dual-function material for sustainable water treatment and pathogen control.

ORDERED MNG-COMPOSITE BASED ON A CUBIC LATTICE OF METAL NANOCYLINDER DIMERS

L. O. Abramenko¹, A. V. Korotun^{1,2}, V. M. Matiushyn¹

¹Zaporizhzhia Polytechnic National University, Zaporizhzhia, 69011, Ukraine ²G.V. Kurdyumov Institute for Metal Physics of National Academy of Sciences of Ukraine, Kyiv, 03142, Ukraine

Currently, the activities of many scientific teams are focused on the synthesis of artificial environments with negative refraction [1]. One of the candidates for such media are ordered composites based on cubic lattices of dimers of metal nanoparticles of various shapes. In particular, in [2], a frequency band was determined in the optical range where a composite with dimers of spherical nanoparticles has a negative refractive index, i.e. the real part of the effective dielectric and magnetic permeability of such a material is negative. It should be noted that it is much easier to achieve the condition $Re\epsilon_{\rm eff} < 0$ (ENG-materials) than $Re\mu_{\rm eff} < 0$ (MNG-materials), and the frequency band found in [2] where both of the above inequalities are satisfied (DNG-materials) is very narrow. In view of this, as well as the fact that there are many control parameters by changing which the condition can be satisfied $Re\mu_{\rm eff} < 0$, finding the shapes and sizes of particles that provide the required optical properties is a complex and urgent task.

Consider an ordered composite in which dimers of cylindrical metal nanoparticles are embedded in a medium with dielectric permeability $\epsilon_{\rm m}$ and magnetic permeability $\mu_{\rm m}=1$ such that these dimers are located on the lateral faces of cubic cells (Fig. 1). We assume that the length of a cylindrical nanoparticle L, the diameter of its base D, the distance between particles in the dimer d_0 , and the length of an edge of the unit cell a_l .

The expression for the effective magnetic permeability of the studied composite has the form

$$\mu_{\text{eff}} = 1 + 3\beta \left(\frac{kd}{2}\right)^{2} \frac{1}{\frac{3}{16}D^{2}L\left(\frac{1}{\alpha_{\perp}} + \frac{2}{\alpha_{\parallel}} - \frac{3}{\epsilon_{\text{m}}d^{3}}\right) - \beta \left(\frac{k_{0}d}{2}\right)^{2}},$$
(1)

where the wave number of the incident light $k=\omega\sqrt{\epsilon_{\rm m}}/c$; metal content in the unit cell of the composite $\beta=3\pi D^2L/2a_{\rm l}^3$, and the diagonal component of the

polarizability tensor of a cylindrical nanoparticle within the framework of the equivalent prolate spheroid approach [3]

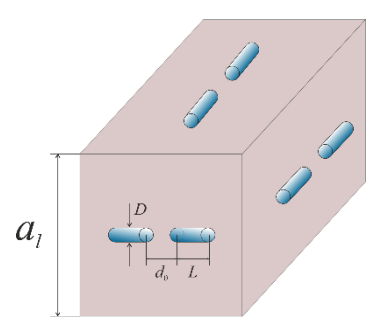


Fig. 1. Unit cell of the studied composite.

$$\alpha_{\perp(||)}(\omega) = V \frac{\epsilon^{\perp(||)}(\omega) - \epsilon_{m}}{\epsilon_{m} + \mathcal{L}_{\perp(||)}(\epsilon^{\perp(||)}(\omega) - \epsilon_{m})}, \tag{2}$$

 $V = \frac{\pi}{4}D^2L$ is the volume of a cylindrical particle.

In formula (2), the depolarization factors

$$\mathcal{L}_{\parallel} = \frac{\varrho_{\text{eff}}^{2}}{2(1 - \varrho_{\text{eff}}^{2})^{3/2}} \left(\ln \frac{1 + \sqrt{1 - \varrho_{\text{eff}}^{2}}}{1 - \sqrt{1 - \varrho_{\text{eff}}^{2}}} - 2\sqrt{1 - \varrho_{\text{eff}}^{2}} \right), \qquad \mathcal{L}_{\perp} = \frac{1}{2} (1 - \mathcal{L}_{\parallel}); \quad (3)$$

aspectual and effective aspectual relation

$$\varrho = \frac{D}{L}, \qquad \qquad \varrho_{\text{eff}} = \frac{\sqrt{3}}{2} \varrho;$$

diagonal components of the dielectric tensor

$$\epsilon_{\perp(\parallel)}(\omega) = \epsilon^{\infty} - \frac{\omega_p^2}{\omega(\omega + i\gamma_{\text{eff}}^{\perp(\parallel)})},$$
(4)

where ϵ^{∞} is the contribution of the crystal lattice to the dielectric constant, ω_p is the plasma frequency, and the transverse and longitudinal components of the relaxation rate are determined by the additive contributions of bulk and surface relaxation and radiative damping

$$\gamma_{\text{eff}}^{\perp(\parallel)} = \gamma_{\text{bulk}} + \gamma_{\text{surf}}^{\perp(\parallel)} + \gamma_{\text{rad}}^{\perp(\parallel)}. \tag{5}$$

In expression (5) γ_{bulk} = const for a particular metal, and the relations for the surface relaxation rates and radiative decay have the form [4]

$$\gamma_{s}^{\perp(\parallel)} = \mathcal{I}_{\perp(\parallel)} \frac{v_{F}}{\ell_{\perp(\parallel)}}; \qquad \gamma_{rad}^{\perp(\parallel)} = \mathcal{I}_{\perp(\parallel)} \frac{v_{F}}{\ell_{\perp(\parallel)}}, \qquad (6)$$

where the effective trajectory lengths are $\;\ell_{\scriptscriptstyle \perp}=D\;$, $\;\ell_{\scriptscriptstyle \parallel}=L\;$;

$$\mathcal{L}_{\perp(\parallel)} = \frac{9}{16} \frac{\mathcal{L}_{\perp(\parallel)}}{\epsilon_{m} + \mathcal{L}_{\perp(\parallel)} (1 - \epsilon_{m})} \left(\frac{\omega_{p}}{\omega}\right)^{2} \mathcal{F}_{\perp(\parallel)} (\varrho_{eff});$$

$$\mathcal{P}_{\perp(\parallel)} = \frac{9V}{128\pi} \frac{\mathcal{L}_{\perp(\parallel)}}{\sqrt{\epsilon_{m} \left[\epsilon^{\infty} + \left(\frac{1}{\mathcal{L}_{\perp(\parallel)}} - 1\right)\epsilon_{m}\right]}} \left(\frac{\omega_{p}}{c}\right)^{3} \left(\frac{\omega_{p}}{\omega}\right)^{2} \mathcal{F}_{\perp(\parallel)} (\varrho_{eff}), \tag{7}$$

and size-dependent functions

$$\mathcal{I}_{\perp}(\varrho_{\text{eff}}) = \left(1 - \varrho_{\text{eff}}^{2}\right)^{-\frac{3}{2}} \left\{ 2\left(\frac{3}{4} - \varrho_{\text{eff}}^{2}\right) \left(\frac{\pi}{2} - \arcsin\varrho_{\text{eff}}\right) + \varrho_{\text{eff}}\left(\frac{3}{2} - \varrho_{\text{eff}}^{2}\right) \sqrt{1 - \varrho_{\text{eff}}^{2}} \right\};$$

$$\mathcal{I}_{\parallel}(\varrho_{\text{eff}}) = \left(1 - \varrho_{\text{eff}}^{2}\right)^{-\frac{3}{2}} \left\{ \frac{\pi}{2} - \arcsin\varrho_{\text{eff}} + \varrho_{\text{eff}}\left(1 - 2\varrho_{\text{eff}}^{2}\right) \sqrt{1 - \varrho_{\text{eff}}^{2}} \right\}.$$
(8)

Calculations of the frequency dependence of the real part of the effective magnetic permeability were performed for an ordered nanocomposite, the matrix medium of which is CaO, and the inclusions are dimers of silver nano-sized cylinders with different base diameters (Fig. 2).

The results of the calculations indicate an expansion of the spectral interval in which the studied nanocomposite is an MNG material with an increase in diameter, however, this expansion occurs in the region of higher frequencies (ultraviolet range). According to the nature of curves 1, 2 and 3, it can be noted that the condition $Re\mu_{\text{eff}} < 0$ begins to be fulfilled from frequencies slightly higher than the frequency at which the function $Re\mu_{eff}\left(\omega\right)$ reaches a maximum ($\omega^* \geq \omega_{max}$). In addition, in order for the frequency band in which $Re\mu_{eff} < 0$ is wider, $max\{Re\mu_{eff}\}$ must have a large amplitude.

Therefore, in order for the condition $Re\mu_{eff} < 0$ to be fulfilled in a wider spectral interval, it is necessary to select the materials (the matrix dielectric and the metal of the dimer-inclusions) in such a way that $max\{Re\mu_{eff}\}$ is large and is achieved at the lowest possible frequency $\,\omega_{_{max}}\,.$

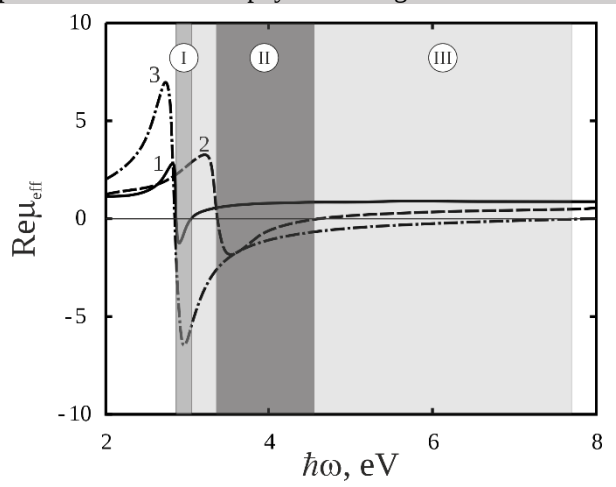


Fig. 2. Frequency dependences of a nanocomposite based on cylindrical Ag nanodimers in CaO for different cylinder diameters: $1-D=20~\rm nm$; $2-D=40~\rm nm$; $3-D=60~\rm nm$.

Thus, it was established that the greatest influence on the width of the frequency band in which the studied composite is an MNG-material is exerted by the diameter of the nanocylinders, as well as the optical characteristics of the matrix dielectric and the metal of the inclusion particles.

- [1] *Handbook of Nano-Metamaterials* by Ed. B. Choudhury, V. K. Tewary, K. K. Varikuntla (Springer, 2025).
- [2] L. O. Abramenko, V. M. Matiushyn, and A. V. Korotun, Funct. Mater. 32, 21 (2025).
- [3] A. V. Korotun, Ya. V. Karandas, and V. I. Reva, Ukr. J. Phys. 67, 849 (2022).
- [4] N. I. Pavlyshche, A. V. Korotun, V. P. Kurbatsky, and R. Yu. Korolkov, Funct. Mater. 32, 108 (2025).

FORMATION OF NANO-SIZED SOLIDIFICATION STRUCTURE AND SPECIFIC SEGREGATION OF COMPONENTS IN MEDIUM-ENTROPIC CO-NI-CR ALLOYS

V. K. Nosenko, O. P. Fedorov, T. V. Pryadko, V. A. Dekhtyarenko, T. P. Vladimirova, O. M. Semyrga, I. V. Zagorulko G. V. Kurdyumov Institute for Metal Physics of the N.A.S. of Ukraine, Kyiv, 03142, Ukraine

The concept of an alloy with several principal components with different crystal structures (or a five-component alloy without a base element), proposed by Cantor et al. [1], marked the beginning of a new era in the development of metallic materials widely known as high-entropy alloys (HEAs). The unexpected formation of a ductile single-phase microstructure instead of the anticipated brittle intermetallic compounds was explained by the high mixing entropy and immediately attracted the attention of the scientific community. Variants of the Cantor alloy, called medium-entropy alloys (MEAs), are of significant interest since they demonstrate better industrial potential than both HEAs and conventional alloys. Among the 15 possible equiatomic MEA combinations obtained by Cantor, the ternary CrCoNi and quaternary CrFeCoNi alloys have shown the most attractive properties [2]. At the same time, it was found [3] that the ternary CrCoNi alloy exhibits even better properties at 77 K. Therefore, in the present work we consider an equiatomic medium-entropy alloy containing only three principal elements, CrCoNi, which forms a single-phase solid solution with a face-centered cubic (FCC) lattice and demonstrates strength and toughness values exceeding those of all high-entropy alloys and most multiphase industrial alloys. At room temperature, the alloy exhibits an ultimate tensile strength of nearly 1 GPa, a fracture strain of ~70%, and a fracture toughness K_{JIc} above 200 MPa·m^{1/2}. At cryogenic temperatures, the strength, ductility, and toughness of the CrCoNi alloy improve further, reaching levels of strength above 1.3 GPa, fracture strain up to 90%, and K_{JIc} of 275 MPa·m^{1/2}, approaching the best values ever reported. Such properties are most likely the result of continuous strain hardening, which suppresses plastic instability arising from pronounced dislocation activity and deformation-induced nanotwinning [4].

The mechanical and corrosion properties of the CrCoNi alloy are largely determined by the hierarchy of defect systems and their interactions (grain boundaries, stacking faults, dislocation clusters). The latter may arise both from inhomogeneities caused by chemical nature and from various external influences.

Therefore, variations in cooling rates and thermo-temporal treatments of the melt appear to be a promising additional tool.

The following are the results of preliminary studies on the effect of cooling rate on the formation of the primary crystalline structure of the equiatomic medium-entropy alloy CrCoNi with a minor technological impurity of silicon (1.5–1.6 at.% Si). Figure 1 presents the DSC heating and cooling curves obtained at different rates for this alloy, which was melted in an induction furnace under a high-purity argon atmosphere using a quartz crucible.

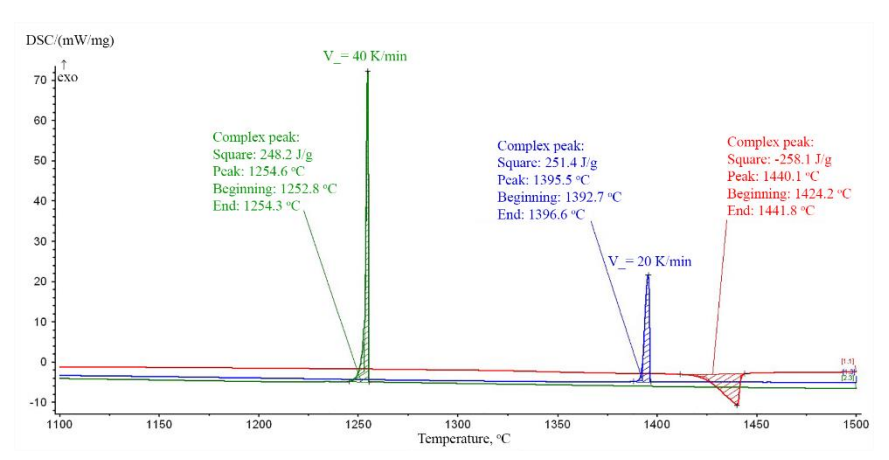


Fig. 1. DSC heating and cooling curves of the Co-Ni-Cr alloy at a rate of 20 K/min and 40 K/min.

The Co-Ni-Cr alloy is capable of undercooling below the liquidus temperature by 44 K during slow cooling. In this case, crystallization occurs within a few seconds over a temperature interval of 3 K (Fig. 1, V=20 K/min). With an increase in the cooling rate, the Co-Ni-Cr alloy exhibits an undercooling of 184 K, and the crystallization of a single-phase solid solution takes place within a narrow interval of 1.5 K (Fig. 1, V=40 K/min).

Even at relatively small degrees of undercooling, achieved during solidification of the melt in a graphite mold, an extremely fine (submicron) primary FCC solid solution structure is formed (Fig. 2). During heat treatment (HT) at 1200 °C in vacuum for 2 hours, recrystallization occurs in the alloy, accompanied by grain growth (Fig. 3). In certain regions slightly enriched with chromium, twinning is observed. Individual dark precipitates of submicron size in the as-solidified state, and of micron size after HT, are identified as silicon oxides.

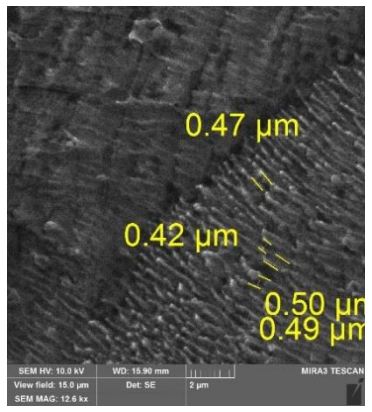


Fig. 2. Image of the initial structure of Co-Ni-Cr alloy the ingot after electrochemical etching (scanning electron microscopy).

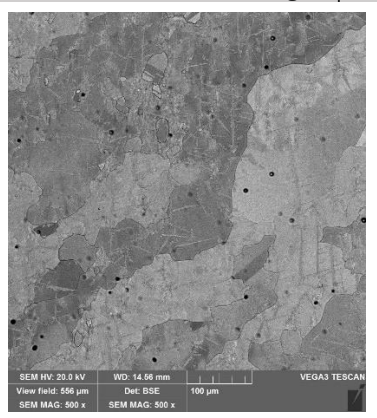


Fig. 3. Alloy sample annealed at 1200 °C in vacuum for 2 hours.

It was found that as a result of HT, the hardness of the HV alloy decreases from 181 to 152.

The authors of [5] note that element segregation around line defects is common in high-entropy alloys (HEAs) and has a significant impact on their mechanical properties. The driving force for segregation generally competes with the formation of chemical short-range order (CSRO), which complicates the understanding of segregation mechanisms. The beneficial effect of elemental segregation on interfacial properties – namely, improved grain boundary strength and a considerable increase in elongation to fracture – has been confirmed by experimental comparisons of the properties of CoNiCrFe alloys with varying Fe additions [5]. This publication highlights the mechanism of heterogeneous elemental distributions in HEAs, where segregation and CSRO coexist, thereby offering the possibility to tailor mechanical properties through modulation of compositional variations.

A recent study [6] demonstrates how a compromise between strength and resistance to crack propagation (fracture toughness) can be achieved through thermomechanical produces processing that partially recrystallized heterogeneous microstructure. The equimolar CrCoNi alloy was rolled at room temperature to generate a high density of three-dimensional crystallographic defect networks. Subsequent heat treatment induced localized recrystallization, resulting in a bimodal microstructure consisting of hard, unrecrystallized grains and soft, recrystallized grains. In this state, the yield strength at 298 K increased by a factor

of 2.75 compared to previously reported values for the same alloy in a fully recrystallized state, while the fracture toughness remained comparable. The yield strength was further enhanced at 77 K without any deterioration in fracture toughness. This favorable strength—toughness combination at 77 K appears to arise from the composite-like nature of the microstructure, where unrecrystallized grains provide strength and recrystallized grains contribute ductility by dissipating stress during crack propagation.

Thus, a new class of medium-entropy alloys produced by induction melting in an inert atmosphere has been presented. In the as-cast state, the alloy exhibits sufficiently high hardness and ductility, while retaining its single-phase FCC structure after HT at 1200 °C. The combination of these properties makes this alloy promising for further modification through targeted alloying, refining, and high-rate melt solidification, as well as thermomechanical processing (forging or rolling) followed by HT for controlled recrystallization. The results obtained in this study indicate the potential for significant enhancement of strength and toughness by employing thermomechanical processing methods aimed at controlling the degree of recrystallization in the alloy.

- [1] Cantor B, Chang I, Knight P, Vincent A. Mater Sci Eng 2004;375e377:213e8., Pages 213-218
- [2] Fabio Da Costa Garcia Filho, Robert O. Ritchie, Marc Andre Meyers, Sergio Neves Monteiro. Journal of materials research and technology 2022;17:1868 e1895
- [3] Gludovatz B, et al. Nat Commun 2016;7:10602
- [4] Jun Ding, Qin Yu, Mark Asta, and Robert O. Ritchie Edited by William D. Nix, Stanford University, Stanford, CA, and approved July 25, 2018 (August 20, 2018 115 (36) 8919-8924
- [5] Ma S., et al. Acta Materialia. 2024. 264(1). 119537
- [6] Connor E. Slone, et al. Communications Materials volume 5, Article number: 263 (2024)

DIELECTRIC RESPONSE OF HfxZr1-xO2 NANOPARTICLES AND **NANOCOMPOSITES**

Oleksii V. Bereznykov¹, Oleksandr S. Pylypchuk¹, Victor V. Vainberg¹, Vladimir N. Poroshin¹, Oksana V. Leshchenko², Victor N. Pavlikov², Eugene A. Eliseev² and Anna N. Morozovska¹

¹ Institute of Physics, National Academy of Sciences of Ukraine,46, Nauky Avenue, 03028 Kyiv, Ukraine

² Frantsevich Institute for Problems in Materials Science, National Academy of Sciences of Ukraine, 3, str. Omeliana Pritsaka, 03142 Kyiv, Ukraine

The Hf_xZr_{1-x}O₂-based nanomaterials are extremely promising materials in modern electronics: they demonstrate unique polar, ferroelectric and dielectric properties and are compatible with silicon technology [1]. At present any direct experimental observation of the ferroelectric properties of Hf_xZr_{1-x}O₂ nanoparticles are absent. Several observations of the o-phases mixture (Pca2₁, Pbca and Pbcm) in the small size (3 - 30 nm) Hf_xZr_{1-x}O_{2-y} nanoparticles were obtained by the X-ray diffraction (XRD) analysis [1]. Unfortunately, these experimental observations are not convincing, because only the o-phase *Pca2*₁ is ferroelectric; the o-phases *Pbca* and *Pbcm* are neither polar nor ferroelectric-like, and the problem requires further studies.

Recently, a "colossal" dielectric response was found in Hf_xZr_{1-x}O₂ nanoparticles (x = 1, 0.6, 0.5 and 0.4) of the 7 - 15 nm size prepared by the solid state organo-nitrate synthesis [2]. We obtained that the dielectric permittivity of the pressed nanopowders of $Hf_xZr_{1-x}O_2$ reached at x = 0.4 and low frequencies colossal values of~1.5×10³ and ~1.5×10⁵, increasing with temperature in the range of 38– 88°C. An almost mirror-like behavior of the temperature dependences of the dielectric permittivity and specific conductivity has been observed (see details in Ref.[2] and Fig. 1). We have shown [2] that these correlations of permittivity and resistivity may be well described based on the Heiwang barrier model [3], applied together with the hopping conduction model in semiconductor ferroelectrics.

For further experimental studies, we prepared nanocomposites: polymer P(VDF-TrFE) with the same Hf_{0.4}Zr_{0.6}O₂ nanoparticles (the content about 30 wt/%) as used in the work [2]. The thickness of the synthesized films was 190 and 280 μm. Measurements of the frequency dependences of the dielectric permittivity and the tangent of the dielectric loss angle were carried out at room temperature, in the frequency range from 4 Hz to 0.5 MHz. In this case, the sample was placed on a measuring stand between two asymmetric contacts, the smaller contact, the area of which is 1 mm², was covered with indium, to avoid possible voids under the contact plate. This also allowed minimizing the influence of the film surface microrelief and provided the opportunity to repeatedly check the uniformity of the film in macro-inhomogeneities of the nanoparticles distribution. Measurements of frequency dependences were carried out on several areal parts of the films.

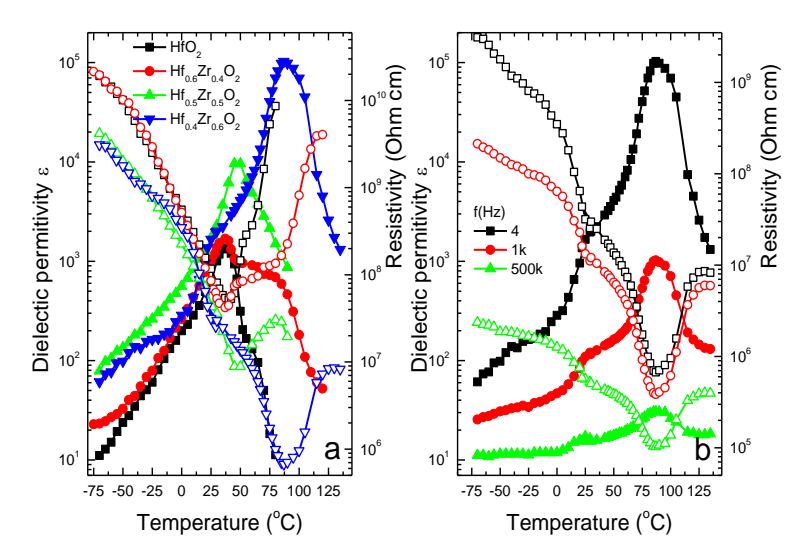


Fig. 1. Temperature dependences of the relative dielectric permittivity (filled symbols) and resistivity (empty symbols) of the pressed $Hf_xZr_{1-x}O_2$ nanopowders measured at the frequency 4 Hz (a) and for $Hf_{0.4}Zr_{0.6}O_2$ nanopowders (b) measured at frequencies 4 Hz, 1 kHz to 500 kHz. The amplitude of the test sinusoidal voltage is 100 mV. Adapted from Ref.[2].

The measurement results depended weakly on both the area positions on the film surface and the thickness of the films within the specified limits of 190 and 280 μm, which indicates good reproducibility of their synthesis technology. **Figure 2(a)** and **2(b)** present the results of measuring the frequency dependence of the dielectric permittivity, loss tangent, and resistivity for P(VDF-TrFE) films with Hf_{0.4}Zr_{0.6}O₂ nanoparticles with thickness of 280 nm and 190 nm, respectively. The dielectric permittivity at low frequencies has a rather large value (about 60 - 70). With increasing frequency, it gradually decreases down to 10, while on some permittivity curves there is a slight inflection, which corresponds to the local minimum of dielectric losses. At high frequencies, the value of the dielectric permittivity almost does not change. The loss tangent also has a local maximum at low frequencies (slightly more than 2). At first, with increasing frequency, it drops very sharply, then gradually towards negligibly small values. We observe certain correlations between the frequency dependence of the dielectric permittivity, losses and resistance, which can be seen in Fig. 2. Note the local minimum at the frequency dependences of the dielectric losses, which correlate with the inflexion at the permittivity frequency dependences, as well as with the similar feature at the resistivity frequency dependences. The physical origin of these features in the composite films and their theoretical description is the subject of our current

studies.

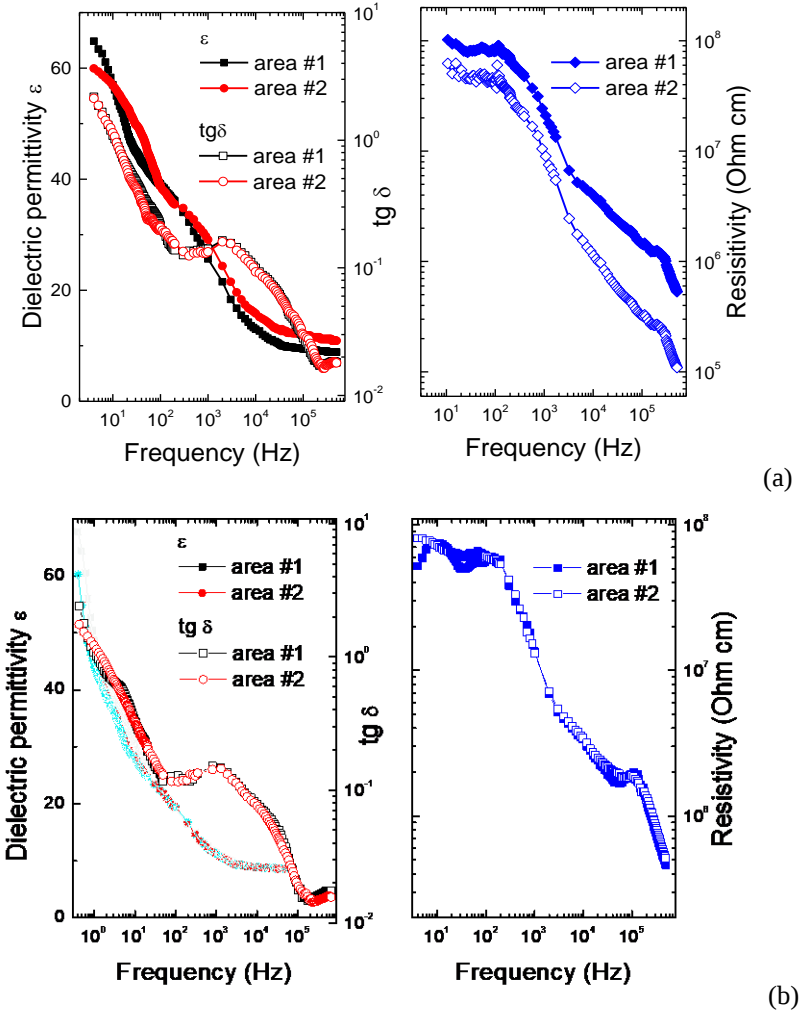


Fig. 2. Frequency dependence of dielectric permittivity and loss tangent for the composite film of P(VDF-TrFE) + Hf_{0.4}Zr_{0.6}O₂nanoparticles for films with thickness of 280 nm (a) and 190 nm (b).

Theoretical modeling of the nanocomposite films dielectric response is performed using the effective medium approximation (EMA), namely the algebraic equation for the effective dielectric permittivity of the binary mixture [2]. Preliminary results of our modelling show that observed peculiarities of the dielectric response can be related to the interfacial barrier-layer capacitance (IBLC) effect [4], as well

as by the inhomogeneous layers between the electrodes and the sample, known as the surface barrier layer capacitance (SBLC) effect [5]. In particular, the colossal dielectric permittivity, observed at low frequencies in the $Hf_xZr_{1-x}O_2$ nanopowders, can originate from the IBLC and/or SBLC effects accompanied by an increase in conduction losses. The EMA describes the IBLC and/or SBLC effects, and, at the same time, includes the limiting cases of the Maxwell layered dielectric model, the Wagner model of spherical nanoparticles, and the columnar model. The fitting results of the measured dielectric response and resistivity, along with the Bayesian optimization using the several working hypotheses of ferroelectric-like response, allow to predict that the ferroelectric-like phase transition may take place in the semiconducting cores of $Hf_xZr_{1-x}O_2$ nanoparticles [2]. We hope that the observed effects can be useful for further development of silicon-compatible ferroelectric nanomaterials, such as $Hf_xZr_{1-x}O_2$ nanoparticles.

Acknowledgments

The work of O.V.B. is funded by the NAS of Ukraine, grant No. 07/01-2025(6) "Nano-sized multiferroics with improved magnetocaloric properties". The work of O.S.P. and A.N.M. are funded by the National Research Foundation of Ukraine (grant N 2023.03/0132 "Manyfold-degenerated metastable states of spontaneous polarization in nanoferroics: theory, experiment and perspectives for digital nanoelectronics"). V.V.V. and V.N.P. acknowledge the Target Program of the National Academy of Sciences of Ukraine, Project No. 5.8/25-II "Energysaving and environmentally friendly nanoscale ferroics for the development of sensorics, nanoelectronics and spintronics". The work of E.A.E is funded by the National Research Foundation of Ukraine (grant N 2023.03/0127 "Siliconcompatible ferroelectric nanocomposites for electronics and sensors"). A.N.M. also acknowledges the support (materials characterization) from the Horizon Europe Framework Programme (HORIZON-TMA-MSCA-SE), project № 101131229, Piezoelectricity in 2D-materials: materials, modeling, and applications (PIEZO 2D). Preparation and characterization of some materials is sponsored by the NATO Science for Peace and Security Programme under grant SPS G5980 "FRAPCOM".

References

- [1] B. Mandal, A.-M. Philippe, N. Valle, E. Defay, T. Granzow, and S. Glinsek. Ferroelectric HfO2–ZrO2 Multilayers with Reduced Wake-Up. ACS Omega, **10** (13), 13141 (2025); https://doi.org/10.1021/acsomega.4c10603
- [2] O. S. Pylypchuk, V. V. Vainberg, V. N. Poroshin, O. V. Leshchenko, V. N. Pavlikov, et al. A colossal dielectric response of HfxZr1-xO2 nanoparticles (2025); https://doi.org/10.48550/arXiv.2508.04697
- [3] W. Heywang. Semiconducting Barium Titanate. J. Materials Science $\bf 6$, 1214 (1971); https://doi.org/10.1007/BF00550094
- [4] J Petzelt, I Rychetsky, D Nuzhnyy, Dynamic ferroelectric—like softening due to the conduction in disordered and inhomogeneous systems: giant permittivity phenomena. Ferroelectrics, **426**, 171-193 (2012); https://doi.org/10.1080/00150193.2012.671732
- [5] J Petzelt, D Nuzhnyy, V Bovtun, M Savinov, M Kempa, I Rychetsky, Broadband dielectric and conductivity spectroscopy of inhomogeneous and composite conductors. Phys. Stat. Sol. A **210**, 2259-2271 (2013); https://doi.org/10.1002/pssa.201329288

INORGANIC OXIDE NANOCOMPOSITES WITH PRONOUNCED BIOACTIVITY FOR BIOMEDICAL APPLICATION (INVITED)

Yu. Yu. Shlapa¹, K. Siposova², A. G. Belous¹

¹V. I. Vernadsky Institute of General and Inorganic Chemistry of the NAS of Ukraine, Kyiv, 03142, Ukraine

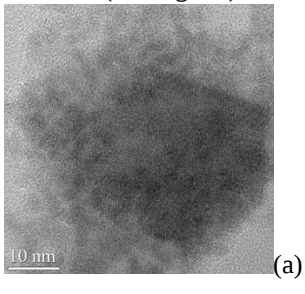
²Institute of Experimental Physics Slovak Academy of Sciences, Kosice, 04001, Slovakia

Magnetic Fe₃O₄ nanoparticles (NPs) have attracted considerable interest due their biocompatibility and biofunctionality. These properties include antimicrobial, antiviral, and antioxidant properties, as well as their ability to generate heat when exposed to an alternating magnetic field [1]. However, Fe₃O₄ NPs are chemically unstable and prone to oxidation in ambient conditions. In order to overcome these limitations, there is a necessity for the development of composite materials, for instance, Fe₃O₄-based "core@shell" nanostructures. This approach offers two key advantages: i) the protective "shell" can significantly improve the chemical stability of Fe₃O₄ NPs by shielding them from oxidation, and ii) the functionalization of Fe₃O₄ NPs with bioactive inorganic materials such as CeO₂ NPs can lead to synergistic effects, enhancing their overall bioactivity compared to individual NPs.

The primary objective of this study was to synthesize Fe₃O₄@CeO₂ nanocomposites (NCPs) with a uniform and stable shell coating, to characterize their physicochemical properties, and to evaluate their bioactivity, including antioxidant and anti-amyloid potential. In order to evaluate the interplay between synthesis method, physicochemical parameters and bioactivity of magnetic nanocomposites, two sets of Fe₃O₄@CeO₂ nanocomposites with the varied "shell" thickness were synthesized using two different approaches.

The first set of Fe₃O₄@CeO₂ "core@shell"-like NCPs was synthesized by deposition of CeO₂-"shell" with the theoretically calculated thickness of 3-, 5-, and 7-nm onto the surface of the pre-fabricated Fe₃O₄ NPs. The HRTEM and EELS studies demonstrated the following morphology of the collected NCPs: a Fe₃O₄ NP "core" with an average size of approximately 23 nm was neatly surrounded by CeO₂ NPs with an average size of approximately 3-3.5 nm (see Fig. 1a). Nonetheless, it was determined that the surrounding was non-uniform. These were hypothesised to be associated with the particle size distribution, a factor which had not been considered in the theoretical calculations of the "shell"-thickness. The second set of Fe₃O₄@CeO₂ "core@shell"-like NCPs was synthesised using the "layer-by-layer" deposition approach, whereby 3-, 5- and 7-layer of CeO₂ "shell" were deposited onto the surface of pre-fabricated Fe₃O₄ NPs. The HR TEM data

and elemental analysis revealed that the synthesis route affects significantly the morphology of the obtained nanocomposites. The "layer-by-layer" deposition approach ensures the obtaining NCPs in which ultrafine CeO_2 NPs are uniformly anchored on the surface of Fe_3O_4 NPs, resulting in the formation of "hedgehog"-like "core@shell" NCPs (see Fig. 1b).



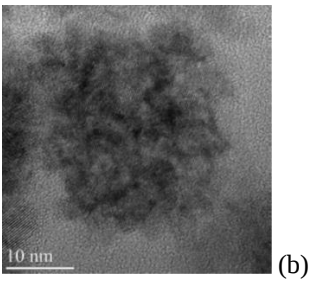


Fig. 1. Representative HRTEM images for Fe $_3O_4$ @CeO $_2$ NCPs: (a) Fe $_3O_4$ @CeO $_2$ NCPs with a theoretically calculated "shell"-thickness of "5 nm"; (b) Fe $_3O_4$ @CeO $_2$ NCPs with a 5-layers "shell" synthesised via "layer-by-layer" deposition.

X-ray photoelectron spectroscopy (XPS) data has validated that Fe^{2^+}/Fe^{3^+} and Ce^{4^+}/Ce^{3^+} on the surface of $Fe_3O_4@CeO_2$ NCPs participate in the redox processes during the nanocomposite's formation. It has been demonstrated that, independently on the synthesis method, the presence of CeO_2 NPs on the surface of Fe_3O_4 NPs in the nanocomposites increases their colloidal stability in the aqueous suspensions, but decreases their saturation magnetization values. However, the composites preserve their ability to heat up effectively and controlled in the alternating magnetic field.

The experimental data, collected for two sets of Fe₃O₄@CeO₂ NCPs synthesised via different routes indicate that the chemical state of the surface and the morphology of NCPs play a crucial role in the synergistic enhancement of bioactivity of Fe₃O₄@CeO₂ NCPs [2], suggesting the possible mechanism for such biofunctionality. In particular, Fe₃O₄@CeO₂ NCPs, whose surface was enriched with simultaneous Fe²⁺ and Ce³⁺ sites available for biocatalytic processes, keeps the most pronounced combined catalase/peroxidase-like activities. In view of these findings, Fe₃O₄@CeO₂ NCPs developed thus far can be recommended for consideration as mediators for magnetic thermal therapy (like individual Fe₃O₄ NPs) or even suggest a possible enhancement in bioactivity in the condition of controlled local heating.

^[1] N. Zhu, et al., Nanomaterials, **8(10)**, 810 (2018).

^[2] Yu. Shlapa, et al., ACS Appl. Mater. Interfaces, 15, 49346 (2023).

ON THE (NON)MONOTONIC STRAIN DEPENDENCE OF THE ENERGY GAP IN THE BAND STRUCTURE OF PHOSPHORENE

M. V. Los¹, I. Yu. Sahalianov², T. M. Radchenko¹, V. A. Tatarenko¹ ¹G.V. Kurdyumov Institute for Metal Physics of the N.A.S. of Ukraine, Kyiv, UA-03142, Ukraine ²Linköping University, Norrköping, SE-60174, Sweden

Black phosphorene has emerged and gained prominence as a quasi-2D material during the post-graphene-discovery period due to its promising electronic properties. Of particular interest is its direct band gap, which can be tuned by varying the material thickness and applying mechanical strain. The latter is the subject of the study in this report.

Like graphene, phosphorene possesses exceptional mechanical properties [1, 2]: it can withstand nondestructive elastic strains up to its failure limits of circa 27– 30% [1] for uniaxial strains and 10–13% [3, 4] for shear strains, depending on the stretching and shearing directions, zigzag (x in Fig. 1) or armchair (y in Fig. 1). The ultimate tensile and shear strengths of phosphorene still seem debatable, since others report a tensile strength of circa 11% (48%) [5] and even 35% (70%) [6] along the zigzag (armchair) direction, and a 30-35% [7] shear strength. Such flexibility offers us an opportunity to consider phosphorene (as an alternative to graphene) as a suitable object of study in a still relatively new research field in condensed matter physics known as "straintronics", in which the strain-induced physical effects in solids act as a tool for tuning the electronic properties.

In recent phosphorene-related studies [8, 9], the authors revealed the linear

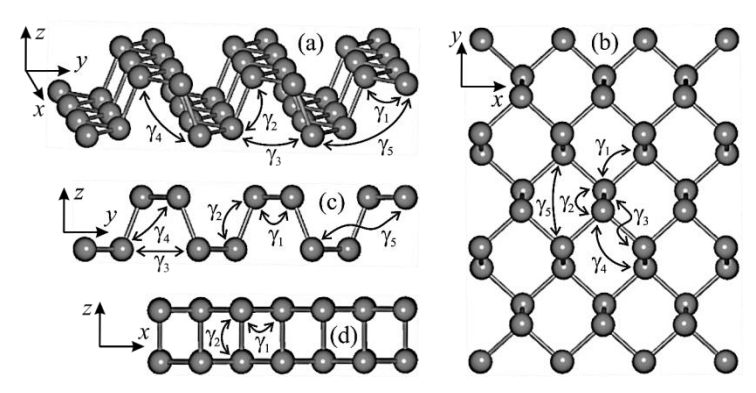


Fig. 1. Perspective (a) and top (b–d) views of the phosphorene crystal lattice, where y_1-y_5 are the hopping integrals for the first five nearest-neighbour atoms.

dependence of the band gap vs. the uniaxial tensile or shear strain (Fig. 2) within the tight-binding (TB) model with both exponential [8] and inversely quadratic [9] bond-length-dependent adjustments to the hopping parameters (γ_1 – γ_5) denoted in Fig. 1. However, here we claim that the strain dependence of the band gap is not linear within the TB model if a certain mechanical characteristic of phosphorene is valid.

We simulated the effect of uniaxial tensile and shear strains (Fig. 2) on the band gap of a phosphorene monolayer of realistic size, comprised of millions of P atoms, using a TB approach. In our model, the initial hopping integrals are adjusted depending on the change in bond lengths resulting from the in-plane and out-of-plane deformation responses to the applied strain. The unique behaviour of the Poisson's ratio as a nonlinear nonmonotonic function of strain, as opposed to its more commonly being a constant, is taken into account, resulting in a correspondingly nonlinear nonmonotonic strain dependence of the band gap (Fig. 3b).

The obtained TB results [10] demonstrate the correlation between mechanical and electronic properties. We conclude that if the response strain is linear and consequently the Poisson's ratio is constant, then the strain-dependent band gap behaves linearly in phosphorene, similar to graphene. This behaviour contradicts the DFT results, which predict that the band gap varies nonlinearly if the phosphorene undergoes expansion (compression) along the armchair or zigzag direction. The disagreement between the TB and DFT findings is overcome by considering the nonlinear contributions in the strain-dependent in-layer and out-of-layer Poisson's ratios. Moreover, if, in addition to the nonlinearity, the Poisson's ratio is nonmonotonic with strain, this behaviour of the mechanical characteristic is reflected in its electronic counterpart: the band gap varies nonmonotonically as well.

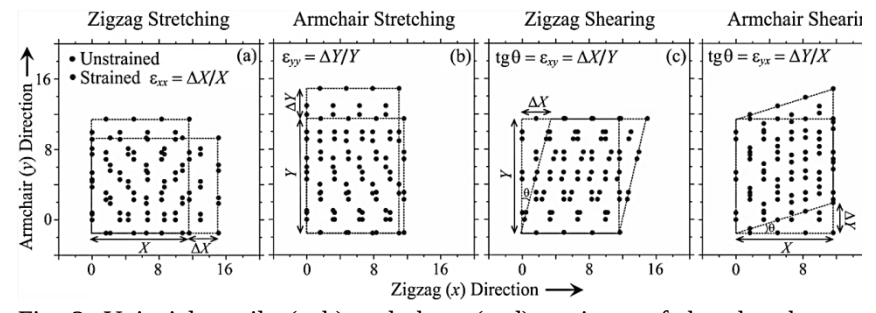


Fig. 2. Uniaxial tensile (a–b) and shear (c–d) strains ε of the phosphorene lattice along two mutually perpendicular directions, zigzag (x) and armchair (y): top

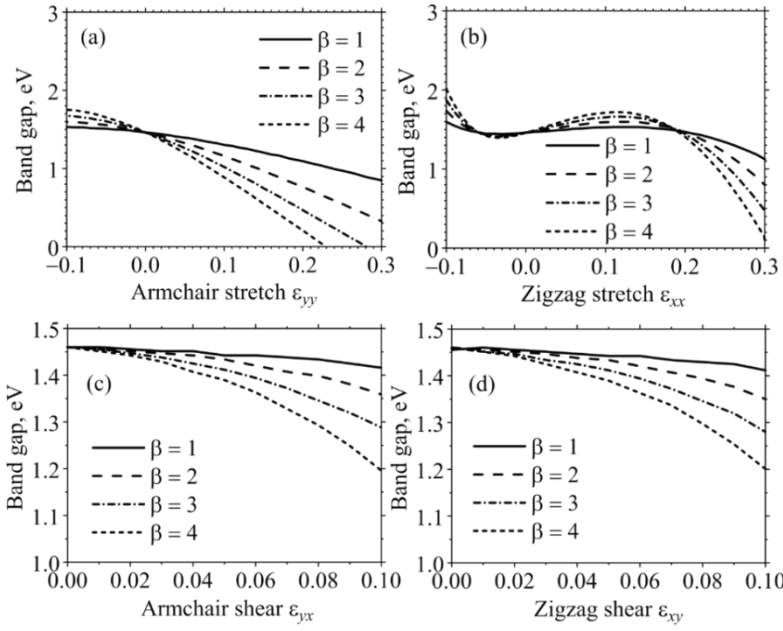


Fig. 3. Influence of the uniaxial tensile (a, b) and shear (c, d) strains on the band gap in the phosphorene electronic structure for various values of the model parameter $\beta = 1, 2, 3, 4$ acting as a decay rate, and various strain directions: armchair (a, c) and zigzag (b, d).

- [1] Q. Wei and X. Peng, Appl. Phys. Let. 104, 251915 (2014).
- [2] X. Peng, Q. Wei, and A. Copple, Phys. Rev. B, 90, 085402 (2014).
- [3] B. Sa et al., Nanotechnology 26, 215205 (2015).
- [4] S. M. Hatam-Lee, H. Peer-Mohammadi, and A. Rajabpour, Mater. Today Commun. 26, 101796 (2021).
- [5] J.-W. Jiang and H. S. Park, J. Phys. D: Appl. Phys. 47, 385304 (2014).
- [6] G. Sahoo and A. Biswal, *Physica B*, **697**, 416742 (2025).
- [7] Y. S. Ranawat and R. Jain, arXiv:1512.05392 (2015).
- [8] A. G. Solomenko, I. Y. Sahalianov, T. M. Radchenko, and V. A. Tatarenko, Sci. Rep. 13, 13444 (2023).
- [9] A. G. Solomenko, I. Y. Sahalianov, T. M. Radchenko, and V. A. Tatarenko, Mol. Cryst. Liq. Cryst. 768, 238 (2024).
- [10] M. V. Los et al., *J. Phys. Chem. C* (2025). https://doi.org/10.1021/acs.jpcc.5c02637

ROOM TEMPERATURE MULTIFERROICS ON THE BASE OF SINGLE-PHASE PEROVSKITES PFN AND PFT DOPED WITH Mn IONS

Andrii V. Bodnaruk¹, Anna N. Morozovska¹, Yuriy O. Zagorodniy², Victor N. Pavlikov², Oksana V. Leshchenko², Myroslav V. Karpets^{2,3}, and <u>Eugene A.</u> Eliseev²

¹ Institute of Physics, National Academy of Sciences of Ukraine,46, Nauky Avenue, 03028 Kyiv, Ukraine

² Frantsevich Institute for Problems in Materials Science, National Academy of Sciences of Ukraine, 3, str. Omeliana Pritsaka, 03142 Kyiv, Ukraine
 ³ Ye. O. Paton Institute of Materials Science and Welding, National Technical University of Ukraine "Igor Sikorsky Kyiv Polytechnic Institute", 37, Beresteisky Avenue, Kyiv, Ukraine, 03056

Experimental and theoretical studies of single-phase room temperature magnetoelectrics (ME), such as solid solutions of perovskites Pb(Fe_{1/2}Nb_{1/2})O₃ (PFN) and Pb(Fe_{1/2}Ta_{1/2})O₃ (PFT), are very important [1, 2, 3]. PFN is an antiferromagnet with G-type spin ordering below at T<T_{Neel}, where the Neel temperature T_{Neel}=143-170 K. PFN is a ferroelectric at temperatures T<T_{Curie}, where its Curie temperature varies in the range T_{Curie}=379 – 393K. PFN has a biquadrartic ME coupling constant 2.2×10⁻²² sm/(VA) at 140K. PFT is an antiferromagnet with the Neel temperature T_{Neel}= 133-180 K and ferroelectric at T<T_{Curie} with the Curie temperature T_{Curie} \approx 250 K. PFT has a biquadrartic ME coupling constant of the same order as that of PFN.

We sintered the ceramics of PFN and PFT doped with 0, 5, 10, 15 and 30 % of Mn ions and study their phase composition, magnetic and ferroelectric properties at room temperature. The XRD analysis confirmed the perovskite structure of the sintered samples. Polarization measurements revealed the ferroelectric hysteresis in the ceramic samples of PFN and PFN doped with Mn (see **Fig. 1(a)**). Magnetostatic measurements, performed using an LDJ 9500 magnetometer with a vibrating sample, reveal the ferromagnetic properties of PFN doped with 5-10 % of Mn, and the paramagnetic behavior or a very weak antiferromagnetic saturation of magnetization in other PFN and PFT ceramics doped with Mn ions (see **Fig. 1(b)**).

We evolved a theoretical model focused on the multiferroic properties, including the appearance of anomalously large value of magnetoelectric coefficient. The comparison of the model with experiments allows establishing the boundaries between the ferroelectric, paramagnetic, antiferromagnetic, ferromagnetic and magnetoelectric phases in the perovskites $Pb(Fe_{1/2}Nb_{1/2})O_3$ (PFN) and $Pb(Fe_{1/2}Ta_{1/2})O_3$ (PFT) doped with Mn ions.

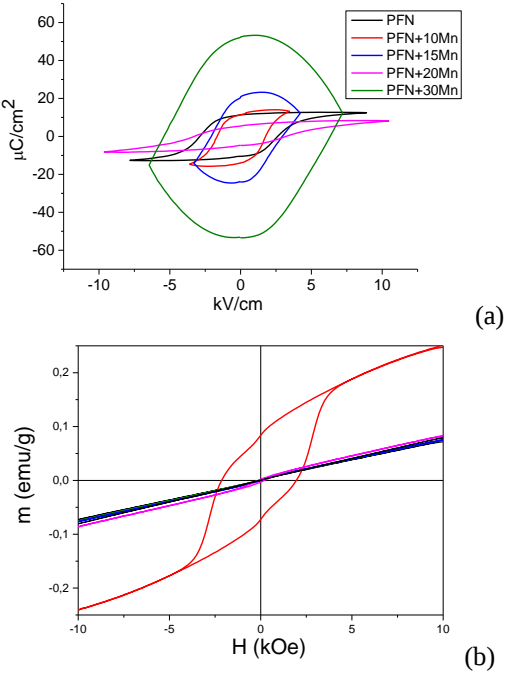


Fig. 1. Polarization hysteresis (a) and magnetization field dependence (b) of the PFN doped with 0, 5, 10, 15 and 30 % of Mn ions.

Acknowledgments

The work of A.V.B. and A.N.M. are funded by the NAS of Ukraine, grant No. "Nano-sized multiferroics with improved magnetocaloric 07/01-2025(6) properties" and by the Target Program of the National Academy of Sciences of Ukraine, Project No. 5.8/25-II "Energy-saving and environmentally friendly nanoscale ferroics for the development of sensorics, nanoelectronics and spintronics". The work of Y.O.Z. V.N.P., OV.L. and E.A.E is funded by the NAS of Ukraine.

References

- [1] D.M. Evans, A. Schilling, Ashok Kumar, D. Sanchez, N. Ortega, M. Arredondo, R.S. Katiyar, J.M. Gregg & J.F. Scott. Magnetic switching of ferroelectric domains at room temperature in multiferroic PZTFT. Nature Communications, 4, 1534 (2013).
- [2] Maya D. Glinchuk, Eugene A. Eliseev, Anna N. Morozovska, New room temperature multiferroics on the base of single-phase nanostructured perovskites. J. Appl. Phys. 116, 054101 (2014) DOI: 10.1063/1.4891459
- [3] Maya D. Glinchuk, Eugene A. Eliseev, and Anna N. Morozovska. Theoretical description of anomalous properties of novel room temperature multiferroics Pb(Fe1/2Ta1/2)x(Zr0.53Ti0.47)1-xO3 and Pb(Fe1/2Nb1/2)x(Zr0.53Ti0.47)1-xO3. J. Appl. Phys. 119, 024102 (2016); doi: 10.1063/1.4939584

OPTICAL AND SENSORY PROPETIES OF 2,4-DINITROPHENYLHYDRAZINE-DOPED FUMED SILICA FILMS

Ya. P. Lazorenko¹, V. P. Mitsai²

¹ G.V. Kurdyumov Institute for Metal Physics of the NAS of Ukraine, Kyiv, 03142, Ukraine

² V.G. Baryakhtar Institute of Magnetism of the NAS of Ukraine, Kyiv, 03142, Ukraine

2,4-dinitrophenylhydrazine (DNP) is used as a selective analytical reagent for detecting acetone in solutions or in the air using indicator tubes that change color. Visual assessment based on color change is insensitive and inaccurate. Therefore, it is important to create a sensor film whose optical sensor signal could be determined by a photometric method. It is known that when interacting with acetone, DNP forms a stable complex – hydrazone [1]. As a result, the absorption band caused by π - π * and n- π * electron transitions exhibits a red shift of 14 nm, with a maximum at 363 nm, and its intensity increases [2,3]. Pyrogenic silicon dioxide or fumed silica (Aerosil) can be used as a matrix for DNP immobilization. Fumed silica is a powder of sintered silicon dioxide nanoparticles, combined into aggregates [4] with high textural porosity and large specific surface area necessary for sensitive sensory detection in a gaseous environment [5]. Such highly sensitive and selective sensors are promising for detecting acetone in exhaled air for non-invasive medical diagnosis or monitoring of diabetes mellitus, as acetone levels exceeding 1.8 ppm (parts per million) are observed in this condition [6].

Samples of composite porous films of fumed silica (Aerosil A-380, average particle size 7 nm, surface area 380 m²/g) doped with DNP, created by the method of direct pressing of fumed silica powder in a cylindrical frame on a glass substrate, which had a round shape with a diameter of 2 mm and a thickness of 0.6 mm, were studied. DNP immobilization was carried out from a saturated aqueous solution (0.1 ml of the solution was added to 15.0 mg of Aerosil A-380) with the addition of hydrochloric and orthophosphoric acids to ensure the possibility of proton transfer, necessary for the formation of a complex with acetone. Optical absorption spectra were measured on a Specord M-40 UV-VIS spectrophotometer. Model mixtures of exhaled air with acetone impurities were obtained by the static volumetric method.

In the electronic spectra of optical absorption of fumed silica films with DNP, a significant increase in optical density is observed in the region of 340-520 nm after the introduction of 150000 ppm of acetone into a 4 ml cuvette with a sample

(Fig. 1). The reason for this, as described above, is the bathochromic shift and increase in the intensity of the absorption band of the DNP-acetone complex compared to DNP. The region up to 340 nm was not investigated due to the strong absorption by the glass substrate of the film.

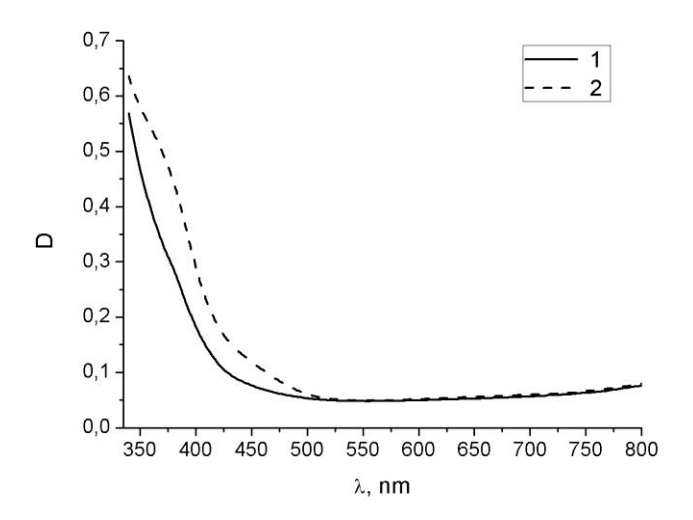


Fig. 1. Optical absorption spectrum of fumed silica film doped with DNP: 1 in air without acetone, 2 – after adsorption of saturated acetone vapor (150000 ppm) in a 4 ml cuvette with the sample. T = 20-25 °C, P = 100 kPa.

When adsorbing acetone molecules from model mixtures of exhaled air (microconcentration range 3-12 ppm), a noticeable increase in the optical absorption of the films was also found, especially at a wavelength of 405 nm. The volume of the pumped air sample with an admixture of microconcentrations of acetone was 1 liter. Fig. 2 shows the dependence of the change in the optical transmittance of such film samples at 405 nm on the acetone concentration. At a concentration of 0 ppm, air in a laboratory room without impurities was taken, which, according to gas chromatographic measurements, contained significantly less than 1 ppm of acetone. The change in optical transmittance ΔT correlates with the acetone concentration in the air C. The dependence is well approximated by a linear function $\Delta T = k \cdot C$ with the slope $k = 0.382 \pm 0.037$ (%/ppm) and the correlation coefficient R = 0.986. Accordingly, when determining the concentration of acetone in exhaled air using a sensor, $C = \Delta T/k$ can be determined by measuring the value of ΔT .

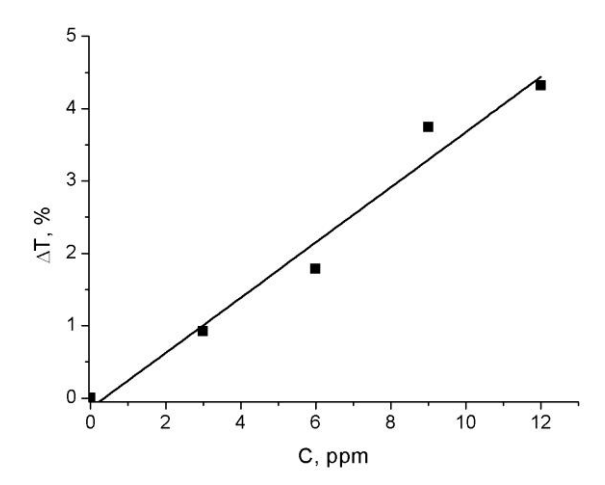


Fig. 2. Dependence of the change in optical transmittance of fumed silica films doped with DNP on the concentration of acetone in the air (0-12 ppm) at 405 nm.

In summary, due to the high specific surface area of the nanomaterial, fumed silica films with DNP exhibit high optical sensitivity to acetone in model mixtures of exhaled air. Since DNP complexes with acetone are stable and form a strong double covalent bond, the disadvantage of such a sensor material is the irreversibility of the response (disposable sensor). However, this also provides an advantage – the ability to increase the sensitivity of the sensor in proportion to the increase in the volume of the analyzed air sample. The films have high selectivity for acetone - complexes are formed mainly only with ketones and aldehydes: there is no interaction with esters, amides, alcohols, carboxylic acids, etc. [1], but when interacting with aldehydes, unlike acetone, there is a decrease in optical density in the range of 340-520 nm [7].

- [1] E. Kozaeva, V. Mol, P. I. Nikel, and A. T. Nielsen, Microb. Biotechnol. 15, 2426 (2022).
- [2] H. A. Harutyunyan, Redox Rep. 22, 160 (2016).
- [3] K. Tachibana, M. Yamamoto, and Y. Y. Maruo, 2016 IEEE 16th International Conference on Nanotechnology (IEEE-NANO) (Sendai, Japan, 2016).
- [4] D. Amoabeng, et al., Polymer **186**, 121831 (2020).
- [5] G. Song, et al., Chem. Eng. J. **440**, 135979 (2022).
- [6] M. R. Jadhay, et al., Diabetes Metab. Syndr.: Clin. Res. Rev. 18, 102931 (2024).
- [7] M. Tummalapalli, and B. Gupta, J. Carbohydr. Chem. 34, 338 (2015).

MACHINE LEARNING APPROACH TO PREDICT CURIE TEMPERATURE IN BINARY ALLOYS

O. P. Ponomarov, S. O. Ponomarova, Yu. M. Koval'

G.V. Kurdyumov Institute for metal physic of the N.A.S. of Ukraine, Kyiv, 03142, Ukraine

This study presents a machine learning approach to predict the Curie temperature in binary alloys, specifically focusing on the Fe-Pt, Fe-Ni, Fe-Pd, and Co-Pt compounds within a concentration range of 10 to 90 atomic per cent.

The optimal mathematical algorithm for this task is the Voting Ensemble algorithm [1], which combines the predictions from multiple individual models to produce a final prediction. The results are validated against classical methods for calculating Curie temperatures [2-3].

The experimental findings indicate that factors such as external pressure, atomic ordering, and alloy composition have a significant influence on the Curie temperatures in all examined binary systems. These factors can be utilised to design alloys with desired Curie temperatures. Additionally, the proposed set of features, feature analysis algorithms, and computational methods can be applied to a variety of materials, including ternary alloys, bulk materials, and nanomaterials.

- [1] M. Schuld, F. Petruccione, Machine Learning with Quantum Computers (Springer, 2021).
- [2] J.Rusz, I. Turek, M. Divis, Journal of Alloys and Compounds, 408, 930 (2006
- [3] S. Ponomarova, et al., J. Nanopart. Res. 18, 213 (2016).

GRAPHENE VIBRATIONAL THERMODYNAMICS

O. P. Ponomarov, S. O. Ponomarova, Yu. M. Koval'

G.V. Kurdyumov Institute for metal physic of the N.A.S. of Ukraine, Kyiv, 03142, Ukraine

We calculated various thermodynamic properties of an ideal and nonperturbed graphene sheet, from phonon dispersion curves in the harmonic approximation of the lattice dynamics [1]. For the evaluation of the phonon frequencies, we used interatomic force constants taken from classical bond order potentials [2-3].

It is expected that the contribution of graphene phonons to the free energy prevails over the electrons' term. It enables the actual application of vibrational thermodynamics models [4] for evaluating the main physical quantities of graphene.

Currently, there is a lack of experimental results on the main thermodynamic properties of the free-standing graphene monolayer. Also, often DFT calculations show unphysical behaviour of phonon frequencies, especially for the ZO-branch [5], which must be parabolic closer to the centre of the Brillouin zone [6]. So, ab initio computations require verification by analytical models. It should also be noted that the ab initio thermodynamic properties of graphene depend on the number of carbon atoms in the computation lattice due to the phonon density of states dependence [5].

For the evaluation of Free energy and other properties, we preferred to use a summation over the Brillouin zone on a uniform grid. It requires less computational capacity but gives better precision than the usage of special points [7].

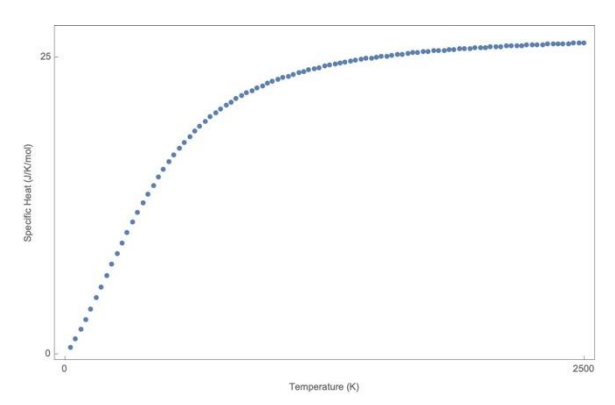


Fig. 1. Graphene heat capacity, evaluated by using interatomic force constants from [3].

- [1] H. Böttcher, *Principles of the Theory of Lattice Dynamics* (Physik-Verlag, Weinheim 1983).
- [2] L. J. Karssemeijer and A. Fasolino, Surface Science 605, 1611 (2011).
- [3] L. Wirtz, A. Rubio, Solid State Commun. 131, 141 (2004).
- [4] B. Fultz, Progress in Materials Science, 5, 247 (2010).
- [5] G. Kaur, S. Mann, S. Gupta, K. Dharamvir, Vacuum, 166, 405 (2019).
- [6] I. Lifshitz, Zh. Eksp. Teor. Fiz. 22, 475 (1952).
- [7] D. Chadi, M. Cohen, Phys. Rev. B. 8, 5747 (1973)

SECTION II. PHYSICS OF CONDENSED MATTER AND PHASE TRANSFORMATIONS

TEMPERATURE-DEPENDENT EPR STUDY OF IRON-DOPED CADIUM MANGANESE TELLURIDE CRYSTALS

A. V. Uriadov¹, I. V. Ivanchenko², E. N. Kalabukhova³, <u>D. V. Savchenko</u>^{1,4}

¹National Technical University of Ukraine "Igor Sikorsky Kyiv Polytechnic Institute", Kyiv, 03056, Ukraine

²O. Usikov Institute for Radiophysics and Electronics, NAS of Ukraine, Kharkiv, 61085, Ukraine

³V. Lashkaryov Institute of Semiconductor Physics, NAS of Ukraine, Kyiv, 03028, Ukraine

⁴Technical Center NAS of Ukraine, Kyiv, 04070, Ukraine

Iron-doped cadmium manganese telluride (Fe:Cd_{1-x}Mn_xTe) crystals represent a class of II–VI semi-magnetic semiconductors with tunable optical and magnetic properties, making them highly suitable for mid-infrared laser applications and spin-based studies [1,2]. The substitution of Cd by Mn introduces localized magnetic moments (Mn²⁺ ions), which interact via antiferromagnetic exchange, leading to complex magnetic phenomena such as spin-glass behavior at intermediate Mn concentrations.

Understanding the magnetic dynamics in such systems is essential for both fundamental solid-state physics and the development of magneto-optical devices. In particular, the interplay between Mn–Mn and Fe–Mn exchange interactions influences spin freezing and magnetic frustration, which are sensitive to both composition and temperature.

 $Cd_{1-x}Mn_x$ Te crystals with Mn content x of 0.45 and 0.7 were synthesized using the Bridgman technique. The crystals were doped with Fe^{2+} ions during the synthesis process (Fe was added into the initial raw materials in the metal powder form) [2] with a Fe^{2+} concentration of about 10^{19} cm⁻³. The cross-section of investigated samples was 5×5 mm², and the thickness was ~ 3 mm. The crystal faces were not coated with any antireflection coatings.

For the investigation of the magnetic properties of Fe: $Cd_{1-x}Mn_x$ Te crystals, the electron paramagnetic resonance (EPR) spectroscopy was utilized. X-band (~9.4 GHz) EPR measurements were performed using a Bruker ELEXSYS EPR E580 spectrometer with an ER 4112HV variable temperature helium-flow cryostat and ER 4122 SHQE SuperX High-Q cavity. The EPR spectra were simulated by the EasySpin 5.2.36 software package [3].

Fig. 1 shows the temperature dependence of EPR spectra measured at T > 40 K in Fe:Cd_{1-x}Mn_xTe crystals with x = 0.45 and x = 0.7. It is observed that the

intense broad signal at $q \sim 2.02$ dominates the EPR spectrum at room temperature, caused by strong exchange interactions between Mn²⁺ ions [4]. With a decrease in temperature, this line broadens, and its intensity drops dramatically, whereas the resonance field position of this line remains temperature independent.

Fig. 2 shows the temperature dependence of the EPR linewidth of this intense signal obtained from the EPR spectra simulation. The observed broadening upon cooling indicates a transition to a spin-glass-like state at low temperatures and is well described by the modified Huber expression [5]:

$$\Delta B_{pp} = A \left(\frac{T_{f\Delta B}}{T - T_{f\Delta B}} \right)^{\alpha_{\Delta B}} + B \left(\frac{\Theta}{T} + 1 \right), \tag{1}$$

where A and B are the fitting constants, $T_{f\Delta B}$ is the temperature of the orderdisorder transition, ΔB_{pp} is the EPR linewidth, $\alpha_{\Delta B}$ is the critical exponent, Θ is the Curie temperature.

As can be seen from Table 1, the obtained Θ , $T_{f\Delta B}$ correspond to those previously reported in $Cd_{1-x-y}Fe_yMn_xTe$ and $Cd_{1-x}Mn_xTe$ crystals.

Such correspondence supports the suggestion made in [7] that Fe²⁺ ions in Fe:Cd_{1-x}Mn_xTe samples are magnetically inactive as well as in the CdTe matrix. The obtained smaller $\alpha_{\Delta B}$ value in Fe:Cd_{1-x}Mn_xTe samples, as compared to Cd₁xMnxTe, reflects the reduction of cooperative spin dynamics and breakdown of long-range correlations, since Fe ions act as magnetic impurities that introduce disorder and frustration into the Mn spin system.

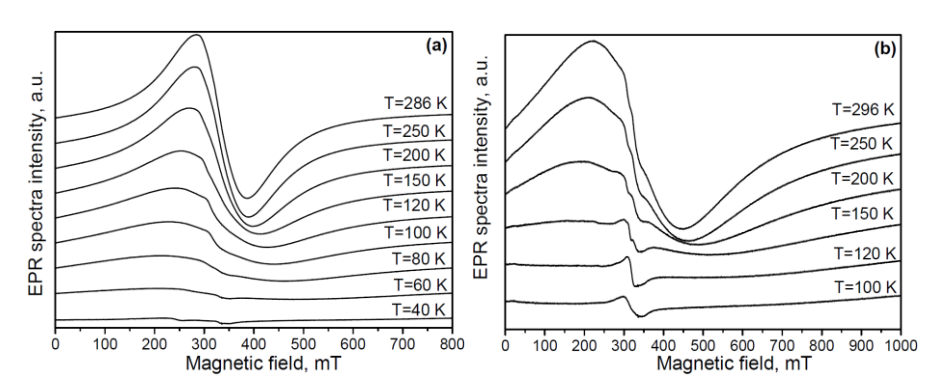


Fig. 1. Temperature dependence of EPR spectra measured in Fe:Cd_{1-x}Mn_xTe crystals with x = 0.45 (a) and x = 0.7 (b).

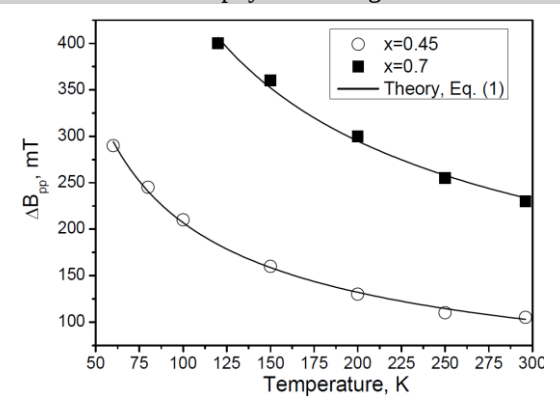


Fig. 2. Temperature dependence of the EPR linewidth of the intense signal in Fe:Cd_{1-x}Mn_xTe crystals with x = 0.45 (open circles) and x = 0.7 (filled squares) obtained from the EPR spectra simulation. The solid line is the result of fitting Eq. (1) to experimental data.

Table 1. The comparison of Θ , $T_{f\Delta B}$, $\alpha_{\Delta B}$ values obtained in this work along with literature data.

Will Include data.					
Sample	X	- Θ, K	$T_{f\Delta B}$, K	$\alpha_{\Delta B}$	Reference
Fe:Cd _{1-x} Mn _x Te	0.45	230	13	0.42	This work
	0.75	370	25	0.40	
$Cd_{1-x-y}Fe_yMn_xTe$ (y=0.01)	0.37	204	-	ı	[6]
	0.58	375	-	ı	
$Cd_{1-x}Mn_xTe$	0.4	230	13	1.5	[5]
	0.6	350	23	1.5	

The authors are grateful to Dr. N. Kovalenko (Helmut Schmidt University, Hamburg, Germany) for supplying samples for the study.

- [1]. V. V. Fedorov, et al., J. Cryst. Growth 310, 4438 (2008).
- [2]. M. E. Doroshenko, et al., Opt. Mater. Express 8, 1708 (2018).
- [3]. S. Stoll and A. Schweiger, J. Magn. Reson. 178, 42 (2006).
- [4]. N. Samarth and J. K. Furdyna, Phys. Rev. B **37**, 9227 (1988).
- [5]. S. B. Oseroff, Phys. Rev. B, 25, 6584. (1982)
- [6]. Y. Irie, T. Sato, and E. Ohta, Phys. Rev. B 51, 13084 (1995).
- [7]. Y. Irie, T. Sato, E. Ohta, J. Magn. Magn. Mater. 140-144, 2027 (1995).

SPIRAL ORDERING IN SPIN 3/2 MAGNETS

M. Yu. Kovalevsky

National Science Center «Kharkiv Institute of Physics and Technology», Kharkiv, 61108, Ukraine

In connection with the development of spintronics and the awareness of the role of the internal inhomogeneous magnetic structure, which has physical properties significant for their practical use, the task of creating and studying such stable formations arises. To date, various magnetic textures are known with their characteristic size in the range of 1 nm - 1 mm [1]. The internal structure violates both continuous symmetry (translations and rotations in orbital space, rotations in spin space) and discrete symmetry (spatial inversion and time reversal) [2]. The nature of the violation of these symmetries is different and can be caused by the chiral properties of the magnet, artificial creation of layered structures, competition of magnetic interactions or spontaneous symmetry breaking. The spin-orbit interaction existing in magnets allows to extend the spatial anisotropy of matter also into the space of magnetic degrees of freedom.

The increased interest in spiral magnetic structures is due to a number of their useful properties. These include the ability to regulate the magnetization of layers using the spin transfer torque mechanism [3], ensuring high density of memory devices, and reducing energy consumption for controlling magnetic structures using the Dzyaloshinsky-Mori interaction [4,5].

The present study is devoted to the investigation of degenerate inhomogeneous equilibrium states in high-spin magnets. We have considered the problem of classifying equilibrium states in which magnetic and spatial symmetries are spontaneously broken for a matter whose particles have a spin s=3/2 and an exchange Hamiltonian has symmetry SU(4). In such physical systems, compared to magnets with a spin s=1/2 [6], the set of magnetic degrees of freedom is significantly expanded and leads to a large variety of equilibrium states. Our approach is based on the concept of quasi-averages [7,8] and the idea of residual symmetry of degenerate equilibrium states [9]. This representation has proven effective in the analysis of superfluid equilibrium states in He-3. To date, seven states out of the theoretically predicted fourteen have been experimentally observed.

We have introduced into consideration residual and spatial symmetry generators and, on their basis, formulated linear differential equations for the

classification of magnetic order parameters in nonhomogeneous equilibrium states. The symmetry subgroups SO(3), SO(3)xU(1), SO(3)xSO(3), SO(4) and SO(5) of the SU(4) group have been studied in detail and analytical expressions for magnetic degrees of freedom have been found in terms of the thermodynamic parameters determined by the residual symmetry of the equilibrium state and the spatial coordinate. Earlier, in this approach, homogeneous equilibrium states with spin s=1, 3/2 and exchange Hamiltonian symmetry SU(3), SU(4) were considered in [10,11].

Using methods of statistical mechanics, we have established the influence of thermodynamic parameters of residual symmetry on the type of spatial and magnetic anisotropy of equilibrium values of magnetic degrees of freedom. The proposed approach does not use any model assumptions about the magnetic Hamiltonian and takes into account only its symmetry properties.

- [1] Tao Yu and Zhaochu Luo, Physics Reports 1009 1 (2023).
- [2] See-Hun Yang and Ron Naaman, Nature Reviews Physics 3 328 (2021).
- [3] J. Slonczewski, Magn., Magn. Mater. 159 L1 (1996).
- [4] I.E. Dzyaloshinskii, Soviet physics JETP, **19**(4) 960 (1964).
- [5] T. Moria, Phys. Rev. Lett. 4 228 (1960).
- [6] A. I. Akhiezer, V. G. Baryakhtar, and S. V. Peletminskii, *Spin Waves* (North-Holland, Amsterdam, 1968).
- [7] N.N. Bogolubov, Physica 26 S1 (1960).
- [8] M.Y. Kovalevsky, S.V. Peletminsky, *Statistical physics of quantum liquids and crystals* (Fizmatlit, Moskow, 2006).
- [9] L.Michel, Rev. Mod. Phys. **52** 617 (1980).
- [10] N.N. Bogolyubov (jr.), A.V. Glushchenko, Theor. Math. Phys. **24** 386 (2018).
- [11] M.Y. Kovalevsky, S.V. Peletminsky, Low Temp. Phys. 46 760 (2020).

STRUCTURE AND ELECTRONIC MAGNETO-TRANSPORT OF EPITAXIAL GRAPHENE PROXIMIZED BY ADSORBED AND INTERCALATED ATOMIC LAYERS

S. Sologub^{1,2}, J. Koch², C. Ghosal², M. Gruschwitz², C. Tegenkamp² ¹Institute of Physics, National Academy of Sciences of Ukraine, Kyiv, 03028, Ukraine

²Institut für Physik, Technische Universität Chemnitz, Chemnitz, 09126, Germany

Proximitized 2D materials present exciting prospects for exploring new quantum properties, enabled by precise control of structures and interfaces through epitaxial methods. The concept of proximity coupling is a promising approach to specifically modify the properties of epitaxial graphene layers by introducing spinorbit coupling (SOC), opening gap in the energy spectrum and changing the carrier density. Keeping that in mind, we performed structural and electronic (magneto)transport investigations of epitaxial monolayer graphene (MLG) grown on SiC(0001) and modified by ultrathin adsorbed layers of high-Z elements bismuth (Bi) [1,2] and lead (Pb) [3], as well as by Pb monolayer intercalated between MLG and SiC substrate [4,5]. Low energy electron diffraction (SPA LEED) and scanning tunneling microscopy (STM) were used to examine ultrathin Bi or Pb nanostructures epitaxially grown on MLG. UHV magneto-transport experiments with the same structures were performed in situ within the magnetic field range ±4 T. Scanning and transmission electron microscopy (SEM, TEM), energy dispersive spectroscopy (EDS) and low-temperature (down 30 K) 4-tip STM were also used to characterize Pb-intercalated MLG.

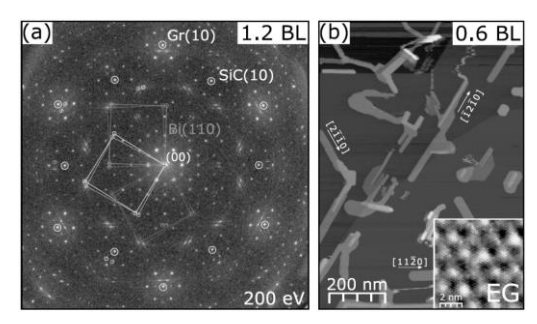


Fig. 1. Figure caption. (a) LEED image of MLG/SiC(0001) with a Bi coverage of 1.2 BL recorded at 200 eV. Three domains of Bi(110) are visible, each having two subdomains rotated by ±1.8°. (b) STM image for Bi coverages of 0.6 BL showing needlelike islands (the inset shows the pristine MLG structure).

We found that deposition Bi at 300 K results in formation of needle-like Bi(110)-terminated islands elongated in the MLG zig-zag direction and aligned at an angle of approximately 1.75° with respect to the MLG armchair direction (Fig. 1). By both strain and quantum size effects, the shape, the orientation and the thickness of the Bi(110) islands can be rationalized. Additionally, a minority phase of Bi(110) islands orthogonally aligned to the former ones were seen. The four sub-domains of this minority structure are attributed to the formation of mirror twin boundaries, resulting in two potential alignments of Bi(110) majority and minority domains with respect to each other, in addition to two possible alignments of the majority domain with respect to graphene. Notably, an annealing step at 410 K or lowering the deposition temperature, significantly increases the concentration of the Bi(110) minority domain. These findings shed light on the *structural control of proximitized 2D materials*, *showcasing the potential for manipulating 2D interfaces* [1].

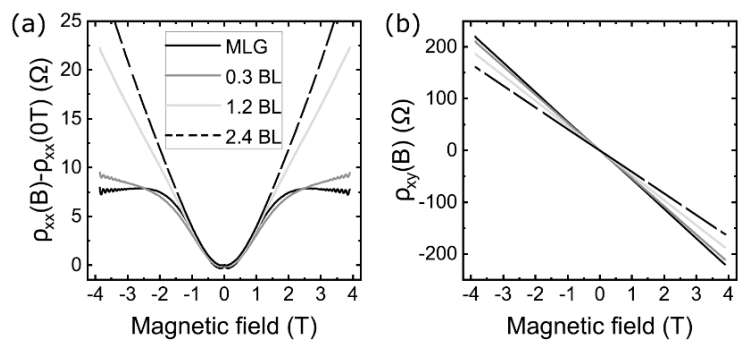


Fig. 1. Figure caption. (a) Magneto-resistivity and (b) Hall resistivity at different Bi coverages deposited on MLG at RT. Measurements performed at 12 K.

The same Bi structures on MLG with average thickness up to 3.6 Bi bilayers (BL) were investigated *in situ* by magneto-transport [2]. It turned out that epitaxial Bi(110) islands locally change the initial n-type doping of MLG. The formation of inhomogeneous carrier concentration profiles on MLG results in a positive and linear magneto-resistivity effect with increasing Bi coverage. Along with this, the slope of the Hall resistivity decreases, suggesting a rise of the carrier concentration. However, by extracting the carrier concentration from the Shubnikov—de Haas oscillations, we confirm that the carrier concentration in the uncovered regions remains constant and that the change of the Hall slope is solely an effect of the inhomogeneity (Fig. 2). Also, the conductivity of MLG has not changed drastically and even at coverages as high as 2.4 BL the mobility in the uncovered region is

reduced by only about 15% of its original value. Moreover, the signatures of weak localization in the magneto-resistivity vanish with increasing Bi coverage, while no signs of weak antilocalization were found at all. Apparently, the proximitized Bi islands induce a well-defined lateral doping profile so that the electrons are not penetrating into the areas of the Bi islands but are reflected at their edges. This scattering process seems to be phase breaking, thus suppressing the weak localization effect. Our results show clearly that both the coupling but also the homogeneity at the interface is crucial for proximity coupling.

Similar structural and magneto-transport experiments were conducted for MLG/ SiC(0001) with deposited Pb(111) islands (average coverage of Pb was up to 30 ML) [3]. The Pb(111) islands turned out to act as donors, increasing the electron concentration of graphene by about 5 × 10¹¹ ML⁻¹cm⁻². However, the doping was found to be homogeneous, in stark contrast to our previous results for Bi islands on MLG. Upon percolation of the Pb layer at around 5 ML, hole transport through the Pb islands has to be taken into account in order to describe the transport data. The Pb(111) islands do not induce any Rashba SOC, contrary to theoretical predictions for an interface between Pb(111) and graphene. Moreover, they seem to screen the defects in the graphene, resulting in a reduction of the intervalley scattering rate in MLG covered by up to 5 ML Pb coverage.

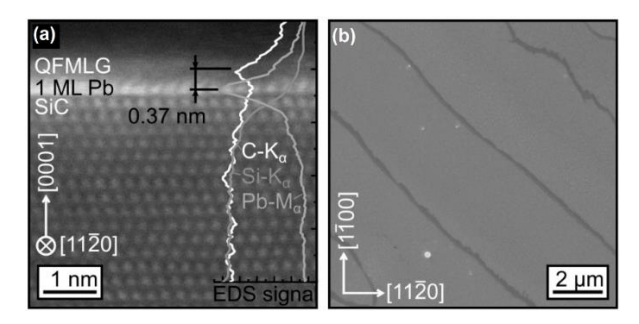


Fig. 3. (a) STEM image and EDS scans showing the intercalation of 1ML Pb at the interface between SiC and graphene. (c) SEM image (15 kV, 1 nA, 300 K) of the surface reveals an average terrace width of 3.75 µm. The dark contrast stems from overgrowth of the step edges by MLG.

On the other hand, by intercalation of a Pb monolayer, a 2D heterostructure of charge-neutral graphene and a crystalline 2D Pb layer on SiC(0001) substrates was epitaxially grown [4], Fig. 3. Thereby, microscopy revealed characteristic defects on microscopic and mesoscopic length scales, e.g., grain boundaries, substrate steps, and nonintercalated terraces. We analyzed in situ the electronic

transport properties of this heterostructure. The systematic variation of the contact geometry and probe spacings, supplemented by finite-element simulations, allowed us to circumvent the problem of sample inhomogeneities and to determine reliably the conductivity of the 2D heterostructure itself. Thereby, the conductivity of $(7 \pm 1) \times 10^5$ S/m is comparable to values measured for monolayer and quasi-free monolayer graphene, but decreases with decreasing temperature down to 30 K, revealing a clear nonmetallic behavior. Our findings are compatible with a small gap opening (1–5 meV) in graphene due to the proximitized 2D Pb layer.

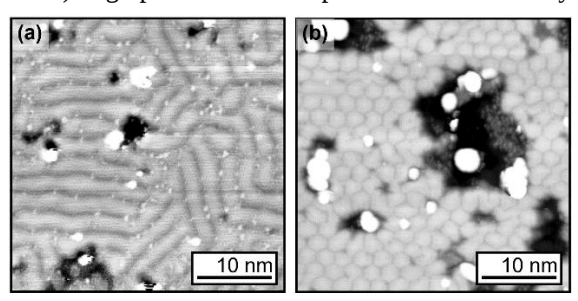


Fig. 4. STM images showing various 2D Pb interface phases at the SiC graphene interface. (a) 2-fold symmetric, three domain stripe phase. (b) hexagonal phase exhibits deformations in close vicinity to defects and non-intercalated areas.

Therefore, it can be concluded that the intercalation of Pb beneath graphene offers a powerful route to stabilizing and protecting novel two-dimensional (2D) phases [5]. The epitaxial growth of Pb monolayers on SiC(0001), combined with the relatively large spacing of the suspended graphene, makes this system particularly distinctive. We have investigated the intercalation process across multiple length scales. Our analysis reveals the formation of different 2D Pb monolayer phases, such as *stripes* and *hexagons* (Fig.4), which emerge due to the interplay between substrate pinning and strain within the Pb layer, depending on local coverage. These findings provide new insights into the strain-driven stabilization of intercalated metal layers and highlight the potential of graphene as a versatile platform for engineering low-dimensional materials.

- [1] J. Koch, S. Sologub, C. Ghosal and C. Tegenkamp, J. Phys.: Condens. Matter **36**, 065701 (2024).
- [2] J. Koch, et al., Phys. Rev. B **109**, 235107 (2024).
- [3] J. Koch, et al., arXiv:2502.20194 [cond-mat.mes-hall].
- [4] M. Gruschwitz et al., Phys. Rev. B 109, 245430 (2024).
- [5] M. Gruschwitz et al., arXiv:2506.10791 [cond-mat.mtrl-sci].

FIRST-PRINCIPLES MODELING OF THE ELECTRONIC STRUCTURE PECULIARITIES IN HIGH-ENTROPY TRANSITION METAL CARBIDES

I. V. Plyushchay¹, O. I. Plyushchay², V. B. Shevchenko¹

¹ Taras Shevchenko National University, Kyiv, 01033, Ukraine ²Kyiv Academic University, Kyiv, 03142, Ukraine ² Institute for Metal Physics of the N.A.S. of Ukraine, Kyiv, 03142, Ukraine

High-entropy transition metal carbides (HECs) are single-phase, multicomponent refractory carbides known for combining ultrahigh hardness, excellent thermal stability, good electrical conductivity, and intrinsic lattice carbon vacancies. For example, a (HfTaZrNb)C HEC exhibits a nanoindentation hardness of \approx 36 GPa (about 30% higher than the rule-of-mixtures of its constituents), while (HfZrTaNbTi)C has a metallic-like resistivity (\sim 0.09 m Ω ·cm, comparable to TiC); the presence of carbon vacancies further enhances electron scattering. These combined attributes make HECs highly promising for extreme environments (e.g. >2000 °C, high heat flux, radiation), as recently reviewed by Feng et al. [1].

Calculations were performed within density functional theory in the generalized gradient approximation using the ABINIT package. Transition metal carbides with the NaCl-type (B1) structure, consisting of two fcc sublattices of metal and carbon atoms, were modeled. A 24-atom supercell was constructed, containing three (111) planes of metal atoms and three (111) planes of carbon atoms (close-packed layers of A, B, and C types), with four atoms per plane. The distribution of different metal atoms was arranged to avoid clustering, employing periodic boundary conditions. Internal stresses were relaxed via numerical annealing, during which the atomic positions evolved according to first-principles calculated forces. The applicability of this supercell was verified by considering a larger, 96-atom supercell with a random distribution of metal atoms, which nevertheless did not significantly alter the main features of the electronic spectra.

Using first-principles methods, we calculated the electronic structure features of transition metal carbides (TMCs) and high-entropy transition metal carbides (HE-TMCs). Figure 1 presents the calculated density of states (DOS) for ZrC, taken as a representative example of group IV TMCs, which all exhibit similar electronic spectra. The vertical arrow indicates the position of the Fermi level; the inset shows an enlarged view of the DOS in the vicinity of the Fermi level. Notably, the local DOS peak at the Fermi level resembles the shape of a Van Hove singularity and may originate from partial fulfillment of an electron diffraction

condition, leading to the formation of a band gap and a corresponding flat region in the electronic dispersion.

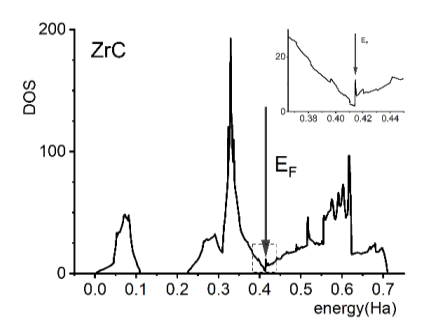


Fig. 1. Electronic states density of zirconium carbide (ZrC). The Fermi level is indicated by the vertical arrow. The inset shows an enlarged view of the region near the Fermi level.

As discussed in our previous work [2], the presence of this local DOS peak—observed for TiC, ZrC, and HfC—plays a key role in the intrinsic nonstoichiometry of these carbides. Specifically, it correlates with the experimentally observed equilibrium concentration of carbon vacancies, explaining the absence of strictly stoichiometric compositions in these materials [2].

Thus, the specific features of the electronic structure of thermally stable transition metal carbides promote the formation of a high concentration of carbon vacancies and a wide homogeneity range on phase diagrams. The presence of such vacancies shifts the Fermi level toward the minimum of the wide pseudogap, thereby stabilizing the structure. We hypothesize that a similar stabilization mechanism may also operate in high-entropy transition metal carbides, which exhibit qualitatively similar DOS profiles. As highlighted in the review [1], the key parameter for these materials is the position of the Fermi level relative to the DOS minimum, with vacancies shifting it toward lower energies. In this work, we also consider transition metal vacancies, which not only reduce the electronic subsystem energy but also increase the configurational entropy—an essential stabilizing factor for this class of materials. In this sense, a transition metal vacancy can be regarded as an additional "component" of the high-entropy compound.

We investigated the electronic structure of high-entropy transition metal carbides with various compositions, selecting them so that the average number of electrons per metal atom systematically varied from 1.75 to 2.5 (the corresponding compositions are listed in Fig. 2).

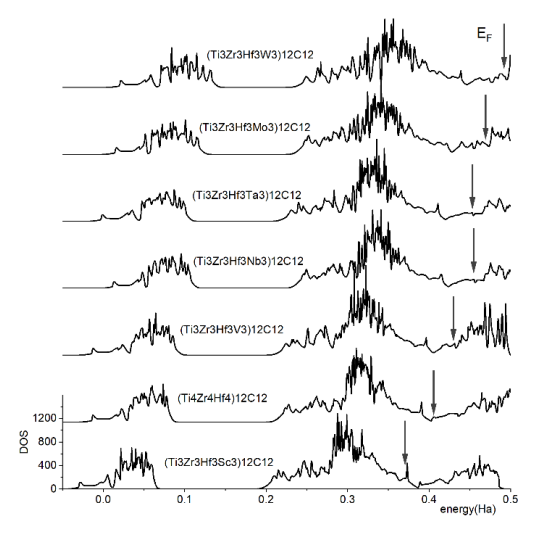


Fig. 2. Calculated density of states for all studied high-entropy transition metal carbides without vacancies. The vertical arrow indicates the position of the Fermi level.

We also examined supercells containing a single transition metal vacancy, which provided an additional means of tuning the total electron count. Changing the composition by increasing the total number of electrons leads to a gradual rightward shift of the electronic spectrum, with the Fermi level shifting even more significantly—further away from the minimum of the pseudogap. Data for the case with a vacancy are not shown here; in that case, the Fermi level shifts leftward toward the pseudogap minimum, but to a lesser extent than predicted by the rigidband model (based solely on electron count). We attribute this difference to the appearance of vacancy-induced states within the pseudogap region. However, the detailed structure of these states in our calculations is likely influenced by the use of an ordered supercell, which does not fully represent the random nature of vacancies in real materials.

^[1] L. Feng, W. G. Fahrenholtz, and D. W. Brenner, Annu. Rev. Mater. Res. 51, 1–26 (2021). doi:10.1146/annurev-matsci-080819-121217.

^[2] I. V. Plyushchay, T. L. Tsaregradska, and O. I. Plyushchay, Metallofiz. Noveishie Tekhnol. 40(8), 1113–1121 (2018) (in Ukrainian). doi:10.15407/mfint.40.08.1113.

IMPACT OF DYSPROSIUM DOPING ON THE MICROSTRUCTURE, IMPURITY CONTENT, AND EXCITONIC PROPERTIES OF CDS THIN FILMS

<u>A.P. Bukivskii</u>¹, Yu.P. Gnatenko¹, A.S. Opanasyuk², P.M. Bukivskij¹, S.A. Iliash¹, M.S. Furier¹

¹ Institute of Physics of NAS of Ukraine, Kyiv, 03028, Ukraine ²Sumy State University, Sumy, 4007, Ukraine

Cadmium sulfide (CdS) thin films are widely recognized as a key II-VI semiconductor material due to their direct band gap (\sim 2.42 eV at room temperature) and high photosensitivity in the visible spectrum, making them suitable for applications in photovoltaic window layers, photodetectors, and optoelectronic devices [1]. This work investigates the structural and optical properties of dysprosium-doped CdS (CdS:Dy) polycrystalline thin films grown by close-spaced vacuum sublimation (CSVS) on glass substrates at substrate temperatures (T_s) ranging from 573 K to 773 K.

We investigated dysprosium doping because rare-earth elements can act as gettering agents that remove unwanted impurities and can also modify the crystal structure and electronic properties. Our study examined how Dy affects the films' microstructure, residual impurities, and excitonic behavior.

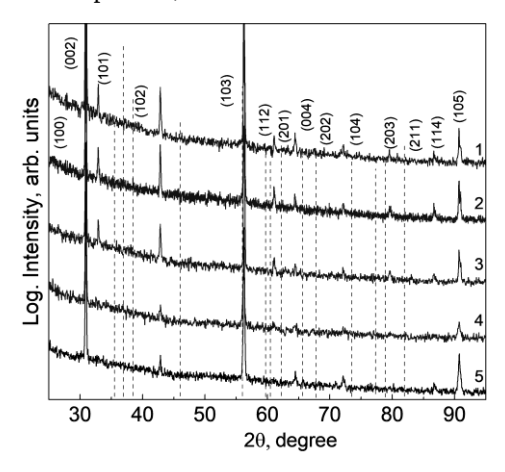


Fig. 2 X-ray patterns of CdS:Dy films deposited at the different substrate temperatures: T_s = 573 K (1); T_s = 623 K (2); T_s = 673 K (3); T_s = 723 K (4) and 773 K, respectively.

Films exhibited average grain sizes of 0.8–1.0 µm and thicknesses of 0.5–0.6 μm. X-ray diffraction confirmed a single-phase hexagonal wurtzite structure for all samples, with a dominant (002) diffraction peak corresponding to the optical c-axis being preferentially oriented perpendicular to the substrate, contrasting with undoped CdS films, which favored the (103) orientation. Pole density analysis revealed a strong one-component texture in the (002)/(004) direction for $T_s = 573$ – 673 K, with the degree of preferred orientation increasing sharply at $T_s = 723$ K. Coherent scattering domain (CSD) sizes varied between 39.9–72 nm depending on growth conditions. Importantly, the microstress level in CdS:Dy films (0.73–0.92 \times 10^{-3}) was consistently lower than in undoped counterparts (1.12–1.55 \times 10⁻³), indicating improved crystal quality. Energy-dispersive spectroscopy showed Dy concentrations below 0.1 mol % for T_s = 573-673 K, rising to about 0.4 mol% at $T_s = 723$ K, correlating with changes in microstress.

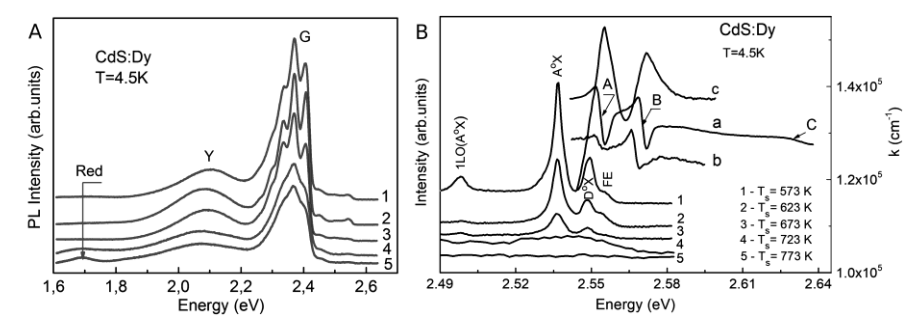


Fig. 2. A: PL spectra of CdS:Dy films grown under different substrate temperatures. Curves 1-5 correspond to the following T_s: 573 K, 623 K, 673 K, 723 K and 773 K, respectively. B: PL spectra associated with the excitonic emission and the excitonic reflection spectra. Curves 1-5 correspond to the CdS:Dy films grown under the following substrate temperatures: 573 K, 623 K, 673 K, 723 K and 773 K, respectively. Curves a and b correspond to the reflection spectra for the film $(T_s = 673 \text{ K})$ and the bulk optically non-oriented CdS:Dy crystal, respectively. Curve c corresponds to the absorption spectrum for the film.

Low-temperature photoluminescence (PL) spectra at 4.5 K (Fig. 2: A) revealed strong green emission bands (2.25-2.50 eV) originating from free-tobound and donor–acceptor pair recombinations involving shallow donor ($E_D \approx 30$ meV, likely Cd interstitials) and acceptor ($E_A \approx 169$ meV, Na_{Cd}) centers. The relative stability of zero-phonon bands (ZPB) with temperature for some samples indicated dominance of free-to-bound transitions, while others exhibited shifts consistent with donor ionization. A yellow band (\sim 2.083 eV) associated with V_{Cd}

and I_{Cd} defects was present but minimally shifted by Dy doping, and a weak red band (~1.70 eV) linked to V_S donor centers indicated low surface defect densities. The overall PL behavior supports the hypothesis of Dy acting as a "cleaning" agent, reducing residual impurities compared to undoped CdS.

High-resolution excitonic PL and reflection measurements (Fig. 2: B) revealed sharp lines corresponding to donor-bound excitons (D^oX at 2.5484 eV), acceptor-bound excitons (A^oX at 2.5364 eV), and free excitons (~2.556 eV). Reflection spectra at 4.5 K displayed well-defined A, B, and C excitonic features (2.5541 eV, 2.5711 eV, and 2.632 eV) with comparable A and B features intensities, confirming c-axis alignment perpendicular to the substrate. These excitonic energies yielded trigonal crystal field and spin-orbit splitting values of 0.017 eV and 0.061 eV, respectively, close to bulk CdS. The widths of reflection lines (3.7 meV for thin films vs. 2.6 meV for bulk) and matching excitonic positions in reflection and absorption spectra further indicates high optical quality.

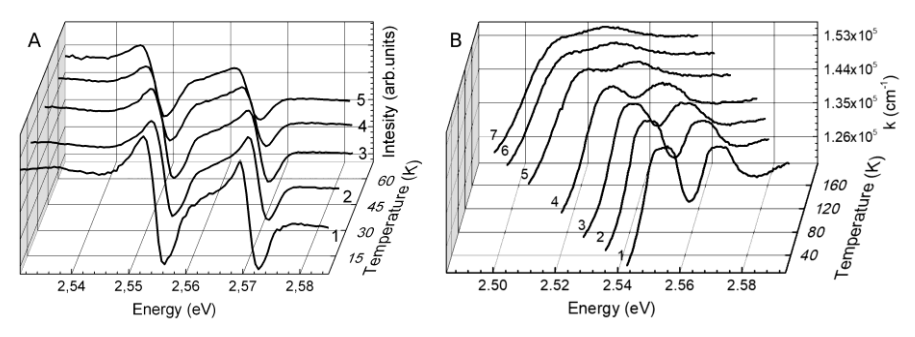


Fig. 3 A: The temperature dependence of exciton reflection spectra of CdS:Dy thin films. Curves 1-5 correspond to 4.5, 20, 40, 60, 70 K, respectively. B: The temperature dependence of exciton absorption spectra of CdS:Dy thin films. Curves 1-7 correspond to 25, 70, 100, 130, 160, 180, 90, 210 K, respectively.

Free exciton energies allowed determination of the band gap at 4.5 K: 2.5816 eV, in excellent agreement with literature for bulk CdS. Temperature-dependent exciton reflection and absorption measurements (Fig. 3) showed a redshift and broadening of A and B bands with heating, accompanied by decreased amplitude and eventual disappearance of A-band absorption above about 210 K. The trigonal crystal field splitting ($\Delta_{\rm Cr}$) remained nearly constant up to about 130 K before decreasing, likely due to thermally induced film deformation from substrate—film thermal expansion mismatch. This depolarization effect coincided with reduced c-axis orientation at higher temperatures.

Fitting the temperature dependence of the band gap to Varshni's equation [2]: $Eg(T) = Eg(0) - \alpha T^2 / (\beta + T)$, vielded Eg(0) = 2.5825 eV, $\alpha = 3.06 \times 10^{-3}$ eV/K, and β = 2156 K, values consistent with high-quality CdS material. The correlation between low microstress, strong excitonic features, and Dy-induced impurity gettering suggests that Dy doping via CSVS is an effective method for enhancing both crystalline and optical quality of CdS thin films.

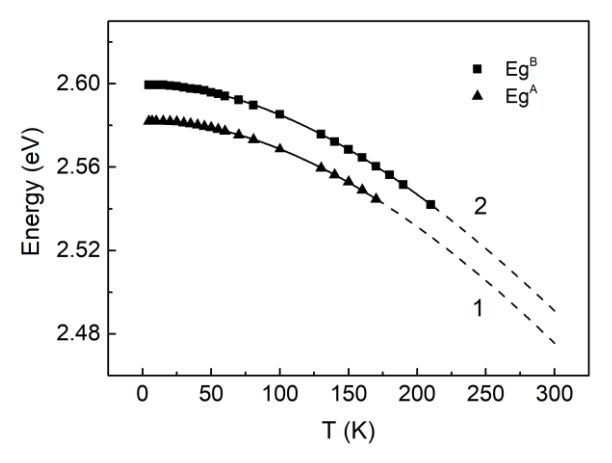


Fig. 10 The temperature dependence of the bandgap for CdS:Dy thin films. Curves 1 and 2 correspond to the bandgap between the conduction and upper valency bands as well as the conduction band and the valency band splitted by trigonal crystal field.

In conclusion, Dy doping of CdS thin films deposited by CSVS under optimized substrate temperatures (573-673 K) yields material with improved texture, reduced microstress, enhanced excitonic signatures, and diminished impurity-related emissions. These improvements are attributed to rare-earthinduced impurity passivation and controlled crystallographic orientation. The results demonstrate that CdS:Dy films grown under these conditions possess qualities comparable to bulk crystals in excitonic behavior, making them promising candidates for high-performance optoelectronic and photovoltaic applications.

[1] R. Lozada-Morales, O. Zelaya-Angel, G. Torres-Delgado, Applied Surface Science 175-**176,** 562-566, (2001).

[2] R. Boyn, 4f-4f Luminescence of Rare-Earth Centers in II-VI Compounds, Phys. Status Solidi 148, 11-47, (1988).

LOW-TEMPERATURE STUDY OF THE MAGNETIC POLARON EFFECT IN CD_{1-x}Dy_xTE DILUTED MAGNETIC SEMICONDUCTORS

P.M. Bukivskij¹, Yu.P. Gnatenko¹, A.P. Bukivskii¹

¹Institute of Physics NAS of Ukraine, Kyiv, 03028, Ukraine

This study devotes the low-temperature magnetic polaron (MP) effects in $Cd_{1-x}Dy_xTe$ (x=0.0066), a new class of diluted magnetic semiconductors (DMS) doped with rare-earth dysprosium (Dy) ions. Unlike conventional DMSs based on 3d transition metals (e.g., Mn), rare-earth-doped systems provide a unique opportunity to investigate spin-dependent interactions originating from 4f electrons. Photoluminescence (PL) and exciton reflection spectra were measured over the low-temperature range 1.8–45 K, revealing the formation and evolution of magnetic polarons in excitonic and impurity-bound states.

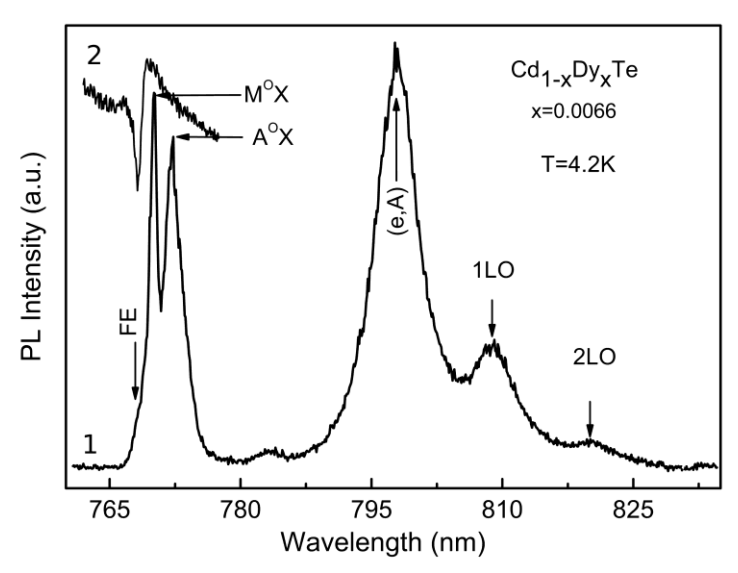


Fig. 1 PL spectrum (1) and exciton reflection spectrum (2) of $Cd_{1-x}Dy_xTe$ (X=0.0066) at T=4.2 K

Figure 1 presents low temperature (T = 4.2 K) PL and exciton reflection spectra of $Cd_{1-x}Dy_xTe$ crystals which were grown by the vertical Bridgman method with a Dy concentration of 1×10^{20} cm⁻³. The PL spectrum for CdTe crystals doped with Dy at such high concentration exhibits a rich excitonic structure. At 4.2 K, sharp lines associated with acceptor-bound excitons (A^oX) and

a new line labeled M^oX are observed, indicating more complex interactions likely influenced by Dy-induced magnetism and local lattice deformation. In addition, a broad donor-acceptor pair (DAP) band ((e-A) transitions) and phonon replicas (1LO, 2LO) are visible. Exciton reflection spectra (curve 2) make it possible to determine accurate energy positions for free exciton (FE) transitions.

It was found that the exciton reflection band (curve 2) is shifted toward shorter wavelengths compared to that of a CdTe crystal. Here, the FE energy is 1.6126 eV. This indicates the formation of Cd_{1-x}DyxTe solid solutions with x = 0.0066. Since Dy is a magnetic component, these solid solutions belong to a new class of DMS containing a rare-earth element.

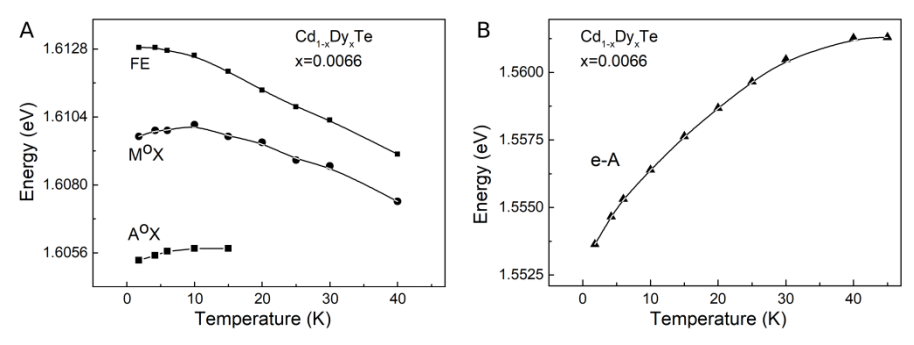


Fig. 2. A) Temperature dependence of the energies of free exciton (FE), M^oX exciton, acceptor-bound exciton (A⁰X), and B) donor-acceptor pair transition (e-A) in $Cd_{1-x}Dv_{x}Te$ (x = 0.0066) single crystals.

Temperature-dependent studies (T = 1.8-45 K) of PL and exciton reflection spectra for Cd_{1-x}Dy_xTe crystals (Figure 2) showed a long-wavelength shift with temperature decreasing (in range from 10 to 1.8 K) in the positions of free exciton (FE) lines, acceptor-bound excitons (A⁰X), localized M⁰X excitons, and especially the (e-A) line. This happens due to increase in binding energy (stronger localization) with decreasing temperature, which is consistent with the formation of localized exciton magnetic polarons. This localization occurs initially on potential fluctuations of the crystal lattice due to fluctuations in Dy concentration, which act as the initial trapping potential necessary for MP formation. The small increase in binding energy from 5.0 K to 1.8 K further supports the interpretation of weakly self-localized MPs in the low-temperature regime.

For detailed analysis of such long-wavelength PL shifts, the MP theory presented in [1], developed for the donor electron in zero magnetic field, was applied. The average spin splitting $\langle \Delta \rangle / 2$ was calculated using an analytical equation for the zero-field case, where the first term defines the contribution from magnetization fluctuations and the second term from the average exchange field.

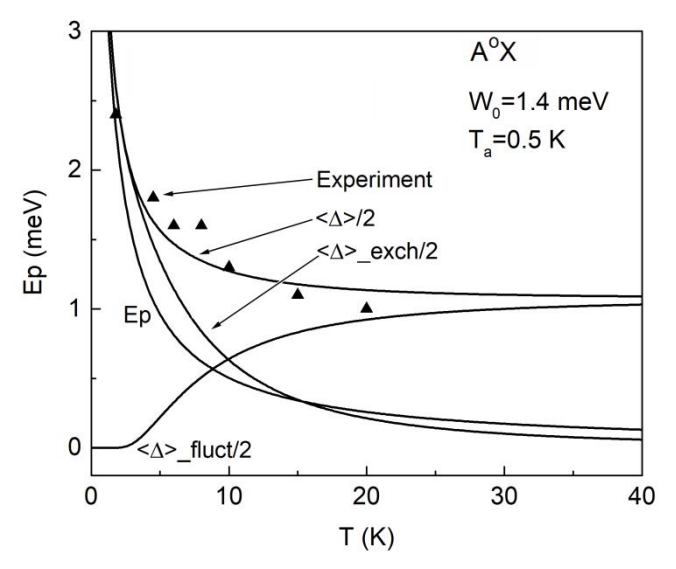


Fig. 3. Temperature dependence of the magnetic polaron binding energy for the A°X exciton line in $Cd_{1-x}Dy_xTe$ (x = 0.0066).

For the A^0X line, the best agreement between calculated curves and experimental spin splitting values was obtained for $W_0 = 1.4$ meV and $T_a = 0.5$ K.

For the (e–A) line, the magnetic contribution to spin splitting was determined using the formula: $E_{mag}=E_{sum}+\frac{1}{2}kT-58$ meV. The best fit to experimental data was achieved for $W_0=4.5$ meV and $T_a=0.5$ K.

The experimental results obtained in this work, within the donor electron model in zero external magnetic field, make it possible to determine the contributions to spin splitting from the average exchange field and from thermodynamic magnetization fluctuations, as well as to calculate the magnetic polaron binding energy and to estimate the exchange constants.

Detailed modeling of the temperature dependence allowed decomposition of the exciton binding energy into non-magnetic, exchange, and spin fluctuation components. For the A^oX line at 1.6055 eV, the average exchange field and thermodynamic spin fluctuations were extracted using the modified MP theory. At T < 2.5~K, the magnetic contribution was dominated by exchange interactions, whereas at T > 40~K, fluctuation effects saturated at $\sim 1~meV$.

The broad PL band at 1.5542 eV, attributed to (e–A) recombination via Na- or Li-related acceptors, also exhibited a temperature-sensitive MP effect. Below 10 K, magnetic binding energy contributions were minimal but increased significantly with temperature, reaching saturation near 45 K. These findings confirm the existence of MPs bound to acceptor holes at cryogenic temperatures—a feature previously observed mainly in Mn-based systems.

Finally, the hole exchange constant $|\beta N_0|$ was estimated from the experimental data to be ~717 meV, which is close to values for Cd_{1-x}Mn_xTe, indicating similar spin-interaction strengths despite different magnetic dopants.

In conclusion, this work provides the first evidence of low-temperature magnetic polaron formation in rare-earth-doped Cd_{1-x}Dy_xTe crystals. The results demonstrate that Dy-based DMSs exhibit magnetic phenomena similar to their Mnbased counterparts and are promising candidates for spintronic applications, particularly where low-temperature control of spin states is required.

[1] J. Spalek, J. Kossut, Bound magnetic polaron in diluted magnetic semiconductors: analytic results, Solid State Commun. 61, 483-486, (1987), https://doi.org/10.1016/0038-1098(87)90496-0

BAROCALORIC MATERIALS FOR HEATING AND COOLING (INVITED)

X. Mova¹

¹Department of Materials Science, University of Cambridge, UK

Half of the world's CO₂ emissions can be attributed to heating and cooling [1]. This is primarily due to heating with natural gas and cooling with compression of greenhouse gases, which are neither environmentally friendly nor energy efficient. Therefore there is great interest in developing alternative technologies that can replace these gas-based environmentally damaging systems [2,3]. Barocaloric materials are at the core of novel solid-state heat-pump technologies [4]. During this talk I will describe our work on mechanically responsive barocaloric materials, and present our recent advances on barocaloric systems for heating and cooling applications.

- [1] Climate change: science and solutions low-carbon heating and cooling, Royal Society, 2021.
- [2] X. Moya, S. Kar-Narayan and N. D. Mathur, Nature Materials 13, 439 (2014).
- [3] X. Moya and N. D. Mathur, Science **370**, 797 (2020).
- [4] P. Lloveras et al., Nature Communications 10, 1083 (2019).

EFFECTIVE AND ASYMPTOTIC CRITICALITY OF STRUCTURALLY DISORDERED MAGNETS (INVITED)

J. J. Ruiz-Lorenzo¹, M. Dudka^{2,3,4}, M. Krasnytska^{2,3}, <u>Yu. Holovatch</u>^{2,3,5,6}

¹Departamento de Física & Instituto de Computación Científica Avanzada (ICCAEx), Universidad de Extremadura, 06071 Badajoz, Spain ²Yukhnovskii Institute of Condensed Matter Physics, National Academy of Sciences of Ukraine, 79011 Lviv, Ukraine

³L4 Collaboration & Doctoral College for the Statistical Physics of Complex Systems, Leipzig-Lorraine-Lviv-Coventry, Europe

⁴Lviv Polytechnic National University, 79013 Lviv, Ukraine

⁵Centre for Fluid and Complex Systems, Coventry University,

Coventry, CV1 5FB, United Kingdom

⁶Complexity Science Hub, 1030 Vienna, Austria

Changes in magnetic critical behaviour of quenched structurally-disordered magnets are usually exemplified in experiments and in MC simulations by diluted systems consisting of magnetic and non-magnetic components. An archetypal example is given by diluted uniaxial magnets $Fe_cZn_{1-c}F_2$, $Mn_cZn_{1-c}F_2$ obtained as a crystalline mixture of two compounds when a corresponding diluted alloy is prepared by a substitution of a non-magnetic isomorph ZnF_2 for its antiferromagnetic counterpart (FeF $_2$ or MnF $_2$). Relaxation times of such systems are much larger than typical observation times which allows one to perform their theoretical and numerical analysis in terms of quenched diluted random-site Ising model, see e.g. review [1] or Ref. [2] for a more recent reference.

In present report we aim to show that similar effects can be observed not only for diluted magnets with non-magnetic impurities but may be implemented, e.g., by the presence of two (and more) chemically different magnetic components as well. To this end, we consider a model of the structurally-disordered quenched magnet where all lattice sites are occupied by Ising-like spins of different lengths L. In such a random spin length Ising model, the length L of each spin is a random variable governed by the distribution function p(L). We demonstrate that this model belongs to the universality class of the site-diluted Ising model. This proves that both models are described by the same values of asymptotic critical exponents. However, their effective critical behaviour differs.

As a case study, we consider a quenched mixture of two different magnets with values of elementary magnetic moments 1 and s, and of concentration c and 1

-c, correspondingly, governed by the two-parameter distribution function $p(L) = c \delta (L-1) + (1-c) \delta (L-s)$. We apply both analytical and numerical methods to study the emergence of a low-temperature magnetically-ordered phase in such a system.

First, we use the field-theoretical renormalization group approach to study the peculiarities of critical behaviour in the vicinity of the phase transition point [3]. We analyse the renormalization group flow for different initial conditions, triggered by s and c, and calculate effective critical exponents further away from the fixed points of the renormalization group transformation. We show how the effective exponents are governed by difference in properties of the magnetic components.

Second, we set up extensive Monte Carlo simulations of a random mixture of two Ising-like magnets that differ in spin length s and concentration c [4]. In doing so, we analyze the effect of structural disorder per se without appealing to the presence of a non-magnetic component. Our results demonstrate the emergence of the 3D randomly diluted Ising model universality class in a random mixture of two Ising magnets. While the asymptotic critical exponents coincide with those known for the site-diluted 3D Ising model, the effective critical behavior is triggered by parameters s and c. The impact of their interplay is a subject of detailed analysis.

This leads to the strong conclusion that we can create new types of critical behaviour in disordered Ising-like systems by considering systems with multiple magnetic components, where spin length and concentration can be used to fine-tune critical properties.

- [1] R. Folk, Yu. Holovatch, T. Yavors'kii. Phys. Uspekhi 46, 169 (2003).
- [2] M. V. Kompaniets, A. Kudlis, A. I. Sokolov. Phys. Rev. E 103, 022134 (2021).
- [3] M. Dudka, M. Krasnytska, J. J. Ruiz-Lorenzo, Yu. Holovatch. JMMM 575, **170718** (2023)
- [4] J. J. Ruiz-Lorenzo, M. Dudka, M. Krasnytska, Yu. Holovatch. Phys. Rev. E 111, **02412** (2025)

ASPECTS OF ELECTRO-MAGNETIC PROPERTIES OF MANGANITES AND POLARON EXCITATION

V. V. Chabanenko¹, E. E. Zubov², A. Nabiałek³

¹O. Galkin Donetsk Institute for Physics and Engineering of NAS of Ukraine, Kyiv, UA-03028. Ukraine

²Kyiv Academic University, Kyiv, UA-03142, Ukraine ³Institute of Physics, Polish Academy of Sciences, Warsaw, PL-02668, Poland

The influence of local electron-phonon interaction on the formation of longrange order and electron dynamics in lanthanum-calcium manganite is considered within the framework of the diagrammatic method of time-dependent perturbation theory in the first order over the reciprocal effective interaction radius [1]. It is shown that consistent consideration of correlation contributions with strong electron-electron and electron-phonon interactions allows one to correctly describe dynamic phenomena in manganites. The presented theory yields a spectral density at the level of chemical potential equal to zero, which made it possible to study the fine structure of polaron excitations. A sharp increase in conductivity below the ferromagnetic ordering temperature was detected. It is assumed that this phenomenon is associated with the appearance of mobile polarons of intermediate size in a certain temperature range. The obtained dispersion equations for elementary excitations allow us to estimate the contribution of polarons to electron transport phenomena. The results of theory and experiment are compared using lanthanum-calcium manganite La_{0.5}Ca_{0.5}Mn_{0.94}Fe_{0.06}O₃ with a weak nonstoichiometric content of transition metal ions [2, 3] as an example.

Manganites are characterized by a strong interaction of the electron, lattice and spin subsystems, leading to various phase transitions and different types of ordering. Metal-insulator and structural transitions are observed, as well as various types of magnetic, orbital and charge ordering [4-7]. Interest in such materials has grown in connection with the discovery of possible applied properties of La_{2/3}Ca_{1/3} MnO₃ [4], namely, the high dependence of the permittivity on the magnetic field.

In accordance with E.O. Wollan and W.C. Koehler [8] for $La_{0.5}Ca_{0.5}MnO_3$ at low temperatures we have CE type of antiferromagnetic insulator state as a result of charge and orbital ordering [9]. Apparently, the embedding of Fe^{3+} ions on Mn site in $La_{0.5}Ca_{0.5}Mn_{1-y}Fe_yO_3$ destroys the orbital ordering partially. As consequence, the AFM indirect exchange competing with the double exchange decreases. Therefore, with increasing the Fe^{3+} content the FM properties of $La_{0.5}Ca_{0.5}Mn_{1-y}Fe_yO_3$ must be enforced. For example, it was experimentally observed in

Pr_{0.5}Ca_{0.5}Mn_{1-v}Cr_vO₃ [10] as an increasing of FM fraction in specimen volume. This is a critical value of y above of which the FM order disappears. We suppose that the observed jumps (Fig. 1(d)) of conductivity at 2K and magnetization caused by anisotropy fields to be enforced by Fe³⁺ ions. Indeed, as a rule in FM phase of manganites we have a weak anisotropy fields. At low temperatures the saturation magnetization fields do not exceed of several Tesla [9] and the coercitivity is low too. Although the effects of irreversibility are observed at temperatures $T \sim T_c$ they do not reflect the influence of anisotropy field directly. Very likely the embedded Fe³⁺ ions form on the domain surface the certain cubic structure (for example, austenite structure) with strong anisotropy. With increasing applied field H the magneto-structural transition is realized. The martensite microstructures appear in domain. The formation of these microstructures is accompanied by strong deformation of environment. As a rule this deformations induce additional magnetic moment. Since this structural transition occurs as the phase transition of the first kind we observe the magnetization and conductivity jumps.

We have studied experimentally the high quality polycrystalline samples of $La_{0.5}Ca_{0.5}Mn_{0.94}Fe_{0.06}O_3$ prepared by the solid state reaction from very fine powders of the initial components. Admittance $Y(H_{ext})$ of capacitor with the sample of manganite inside (Y=G+iB, real part of Y is conductance $G\sim 1R_p$, imaginary part is susceptance $B \sim C$; where R_p is parallel resistance, C - is capacitance) versus external magnetic field H was measured by Agilent HP4282A precision RCL bridge with using 4-terminal method at 1kHz frequency.

In fig. 1, together with (a) - magnetization, the temperature dependences of conductance $G(T) \sim \sigma(T)$ and (b) - susceptance B(T) in zero magnetic field for heating and cooling of the sample are presented. As can be seen from the figure, a pronounced conductance peak is observed below the temperature T_C , which reflects the appearance of mobile polarons according to calculations. It can be argued that at temperatures of about 60 K in the La_{0.5}Ca_{0.5}Mn_{0.94}Fe_{0.06}O₃ manganite, mobile polarons significantly reduce electron-electron scattering, contributing to an increase in the degree of coherence of electron-phonon excitations and an increase in conductivity.

Some of the new features at remagnetization in the strong magnetic field were found. Huge jumps and change of sign of susceptance $B(H_{ext})$ has been observed for forward and backward magnetic field direction. This phenomenon has a hysteresis by magnetic field. Hysteresis loops in magnetization and conductivity (fig. 1 (c, d)) with staircase behavior has been observed at 2K. This and other properties of the manganite are discussed.

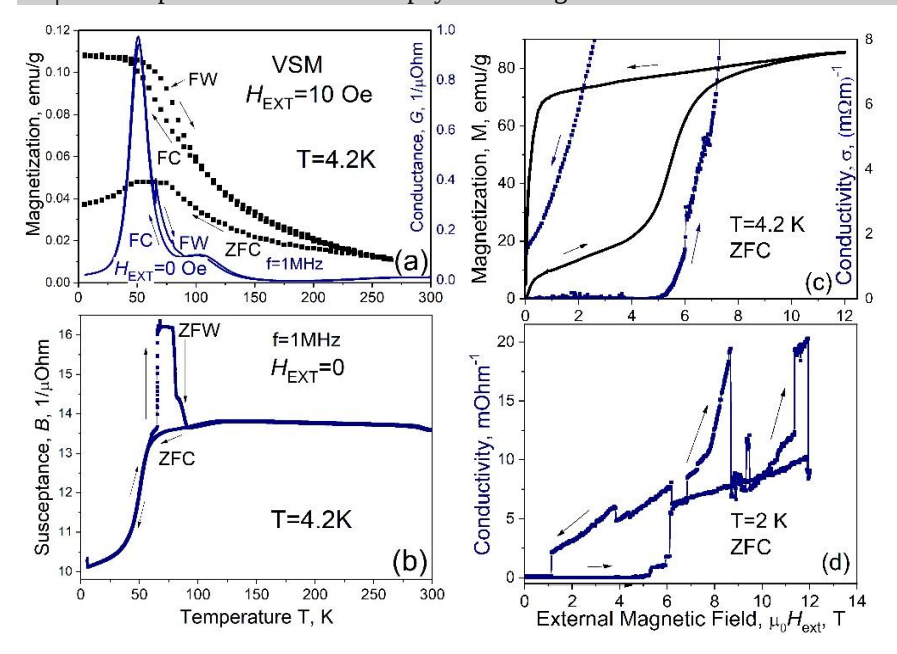


Fig.1. Temperature dependencies (a) - of the magnetization (in the field $H_{\text{ext}} = 10 \text{ Oe}$) and conductance G and (b) - susceptance B during warming from 4.2K after zero field cooling (ZFC) and field cooling (FC) of La_{0.5}Ca_{0.5}Mn_{0.94}Fe_{0.06}O₃, and subsequent field warming process (FW); (c, d) - field dependencies of the magnetization M and conductivity on the D.C. with staircase behavior of manganite; ZFC regime.

- [1] E. E. Zubov, V. P. Dyakonov and H. Szymczak, J. Phys.: Condens. Matter. 18, 6699 (2006).
- [2] P. Levy, et al., Phys. Rev. Lett. 89, 137001 (2002).
- [3] R. Mahendiran, et al., Phys. Rev. Lett. 89, 286602 (2002).
- [4] B. Raveau et al, J. Solid State Chem. 130, 162 (1997).
- [5] F. Damay et al, Appl. Phys. Lett. 73, 3772 (1998).
- [6] J. C. Loudon, N. D. Mathur, and P. A. Midgley, Nature 420, 797 (2002).
- [7] J. Rivas, et al., Appl. Phys. Lett. 88, 242906 (2006).
- [8] O. Wollan and W.C. Koehler, Phys. Rev. 100, 545 (1955).
- [9] J. Goodenough, Phys. Rev. 100, 564 (1955).
- [10] J. M. D. Coey and M. Viret, Advances in Physics, 48, 167 (1999).

MAGNETIC AND MAGNETOCALORIC PROPERTIES OF FERROMAGNETS UNDERGOING STRUCTURAL PHASE TRANSITIONS (INVITED)

V. A. L'vov¹, O. Salyuk^{1,2}, A. Kosogor^{1,3,4}

¹V.G. Baryakhtar Institute of Magnetism of NAS of Ukraine, Kyiv, 03142, Ukraine ² Igor Sikorsky Kyiv Polytechnic Institute, Kyiv, 03056, Ukraine ³University of Vienna, Faculty of Physics, Vienna, 1090, Austria ⁴University for Continuing Education, Krems, 3500, Austria

Magnetocaloric effect (MCE) observed in ferromagnetic and paramagnetic solids is characterized by the temperature change $\Delta T(H)$ caused by the applied magnetic field *H*. The structural phase transition (SPT) observed at the temperature T_{TR} , which is close to Curie temperature of ferromagnet (FM), can strongly affect the temperature dependences of magnetization and heat capacity (M(T) and C(T), respectively). Moreover, it is commonly recognized that SPT can intensify the MCE observed in FM [1,2].

In the present communication the influence of SPT on the magnetic, caloric and magnetocaloric properties of FM is analyzed. It is emphasized that SPT has influence on the energy of magnetic subsystem of FM. The thermodynamic equations [3] and a modified Maxwell relation [4], which establish the interdependence between the energy change, caused by SPT, and M(T), C(T), $\Delta T(H)$ functions are used for computations. The applicability of these equations to real ferromagnets undergoing SPTs is verified by computation of the temperature dependences of magnetization of Ni_{52.6}Mn_{23.5}Ga_{23.9} and Ni_{53.1}Mn_{26.6}Ga_{20.3} Heusler alloys. A quantitative agreement between theoretical and experimental dependences is achieved (see Fig. 1), assuming that SPT results in the energy change $U_0 \rightarrow U = U_0 + \Delta J(T)M^2(T)/2$, where $U_0 = J_m M^2(T)/2$ is magnetic energy of the high-temperature phase, $J_m = const$, parameter $\Delta J(T)$ characterizes the influence of SPT on the spin-exchange and/or magnetic anisotropy energies of FM and varies from zero to $0.1J_m$ in the temperature range of the first-order SPT.

The computations of caloric and magnetocaloric properties of ferromagnets are carried out taking into account that two research trends of MCE are noticeable others. First. the research of magnetocaloric properties among quasistoichiometric Heusler alloys, which undergo structural PTs in the temperature range adjusted to Curie temperature by the purposeful change of chemical composition of the alloys, second, the research of intermetallic rear-earth alloys, undergoing the magnetostructural PTs from paramagnetic to ferromagnetic

state at the temperatures, which are close to the boiling point of natural gas, $T_b \approx 111$ K. To unite these trends a representative ferromagnet, undergoing SPT at the temperature T_{TR} , which is close to Curie temperature $T_C = 110$ K, is considered. The low-temperature limit of saturation magnetization $M_S(0) = 55$ emu cm⁻³ is accepted for computations.

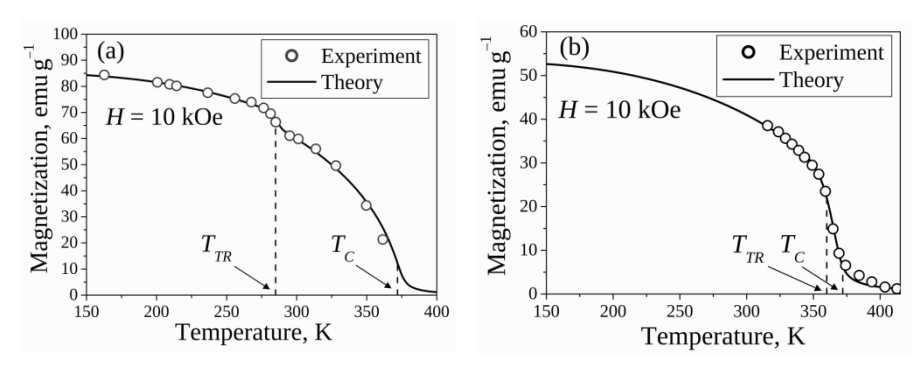


Fig. 1. Experimental [5] and theoretical [6] temperature dependences of magnetization of Ni_{2.1}Mn_{0.94}Ga_{0.96}, (a), and Ni_{2.12}Mn_{1.06}Ga_{0.82}, (b).

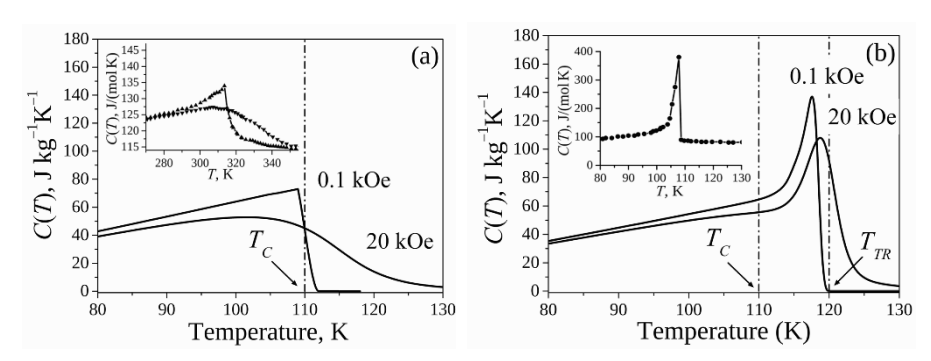


Fig. 2. Theoretical temperature dependences of the heat capacity of magnetic subsystem of the representative alloy, which does not undergo SPT, (a), undergoes SPT that increases magnetic energy of the alloy, (b). Insets: the heat capacity of $Ni_2Mn_{1.4}Sn_{0.6}$ measured in the magnetic fields of 0 kOe and 20 kOe [7], (a); the heat capacity of Nd_2In [8].

Figure 2 shows theoretical temperature dependences of the heat capacity of magnetic subsystem of the representative ferromagnet. The heat capacity $C(T) = \frac{\partial U}{\partial T}$ was computed for $\Delta J(T) = 0$ (Fig. 2 (a)) and for $0 < \Delta J(T) < 0.1 J_m$, $T_{TR} = T_C + 10$ K (Fig. 2 (b)). Figure 2 (a) proves that the theory properly describes the temperature dependence of the heat capacity of ferromagnet, which does not

undergo SPT. Theoretical curves shown in Fig. 2 (b) properly describe a peculiar temperature dependence of the heat capacity observed in experiments with ferromagnets, undergoing SPTs near Curie point.

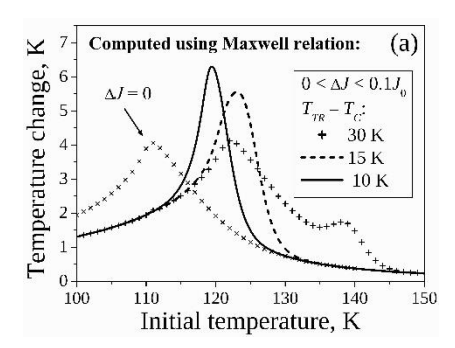
In the absence of SPT the magnetic energy is equal to U_0 . This energy depends on the temperature through the function M(T) only, the *partial* derivative $\partial U_0/\partial T$ is equal to zero and a thermodynamic Maxwell relation,

$$\partial S/\partial H = \partial M/\partial T,\tag{1}$$

follows from the mathematical expression for the differential of the Gibbs free energy. The magnetic energy U of the ferromagnet, which undergoes SPT, explicitly depends on the temperature due to the temperature-dependent coefficient $\Delta J(T)$. Therefore, $\partial U/\partial T \neq 0$ in the temperature range of SPT and a modified Maxwell relation,

$$\partial S/\partial H = \partial M/\partial T + \partial^2 U/\partial H \partial T, \tag{2}$$

must be used for computations of caloric and magnetocaloric properties of ferromagnet.



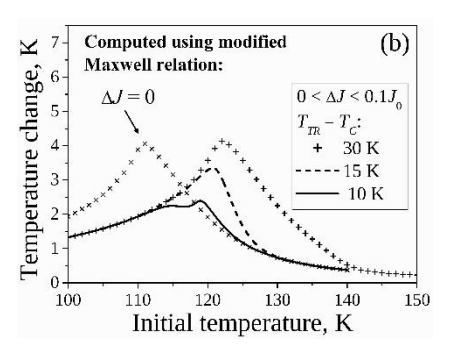


Fig. 3. The temperature changes caused by the application of magnetic field of 20 kOe to the ferromagnets, undergoing SPT at the phase transition temperatures of 140 K (crosses), 125 K (dashes) and 120 K (solid lines).

Figure 3 shows the temperature changes caused by the sudden increase of the magnetic field, which took place at the initial temperature of ferromagnet, T.

Comparing Fig. 3 (a) with Fig. 3 (b) one can see that the computations carried out using the Maxwell relation results in the considerable overestimation of magnetocaloric effect: Figure 3 (a) shows that the narrower is the interval between the phase transition temperature and Curie temperature, the larger is maximum value of the magnetic-field-induced temperature change computed using the Maxwell relation, Eq. (1); Figure 3 (b) shows that the narrower is the interval between the phase transition temperature and Curie temperature, the smaller is

maximum value of the magnetic-field-induced temperature change computed using the modified Maxwell relation, Eq. (2).

It should be summarized that the proper consideration of the influence of structural phase transition on the energy of magnetic subsystem of ferromagnet i) enabled quantitative description of the temperature dependence of magnetization of FM [3,6]; ii) explained the peculiar temperature dependence of the heat capacity of FM, undergoing SPT [4]; iii) resulted in the replacement of the commonly known Maxwell relation, Eq. (1) by the modified Maxwell relation, Eq. (2) [4]; iv) showed that the SPT can noticeably reduce the magnetocaloric effect [4].

The points iii), iv) are practically important, because Eq. (1) is commonly applied to FMs exhibiting SPT (see e.g., Refs. [8,9] and references therein), but Fig. 3 shows that this equation results in the noticeable overestimation of the magnetic-field-induced temperature change, which is the practically important feature of MCE.

Present communication is aimed to motivate the cooperative experimental and theoretical research of MCE in those ferromagnetic solids, which undergo SPTs near the Curie points.

- [1] V. K. Pecharsky and K. A. Gschneidner, Phys. Rev. Lett. 78, 4494 (1997).
- [2] V. Franco et al., Prog. Mater. Sci. 93, 112 (2018).
- [3] V. A. L'vov and O. Salyuk, Low Temp. Phys., 51, 2025.
- [4] V. A. L'vov, O. Salyuk and A. Kosogor (in press), *Thermodynamic analysis of magnetocaloric properties of ferromagnet undergoing structural phase transition near Curie temperature*. Scientific Reports (2025).
- [5] V. A. Chernenko, V. A. L'vov, S. P. Zagorodnyuk and T. Takagi, Phys. Rev. **B** 67, 064407 (2003).
- [6] V. A. L'vov, Fizyka Nyzkykh Temperatur/Low Temperature Physics, 51, 1030 (2025).
- [7] V. A. Chernenko, et al., J. Magn. Magn. Mater. 324, 3519 (2012).
- [8] A. Biswas, et al., Phys. Rev. Mater. 6, 114406 (2022).
- [9] Bruno, N. M., The magnetocaloric and elastocaloric effects in magnetic shape memory alloys. Ph.D. thesis, Texas A&M University (Texas, College Station, 2015).

LOW-TEMPERATURE STUDIES OF THERMAL CONDUCTIVITY OF CARBON MATERIALS

Yu. V. Horbatenko¹, V.V. Sagan¹, A. I. Krivchikov¹, O. A. Korolyuk¹, O. O. Romantsova^{1, 2}, D. Szewczyk²

¹B. Verkin Institute for Low Temperature Physics and Engineering of NAS of Ukraine, Kharkiv, 61103, Ukraine

²Institute for Low Temperatures and Structure Research, Polish Academy of Sciences, 50-422 Wroclaw, Poland

We have experimentally investigated the temperature dependences of thermal conductivity of pure trGo, trGO-composite with hydrated fullerene (HyFn) and composites based on expanded graphite with multi-walled carbon nanotubes (EG-MWCNT) in a wide temperature range of 4 - 300 K using the the steady-state flux method. We have investigated effects on $\kappa(T)$ induced by the annealing and pressure, which are influenced on eventual trGO-composite characteristics, and we also estimated the changes in the thermal conductivity behavior of trGO-HyFncomposites and pure trGo, as well as the dependence of thermal conductivity $\kappa(T)$ on the density of trGO-HyFn samples. The preparation of samples is given in [1]. We have seen that thermal conductivity behavior for pure trGo and trGO-HyFn samples does not change qualitatively. Thermal conductivity data for trGo- and trGO-HyFn composites were compared with data for another carbon material, detonated nanodiamond ceramics (dnd crmc) [2].

EG-MWCNT-composites with different density (d) show behavior of temperature dependences of thermal conductivity similar to trGo-composites, which were pressed and annealed at different temperatures. Finally, a power-law correlation between pre-exponential factors κ_n and characteristic energy E for all investigated materials was found.

- [1] A. Dolbin, et al. Applied Surface Science **361**, 213-220 (2016).
- [2] D. Szewczyk, & M. A. Ramos, Crystals, 12 (12), 1774, (2022).

Acknowledgement: this work supported by the National Research Foundation of Ukraine (Grant 2023.03/0012).

THE INFLUENCE OF SCALE FACTORS ON NUCLEATION AND CRYSTALLIZATION

A. S. Nuradinov¹, K. A. Sirenko¹, I. A. Nuradinov¹, O. V. Chystiakov¹, D. O. Derecha^{1,2}

- ¹ Physico-technological Institute of Metals and Alloys, Natl. Acad. of Sci. of Ukraine, Kyiv, 03680, Ukraine
- ² V.G. Baryakhtar Institute of Magnetism, Natl. Acad. of Sci. of Ukraine, Kyiv, 03142, Ukraine

Crystal nucleation is a process where the scaling effects is a critical parameter that determines characteristics of microstructures [1,2]. In this work the mechanisms of nucleation kinetics in different geometric configurations, revealing scale-dependent transitions in crystallization behavior that directly impact material properties were investigated.

The experiments were carried out by using the physical modeling with Wood's metal alloy and transparent organic media including camphene ($C_{10}H_{16}$) and diphenylamine ($C_{12}H_{11}N$). Two distinct sample geometries were used: thin flat samples with thickness $\delta=0.2$ mm to isolate surface-dominated effects, and bulk cylindrical samples in quartz tubes (Ø 8 mm, volume up to 18×10^{-6} m³) to investigate volume-dependent phenomena.

Temperature-controlled crystallization experiments were performed using setup that allow to control the superheat temperatures (Δt^+) and measurement of supercooling degrees (Δt^-) with $\pm 0.1^{\circ}C$ accuracy. The nucleation rate I was calculated from crystal counting during isothermal crystallization according to I = $(dn/d\tau)/V$, where dn represents crystals formed during time $d\tau$ in volume V.

In thin samples, the non-stationary behavior of nucleation was observed that characterized by extreme time-dependent rates. The nucleation rate initially increased rapidly, reached maximum values I_{max} , then decreased to zero, following the relationship $I_n=I$ exp(- τ_r/t), where τ_r represents relaxation time [3]. The dependence between $ln(I_n)$ and τ_r/t confirmed heterogeneous nucleation mechanisms. Increasing superheat temperature caused I_{max} the reduction and temporal shift toward longer crystallization times, indicating surface activity at the melt-mold interface [4].

Dispersion in the crystal size showed correlation with nucleation rates, varying by one order of magnitude. For camphene, nucleation rates spanning from 6×10^5 to 29×10^5 m⁻³ corresponded to different grain structures and demonstrating the importance of controlled nucleation for microstructural refinement.

The bulk samples demonstrate other behavior in dependence of the scaling factors. Unlike thin samples with reproducible surface-controlled nucleation, bulk systems exhibited significant scatter in supercooling values. Wood's alloy showed excellent reproducibility (±1°C variation), while organic media demonstrate moisture-dependent supercooling variations that decreased with dehydration.

The relationship between maximum supercooling and sample volume demonstrated non-linear characteristics, contradicting linear scaling laws observed in droplet studies [3]. For both camphene and diphenylamine, supercooling values decreased with increasing volume before reaching plateau regions for $V > 12 \times 10^{-6}$ m³. This behavior indicates transition from surface-dominated to volumecontrolled nucleation mechanisms.

Analysis of surface area to volume ratio (S/V) effects revealed that its values decreasing initially caused gradual supercooling reduction, followed by sharp transitions to constant values. This reflects the probability of active impurity presence in larger volumes, enhancing heterogeneous nucleation sites availability.

Statistical analysis showed improved supercooling reproducibility with increasing sample volume. For diphenylamine samples ranging from 3×10⁻⁶ to 18×10⁻⁶ m³, supercooling scatter decreased from 19% to 5%, while camphene showed reduction from 17% to 4%. This confirms the statistical nature of nucleation in bulk systems where multiple competing nucleation sites exist.

Thus, there are the scaling transitions in nucleation mechanisms: thin samples exhibit purely surface-controlled heterogeneous nucleation with high reproducibility, while bulk samples include the volume effects such as temperature fluctuations, density variations, convection, impurity distribution and inhomogeneities.

As result, the control of process parameters such as superheat temperature, cooling rate, and mold surface conditions allows to change the supercooling degrees and crystal formation rates. This allows to optimize the structures through process parameter control for direct applications in developing materials with enhanced mechanical properties through microstructures changing.

^[1] K. Sangwal, Nucleation and Crystal Growth: Metastability of Solutions and Melts (John Wiley & Sons, 2018).

^[2] J. Frenkel, *Kinetic Theory of Liquids* (Peter Smith Publisher, 1984).

^[3] A. S. Nuradinov, et al., Physica Scripta 100, 035909 (2025).

^[4] B. Yang, et al., J. Chem. Phys. 140, 104513 (2014). [5] J. H. Perepezko, Mater. Sci. Eng. A 413, 389 (2005).

CRITICAL PROPERTIES OF STRUCTURALLY DISORDERED MAGNETS WITH LONG-RANGE INTERACTIONS

M. Dudka^{1,2,3}, D. Shapoval^{1,2}, Yu. Holovatch^{1,2,4,5}

¹Yukhnovskii Institute of Condensed Matter Physics, National Academy of Sciences of Ukraine, 79011 Lviv, Ukraine

²L4 Collaboration & Doctoral College for the Statistical Physics of Complex Systems, Leipzig-Lorraine-Lviv-Coventry, Europe ³Lviv Polytechnic National University, 79013 Lviv, Ukraine ⁴Centre for Fluid and Complex Systems, Coventry University, Coventry, CV1 5FB, United Kingdom ⁵Complexity Science Hub, 1030 Vienna, Austria

Some physical systems, although different by their microscopic nature, in the vicinity of critical points can have similar thermodynamic and structural properties governed by universal power laws. Such systems are grouped into the so-called universality classes. The latter are determined by such global characteristics as the type of interaction, space dimensionality, symmetry, and the number of components of the order parameter. Therefore, it is interesting to investigate how the mutual influence of these characteristics can affect the critical features of the system.

While the critical behaviour of ideal magnetic systems with short-range interaction is well known [1], the goal of our research is to analyze the a challenging issue of a mutual impact of long-range interaction and weak structural disorder on the critical behavior of a many-particle magnetic system. Using the field-theoretical n-vector model in a d-dimensional space, we investigate ferromagnetic ordering in a structurally disordered magnet with the long-range interaction decaying with the distance x as $J(x) \sim x^{-d-\sigma}$, with the control parameter $\sigma > 0$ meaning weak long-range interaction. The analysis is carried out using the field-theoretical renormalization group methods, which makes it possible to identify the universality classes of the system under consideration, their change with global parameters, and to determine the universal characteristics of critical behavior (critical exponents and marginal dimensions). It is known that there exists such a region of parameters (d,n,σ) , where the long-range interaction and structural disorder lead to a synergistic effect resulting in emergence of a new, "random long-range" universality class [2], see Fig.1.

We have calculated an order parameter marginal dimension defining stability boundary of this region [3] within the *three-loop approximation* as perturbation

theory series in $\epsilon' = 2\sigma - d$. Quantitative estimates of the border are extracted from this expansion using asymptotic series resummation methods. We also have calculated the correlation length critical exponent $v(\epsilon',n)$ characterizing new universality class [4].

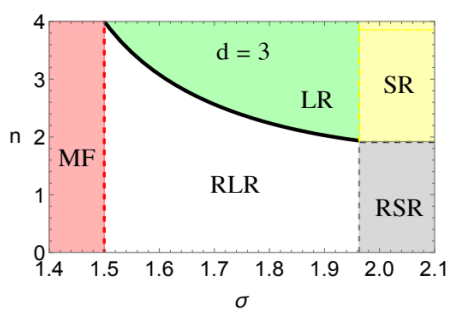


Fig. 1. Universality classes of a structurally disordered magnet with longrange interaction in the σ – n parameter space for d=3. The marginal dimension of the order parameter (solid black line, our result) separates the universality class of the "pure" long-range model (LR) from the universality class induced by structural disorder (RLR). Mean-field (MF) behaviour is observed for $\sigma < d/2 = 1.5$. For large σ the behavior of the short-range model is realized: for n>1.912 – the "pure" model universality class (SR); for n<1.912– the universality class induced by disorder (RSR).

To get more reliable data we extract values of stability border as well as the critical exponent v from applying resummation procedure directly to the perturbative renormalization group functions using fixed spatial dimension approach at d=3.

M.D. and D.S. acknowledge the support of the U.S.Department of Energy (DOE), Office of Science, Basic Energy Sciences, Materials Science and Engineering Division, under Award No.DE-SC0013599 (Subaward No. UTAUS-SUB00000795)

- [1] Order, Disorder And Criticality Advanced Problems Of Phase Transition Theory, Yu. Holovatch (Ed.), vols.1-8 (World Scientific, Singapore, 2004-2025)
- [2] Y. Yamazaki, Physica A 90, 547 (1978)
- [3] D. Shapoval, M. Dudka, Yu Holovatch, Low Temp. Phys. 48, 1049 (2022).
- [4] M. Dudka, D. Shapoval, Yu. Holovatch, Journal of Physical Studies 28, 2601 (2024).

INFLUENCE OF NON-HEISENBERG EXCHANGE ON THE ENTROPY OF AN ISOTROPIC FERROMAGNET

S. O. Reshetniak^{1,2}, G.Yu. Lavanov^{1,3}, V. M. Kalita ^{1,4}

¹National Technical University of Ukraine "Igor Sikorsky Kyiv Polytechnic Institute", Kiev, 03056, Ukraine ² V. G. Baryakhtar Institute of Magnetism of the NAS of Ukraine, Kiev, 03142, Ukraine

³National Aviation University, Kiev, 03058, Ukraine ⁴Institute of Physics National Academy of Sciences of Ukraine, Kiev, 03028, Ukraine

The non-Heisenberg four-order spin exchange leads to a strong nonlinearity of the exchange field with respect to the mean spin. When the contribution of such four-spin exchange is of the ferromagnetic type, the nonlinear addition to the exchange field contributes to the additional magnetic ordering. The additional nonlinear contribution to the exchange field from the four-spin exchange affects the magnetization, changing the isofield temperature dependences for the magnitude of the mean spin. Due to the four-spin exchange, a faster saturation of the spontaneous magnetization should occur. Therefore, the four-spin exchange should affect the properties and critical behavior of the ferromagnet in the vicinity of the Curie temperature. This is important when studying the magnetocaloric effect, the magnitude of which depends on the change in magnetic entropy induced by a magnetic field upon the ferromagnet's magnetization and which is most pronounced in the vicinity of the Curie temperature of a second-order phase transition.

The change in entropy at the magnetizing a ferromagnet depends on the change in its degree of ordering; therefore, the greater the change in the magnitude of the mean spin (order parameter), the greater the change in entropy should be, which should promote the magnetocaloric effect. An additional ferromagnetic-type Heisenberg contribution to the exchange field enhances the effect of an external magnetic field and should additionally lead to an increase in ordering, and, accordingly, the magnetocaloric effect should increase.

We found that even in a weak magnetic field, a significant change in magnetic entropy can be observed for a low-spin system, which is interesting from the point of view of searching for low-spin materials with a large magnetocaloric effect observed in weak external magnetic fields.

We have theoretically investigated an isotropic ferromagnet with a four-spin exchange with ion spins equal to $\pm 1/2$ [1]. An expression for the nonequilibrium free energy as a function of the mean spin was written, from the minimum condition of which the equation of state was written. An expression for the Landau-Devonshire potential was also obtained.

Figure 1 shows the calculated temperature dependences for the mean spin value $s(\tau)$ of the ferromagnet's ions at different values of the four-spin exchange parameter k, in a constant small field $h=10^{-5}$, where τ and k are temperature and the four-spin exchange parameter, which are normalized to the constant of the spin-bilinear Heisenberg exchange, and *h* is the magnetic field normalized to the magnitude of the Heisenberg exchange field.

The behavior of the $s(\tau)$ curves is typical for a second-order phase transition. Note that at $k > k_{cr} = 4/3$, the transition between the paramagnetic and ferromagnetic phases will change to the first order [1]. From the figure, it can be seen that at temperatures below the Curie temperature, $\tau < \tau_c = 1/4$, the value of the mean spin $s(\tau)$ additionally increases due to the non-Heisenberg contribution; at larger values of *k*, the value of the mean spin increases.

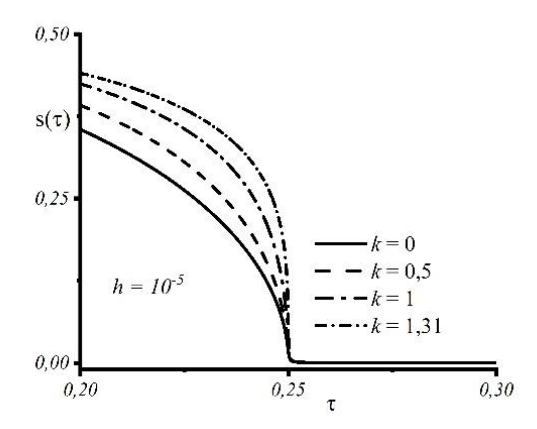


Fig. 1. Temperature dependence of the mean spin on temperature for different values of the four-spin non-Heisenberg exchange parameter in a small constant field.

The accelerated magnetization due to the action of the non-Heisenberg 4-spin exchange leads to a faster change in entropy near the Curie temperature. Fig. 2 shows the isofield temperature dependences for the ferromagnet's magnetic

entropy change $\Delta \sigma(h) = \sigma(\tau, h \neq 0) - \sigma(\tau, h = 0)$ taken with a minus sign, due to its magnetization by a field h. The dependences in Fig. 2 are plotted based on the data given in Fig. 1.

As expected, the magnetic entropy increase has a maximum at the Curie temperature, and the magnitude of the increase depends on the non-Heisenberg exchange parameter. We have that due to the influence of the non-Heisenberg addition, even in a small external magnetic field, a significant change in the magnetic entropy can be observed, compared to a Heisenberg (k=0) ferromagnet.

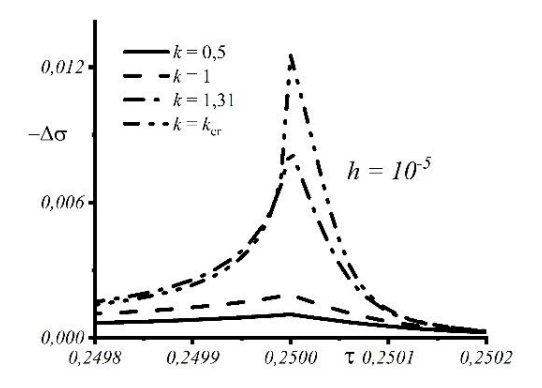


Fig. 2. Change in entropy with temperature at a small constant field h=10⁻⁵ for different values of the 4-spin non-Heisenberg interaction constants.

Also, for a ferromagnet with a 4-spin exchange, the influence of the parameter k on the critical exponents was analyzed. It was found that when only a second-order phase transition is possible in the ferromagnet, i.e., when k takes values from the interval $k \in [0, k_{cr}]$, the values of the critical exponents lie in intervals whose boundaries are determined by the numerical values obtained in the mean-field model, the tricritical mean-field model, and other models, which is important for the analysis of the magnetic and caloric properties of ferromagnets.

[1] G. Yu. Lavanov, S. O. Reshetniak, V. M. Kalita, Physica B: Condensed Matter **716**, 417664 (2025).

ALTERMAGNETISM: NEW CONCEPT OR WELL-FORGOTTEN OLD (INVITED)

B.A. Ivanov^{1,2}

¹ V.G. Baryakhtar Institute of Magnetism of the NASU, Kyiv 03142, Ukraine ² Radboud University, IMM, Nijmegen 6525AJ, The Netherlands

Magnetic materials are divided into two wide classes: ferromagnets (or ferrimagnets) with spontaneous net magnetization, and antiferromagnets, which are often referred to as magnets with no magnetization. Antiferromagnets are known for almost one century, and many of their properties were understood in the past century [1]. In recent decades, the interest in antiferromagnets has been fueled by their potentials for technological applications, mostly thanks to their ultrafast (a few orders of magnitude faster than that for ferromagnets) spin dynamics. Recently, a possibility of presence a novel class of spin-compensated materials, called altermagnets, was discussed [2,3]. The aim of this talk is to compare two pictures of compensated magnets, based on standard approach [1] and on altermagnetic concept.

Magnetic structure of antiferromagnets consists of a few magnetic sublattices, which are equivalent from the viewpoint of the crystal symmetry group [1]. For the case of "binary" magnetic structure with "up" or "down" spins only, antiferromagnets can be described by the net magnetization M and so-called Néel vector L, which is the difference of sublattice spins. The key feature of antiferromagnets within the standard approach is that the action of at least one element of the crystal symmetry group changes the sign of the L-vector; such elements are called odd elements [1]. The properties of antiferromagnets are extremely sensitive to their crystal structure that is in a strict contrast to ferro- and ferrimagnets, which may even be amorphous. The bright textbook example: two antiferromagnetic transition metal oxides with identical crystal structures, hematite α-Fe₂O₃ and chromium oxide Cr₂O₃, have radically different magnetic properties. It is important to stress that the determination of sublattice structure of antiferromagnet is determined by exchange interaction only. All antiferromagnets can be divided into three classes, including one, which is now classified as altermagnetic [4]. These classes are as follows.

1. The odd element is a lattice <u>translation</u>, i.e., the magnetic unit cell is larger than the chemical unit cell. For such antiferromagnets the sign of the Néel vector does not make much sense, e.g., areas with opposite orientations of the Néel vector are not necessarily separated by a domain wall [5].

- 2. The odd symmetry element is space inversion, these antiferromagnets allow magnetoelectric effect and they are known as those having PT-symmetry.
- 3. The odd symmetry elements are only rotations (proper or improper). Antiferromagnets from this class were called canted antiferromagnets or weak ferromagnets, their weak magnetic moment, caused by non-collinearity of sublattices, is attributed with relativistic (or exchange-relativistic) interactions [1].

Altermagnets are also defined as antiferromagnets with the exchange symmetry as for third class; but they are described by models with non-relativistic interactions only. By definition, altermagnets have zero net magnetization, but they allow some effects, typical for ferromagnets, like spontaneous Faraday effect and anomalous Hall effect [2].

Long ago, the aforementioned effects were known for antiferromagnets of the third class; note the observation of **L**-dependent Faraday effect in orthoferrites [6] or Hall effect in hematite [7]. Of course, the symmetry arguments say nothing about the physical origin of magnetooptical or galvanomagnetic effects. The lifting of degeneration of magnons with opposite chiralities, found for altermagnetic RuO₂ with use of density-functional-theory calculations [8] was not discussed within the standard approach, but this effect can be described by accounting for an extra exchange term of the form of $(\partial \mathbf{M}/\partial x \cdot \partial \mathbf{L}/\partial y)$ [9]. Note what for any antiferromagnets allowed relativistic term of the form of $D_{ij}M_iL_j$, an exchange term $A_{ij}(\partial \mathbf{M}/\partial x_j \cdot \partial \mathbf{L}/\partial x_j)$ can be constructed, with the same symmetry of the tensors D_{ij} and A_{ij} , what was probably overlooked before. Thus, the most important features of these two groups of magnets coincide, and it is worth keeping the wording "altermagnets" for antiferromagnets of the third class, allowing weak magnetic moment "in real life", when the presence of the relativistic interactions is unavoidable.

- [1] E. A. Turov, A. V. Kolchanov, M. I. Kurkin, I. F. Mirsaev, V. V. Nikolaev, *Symmetry and Physical Properties of Antiferromagnets* (Cambridge International Science, Cambridge, UK, 2010).
- [2] L. Smejkal, J. Sinova, and T. Jungwirth, Phys. Rev. X 12, 031042 (2022).
- [3] L. Smejkal, J. Sinova, and T. Jungwirth, Phys. Rev. X 12, 040501 (2022).
- [4] A.V. Kimel, Th. Rasing, and B.A. Ivanov, J. Magn. Magn. Mater. **598**, 172039 (2024).
- [5] I. E. Dzyaloshinksii, JETP Lett. 25, 8 (1977).
- [6] B. B. Krichevtsov, K. M. Mukimov, R. V. Pisarev, and M. M. Ruvinshtejn, JETP Lett. **34**, 379 (1981)
- [7] K. B. Vlasov, V. N. Novogrudskiy, and E. A. Rozenberg, Fiz. Met. Metalloved. 42, 513 (1976).
- [8] L. Smejkal, et al., Phys. Rev. Lett. 131, 256703 (2023).
- [9] O. Gomonay, et al., npj Spintronics 2, 35 (2024)

FLUORESCENT RESPONSE OF HYBRID FILMS WITH A COUMARINE7/FLUORESCEIN DYE SYSTEM TO GASEOUS AMMONIA.

V. P. Mitsai¹, Ya. P. Lazorenko²

¹ V.G. Baryakhtar Institute of Magnetism of the NAS of Ukraine, Kyiv, 03142, **Ukraine**

² G.V. Kurdyumov Institute for Metal Physics of the NAS of Ukraine, Kyiv, 03142, Ukraine

Human exhaled air contains over 3000 volatile organic and inorganic components that reflect the individual metabolic profile of a person, and its components change in various pathological conditions and diseases. Such substances are called biomarkers, and knowing their concentration allows you to detect these pathologies. Therefore, recently, in the course of searching for new opportunities in medical diagnostics, the problem of analyzing human exhaled air has gained special interest [1].

Endogenous gaseous ammonia (NH₃) attracts special attention of researchers. It is known that ammonia is a marker of diseases such as renal failure; liver failure in hepatitis, liver cirrhosis, lung cancer. The concentration value of endogenous ammonia in exhaled air are in the range of 100-150 billion ⁻¹ for healthy people, while in the case of pathology, the concentration of ammonia in exhaled air is > 1ppm [2]. Therefore, it is necessary to have methods that can detect ammonia gas at very low concentrations (units of ppm).

Today, there are a number of methods for the determination of gaseous ammonia, based on electrochemical cells, semiconductor metal oxides, and optical detection methods [3].

Optical methods for the detection of gaseous ammonia include optical chemical sensors based on optical absorption and luminescence. The principle of measurement in such sensors is based on a change in the absorption or luminescence (fluorescence) spectra of a pH indicator or a fluorescent dye sensitive to ammonia, which is deprotonated in the presence of ammonia or undergoes fluorescence quenching by one of the existing quenching mechanisms (static or dynamic). Dye pairs can also be used in such sensors.

Such dyes are usually immobilized in transparent polymer films (matrices) deposited on various types of substrates. Changes in their absorption spectra and changes in fluorescence intensity are measured by spectroscopic methods or optoelectronic devices [4].

Among scientific publications, reports of fluorescent ammonia sensors, the sensitivity mechanism of which is based on Förster resonance energy transfer (FRET), are of particular interest. This is a non-radiative energy transfer between two fluorescent dyes, one of which acts as an energy donor and the other as an energy acceptor. This process occurs if the emission spectrum of the donor overlaps with the absorption spectrum of the acceptor. The efficiency of energy transfer in FRET depends on the distance between the donor and the acceptor (it should not exceed 10 nm) [5].

Such sensors use a dye system in which one dye is sensitive to ammonia and the other molecule can exhibit the necessary spectral properties of fluorescence. By studying the change in the fluorescence intensity of such a dye system at different wavelengths, ammonia can be detected. The prospect of using such complexes with FRET energy transfer between them arouses interest in their further study.

We synthesized and investigated gas-sensing nanostructured films based on ethylene vinyl acetate polymer with a SiO2 sorbent layer doped with Coumarin 7 and films doped with the Coumarin7+Fluorescein dye complex.

Coumarin 7 with a fluorescence wavelength of λ =493 nm and absorption of λ =435 nm and fluorescein with a fluorescence wavelength of λ =520 nm and absorption of λ =490 nm are well-studied fluorescent dyes that are widely used in various fields of science due to their fluorescent properties.

Coumarin dyes and their derivatives have intense fluorescence in the blue-green region. Coumarins with a non-rigid structure (containing six-membered heterocycles), due to intramolecular charge transfer, are sensitive to the polarity of the medium [6]. Fluorescein belongs to the xanthene dyes (and also has six-membered heterocycles in its structure) and has yellow-green fluorescence. In fluorescence spectroscopy, it is used as a reference (standard) for measuring the quantum yield of fluorescence. It is known that the dye fluorescein is sensitive to gaseous ammonia. It changes its proton form. depending on the pH of the environment [7].

Förster resonance energy transfer (FRET) is assumed in the coumarin7/fluorescein dye system. Since the absorption spectrum of fluorescein (energy acceptor) overlaps with the fluorescence spectrum of coumarin7 (energy donor).

It is also known that porous films of silicate sorbents have a large specific surface and are actively used for adsorption of volatile molecules from a gaseous medium. The greater porosity of the film surface provides a faster diffusion of gases into its volume and accelerates the reaction (i.e., response) to it.

The films were prepared by layer-by-layer application of components onto a transparent glass substrate. First, a layer of EVA polymer was applied, which,

being in a liquid state, was covered with a layer of finely dispersed SiO₂ sorbent (in powder form). Then, the mixture of ethyl solutions of dyes coumarin 7 with fluorescein, with a concentration of 10⁻³M, in the ratio 1:1 was applied. The samples were dried at room temperature.

For the obtained samples, a study was conducted of their fluorescence output intensity and their response to ammonia vapors of several concentrations was carried out. The fluorescence intensity of the samples and their fluorescent response to ammonia were measured using a Flx-800T fluorimeter.

An air-based gas mixture with the the necessary quantity of ammonia was prepared by evaporating a 10% ammonia solution and successive multiple dilutions in glass containers to the desired concentration.

To measure the response of the samples to ammonia, the prepared gas mixture with concentrations of 5000 ppm, 5 ppm was pumped through a gas cuvette with a sample placed in a fluorimeter, and the change in the fluorescence intensity of the sample was recorded. The fluorescent response of the films to the presence of ammonia was recorded in the fluorescence dynamics mode with excitation at 485 nm and reception at a wavelength of 528 nm.

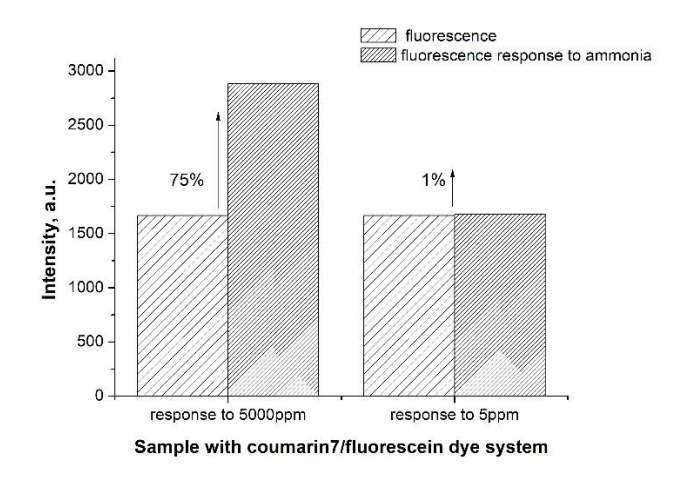


Fig. 1. Fluorescent response of a film sample with a coumarin7/fluorescein dye system at 5000 ppm and 5 ppm of ammonia gas.

As can be seen from the diagram (Fig. 1), the fluorescence intensity of the sample containing a complex of two fluorescent dyes (coumarin7|fluorescein dye system) increased by 75% when gaseous ammonia was pumped through with a concentration of 5000 ppm.

After pumping ammonia gas at a concentration of 5 ppm, the fluorescence intensity of the same film sample increased by 1% compared to the initial intensity of the sample..

If we consider the dye coumarin7 separately, then under the influence of ammonia, a decrease in its fluorescence intensity is usually observed [6], which can be explained by the formation of non-fluorescent complexes in which non-radiative energy transfer occurs with subsequent scattering - a process of static fluorescence quenching.

In the case of the sample with the coumarin7/fluorescein system, we observe, on the contrary, an increase in the fluorescence intensity of the sample, which can be explained as follows. It is known that, depending on the pH of the environment, fluorescein exists in cationic, neutral, monoanionic or dianionic forms or in the form of a mixture of them [7]. Under the influence of ammonia, fluorescein undergoes deprotonation, the fluorescein molecule passes into the dianionic form (with two anionic centers (–O- and –COO-) which is the most stable and intensely fluorescent form of the molecule, which leads to an increase in fluorescence at the wavelength of its emission. At the same time, the transition of fluorescein to the dianionic form led to a greater overlap between the spectra of coumarin 7 and fluorescein in the FRET system, leading to a decrease in the fluorescence of coumarin7 due to increased energy transfer to fluorescein.

So, we synthesized a new type of gas sensor film samples based on the donor-acceptor complex coumarin7/fluorescein, and discovered the presence of a fluorescent response of the synthesized samples and its magnitude. For high ammonia concentrations of 5000 ppm, the response of the samples is 75%, while for trace ammonia concentrations of 5 ppm, the response is 1%. Thus, the presence of a significant response of the created nanostructured films with the coumarin7/aluorescein dye system to ammonia molecules, gives prospects for the use of these materials for the detection of gaseous ammonia in the air environment in low concentrations, in particular for non-invasive diagnostics of diseases.

- [1] E. K. Alenezy, et al., Biosens. Bioelectron. **278**, 117094 (2025)
- [2] A. Abbaszadeh, S. Makouei, S. Meshgini, Photonics Nanostructures Fundam. Appl. **44,** 100917 (2021).
- [3] C. McDonagh, C. S. Burke and B. D. MacCraith, Chem. Rev. 108, 400-422 (2008).
- [4] L. Peng, et al., Opt. Commun. 284, 4810-4814 (2011).
- [5] R.E. Bailey, A.M. Smith, S. Nie, Physica E **25**, 1 (2004).
- [6] V.P. Mitsai, Ya.P. Lazorenko, A.G. Misyura, S.O. Mamilov, Nanosistemi, Nanomateriali, Nanotehnologii **19**, 941 (2021).
- [7] R. Sjöback, J. Nygren and M. Kubista, Spectrochim. Acta, Part A 51, L7-L21 (1995).

ENERGY BAND STRUCTURE AND RESONANT **INELASTIC X-RAY SCATTERING IN SOME IRIDATES**

D. A. Kukusta, V. N. Antonov, L. V. Bekenov

G. V. Kurdymov Institute for Metal Physics of the N.A.S. of Ukraine, Kyiv, 03142, Ukraine

The band energy structure and magnetic properties of hyperkagome iridates Li₃Ir₃O₈ [1] and β -Li₂IrO₃ [2] as well as pyrochlore iridates R_2 Ir₂O₇ (R = Y, Pr, and Eu) [3] together with the resonant inelastic x-ray scattering (RIXS) spectra at the Ir L_3 absorption edge are investigated theoretically using first-principle calculations in the frame of the fully relativistic spin-polarized Dirac LMTO band-structure method in GGA+U.

The energy band structure calculations show that Li₃Ir₃O₈ hosts a spin-orbit induced semimetallic state. The spin-orbit induced semimetallic electronic structure seems to be robust against the small change of structural parameters, which is the consequence of the large energy scale of bonding-antibonding splitting for the molecular orbitals and spin-orbit coupling as compared with crystal field effect from the change in lattice distortion. The peak in RIXS spectrum of Li₃Ir₃O₈ at 1.2 eV is the excitation from the J_{eff} = 3/2 bands to empty $J_{\rm eff}$ = 1/2 bands above $E_{\rm F}$. The low-energy peak at around 0.3 eV is the excitation between the $J_{\rm eff}$ = 1/2 valence and conduction bands. The agreement of low-energy excitations between the calculated and experimental RIXS spectra proves a spinorbit induced semimetallic state in Li₃Ir₃O₈. The energy of t_{2g} – e_g excitation centered at 4.0 eV is smaller than its calculated value of 4.3 eV. This is too large to be ascribed to the possible non-stoichiometry of the sample, namely a small deviation of valence state from Ir^{4.33+} and may be caused by the spherically averaged potential and/or basis set used for the band structure calculations as the position of the Ir e_g state is quite sensitive to the choice of basis set.

The correct ground state β-Li₂IrO₃ in the orthorhombic structure can be obtained only when the Coulomb interaction and SO coupling are both incorporated. The Coulomb repulsion $U_{\rm eff}$ splits the half-filled $J_{\rm eff}$ = 1/2 band into an empty upper, with pure $d_{5/2}$ character, and occupied low Hubbard bands. The pressure-induced structural $Fddd \rightarrow C2/c$ phase transition is accompanied by the formation of Ir2 dimers on the zigzag chains. The strong dimerization stabilizes the bonding molecular-orbital state, leads to the collapse of the magnetism, and opens the energy gap with a concomitant electronic phase transition from the magnetic Mott insulator to nonmagnetic noncorrelated band insulator. This phase does not

accommodate local $J_{\rm eff}$ = 1/2 moments, indicating a delicate balance between magnetism and the intermetallic covalency. This naturally implies the nonessential role of Hubbard U and SO coupling in the high-pressure monoclinic structure. RIXS measurements show the drastic reconstruction of the energy band structure associated with the Ir dimerization. The reconstruction of the RIXS spectral peak at 0.7 eV associated with the structural phase transition can be related to the disappearing of the Coulomb correlations in the ambient pressure Fddd phase. The calculations shift the Ir $t_{\rm 2g} \rightarrow e_{\rm g}$ peak towards higher energy and overestimate the intensity of the fine structure in the 1 to 1.5 eV energy range but produce excellent agreement in the energy position and intensity of the prominent peak at 0.7 eV.

The IrO₆ octahedra are trigonally compressed in the pyrochlore iridates R₂Ir₂O₇. Larger *R* ions tend to result in a smaller distortion, increased hopping and bandwidth which leads to a stronger metallic character. When R changes from Y^{3+} to Pr^{3+} the size of R increases, the system becomes a semimetal and remains metallic down to the lowest temperature. The admixture of the $J_{\rm eff}$ = 3/2 component to the $J_{\rm eff}$ = 1/2 states is increased while going from R = Y to Pr. The structure of the Ir t_{2g} energy bands is identical in R_2 Ir₂O₇, that's why these compounds exhibit qualitatively similar RIXS spectra. The empty upper energy bands ($J_{eff} = 1/2$) are split in $R_2 Ir_2 O_7$, the splitting is the smallest for R = Y and the largest for R = Eu. It is responsible for the fine structure of the low energy peak in RIXS spectra. We found that the one-dimensional $c\Gamma_{3+}$ representation with the AIAO AFM configuration is the ground magnetic state in Y₂Ir₂O₇ as well as in Pr₂Ir₂O₇. The Eu₂Ir₂O₇ compound possesses several symmetry protected magnetic configurations such as $c\Gamma_{3+}$ and $c\Gamma_{7+}$ for both or one of the Ir or Eu sites. They have very close total energies which differ from each other just by several meV. However, the AIAO ($c\Gamma$ 3+) configuration for both the Ir and Eu sites is the ground state in Eu₂Ir₂O₇. The experimentally measured RIXS spectra for all R possess sharp features below 2 eV corresponding to transitions within the Ir t_{2g} levels, and a strong intense peak stretching from 2.5 to 5 eV that according to the calculations corresponds to d–d transitions between the Ir t_{2g} and e_{g} manifolds. The double peak structure from 0.3 to 1.3 eV can be assigned to the local excitations between the filled and empty parts of split $J_{\text{eff}} = 1/2$ band. The fine structure in the 1.3–2.3 eV energy range is due to the local excitation between the filled $J_{\rm eff} = 3/2$ and empty $J_{\rm eff} = 1/2$ states but its intensity is overestimated in our band structure calculations.

^[1] T. Takayama, et al., Phys. Rev. Materials 4, 075002 (2020).

^[2] V. N. Antonov, et al., Phys. Rev. B 103, 235127 (2021).

^[3] V. N. Antonov, L. V. Bekenov and D. A. Kukusta, Phys. Rev. B 102, 195134 (2020).

ELECTRONIC STATE AND MAGNETIC PROPERIES OF HALF-METAL TYPE HEUSLER ALLOYS (INVITED)

R. Y. Umetsu^{1,2}

¹Institute for Materials Research, Tohoku University, Sendai, 980-8577, Japan ²Center for Science and Innovation in Spintronics, Tohoku University, Sendai, 980-8577, Japan

Half-metallic ferromagnets (HMFs) have been intensively investigated in field of spintronics, since half-metallic electronic structures were theoretically predicted in some half-Heusler and full-Heusler alloys in 1980s. The HMFs must be very useful as a ferromagnetic electrode for the spin injection and tunnel magneto resistance as well as in various spin utilizable devices when the electrons around the Fermi level (E_F) are completely spin-polarized. Recently, we successfully detected the electronic structures of some full-Heusler alloys of bulk single crystals by angle-resolved photoelectron spectroscopy (ARPES) [1] and by resonant inelastic X-ray scattering (RIXS) in an external magnetic field and its magnetic circular dichroism (MCD) [2-4]. The RIXS is a photon-in/photon-out spectroscopy by tuning the incoming photon energy to the core-level absorption edges, and the MCD is effective to probe the magnetic excitations in the magnetically ordered states and the spin-polarized electronic structures.

Bulk single crystals in some full-Heusler alloys (Mn₂VAl, Co₂MnSi, Co₂MnGa and Co₂MnGe) were grown by Bridgman method. Strip shaped specimens with the direction <100> was used for RIXS and ARPES experiments. The RIXS measurements were performed at room temperature at SPring-8 BL07LSU using the left and right circularly polarized light. The external magnetic field of 0.25 T was applied by a magnetic circuit with a permanent magnet. The energy resolution of Mn was ~170 meV. The ARPES measurements were performed at SPring-8 BL25SU at a temperature of \sim 30 K. The beam spot size was adjusted to 10 \times 10 μm . The energy and angular resolutions for ARPES were < 80 meV and < 0.2°, respectively.

For the RIXS experiments, RIXS-MCD are clearly observed in the present full-Heusler alloys. Figure 1 (a) and (b) indicate RIXS-MCD in Mn 2p_{3/2} edge in Co₂MnSi and Mn₂VAl, respectively [3,4]. Because the composition and the environment of Mn atoms are different in these alloys, spectra of the RIXS-MCD are different even in the same atom of Mn. From the comparison with the calculated spectra obtained by Kramers-Heisenberg formula based on the density functional theory, it is found that we can discuss the value of the Zeeman splitting

energy, width of the gap and which spin sub-band opens the half-metallic gap around the $E_{\rm F}$.

The RIXS-MCD experiments for Co_2MnGa were recently performed at new synchrotron facility in Japan, *NanoTerasu*, at the campus of Tohoku University. The energy resolutions of Mn at BL07U and BL02U were ~70 meV and ~8 meV, respectively, being highest class in the world.

For the ARPES experiments in Co_2MnGe full-Heusler alloy, no contribution of the minority spin band structures to E_F was observed. All the observed Fermi surfaces were reproduced by the calculated results for the majority spin channel, showing evidence of the half-metallicity.

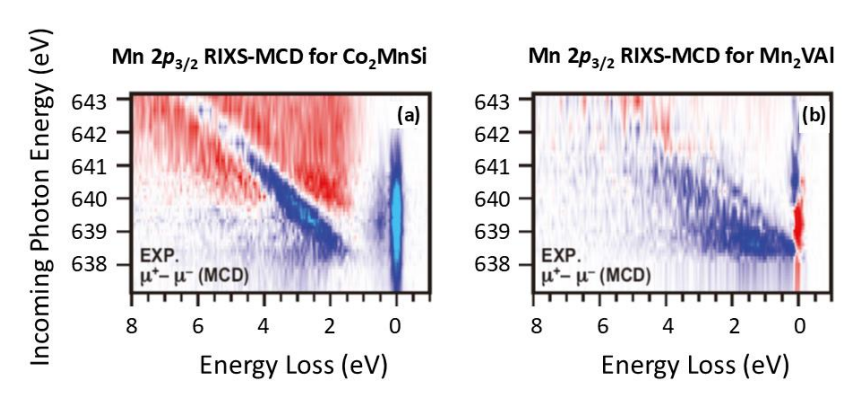


Fig. 1. Mapping of resonant inelastic X-ray scattering (RIXS)- magnetic circular dichroism (MCD) in Mn $2p_{3/2}$ edge in Co₂MnSi (a) and Mn₂VAl (b)

Acknowledgement

The above systematic studies were performed under the cooperated research with Assistant Professor Hidenori Fujiwara, Professor Akira Sekiyama, Emeritus Professor Shigemasa Suga, Dr. Fumiaki Kuroda (currently NIMS), Professor Tamio Oguchi (currently Specially Appointed Professor) in Osaka University, and Assistant Professor Jun Miyawaki (currently QST), Professor Yoshihisa Harada in the University of Tokyo, Professor Akio Kimura in Hiroshima University. The author deeply appreciates their kind cooperation.

- [1] T. Kono, et al., Phys. Rev. Lett. **125**, 216403 (2020).
- [2] K. Nagai, et al., Phys. Rev. B 97, 035143 (2018).
- [3] R.Y. Umetsu, et al., Phys. Rev. B 99, 134414 (2019).
- [4] H. Fujiwara, R.Y. Umetsu, et al., Sci. Rep. 11, 18654 (2021).

MAGNETIC INTERACTIONS IN HIGH-ENTROPY OXIDES AND THEIR CORRELATION WITH ATOMIC STRUCTURE PARAMETERS

Y. I. Mazur, M. P. Semenko, R. V. Ostapenko

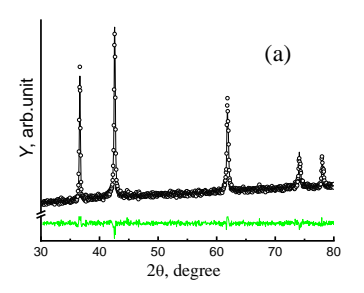
Department of Metal Physics, Faculty of Physics of Taras Shevchenko National University of Kyiv. City of Kyiv, Ukraine, 01601.

High-entropy oxides (HEOs) are a class of materials in which the highentropy effect, first observed in metallic alloys, manifests itself. In this work, we magnetic interactions in the HEO investigate the of composition Co_{0.2}Ni_{0.2}Mg_{0.2}Cu_{0.2}Zn_{0.2}O, one of the first representatives of this family. HEOs of this composition, like other similar oxide structures, exhibit properties with potential for practical applications.

The magnetic parameters were studied by the Faraday method, and the structure was investigated using X-ray diffraction (DRON-4 diffractometer, Cu_{α} radiation). The results are presented for two samples of this composition, synthesized as powders from identical precursors by solid-state synthesis, but under somewhat different conditions, with different aging times (560 and 310 days) and subsequent annealing.

It was found that the structure of both HEOs after synthesis and aging remains stable (rock-salt type). A typical diffraction pattern is shown in Fig. 1a, which can be well approximated using the Rietveld method. Fig. 1b shows the temperature dependence of the magnetic susceptibility $\chi(T)$. Its shape and the linearity of $\chi^{-1}(T)$ make it possible to identify it with the Curie-Weiss dependence. Approximation parameters allowed determination of the Curie temperature and the value of the localized magnetic moment. It was found that the Curie temperature is negative, reflecting an antiferromagnetic low-temperature type of ordering characteristic of this compound [1,2].

The diffraction pattern and the character of $\chi(T)$ dependences remained unchanged during aging and additional annealing. However, numerical values characterizing the structure (lattice parameter a) and magnetic properties (paramagnetic Curie temperature T_c, magnetic μ) differed somewhat between the samples and their aging states. Although these differences were slightly higher than experimental errors, they were reasonably consistent with similar parameters often reported in the literature (especially parameter a). Initially, such deviations and nonmonotonic behavior during aging were considered as uncontrolled factors introducing additional errors into the experimental results. However, comparison of structural and magnetic parameters obtained simultaneously (at the same aging times and after the corresponding heat treatments) revealed certain correlation features between magnetic and structural parameters.



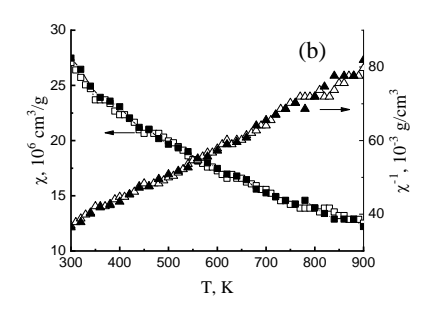


Fig. 1. Typical diffraction pattern with the difference curve between experimental and Rietveld-approximated data (a), and typical temperature dependences of $\chi(T)$ and $\chi^{-1}(T)$ (b) for the studied HEOs.

Fig. 2 shows the dependence of T_c on a obtained for different samples. As can be seen, this dependence is not random, as would be expected if the variations were due only to experimental error, but reveals a certain correlation (close to linear). Regarding the $\mu(a)$ dependence, no such correlation was observed, which may either be a consequence of the small change of μ (~2 μ B), amounting to only a few percent (1.95 μ B – min, 2.05 μ B – max), or its constancy.

The $T_{\rm c}$ – a correlation may indicate certain processes occurring in such materials. In principle, this correlation could be regarded as a consequence of metastability, which characterizes HEOs. It could also be related to possible variations in oxygen concentration, which may occur in oxides. However, most likely this correlation is due to structural features of HEOs.

Indeed, the clear diffraction pattern, similar to those of ordered crystalline structures but strongly different from typical HEC diffraction patterns, can be explained by a structure in which cations occupy equilibrium positions, while anions compensate for the difference in ionic radii by displacements from equilibrium positions. Since in HEOs the exchange interaction is mediated through oxygen (indirect), the observed $T_{\rm c}$ – a correlation can be explained as a result of changes in orbital overlap between anions and cations, not only due to distance variation but also due to the angle between neighboring cations and anions. A similar explanation is used to interpret the diversity of perovskite properties, where indirect exchange interaction is determined not only by the size of the octahedral environment of cations but also by the orientation of octahedra relative to each

other [3]. The rock-salt structure can also be represented as octahedra continuously filling the space. This, together with the different cation radii, complicates certain quantitative estimates.

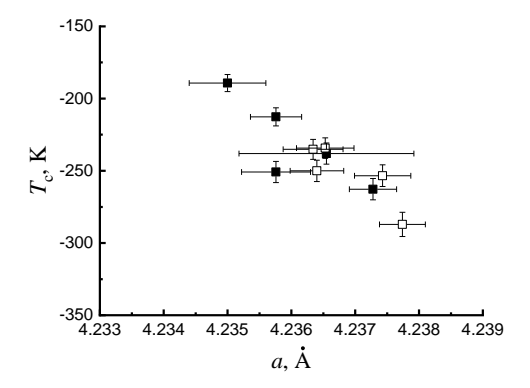


Fig. 2. Correlation between the paramagnetic Curie temperature and the lattice parameter of the HEO.

Establishing the real reasons for such correlations, as well as the physical mechanisms of changes in quantitative parameters, requires additional studies and more detailed development of the corresponding models.

- [1] M. P. Jimenez-Segura, et al., Appl. Phys. Lett., 114, 122401 (2019)
- [2] J. Zhang, et al., Chem. Mater., 31, 3705–3711 (2019)
- [3] J. S. Zhou and J. B. Goodenough, Phys. Rev., B 77, 132104 (2008)

SECTION III. THIN FILMS AND COATINGS

TAILORING STRUCTURAL AND MAGNETIC PROPERTIES OF Co/Pt FILMS VIA STACKING ENGINEERING, ANNEALING, AND ION IRRADIATION (INVITED)

R. Pedan¹, <u>I. Vladymyrskyi</u>¹

¹National Technical University of Ukraine "Igor Sikorsky Kyiv Polytechnic Institute", Kyiv, 03056, Ukraine

Developmeny of high-performance magnetic thin films for spintronic and data storage applications requires a precise control over their structural and magnetic properties [1-4]. Co-Pt alloys, known for their unique magnetic properties and thermal stability, are promising candidates for such technologies [5–8]. In this report, we explore various complementary approaches aimed to provide possibilities for tuning the structural and magnetic properties of Co/Pt based thin films through thermally-induced diffusion-driven mechanisms (fig. 1).

Firstly, we demonstrate that thermal treatment of magnetron-sputtered Pt/Co stacks at temperatures exceeding 500 °C leads to the formation of chemically disordered yet magnetically hard CoPt alloy [9]. At these temperatures, bulk diffusion is suppressed, and grain boundary diffusion becomes the dominant mechanism. This enables the realization of short-range chemical ordering, which strongly enhances the coercive field despite the absence of long-range ordering. Our results show that the microstructure and magnetic properties of the films can be tuned via controlled low-temperature processing.

Secondly, we investigate the influence of stacking sequence (Pt/Co vs. Co/Pt) and the addition of the Au intermediate layer on the thermally-induced diffusiondriven phase formation. Systematic structural and magnetic characterization reveals that both stacking inversion and Au insertion significantly affect the grain boundary network, stress distribution, and diffusion kinetics. The effective diffusion coefficients of Co and Pt species range from 10⁻¹⁶ cm²/s to 10⁻¹³ cm²/s within the 150 °C - 350 °C temperature range. Introduction of a 2 nm-thick Au layer enhances the coercivity by up to twice, attributed to the reduction of exchange coupling between magnetic grains mediated by Au segregation along grain boundaries [10].

Finally, we explore a two-stage treatment involving irradiation with different types of ion projectiles at the energy of 110 keV followed by heat treatment. Ion irradiation acts on the diffusion, slowing down the Co/Pt intermixing but simultaneously increasing the coercivity by up to 38% compared to non-irradiated annealed stacks. This effect is linked to disrupted exchange interactions and

localized paramagnetic Pt segregation, which reduces magnetic coupling between ferromagnetic Co Pt alloy grains [11].

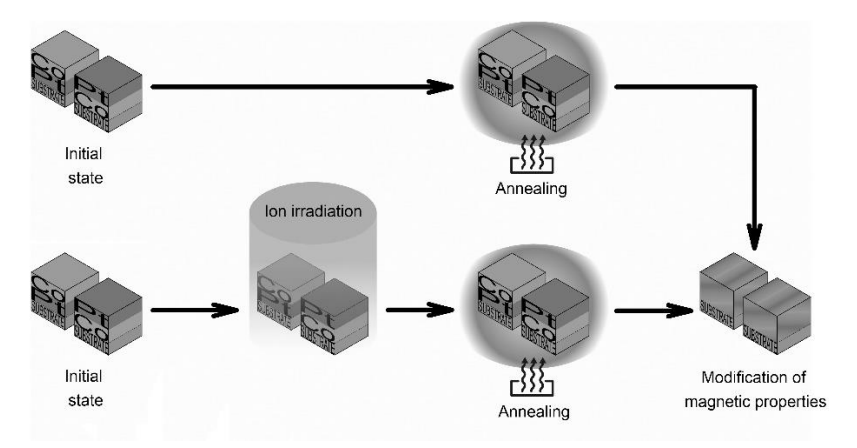


Fig. 1. Schematics of the experimental procedure aiming at the transformation of Co-Pt based stacks into a homogenous alloy film relying on thermal annealing only as well as on ion irradiation followed by thermal annealing

To summarize, our findings show that heat treatment, introduction of the additional element's layers, and ion irradiation offer distinct but complementary methods of tailoring Co/Pt thin film properties. These approaches open promising routes for engineering of the CoPt based magnetic thin film materials with tailored magnetic and structural properties for novel nanoscale devices.

- [1] Tran Thi Be Lan, et al., Journal of Alloys and Compounds. 938, 168441 (2023).
- [2] S. Qiu, et al., Surface and Coatings Technology. **436**, 128312 (2022).
- [3] A. Mahendra, et al., Journal of Alloys and Compounds. 910, 164902 (2022).
- [4] Y.N. Dong, et al., U Journal of Magnetism and Magnetic Materials. 559, 169546 (2022).
- [5] A. Hafarov, et al., Uspehi Fiziki Metallov. 22, P. 175-203 (2021).
- [6] A. Hafarov, et al., Modern Magnetic and Spintronic Materials. NATO Sci. Peace Secur. B: Phys. Biophys., P. 73-84 (2020).
- [7] T.Y. Lee, et al., J. Appl. Phys. 113, 216102 (2013).
- [8] J. Mohapatra, J. Alloys Compd. 824, 153874 (2020).
- [9] R. Pedan, et al., J. Phys. D: Appl. Phys. 55, 405004 (2022).
- [10] R. Pedan, et al., Nanotechnology **35**, 195707 (2024).
- [11] R. Pedan, et al., Mater. Chem. Phys. **327**, 129862 (2024).

STRUCTURAL AND MAGNETIC PROPERTIES OF EPITAXIAL CO₂FEGE FILMS: EFFECT OF THERMAL PROCESSING

A. Vovk¹, D. Popadiuk^{2, 3, 4}, B. Postolnyi^{1, 5}, S. Bunyaev¹, P. Strichovanec⁶, J. A. Pardo^{6, 7}, P. A. Algarabel⁶, O. Salyuk³, V. Korenivski², G. N. Kakazei¹, V. O. Golub³, and J. P. Araujo¹

¹Institute of Physics for Advanced Materials, Nanotechnology and Photonics (IFIMUP) Departamento de Física e Astronomia, Universidade do Porto, Porto 4169-007, Portugal

²Nanostructure Physics, Royal Institute of Technology, 10691 Stockholm, Sweden ³Institute of Magnetism NAS of Ukraine and MES of Ukraine, 03142 Kyiv, Ukraine ⁴Institute of Spintronics and Quantum Information Faculty of Physics Adam Mickiewicz University 61-712 Poznan, Poland

⁵Department of Nanoelectronics and Surface Modification, Sumy State University, 40007 Sumy, Ukraine

⁶Instituto de Nanociencia y Materiales de Aragón, Universidad de Zaragoza -CSIC, 50018 Zaragoza, Spain

⁷Departamento de Ciencia y Tecnología de Materiales y Fluidos, Universidad de Zaragoza, 50018 Zaragoza, Spain

The structure and magnetic properties of epitaxial Heusler alloy films Co₂FeGe deposited on MgO (100) substrates were investigated. Films with thickness of 60 nm were prepared by magnetron co-sputtering at different substrate temperatures (Ts) and those deposited at room temperature (RT) were subsequently annealed at various temperatures (T_a). The details of preparation procedure were reported in [1]. Chemical composition (in atomic percent) for all films was evaluated by EDAX as Co₄₈Fe₂₂Ge₃₀ (±1 at. % error). X-ray diffraction confirmed (001) [110] Co₂FeGe || (001) [100] MgO epitaxial growth. Analysis of XRD rocking curve widths suggested an oxide type of epitaxial growth mode. The epitaxial quality improved with increasing Ts and Ta. The films deposited at T_S=RT exhibited tetragonal distortion associated with in-plane tensile strain caused by the lattice mismatch between Co₂FeGe and MgO. This distortion was reduced by processing at elevated temperatures. The atomic ordering of the films deposited at T_S=RT was of B2 type. At higher deposition or annealing temperatures, additional superlattice reflections (111) and (311) appeared suggesting the formation of an L2₁-ordered phase or the regions enriched with Ge.

The lowest magnetization values were obtained for Ts=RT. This was attributed to atomic disorder and the reduced epitaxial quality. Increase in Ts and

 T_a lead to higher magnetization. The measured values of M_S for the films under investigation correspond to the magnetic moment $\sim 4-4.8~\mu_B$ per formula unit (μ_B is Bohr magneton), which is lower than the 6 μ_B /f.u. predicted for fully ordered stoichiometric Co_2FeGe [2]. However, these values are consistent with previously reported for Co_2FeGe films [3, 4], but are lower than those for bulk alloy [5], foils [6] and Co_2FeGe enriched films [7]. The reduction in magnetization is likely due to a slight Ge enrichment, atomic disorder and/or tetragonal deformation of the unit cell.

In terms of dynamic properties, the best performance was observed for the film deposited at $T_s = RT$ and annealed at $T_a = 573 K$. From FMR measurements a low Gilbert damping parameter $\alpha \approx 0.004$ and inhomogeneous broadening $\Delta H_0 \approx 40$ Oe were obtained for this film, indicating its suitability for magnonic applications. In contrast, annealing at $T_a = 773 K$ resulted in partial degradation of the magnetic properties, as evidenced by a pronounced increase in both α and ΔH_0 in FMR measurements. This degradation is likely caused by the formation of defects and chemical inhomogeneities, such as Ge-enriched nanoregions, suggesting that excessively high processing temperatures are inappropriate for fabricating epitaxial Co_2FeGe films for magnonics applications.

Finally, the study showed that the magnetic anisotropy axis changes direction with thermal treatment, shifting from [110] in Co_2FeGe at lower processing temperatures to [100] at higher temperatures. This change is associated with the reduction of tetragonal distortion.

These results provide valuable guidelines for optimizing thermal processing conditions to achieve desired structural and magnetic properties of Co_2FeGe films, thereby enhancing their potential for practical applications.

- [1] A. Vovk, et al., Nanomaterials 14, 1745 (2024).
- [2] B. Balke, et. al., Sci. Technol. Adv. Mater. 9, 014102 (2008).
- [3] A. Vovk, et al., Nanomaterials 11, 1229 (2021).
- [4] S. Maat, M. J. Carey, J. R. Childress Appl. Phys. Lett. 93, 143505 (2008).
- [5] K. H. J. Buschow, P. G. van Engen, R. Jongebreur Magn. Magn. Matter. 38, 1 (1983).
- [6] R. Kumar, et.al., IEEE Trans. Magn. 45, 3997 (2009).
- [7] N. V. Uvarov, et. al., J. Appl. Phys. 112, 063909 (2012).

INFLUENCE OF ATOMIC SURFACE DIFFUSION ON THE STRUCTURE AND MORPHOLOGY OF DEPOSITED TANTALUM THIN FILMS

R. A. Osypova¹, S. I. Bogatyrenko¹, A. P. Kryshtal² ¹ V.N. Karazin Kharkiv National University, Kharkiv, 61022, Ukraine ² AGH University of Science and Technology, Kraków, PL-30059, Poland

Tantalum thin films can crystallize predominantly in two structural modifications: α -Ta, which adopts a body-centered cubic (bcc) lattice, and β -Ta, a metastable tetragonal phase. These polymorphs possess markedly different physical properties, influencing their potential applications and being highly dependent on the deposition method employed. Of particular interest for spintronic applications are β-Ta films, which are characterized by strong spin-orbit coupling and a pronounced spin Hall effect, which enables efficient conversion of charge current into spin current [1,2].

Although β-Ta has been investigated extensively since the 1960s, the precise factors governing its nucleation and stabilization remain ambiguous. Most earlier studies focused on micrometer-thick tantalum layers, whereas reliable data for nanometer-scale films are scarce.

In magnetron sputtering, the kinetic energy of the incoming molecular flux is typically on the order of $E_d \approx 20~\text{eV}$ or more. Under these conditions, deposition effectively acts as an energetic bombardment of the substrate by adatoms [3], a process capable of significantly influencing the resulting phase composition.

The aim of the study was to investigate the phase composition and thermal stability of the β-Ta phase in nanometer-thick deposited films, free from the influence of molecular beam energy and substrate material. For this purpose, electron-beam evaporation was chosen as the deposition technique, since it yields a molecular flux with an average energy of $E_d \approx 0.5$ eV (~kT). At such low energies, the mobility of atoms in the condensed layer is insufficient to induce significant rearrangements in the already-formed crystalline structure of nanoscale films. A role of the substrate was performed an amorphous carbon film.

The research was carried out in two consecutive experimental stages, focusing on two specimen types: (i) films grown at room temperature followed by postdeposition annealing at various temperatures; (ii) films deposited directly onto heated substrates.

In the first stage, tantalum films with thicknesses between 5 and 50 nm were deposited by electron-beam evaporation at 1 nm/s onto amorphous carbon supported on freshly cleaved KCl crystals, under a vacuum of 1×10⁻⁷ mmHg. The

carbon layer, 20 nm thick, had been produced by arc evaporation. Immediately after tantalum deposition, a protective 20 nm carbon overlayer was applied to prevent oxidation or environmental contamination.

The resulting film was then separated from the KCl support and placed on a nickel grid fitted into a custom-built TEM heating holder [4] for *in situ* observations. The specimen was heated stepwise from 10 to 1100 °C in 100 °C increments, with electron diffraction patterns recorded at each step. The corresponding interplanar spacings were measured to determine the film's phase composition.

To investigate polymorphic transformations in thicker tantalum films, which are not transparent to 100 keV electron beam in TEM, X-ray diffraction (XRD) analysis was employed. In this case, a 160 nm Ta film was deposited at room temperature onto a polished sitall substrate (a TiO₂-based glass—ceramic) without a carbon overlayer. The specimen was heated in high vacuum in 250 °C steps up to 1000 °C, cooled, and subsequently analyzed.

In the second stage, tantalum films were deposited onto amorphous carbon substrates preheated to temperatures between 50 and 300 °C. These samples served to evaluate the effect of substrate temperature on both phase composition and film morphology, with Selected Area Electron Diffraction (SAED) used for phase identification.

The experiments showed that films deposited at room temperature on amorphous carbon at a rate of 1 nm/s predominantly crystallized in the β -phase. *In situ* TEM observations demonstrated that this phase remained stable upon heating until the onset of chemical interaction with carbon. The threshold temperature for this interaction decreased with decreasing Ta film thickness, revealing a strong size effect on phase stability. For example, the β -phase persisted up to ~500 °C in 12.5 nm films and to ~800 °C in 50 nm films. In contrast, XRD analysis of 160 nm films without a carbon layer indicated the onset of the $\beta \rightarrow \alpha$ transition at ~750 °C, a temperature lower than the Ta–C interaction temperature for 50 nm films. This confirms that thinner films exhibit greater β -phase thermal stability.

The investigation of the influence of pre-heated substrate temperature on the phase composition of the deposited film demonstrated that tantalum is highly sensitive to this parameter, more so than to direct heating of the already condensed films. This can be attributed to the fact that elevated substrate temperatures significantly enhance surface mobility of adatoms during condensation. In contrast, direct heating of an already-formed nanoscale film does not provide sufficient thermal energy to break the bonds in the metastable tetragonal lattice of the β -phase. Nanoscale films with a thickness of 12.5 nm exhibited an almost continuous

and smooth morphology in the temperature range of approximately 100-200 °C, whereas outside this range, the films displayed a distinctly granular structure which was also accompanied by an increase in grain size. The evolution of grain size in Ta films with increasing substrate temperature is shown in Fig. 1.

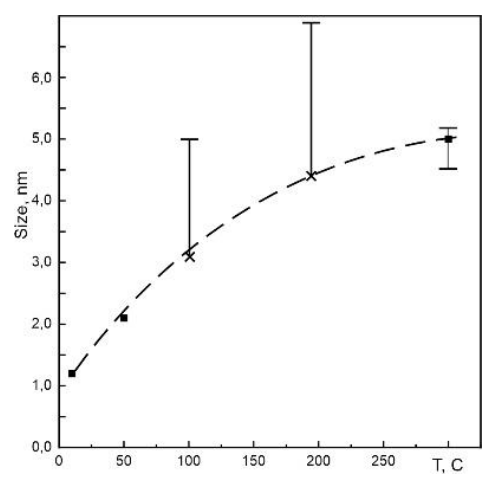


Fig.1 Dependence of grain size in Ta films on substrate temperature.

These findings are of practical relevance for thin-film fabrication, as they demonstrate that controlling adatom mobility during growth offers a viable route to obtaining metastable β-W-type structures in refractory metals.

Acknowledgments

Authors acknowledge support of the BMBF German - Ukrainian Project "Advanced Plasma Technology for Spintronic and Energy Materials" PLASMA-SPIN-ENERGY (grant No. 01DK24006) and STCU grant No. 9918 under the "2025 IEEE Magnetism in Ukraine initiative".

- [1] X. Yang, R. Yu, J. Cao et al. Spin-to-Charge Conversion in Tantalum with Structural Phase Transition. Phys. Scr. 98 (2023).
- [2] L. Liu, C.-F. Pai, Y. Li et al. Spin-Torque Switching with the Giant Spin Hall Effect of Tantalum. Science. 336 (2012) 555-558.
- [3] E. Alfonso, J. Olaya, G. Cubillos. Thin Film Growth Through Sputtering Technique and Its Applications, in: Crystallization - Science and Technology Edited by Marcello Andreeta, InTech, 2012 pp. 397-432.
- [4] S. Bogatyrenko, A. Kryshtal, A. Kruk, O. Skryl. Mixing of Immiscible Components by the Size Effect: A Case Study of Au-Ni Nanostructures. J. Phys. Chem. C. 124 (2020) 25805-25811.

SECTION IV. SUPERCONDUCTIVITY

MAGNETISM AND SUPERCONDUCTIVITY: LOCAL SPIN-TRIPLET PAIRS IN HALF-METALLIC MANGANITES - A BASE PLATFORM FOR QUANTUM MATERIALS WITH UNIQUE SUPERCONDUCTING **CHARACTERISTICS**

V. N. Krivoruchko, V. Yu. Tarenkov

Donetsk Institute for Physics and Engineering named after O. O. Galkin, NAS of Ukraine, Kyiv 03028, Ukraine

Quantum materials can be classified as artificial ones with exotic quantum characteristics. The unique properties of quantum materials are revealed to produce novel technologies due to the emergence of their unconventional behaviors. The interest in 'hybrid' quantum materials, the proximity-coupled superconducting and ferromagnetic metals, has increased due to their novel physical phenomena and potential as platforms for revolutionary new technologies.

Superconductors (SWs) with spin-triplet pairing are nowadays the subject of both fundamental and application interest. This interest is driven by the possibility of using these materials as a platform for new advanced technology superconducting spintronics [1 - 5]. Natural spin-triplet SCs are exceptional ones and require quite low temperatures to transition into this quantum state. One promising way to overcome this problem is to use quantum materials with hightemperature triplet superconductivity, such as 'hybrid' nanostructures of conventional spin-singlet SCs and metallic ferromagnets. Theory predicts a singletto-triplet symmetry pairing conversion in these systems due to the proximity effect. Among these systems, SC/half-metallic ferromagnet (hmF) structures have attracted special attention [6-13]. Experimental results evidence unconventional superconducting proximity effect in SC/hmF manganite structures. As an example, the supercurrent was observed through YBa2Cu3Ov/La0.7Ca0.3MnOz/YBa2Cu3Ov junctions even at the thickness of the manganite layer up to 200-500 nm [12,13], i.e., about 100 times larger than the theory predicts for SC/conventional ferromagnetic metal structures.

In an SC with a small superfluid density, the spatial fluctuations of the order parameter $\Delta(\mathbf{r})$, e.g., due to thermal effects, become crucial in the regions where the pairing energy value $|\Delta(\mathbf{r})|$ is small. As a result, thermal fluctuations of the order parameter's global phase coherence are the most important ones. The fluctuations of the order parameter phase $\varphi(\mathbf{r})$ in mesoscopic 'islands' prevent the long-range superconductivity. The sample's bulk superconducting transition temperature T_c is determined by the global phase coherence, whereas the local pair

condensate exists well above $T_c = T_\phi < T_\Delta$. Therefore, for systems with low conductivity and small superfluid density, the temperature of the system's global phase coherence T_ϕ can be significantly reduced and smaller than the 'islands' (local) pairing temperature T_Δ .

An important consequence/manifestation of the Cooper pairs' fluctuation above the transition temperature T_c is the appearance of the so-called pseudo-gap, i.e., a reduction of the single-electron density of states near the Fermi level [14]. In doped hmF manganites, $(La_{1-x}A_x)MnO_3$, A = Sr, Ca, etc., that are bad metals, a large pseudo-gap is detected in numerous experiments on manganites [15]. It may be suggested that at least a part of the observed pseudo-gap value is due to pairing without the global phase coherence. Note also that the transport measurements obtained on magnetic tunnel junctions with manganite $(La_{1-x}A_x)MnO_3$ suggest that the electrical current spin polarization in manganite is at least 95% [16].

In this report, we discuss a promising way for creating artificial quantum materials with high-temperature spin-triplet superconductivity. These are hybrid spin-singlet SCs—hmF manganite nanostructures. The experimental results [17–23] demonstrate unconventional superconducting proximity effect in SC/hmF manganites hybrid structures. Point-contact spectroscopy of proximity-coupled MgB₂/La_{0.67}Sr_{0.33}MnO₃ structures reveals a proximity-induced gap three times larger than the coupling energy of 'parental' SC MgB₂ [17]. These and other results indicate that in the SC/hmF manganite proximity-coupled structures, a key factor is *the local high-temperature triplet superconductivity of half-metallic manganites*.

The specific interest is the collective excitations in the multi-component superconducting state in MgB₂/hmF manganite hybrid structures. The experimental results provide evidence of an unconventional, proximity-coupled *spin singlet/triplet frequency even/odd, three-gaps* superconducting state in MgB₂/hmF manganite nanocomposites. A general description for collective dynamics in proximity-coupled superconducting condensates – the Leggett's and the Higgs excitations (i.e., collective relative phase and amplitude oscillations of the order parameters) – is formulated based on reports [21 – 23]. The detection of the dynamic phenomena in unconventional multi-component superconducting state in MgB₂/hmF manganite nanostructure – the collective excitations associated with the relative phase oscillations between singlet/triplet-spin and even/odd-frequency superconducting condensates – confirms the unconventional superconductivity in these nanostructures. Out-of-phase modes in multi-band SCs with interrelated odd-frequency *s*-wave and even-frequency *p*-wave superconducting condensates remain

an open question and motivate future intensive studies of SC/hmF proximitycoupled structures.

The systematic character and repeatability of the key experimental facts detected in the MgB2-hmF manganite proximity-coupled nanostructures identify some general physical phenomena. The experimental results show that SC/hmF manganite hybrids provide the opportunity for the creation of artificial quantum materials where a nontrivial superconducting state can be realized. The basic factor (fluctuating) high-temperature conclusions is a local half-metallic manganites. superconductivity in The latent spin-triplet superconductivity of half-metallic manganites gives an experimentally accessible platform to overcome the bottleneck of spin-triplet pairing generation in proximity structures of spin-singlet SCs with time-reversal symmetry-breaking counterparts, opening a new framework in high-temperature triplet superconductivity. Still, the properties of proximity-coupled SC-half-metallic manganite heterostructures as a platform for unique quantum systems and advanced technology applications are a subject of further research.

- [1] I. Žutić, J. Fabian, and S. Das Sarma, Rev. Mod. Phys. 76, 323 (2004).
- [2] S. Anders, et al., Physica C 470, 2079 (2010).
- [3] Y. C. Tao and J. G. Hu, J. Appl. Phys. Mod. 107, 041101 (2010).
- [4] J. Linder and J.W.A. Robinson, Nature Phys. 11, 307 (2015).
- [5] M. Eschrig, Rep. Prog. Phys. 78, 104501 (2015).
- [6] M. Eschrig and T. Löfwander, Nat. Phys. 4, 138 (2008).
- [7] M. Eschrig, J. Kopu, J. C. Cuevas, and G. Schön, Phys. Rev. Lett. 90,137003 (2003).
- [8] Y. Kalcheim, T. Kirzhner, G. Koren, and O. Millo, Phys. Rev. B 83, 064510 (2011).
- [9] C. Visani, et al., Nat. Phys. 8, 539 (2012).
- [10] Y. Kalcheim, et al., Phys. Rev. B 85, 104504 (2012).
- [11] R. S. Keizer, et al., Nature (London). 439, 825 (2006).
- [12] M. Kasai, et al., Jpn. J. Appl. Phys. 29, L2219 (1990).
- [13] M. Kasai, Y. Kanke, T. Ohno, and Y. Kozono, J. Appl. Phys. Mod. 72, 5344 (1992).
- [14] A. L. Solovjov and K. Rogacki, Low Temp. Phys. 49, 375(2023).
- [15] J. Mitra, et al., Phys. Rev. B 68, 134428 (2003).
- [16] M. Bowen, et al., Appl. Phys. Lett. 82, 233 (2003).
- [17] V. N. Krivoruchko and V. Yu. Tarenkov, Phys. Rev. B 75, 214508 (2007).
- [18] V. N. Krivoruchko and V. Yu. Tarenkov, Phys. Rev. B 78, 054522 (2008).
- [19] V. N. Krivoruchko and V. Yu. Tarenkov, Phys. Rev. B 86, 104502 (2012).
- [20] V. N. Krivoruchko, Low Temp. Phys. 47, 901 (2021).
- [21] V. N. Krivoruchko, and V. Yu. Tarenkov, Low Temp. Phys. 50, 655(2024).
- [22] V. N. Krivoruchko, V.Yu. Tarenkov and M. Belogolovskii, J. Supercond. Novel Magnet. 37, 1069 (2024).
- [23] V. N. Krivoruchko, Low Temp. Phys. 51, 557(2025).

EDGE INHOMOGENEITIES AND DIODE-LIKE CURRENT-VOLTAGE CHARACTERISTICS OF SUPERCONDUCTING MoRe FILMS

<u>D. Menesenko</u>^{1,2}, V. Tarenkov^{1,3}, V. Krivoruchko³, A. Shapovalov^{1,2}, V. Shamaev⁴

¹G.V. Kurdyumov Institute for Metal Physics, National Academy of Sciences of Ukraine, Kyiv 03142, Ukraine

²Kyiv Academic University, Kyiv 03142, Ukraine

³Donetsk Institute for Physics and Engineering named after O.O. Galkin, National Academy of Sciences of Ukraine, Kyiv 03028, Ukraine

⁴Donetsk National Technical University, Drohobych 82111, Lviv region,

Ukraine

The superconducting diode phenomenon reveals itself in different values of the critical current I_c of a superconducting bridge depending on the direction of the transport current, *i.e.*, $+I_c \neq -I_c$ [1]. Using the effect in low-temperature electronic devices, low-power circuits and logic elements can be developed. The diode effect may arise from edge inhomogeneities or defecths locally suppressing the superconducting order parameter and thus significantly reducing the edge barrier for the entry of Abrikosov vortices. Note that the effect is observed only in the presence of an external magnetic field created by the upper sputtered magnetic film, or an external field oriented normally to the bridge film [2]. The transport current, like the Meissner current induced by an external magnetic field, is located near the edges of the superconducting film. Depending on the direction of the current sweep, the transport current may add to the Meissner current, facilitating the entry of Abrikosov vortices into the film at locations where edge inhomogeneities suppress the superconducting order parameter [3,4]. In the opposite direction, the transport and Meissner currents partially cancel each other. In this case, a higher transport current is required to overcome the edge barrier for vortex entry, resulting in the asymmetry observed in the current-voltage characteristics of the studied bridges.

In this work, we investigated the role of edge inhomogeneities in the formation of diode characteristics of a superconducting bridge. If the role of edge inhomogeneities of the film is reduced to the suppression of the superconducting order parameter, then such process can be controlled, for example, using the proximity effect, by applying a normal metal film to the edge of the bridge. We have studied the nature of the destruction of the superconducting state in MoRe

film bridges in the presence of a transport current under an external magnetic field H = 150 Oe.

The samples obtained by magnetron sputtering in an argon atmosphere were MoRe film bridges with a width of h = 0.3 - 0.5 mm, a length of l = 2 mm, and a thickness of $d \approx 30-100$ nm. Their configuration allowed measurements to be carried out using a standard four-contact scheme. The critical temperature of the superconducting transition for the MoRe films under study, found from the resistive measurement curves, was $T_c = 8.7 \text{ K}$ with a transition width $\Delta T_c = 0.3 \text{ K}$. The results of the current-voltage characteristic measurements showed that the current value leading to the destruction of superconductivity in the sample and its transitions to the normal state at positive and negative sweep currents were +30 mA and -28 mA. This result indicates that the edge barrier and the defect density at the edges of the bridge are practically the same.

The superconducting proximity effect was used to modify the edge barrier for the entry of current vortices in a superconducting film bridge by coating one edge with a silver film of thickness d = 100 nm. The bridge width is h = 0.1 mm. For the MoRe-Ag film sandwich, the superconducting proximity effect was identified by the magnitude of the change in the temperature transition from the normal state to the superconducting state. The critical transition temperature of the studied sandwich decreased to T_c = 8.1 K, compared to T_c = 8.7 K for the original MoRe film, and the broadening width increased almost fourfold, to $\Delta T_c = 1.1 \text{ K}$. Measurements of the current-voltage characteristics of bridges with a suppressed edge barrier showed a pronounced diode effect. The critical currents for superconductivity breakdown were $I_c = +225 \text{ mA}$ in the positive direction and $I_c = -107 \text{ mA}$ in the negative direction. Therefore, it is possible to control the characteristics of a superconducting diode using the proximity effect of the suppressed edge barrier for the vortex entry.

This work was partially supported by the National Academy of Sciences of Ukraine through the research program No. 0125U000295 (Innovative materials for quantum sensing).

- [1] M. Nadeem, M.S. Fuhrer, and X. Wang, Nat. Rev. Phys. 5, 558 (2023)
- [2] M. V. Milošević, G. R. Berdiyorov, and F. M. Peeters,. Phys. Rev. Lett. 95 147004 (2005).
- [3] K. Nakamura, A. Daido, and Y. Yanase, Phys. Rev. B 109 094501 (2024).
- [4] D. Y. Vodolazov and F. M. Peeters.. Phys. Rev. B 72, 172508 (2005).

FERROMAGNETIC-SUPERCONDUCTING HYBRIDS FOR LOCAL CONTROL OF MAGNETIZATION CONFIGURATION AND DYNAMICS (INVITED)

J. Kharlan^{1,2}, G. Centała¹, K. Szulc¹, K. Sobucki¹, S. Memarzadeh¹, K. Guslienko³, V. O. Golub², <u>J. W. Kłos</u>¹

¹ISQI, Faculty of Physics and Astronomy, Adam Mickiewicz University, 61-712 Poznan, Poland

²Institute of Magnetism NASU and MESU, 03142 Kyiv, Ukraine Depto. Polimeros y Materiales Avanzados: Fisica, Quimica y Tecnologia, ³Universidad del Pa´ıs Vasco, UPV/EHU, 20018 San Sebastian, Spain EHU Quantum Center, University of the Basque Country, UPV/EHU, 48940 Leioa, Spain

IKERBASQUE, the Basque Foundation for Science, 48013 Bilbao, Spain

One of the key challenges in magnonics is achieving local control over both the static magnetization configuration and magnetization dynamics. A promising approach involves hybrid nanostructures combining ferromagnetic (FM) and superconducting (SC) nanoelements. It is possible to use SC nanoelements, which respond to a uniform external magnetic field by generating screening currents, to create magnetic field landscapes that strongly influence magnetization in nearby pristine FM layer.

We investigated spin-wave confinement induced in a uniform perpendicular magnetic anisotropy (PMA) layer by the stray field of an SC strip [1] placed above it. The SC strip produces an effective field well within the FM layer, capable of confining spin waves with frequencies lower than the ferromagnetic resonance frequency of the pristine FM layer [Fig. 1(c)]. The depth of this well and the number of bound states depend on the strength of the applied magnetic field.

Furthermore, we examined the possibility of creating a reconfigurable magnonic crystal in a pristine FM layer by applying a periodic sequence of SC strips [2]. The depth of the internal field modulation, and consequently the width of the magnonic band gaps, can be tuned by the applied uniform field.

Finally, we explored the use of the stray field of an SC nanoelement (ring) to stabilize a skyrmion in a uniform PMA layer in the absence of Dzyaloshinskii—Moriya interaction (DMI) [3]. We determined the range of SC ring sizes and FM material parameters for which such stabilization is possible.

Our studies demonstrate the feasibility of controlling magnetization textures and spin-wave dynamics locally by means of a uniform external magnetic field in hybrid FM–SC systems.

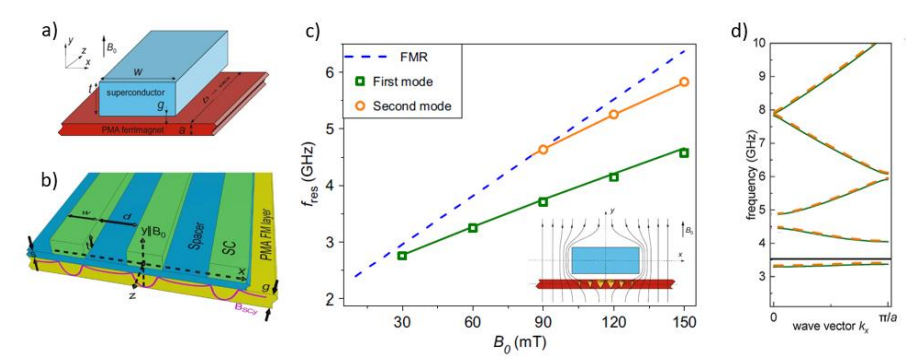


Fig. 1. A single superconducting strip (a) and a periodic sequence of superconducting strips (b) create a local well in the internal magnetic field [1] or a periodic field profile [2], which can confine (c) or scatter (d) spin waves.

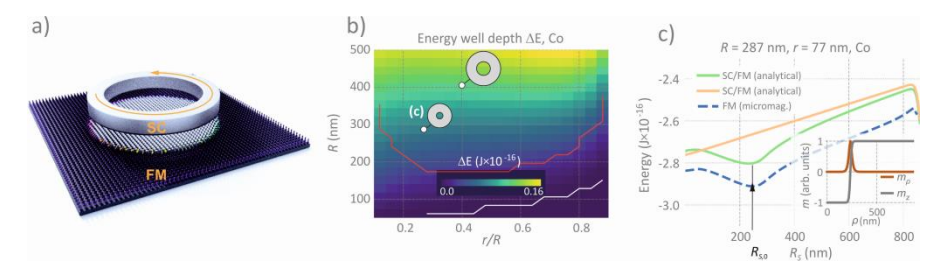


Fig. 2. A superconducting ring placed above an FM layer with PMA (a) can stabilize a skyrmion in the absence of DMI [3]. For appropriately chosen ring sizes (b), a skyrmion of a particular radius corresponds to an energy minimum of the magnetization texture.

The work was supported by the National Science Center, Poland under Grants No. UMO-2019/35/D/ST3/03729, No. UMO-2021/43/I/ST3/00550, No. UMO-2021/41/N/ST3/04478, No. UMO-2020/39/O/ST5/02110.

- [1] J. Kharlan, K. Sobucki, K. Szulc, S. Memarzadeh, J. W. Kłos., Phys. Rev. Appl. 21, 064007 (2024).
- [2] J. Kharlan, K. Szulc, J.W. Kłos, G. Centała, Sci. Rep. 14, 25594 (2024).
- [3] J. Kharlan et al., arXiv:2505.07133 [cond-mat.mes-hall] (2025).

SECTION V. SPINTRONICS, MAGNONICS AND MICROWAVE MAGNETISM

QUANTUM TOPOLOGICAL PHASE AND ELECTRIC FIELD CONTROL OF SPIN-WAVES' DYNAMICS IN MAGNETIC INSULATORS (INVITED)

V. N. Krivoruchko

Donetsk Institute for Physics and Engineering named after O. O. Galkin, NAS of Ukraine, Kyiv 03028, Ukraine

Condensed matter physics is undergoing a revolution by introducing concepts borrowed from topology to characterize the state and properties of a system. With the introduction of topology, the description of complex systems moves on to the characterization of their global quantities, which are measured non-locally and endow the system with global resilience to disturbances [1]. In magnetism, the mainstream of topological concepts can be conditionally divided into two alternative scenarios: (i) a non-trivial topology of a static magnetic order in real space, e.g., a magnetic structure such as skyrmions, magnetic topological structure induced by curved geometries, etc., [2] and (ii) topological quantum effects in magnetization dynamics [3]. One of the distinctive features of topological magnetic states and topological dynamics is stability against external influences. Another unique feature is that purely quantum topological effects have no classical interpretation. With the introduction of topology, the physical picture changed from describing complex systems in terms of local (Landau) order parameters to characterizations of global non-local quantities. Among the various topological effects, an extra quantum geometrical phase acquired by chargeless bosonic quasiparticles with a magnetic dipole m moving in an external electric (E) field, predicted by Aharonov and Casher [4], is currently a leading area of research in magnetism [5].

The bosonic nature of spin waves (SWs) or their quanta, magnons, which can actively participate in quantum information processing, stimulates active discussion of the AC phase effects on long-range pure spin transport [6 - 12]. In magnetic materials, the impact of the static external electric field on SW dynamics, the AC effect, can be accounted in a linear approximation by adding a Dzyaloshinskii-Moriya-like interaction between neighboring spins, the magnitude of which is proportional to the applied **E** field, the exchange coupling and the spinorbit coupling between magnetic ions [6]. This topological phenomenon has recently been experimentally detected for SWs propagating in the classical magnetic insulator Y₃Fe₅O₁₂ [7,8]. This finding brought to life the idea of tuning the properties of magnons, an essential ingredient for magnonic devices, by the E field. From the fundamental point of view, the discussed quantum

108 | Modern problems of solid state physics & magnetism

phenomena open a new avenue for quantifying topological effects in magnetization dynamics. From the technology's point of view, the **E** field control of SW dynamics can be a key factor for designing quantum magnonic nanodevices, giving efficient control and manipulation in real-time of the SWs' phase, amplitude, and propagation direction.

We discuss the fundamental origin of the AC effect in ferromagnetic and antiferromagnetic *insulators*, emphasizing the difference between this effect and an external effect on the static and dynamic properties of a magnetic system from the point of view of the local (Landau) state of the order parameter and the global topological state, and consider the static external **E** field effects on such fundamental dynamic characteristics of SW as phase, amplitude, and propagation direction. Modifying and tuning these SW characteristics is one of the most important requirements for engineering magnonic devices. A few examples, such as electric field tunable Snell's law for SWs in ferromagnetic nanostrips, controlled by **E**-field refraction and focusing of SWs, have been discussed [9 - 11].

The unique characteristic of magnetization dynamics - fast speed, up to terahertz, and distinct right-handed and left-handed magnons' chirality - gives grounds to consider *antiferromagnets* (AFMs) as a prospective material platform for the realization of a variety of high-density and fast-speed magnonic devices. For example, right-handed (RH) and left-handed (LH) polarized SWs can be used as the basic elements for encoding information, such as the spin-up and spin-down electrons in modern computers. Possessing these unique features, AFMs have great potential for applications in information technology. The main challenges for implementing AFMs in magnonic devices are uncovering the mechanisms for the separate manipulation of RH and LH SWs dynamics and their detection. Methods for controlling magnetic dynamics in AFM are currently being actively discussed.

Damping makes the magnon's dispersion anomalous, and superluminal-like magnon velocity $\sim\!650$ km/sec at nanoscale distances has been recently experimentally detected in the antiferromagnetic NiO layer [12]. The superluminal-like magnon velocity owing to the damping is of considerable interest from the viewpoint of fundamental science and importance from the application point of view because it allows one to operate nanoscale magnonic devices at a far higher speed than what has been thought to be the fundamental limit of magnonic devices.

The topological AC effect on magnetization dynamics in AFM insulators is discussed. We study the topological AC effect on magnetization dynamics in two-sublattice easy-axis AFMs [13,14]. Analytical calculations demonstrate that the electric field can successfully manage the right- and left-handed SWs' spectrum, amplitude, and propagation length without adding the magnetic field. The

attenuation of given chirality magnons can also be enhanced or weakened separately, depending on the direction and magnitude of the E field. Motivated by the experimental results [12], and to explore the potential anomalous behavior of magnetization dynamics, an external E field control of the superluminal-like magnon velocity region in AFMs has been considered [13,14]. The external E field can dramatically change the kinetic properties of magnons, such as the wave vector at which the superluminal propagation of a given chirality magnon occurs. This chirality-selective topological effect on the superluminal propagation of SWs behavior paves the way to develop advanced magnonic devices.

The topological Aharonov–Casher effect on magnetization dynamics provides a perspective platform for developing ultrafast topological magnonics. The possibility of the electric field controlling SW propagation and handedness will stimulate a new direction for spin-based device development and a new way of controlling magnon transport steering in various THz magnonic devices. This solves one of the important problems of magnonics, making it a quantum technology platform and an alternative computing scheme for quantum technological applications [15,16]. We hope the obtained results will contribute to the fundamental understanding of topological effects in chirality-dependent SWs' dynamics in collinear AFM insulators in different energy ranges, which is a key factor for practical applications of antiferromagnets in magnonics.

- [1] Topological Matter Topological Insulators, Skyrmions and Majoranas. 48th IFF Spring School, (ed. S. Blügel, et al., 2017).
- [2] M. V. Berry. Proc. R. Soc. London, Ser. A. 392, 45 (1984).
- [3] X. S. Wang, H.W. Zhang, and X. R. Wang, Phys. Rev. Appl. 9, 024029 (2018).
- [4] Y. Aharonov and A. Casher. Phys. Rev. Lett. 53, 319 (1984).
- [5] E. Cohen, et al., Nature Rev. 1, 437 (2019).
- [6] T. Liu and G. Vignale, Phys. Rev. Lett. 106, 247203(2011).
- [7] X. Zhang, T. Liu, M. E. Flatté, and H. X. Tang, Phys. Rev. Lett. 113, 037202 (2014).
- [8] R. O. Serha, V. I. Vasyuchka, A. A. Serga, and B. Hillebrands, Phys. Rev. B 82, -L220404 (2023).
- [9] V. N. Krivoruchko, A.S. Savchenko, and V.V. Kruglyak, Phys. Rev. B 98, 024427 (2018).
- [10] V. N. Krivoruchko and A.S. Savchenko, J. Magn. Magn. Mater. 474, 9 (2019).
- [11] V. N. Krivoruchko and A.S. Savchenko, Phys. Rev. B 109, 184437 (2024).
- [12] K. Lee, et al., Nat. Nanotechnol. 16, 1337 (2021).
- [13] O. O. Boliasova and V. N. Krivoruchko, Phys. Rev. B 111, 174440 (2025).
- [14] O. O. Boliasova and V. N. Krivoruchko, Metalloph. Advan. Techn. 47, 581 (2025).
- [15] P. K. Pal, A. K. Mondal, and A. Barman, J. Phys.: Condens. Matter. 36, 441502 (2024).
- [16] B. Flebus, et al., J. Phys.: Condens. Matter. 36, 363501 (2024)

PROBALISTIC COMPUTING WITH JOSEPHSON-LIKE ANTIFERROMAGNETIC SPIN HALL OSCILLATOR

D.V Slobodianiuk¹, R. V. Verba¹.

¹V. G. Baryakhtar Institute of Magnetism of the NAS of Ukraine, Kyiv 03142, Ukraine

Probabilistic computing is an emerging field that utilizes the principles of probability theory and stochastic processes to perform computations. Unlike traditional digital computers that rely on deterministic logic gates (which produce a single, predictable output for a given input), probabilistic computers use components (p-bits) that operate on a probabilistic basis, meaning their outputs are not fixed but are instead drawn from a probability distribution [1]. This approach offers a novel way to tackle problems that are inherently uncertain or difficult for deterministic systems, particularly in areas like machine learning, optimization, and complex systems modelling. The core idea is to encode information not as a single bit (0 or 1) but as a probability of being in a certain state, allowing the system to explore a vast range of possible solutions simultaneously.

On the other hand Antiferromagnetic (AFM) spintronics is an emerging field of science and technology focused on the study and utilization of static and dynamic magnetic states in antiferromagnets. One of the novel elements of those is so-called Josepson-like antiferromagnetic spin Hall oscillators (AFM SHO) [2], that effectively allow one to convert applied DC current into terahertz signal, arising from rotation of AFM material magnetic moments. This opens up a whole new field of possible applications of such a system. Moreover AFM SHO demonstrate all the key features of conventional oscillators, namely demonstrating conventional [3] or fractional [4] synchronization.

If was shown [5], that applying AC current to such a system one can drive AFM SHO into stochastic generation regime, when output signal becomes noiselike, however keeping in terahertz timescale nature. Fig.1 shows typical output signal of AFM SHO, when it is driven by a AC current. As we can see, despite stochastic nature of the signal, the timescale of it is indeed very promising, thus providing the possibility of creation so-called p-bits, utilizing such systems [5].

Next step is creation basic logic elements, using AFM SHO based p-bits. To make an AND elements one needs three AFM SHOs, that minimize the cost function of the form: $E(x_1,x_2,y_1)=3y_1+x_1x_2-2x_1y_1-2x_2y_1$. Where x_1, x_2 – are p-bits inputs and y_1 is a p-bit output. Moreover, after such a system has been created and tuned, one can use in reverse mode, fixing the output bit and reading the input bits,

that will be consistent with the output, effectively and easily solving the reverse problem, that is one of the strongest benefits when using probabilistic systems. In this work we theoretically demonstrate, how such AND gate could be architectured using AFM SHO, and what are the typical response times of it.

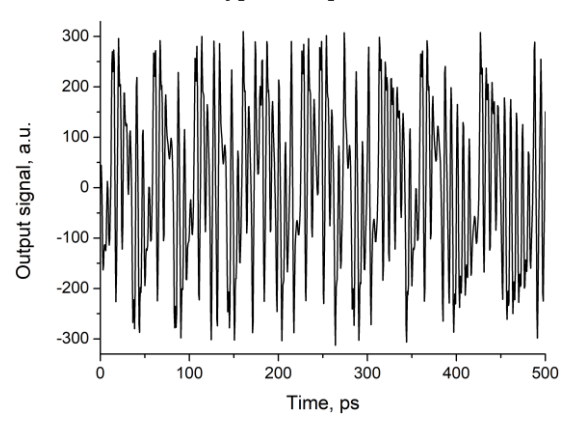


Fig. 1. AFM SHO output signal in the stochastic regime, when driven by an AC current

It should be noted, that the drawback of the proposed system is that it needs additional AFM SHO generating driving AC terahertz signal for each of the p-bits.

In conclusion we have demonstrated a possibility of utilizing AFM SHO for creation of probabilistic computing systems. Such system have numerous advantages comparing to classical ones, with the key benefit being terahertz frequency operation and thus picoseconds frequency responses, that an order of magnitude better then magnetic system utilizing magnetic tunnel junctions [6,7].

- [1] K. Camsari, R. Faria, B. Sutton, and S. Datta, Phys. Rev. X 7, 031014 (2017).
- [2] R. Khymyn, I. Lisenkov, V. Tiberkevich, B. Ivanov, and A. Slavin, Sci. Rep. 7, 43705 (2017).
- [3] D. Slobodianiuk and O. Prokopenko, J. Nano- Electron. Phys. 12, 05013 (2020).
- [4] D. Slobodianiuk and O. Prokopenko, IEEE 11th International Conference Nanomaterials: Applications and Properties pp. 1-4 (2021).
- [5] D.V. Slobodianiuk, and O.V. Prokopenko, Journal of Applied Physics 134(15), 153903 (2023).
- [6] M. Bapna and S. Majetich, Appl. Phys. Lett. 111, 243107(2017).
- [7] M. Daniels, A. Madhavan, P. Talatchian, A. Mizrahi, and M. Stiles, Phys. Rev. Applied 13, 034016 (2020).

ON MAGNETO-CONTROLLED ELECTRIC CAPACITANCE IN MAGNETIC JUNCTIONS

A. M. Korostil, M. M. Krupa

V. G. Baryakhtar Institute of Magnetism NAS of Ukraine, Kyiv, 03142, Ukraine

Magnetic tunnel junctions (MTJs) are cornerstone elements of spintronic devices, widely used in magnetic memory and sensor technologies. While most studies have traditionally focused on their magnetoresistive properties, increasing attention is now paid to the magnetocapacitive (MC) effect, where the capacitance of the junction changes with the relative magnetization configuration of electrodes. Understanding and controlling this effect is crucial for the development of multifunctional devices that exploit both the charge and spin degrees of freedom.

In this work, we address the problem of the description and qualitative understanding of the MC effect in MTJs with ferromagnetic electrodes and ultrathin insulating barrier. The objective is to investigate how the capacitance depends on the magnetic configuration, and what physical mechanisms are responsible for this behavior. The general microscopic model is used to describe the overall capacitance, accounting for contributions from the geometric capacitance, interface states, and spin-dependent quantum capacitance. To capture the spin-dependent effects at the microscopic level, a quantum-tunneling model based on the spin-dependent density of states (DOS) for tunneling through a barrier is applied. We considered several mechanisms contributing to the MC effect.

As a result, the spin-dependent screening length in ferromagnetic metals leads to asymmetric charge accumulation at the interface. Variation of the spin-polarized density of states at the Fermi level in different magnetization configurations affects the interfacial quantum capacitance. The important role belongs to magneto-induced interface states and their occupation depending on spin alignment. The spin-dependent tunneling rates influence charge relaxation and dynamic capacitance. The magnetocapacitance is not only sensitive to the magnetic configuration but also to the thickness and material composition of the barrier, and to the electronic properties of the electrodes.

The magnetocapacitive (TMC) effect in magnetic tunnel junctions (MTJs) originates from spin-dependent electrostatic screening at the interface between a ferromagnetic electrode and a tunneling barrier, typically MgO. At the microscopic level, this phenomenon arises due to differences in the spin-resolved density of states (DOS) near the Fermi level in the ferromagnetic contacts. When an electric field is applied across the junction, electrons in the electrodes rearrange to screen

the field, leading to the formation of an interfacial charge layer. This screening is inherently spin-dependent: for example, in the parallel (P) magnetic configuration, spin-up and spin-down electrons contribute differently to the screening process than in the antiparallel (AP) configuration. As a result, the effective capacitance of the junction becomes sensitive to its magnetic state.

The total capacitance of an MTJ can be described as a series combination of the geometric (or dielectric) capacitance of the barrier and the quantum capacitance associated with the electronic response in the electrodes. The latter, in particular, exhibits strong spin dependence in ferromagnetic materials and gives rise to the observed TMC effect. Microscopically, the spin-dependent quantum capacitance is susceptibility: $C^{\sigma} = \int D^{\sigma}(E) \partial_{E} f(E - e \phi^{\sigma}) dE$, calculated via the charge where $D^{\sigma}(E)$ is the spin-resolved DOS, f is the Fermi-Dirac distribution, and \emptyset^{σ} is the local electrostatic potential for spin, σ .

The frequency dependence of the TMC effect becomes significant at gigahertz (GHz) regimes. At low frequencies ($\omega \rightarrow 0$), the spin-dependent screening can fully follow the applied field and the TMC effect manifests as a static difference in capacitance between P and AP states. However, at higher frequencies, the spinpolarized electronic response cannot instantaneously adjust to the oscillating field, leading to phase delays and a reduction in screening efficiency. This results in a complex, frequency-dependent admittance: $Y(\omega) = G(\omega) + iG_{\rm eff}(\omega)$, where both the conductance $G(\omega)$ and the effective capacitance $C_{\rm eff}(\omega)$ depend on the magnetic configuration. Notably, $C_{\text{eff}}^{P}(\omega) \neq C_{\text{eff}}^{AP}(\omega)$, even in the presence identical barrier geometry, due to dynamic spin screening differences.

This frequency-dependent behavior implies that the TMC effect is not only a static property of the junction but also encodes information about the dynamic response of the spin system. It also highlights the importance of considering both reactive and dissipative components of the tunneling current in high-frequency spintronic applications. In particular, at GHz frequencies relevant for nextgeneration MRAM and spin-based RF devices, the TMC effect can introduce parasitic components into the total impedance, impacting the readout fidelity of TMR-based systems unless properly compensated or exploited.

These findings open up new avenues for tailoring the capacitive response in spintronic devices and suggest possible application in spin-based capacitive sensing, tunable filters, and hybrid logic elements.

STOCHASTIC DOMAIN WALL AND SKYRMION MOTION ON THE RANDOMLY INHOMOGENEOUS RACETRACK MEMORY

O.L. Andrieieva¹, A.V. Hlushchenko¹, O.V. Chechkin^{1,2}

¹Kharkiv Institute of Physics and Technology, 61108, Kharkiv, Ukraine ²German – Ukrainian Core of Excellence "Plasma-Spin-Energy", Max Planck Institute of Microstructure Physics, 06120, Halle, Germany

Racetrack memory is a new generation of non-volatile memories in which domain walls, or skyrmions, are efficiently moved by electric current [1-2]. One of the main challenges in creating such magnetic memory is the accurate detection of magnetic textures on racetracks at the nanoscale [3]. In this work, we aim to study quenched disorders [4,5], which can lead to both thresholds of magnetic texture motion and additional random displacements during the stochastic motion of magnetic textures, preventing their accurate detection. Using fractal analysis of racetrack surfaces, we also intend to study the role of inhomogeneities in the magnetic material that inevitably arise during the manufacturing of racetracks. We investigate how the roughness of the surface and edges of racetracks affects the thresholds as well as the stochastic motion of magnetic textures. The presence of defects in the structure of the sample also can lead to a reduction in current-driven skyrmion or DW velocities, pinning, and current-induced merging and annihilation of magnetic textures. Thus, a deeper understanding of stochastic processes on racetracks is critical for the design and stability of next-generation high-speed, high-density spintronic devices.

In the general case, it is necessary to take into account the random inhomogeneity parameter of anisotropy and the Dzyaloshinsky–Moriya interaction parameter [5], here we limit ourselves to specifying only the inhomogeneous anisotropy parameter $K_u(x, y)$ as:

$$K_{u}(x,y) = K_{u}^{0} + \frac{a_{m}}{2}\overline{W(x,y)}, \qquad \left\langle \overline{W(x,y)} \right\rangle = 0, \ \left| \overline{W(x,y)} \right| \leq 1.$$

where K_u^0 is introduced as an average anisotropy. In contrast to the traditional approach [6], where the heterogeneity is specified by a random functions N(x,y) with the normal distribution, here we consider the Weierstrass function, which allows us to vary not only the amplitude of the heterogeneity a_m but also its scale s (see Fig. 1). Different methods of manufacturing magnetic films for racetrack memory lead to different scales of heterogeneity, which affects the thresholds of movement of magnetic textures [7].

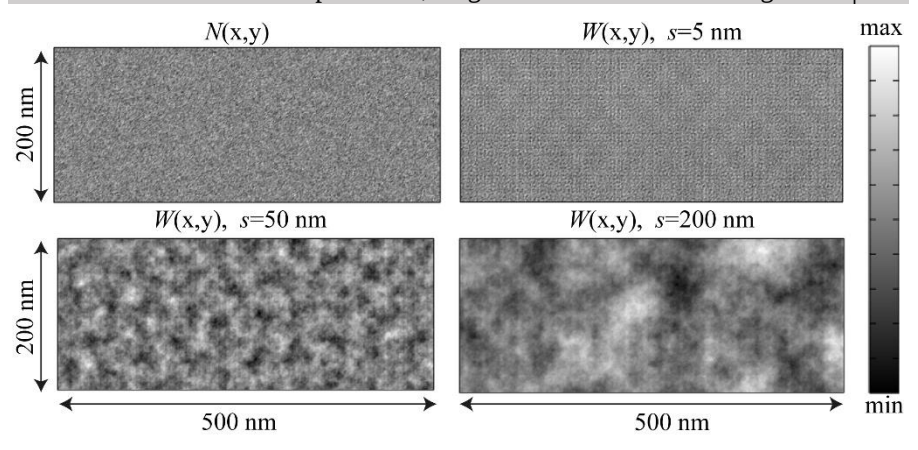


Fig. 1. Representation (x-y plane section) of the extended randomized Weierstrass function W(x,y) depending on the scale factor s and random functions N(x,y) with the normal distribution.

New materials and thin-film structures created at the atomic level increase speed and reduce the threshold current required to manipulate data bits. At the nanoscale, the influence of random inhomogeneity of racetrack sample increases, which is due to the presence of inhomogeneities comparable to the size of magnetic textures. The results of our work on studying the mechanisms of stochastic dynamics of domain walls and skyrmions and the formation of movement thresholds will form the basis for optimizing the parameters of a new generation of magnetic memory.

- [1] S. S. P. Parkin et al. Science 320, 190 (2008). DOI: 10.1126/science.1145799
- [2] S. Woo et al., Nat. Mater. 15, 501–506 (2016). DOI: 10.1038/nmat4593
- [3] J.-C. Jeon et al., Science 386, 315 (2024). DOI: 10.1126/science.adh3419
- [4] C. Reichhardt et al., Rev. Mod. Phys. 94, 035005 (2022). DOI: 10.1103/RevModPhys.94.035005
- [5] M. Ishibashi et al., Sci. Adv. 10, eadq0898 (2024). DOI: 10.1126/sciadv.adq0898
- [6] T. Herranen, L. Laurson, Phys. Rev. Lett. 122, 117205 (2019). DOI: 10.1103/PhysRevLett.122.117205
- [7] A. Soumyanarayanan et al, Nature Mater., 16, 898–904 (2017). DOI: 10.1038/nmat4934

Authors acknowledge support of the BMBF German - Ukrainian Project "Advanced Plasma Technology for Spintronic and Energy Materials" PLASMA-SPIN-ENERGY (grant No. 01DK24006) and STCU grant No. 9918 under the "2025 IEEE Magnetism in Ukraine initiative".

THERMAL AND SPIN CURRENT NOISE IN THE RACETRACK MEMORY WITH DOMAIN WALLS AND SKYRMIONS

A.V. Hlushchenko¹, M.I. Bratchenko¹, O.V. Chechkin^{1,2}

¹Kharkiv Institute of Physics and Technology, 61108, Kharkiv, Ukraine ²German – Ukrainian Core of Excellence "Plasma-Spin-Energy", Max Planck Institute of Microstructure Physics, 06120, Halle, Germany

Current-driven motion of domain walls (DW) and skyrmions is of key importance for the operation of non-volatile memory devices [1-2]. New materials and thin-film structures created at the atomic level increase speed and reduce the threshold current required to manipulate data bits. DW or skyrmion-based devices are formed from magnetic nanoribbons that have three main components: (i) write ports, which includes the creation and motion of magnetic textures, (ii) a bit storage body (cache), and (iii) read ports. One of the major technological challenges in racetrack memory is to achieve the highest possible packing density of nanoscale magnetic textures [3] and, at the same time, be able to read the domain walls (or skyrmions) when they are densely packed together. Understanding of stochastic processes influencing the stable functioning of new magnetic memory devices is of pivotal importance. We aim to study equilibrium and nonequilibrium stochastic processes [4] that create random displacements in current induced stochastic motion of magnetic textures and prevent their precise detection. We consider both spin transfer torque and spin-orbit torque current injections, which are the basis for different generations of magnetic memory [5]. We use theoretical analysis and micromagnetic modeling to determine the influences of current and thermal noises on the motion of magnetic textures in typical racetrack samples at different experimental conditions. The results of our work on studying the mechanisms of stochastic dynamics of domain walls and skyrmions will be used for optimizing the magnetic memory parameters.

Using Thiele's approach [6], we transform the nonlinear LLG equations into a system of two independent stochastic equations for the center of mass of the magnetic texture. The equivalence of these approaches is confirmed by independent calculations using the Thiele approach as well as micromagnetic simulation. The mean squared displacements obtained from the analysis of micromagnetic modeling of a series of multiple stochastic motion tests of the magnetic textures show convergence to the results of analytical calculations from the Thiele equations.

We calculated the mean squared displacements of the DW as functions of time *t* for the case with thermal noise, spin current noise and their simultaneous consideration, respectively. We also obtained the standard deviation (StDev) of the first passage time (FPT) as a function of distance d of the detector location (Hall bars are supposed to be used as detectors). The parameters of the analytical and numerical calculations were selected in accordance with the typical racetrack sample [3]. Here we consider one-dimensional domain walls, and the random displacements caused by the presence of various types of noise are observed only along the *x*-axis. The stochasticity of the DW motion, caused by both thermal and spin current noise, may be important in determining their position on the racetrack.

A separate investigation was devoted to the study of stochastic motion of twodimensional magnetic textures such as skyrmions. In accordance with the developed approaches, the mean squared displacements of the skyrmions were calculated as functions of time t for the various types of noise. StDev of FPT as a function of distance d is calculated in the presence of typical drift velocity, which is important for the correct detection of skyrmions. In addition, the mean FPT of the racetrack boundary as well as StDev of FPT, which is critical for the stable operation of the racetrack memory, were calculated. The skyrmion drift velocity has only x-component, this is achieved by altering the spin polarization angle leading to the suppression of the skyrmion Hall effect.

We propose an analytical approach to describe the contributions of both thermal and spin current noise. Random displacements of the trajectories of magnetic textures are critical for detecting their positions on the racetrack memory. We demonstrate an overwhelming advantage of current density noise over thermal noise for a typical racetrack sample that operates on the basis of both domain walls and skyrmions. The results obtained with the analytical approach are in perfect agreement with the independent micromagnetic simulations.

Authors acknowledge support of the BMBF German - Ukrainian Project "Advanced Plasma Technology for Spintronic and Energy Materials" PLASMA-SPIN-ENERGY (grant No. 01DK24006) and STCU grant No. 9918 under the "2025 IEEE Magnetism in Ukraine initiative".

- [1] S. S. P. Parkin et al. Science 320, 190 (2008). and C. E. Patton
- [2] S. Woo et al., Nat. Mater. 15, 501-506 (2016).
- [3] J.-C. Jeon et al., Science 386, 315 (2024).
- [4] J. Foros et al., Phys. Rev. Lett., 95, 016601 (2005).
- [5] S.S.P. Parkin, S.H. Yang, Nat. Nanotechnol., 10(3), 195-198 (2015)
- [6] A. A. Thiele, Phys. Rev. Lett., 30, 230 (1973).

EXCITATION OF HIGH FREQUENCY SPIN WAVES IN LOW EXTERNAL FIELD IN HYBRID FERROMAGNETIC-METALLIC SYSTEMS

J. Kharlan^{1,2}, J. Holobradek³, M. Urbanek³, J. Klos¹, V.O. Golub²

¹Institute of Spintronics and Quantum Information, Faculty of Physics and Astronomy, Adam Mickiewicz University, 61-614 Poznań, Poland

²V.G. Baryakhtar Institute of Magnetism of the NAS of Ukraine, Kyiv 03142, Ukraine

³CEITEC BUT, Brno University of Technology, 612 00 Brno, Czech Republic

The last two decades are associated with significant progress in the field of magnonics. Further development in this area faces some fundamental challenges: the increase of operating spin waves frequencies up to tens or hundreds of gigahertz and shortening their wavelength. One of the potential ways to overcome this problem is to use hybrid systems combining ferromagnetic and metallic nanoelements [1].

Only one homogeneous ferromagnetic resonance (FMR) mode can be usually excited by a uniform alternating magnetic field in a single tangentially magnetized ferromagnetic film. It will be demonstrated here that a periodic array of metallic strips placed over the ferromagnetic film enables the excitation of in-plane standing spin waves. Our cavity FMR measurements showed the emergence of multiple standing spin wave modes when a static magnetic field is applied along the metallic strips, while the homogeneous microwave field is perpendicular to the film plane (Fig.1a).

For instance, using 20 nm thick film covered by array of gold stripes (the period of the array is 5 μ m and stripe sizes: 200 nm width, 90 nm thickness and 100 μ m length) up to 15 quantized spin wave modes became visible and their intensities slowly decrease with the mode number. Their frequencies are determined by the period of the array. It is important that the intensity of the first mode can exceed the intensity of homogeneous FMR mode.

The effect is highly sensitive to the orientation of the microwave field. When the field is applied in-plane and perpendicular to the strips, the observed intensities of the higher-order modes are much smaller than the homogeneous mode. Furthermore, when the field is along the strips, only the homogeneous mode is observed (Fig.1b).

The appearance of higher-order spin wave modes can be attributed to the metallic strips acting as dynamic antennas. The homogeneous alternating magnetic

field induces currents in the metallic strips, which, in turn, generate inhomogeneous magnetic fields in the ferromagnetic film. These inhomogeneous fields excite spin waves with discrete wave vectors determined by the system's periodicity.

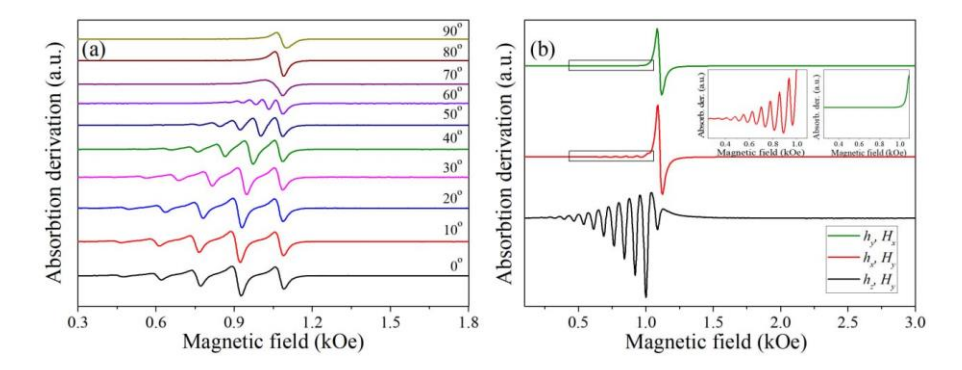


Fig.1. (a) Absorption derivative of the FMR spectrum for different angles of the external static in-plane magnetic field in the case of an out-of-plane alternating magnetic field. (b) FMR spectra for different orientations of the static field \boldsymbol{H} and the alternating field h: H in-plane and perpendicular to the stripes, h along the stripes (top line); H along the stripes, h in-plane and perpendicular to the stripes (middle line); *H* along the stripes, *h* out-of-plane (bottom line).

However, a lot of phenomenon remains puzzling: What is the reason of the inplane standing spin wave excitation by nearly homogeneous microwave fields? Usually they cannot be detected by magnetic resonance technique. What is the mechanism of such strong effect of conducting stripes affect on ferromagnetic layer if their thickness (20-90 nm) is much less than skin-layer thickness? Why the spin wave resonance intensity can be higher than homogeneous precession?

These intriguing questions invite further investigation.

The authors acknowledge the support from the grant of the National Science Center – Poland, No. 2021/43/I/ST3/00550.

[1] V. Flovik et al., J. Appl. Phys. **119**, 163903 (2016).

SURFACE MAGNON-PLASMON HYBRID MODES IN METAL-AFM-METAL WAVEGUIDES

O. Yu. Gorobets¹, V. V. Kulish¹, S. I. Yeromin¹

¹National Technical University of Ukraine "Igor Sikorsky Kyiv Polytechnic Institute", Kyiv 03056, Ukraine

The rapid development of high-frequency spintronic and plasmonic technologies has driven increasing interest in hybrid electromagnetic excitations, particularly magnon-plasmon polaritons (MPPs), which emerge from the coupling of electromagnetic waves with both spin and charge collective modes [1]. These hybrid modes are promising candidates for tunable, low-loss waveguiding in the terahertz (THz) regime—an essential spectral range for future wireless communication and sensing devices [2]. Among various material platforms, antiferromagnetic (AFM) systems are of particular interest due to their intrinsic THz-range resonances and robustness against external perturbations [3].

In this report, we present a theoretical investigation of surface MPPs in a planar heterostructure comprising a thin uniaxial antiferromagnetic film embedded between two semi-infinite non-magnetic metallic layers (Fig. 1). Unlike ferrite-based structures, the AFM materials considered here are characterized by a non-diagonal magnetic permeability tensor, giving rise to qualitatively different hybridization behavior between electric and magnetic wave modes.

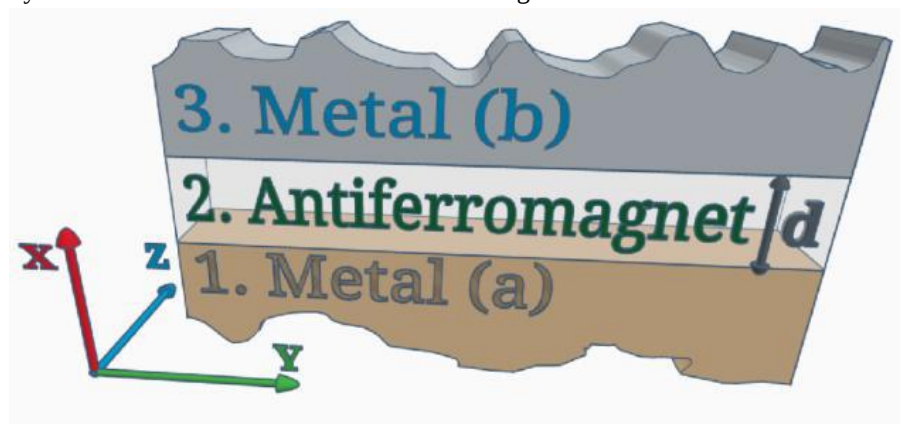


Fig. 1. Investigated layered nanosystem.

The main objective of this study is to derive and analyze the dispersion relations governing surface MPPs in such AFM-metal heterostructures. Using Maxwell's equations and the appropriate boundary conditions, a general dispersion equation is obtained. It is shown that the interaction between E-waves and Hwaves in AFM systems cannot be decoupled, resulting in a single hybridized polaritonic mode. When incorporating the frequency dependence of the permeability tensor components, the dispersion law becomes biquadratic in the squared frequency, producing two distinct solution branches.

Furthermore, an exact (non-linearized) dispersion relation is derived, yielding four frequency branches, which are categorized based on the magnitude of the imaginary part of the frequency. Two branches correspond to significantly attenuated modes, while the remaining two represent low-loss, propagating solutions, asymptotically reaching a characteristic limit at large wavenumbers. The influence of AFM anisotropy and wavenumber magnitude on mode hybridization is examined in detail.

The findings underscore the critical role of anisotropy and intermodal coupling in forming hybrid MPP states in antiferromagnetic systems. These results provide a foundation for the design of next-generation THz devices such as reconfigurable waveguides, resonators, and sensors utilizing AFM-based layered structures.

References:

- 1. Chumak, A. V., Vasyuchka, V. I., Serga, A. A., & Hillebrands, B. (2015). Magnon spintronics. Nature physics, 11(6), 453-461.
- 2. R. H. Tarkhanyan, New class of surface magnon polaritons in enantiomeric antiferromagnetic structures, Prog. Electromagn. Res. B, 39, 55-69 (2012). DOI: 10.2528/PIERB12010705.
- 3. Rezende, S. M. (2020). Fundamentals of magnonics (Vol. 969, p. 301). Cham: Springer.

BLOCH POINT STRUCTURE AND RELAXATION AT FINITE TEMPERATURES

Ivan Yastremsky¹, Alexander Yakimkin¹

¹Taras Shevchenko National University of Kiev, 03127, Kiev, Ukraine

Recent advances in producing and characterizing nano and microstructures as well as the first imaging of 3D magnetic configurations such as complex vortices, Bloch points and hopfions renewed the interest in describing the properties of three-dimensional (3D) magnetic profiles. Among the 3D magnetic profiles with topological protection, we can highlight the Bloch point (BP) [1, 2], which is a structure that presents a singular point at its center, where ferromagnetic order is destroyed. To properly use BPs in technological applications based on their stabilization and motion, it is crucial to analyze the fundamental properties of these structures. In particular, the BP mobility is strongly affected by the distribution of the magnetization length at the BP center [3].

The distribution of the magnetization length at the BP center at finite temperature is studied in Ref. [3-5]. For modelling of the free energy in these studies the Landau energy is adopted. Still in magnetism there is no region where the Landau expansion could be applied rigorously. The purpose of this study is to investigate the distribution of the magnetization length around the singularity of BP adopting more realistic free energy.

We suppose that the magnetization of a ferromagnet M can change its length M. As we study the magnetization length distribution M around the singularity of BP, where the exchange energy dominates we restrict ourself to the case of isotropic ferromagnet. The conditions that determine the structure of a motionless soliton have a clear interpretation that the effective field (generalized forces) in the system equal to zero H=0 [3]. We calculate the radial distribution of M for the free energy in the frame of the mean-field approach and compare this result with those obtained in [3-5] for the energy in the Landau form. The results of these calculations are presented in Fig. 1, 2. The distance from the BP center x is measured in units, which is of the order of 1 nm for parameters of ultrathin films of Co.

These figures demonstrate that the widely used Landau model [3-5] is adequate only for temperatures sufficiently close to the Curie temperature. For low temperatures the Landau model gives substantially lower radius of BP core

compared to the mean-field model. For example, for T=0.2TC, the typical radius of BP within the Landau model is of the order of atomic unit and is about 15 times smaller than within more realistic mean-field model. Consequently, the long-wave approximation, exploited in [3-5], can hardly be justified for description of the variation of the magnetization length for low temperatures.

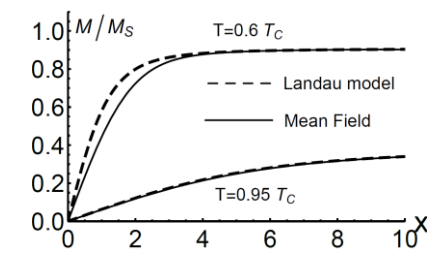


Fig. 1. The radial dependence of the normalized magnetization length for temperatures $T=0.6T_{\rm C}$, 0.95 $T_{\rm C}$ within the Landau and mean-field models.

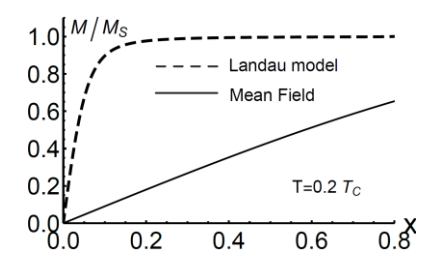


Fig. 2. The radial dependence of the normalized magnetization length temperatures $T=0.2T_{\rm C}$, within the Landau and mean-field models

Using the Landau-Lifshitz-Bar'yakhtar equation and the Landau model Galkina et al. [3] demonstrate that the reason of overdamped dynamics of BPs in the Yttrium-Iron Garnet is the longitudinal nonlocal (exchange) relaxation, which, in turn, is determined by the magnetization length distribution.

The results of this work can be used to develop a complete quantitative phenomenological theory of Bloch points relaxation, which includes both transverse and longitudinal, local and nonlocal relaxation contributions. We predict that the BP's singularity affects both the local and nonlocal relaxation.

- [1] Im, M.-Y. et al., Dynamics of the Bloch point in an asymmetric permalloy disk. Nat. Commun. 10, 593 (2019).
- [2] T. Felipe, J. Fernandez-Roldan, K.Y. Guslienko, R. Otxoa, O. Chubykalo-Fesenko, Giant supermagnonic Bloch point velocities in cylindrical ferromagnetic nanowires, Nanoscale 16, 10737 (2024).
- [3] Galkina, E. G., Ivanov, B. A., Stephanovich, V. A., Phenomenological theory of Bloch point relaxation. JMMM 118, 373 (1993).
- [4] K. M. Lebecki, D. Hinzke, U. Nowak, and O. Chubykalo-Fesenko, Key role of temperature in ferromagnetic Bloch point simulations, Phys. Rev. B **86**, 094409 (2012).
- [5] R. G. Elias and A. Verga, Magnetization structure of a Bloch point singularity, Eur. Phys. J. B 82, 159 (2011).
- [6] Yastremsky, I.A., Magnetization length in the Bloch point at finite temperatures, JMMM **616**, 172834 (2025).

DUAL-ANTIFERROMAGNETIC-LAYER SPIN HALL OSCILLATOR

O. V. Shtanko¹, O. V. Prokopenko¹

¹Educational and Scientific Institute of High Technologies, Taras Shevchenko National University of Kyiv, Kyiv, 01601, Ukraine

Antiferromagnetic (AFM) materials possess numerous essential benefits relevant to spintronic applications [1,2]. Firstly, the intrinsic operational frequencies of the AFM structures fall within the sub-terahertz and terahertz ranges, being significantly higher than the characteristic frequencies in ferromagnets and ferrites. Secondly, zero or almost zero net magnetization of AFM materials makes it possible to avoid high bias magnetic fields. Thirdly, the absence of reaction to nearby magnetic fields perturbations allows AFM spintronic nanostructures to be seamlessly incorporated into contemporary nanoelectronic technologies.

Standard implementations of the mentioned AFM spintronic nanostructures rely on a bilayer geometry, where a heavy metal (e.g. platinum Pt), with strong spin-orbit interaction, resides close to the adjacent AFM layer. The components obtained in this manner are known as spin Hall oscillators (SHOs), given that their functionality relies on the spin Hall effect [3-5]. For all variations of AFM SHOs, there is the functional relationship between the generated frequency and the amplitude of the current, propagating through the heavy metal layer. Consequently, the generated frequency spectrum is determined by experimentally achievable amplitudes of the direct electric current.

This study proposes a method for expanding the AFM SHO frequency range by employing a dual-antiferromagnetic-layer (DAL) SHO, developed from two canted AFM layers possessing a nonzero net magnetization, influenced by Dzyaloshinskii-Moriya interaction. The specified AFM SHO is designed as a five-layer Pt/AFM/NM/AFM/Pt configuration, where NM denotes a certain nonmagnetic material positioned between two conventional Pt/AFM SHOs.

The dynamics of magnetization vectors were described using the macrospin approximation and a coupled system of Landau-Lifshitz-Gilbert-Slonchewski (LLGS) equations $\frac{d m_{1,2}^{T,B}}{dt} = \left(\boldsymbol{T}_p + \boldsymbol{T}_d + \boldsymbol{T}_s \right)_{1,2}^{T,B}$, where superscripts T, B denote the top and bottom AFM layers, whereas subscripts 1,2 correspond to the first and second AFM sublattices respectively. The torque terms \boldsymbol{T}_p , \boldsymbol{T}_d and \boldsymbol{T}_s were introduced to describe the influence of the effective magnetic field, dissipation, and spin-transfer, respectively.

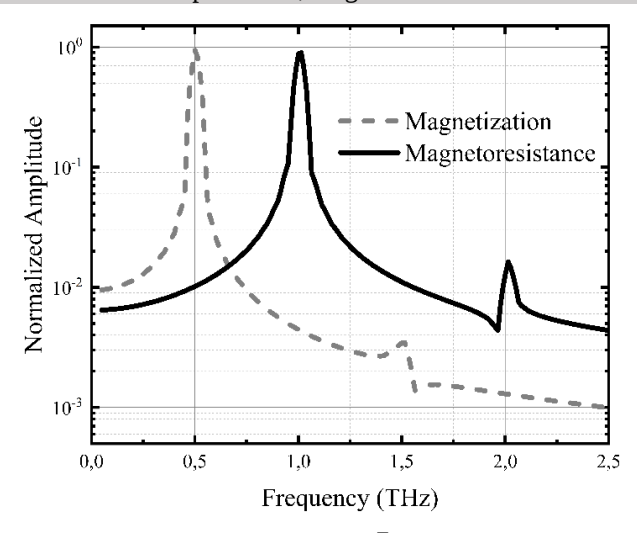


Fig. 1. The spectra of magnetization $\mathbf{M}^{\mathrm{T}}(t)$ oscillations (gray dashed curve) and magnetoresistance R(t) (black solid curve) for the DAL SHO.

The numerical integration of the LLGS system yielded four time-dependent vector functions $\mathbf{m}_1^{\mathrm{T}}$, $\mathbf{m}_2^{\mathrm{T}}$, $\mathbf{m}_1^{\mathrm{B}}$ and $\mathbf{m}_2^{\mathrm{B}}$, served as the basis for calculating, in sequence, the resultant magnetization vectors of the top $\mathbf{M}^{\mathrm{T}} = \mathbf{m}_{1}^{\mathrm{T}} + \mathbf{m}_{2}^{\mathrm{T}}$, and the bottom $\mathbf{M}^{\mathrm{T}} = \mathbf{m}_{1}^{\mathrm{T}} + \mathbf{m}_{2}^{\mathrm{T}}$ AFM layers, and the angle β between them. Relying on the established tunneling magnetoresistance approximation [6], the variable resistance R(t) of the DAL SHO was evaluated. The spectral behavior of both $\mathbf{M}^{\mathrm{T}}(t)$ and R(t) functions is shown on Fig. 1, where the frequency-doubling effect is prominently manifested. The third harmonic peak in the magnetization spectrum reflects the nonlinearity of the employed LLGS equations, while the observed second harmonic of the magnetoresistance arises from its nonlinear approximation [6].

In conclusion, the proposed DAL SHO enhances the frequency tunability in AFM spintronic generators. The results of this study can be applied toward the design and optimization of spintronic components based on AFM nanostructures.

- [1] P. Khalili Amiri, C. Phatak, and G. Finocchio, Annu. Rev. Mater. 54 (2024).
- [2] B. Rimmler, B. Pal, and S. Parkin, Nat. Rev. Mater. **10**, 109-127 (2025).
- [3] S. Gulbrandsen, C. Espedal, and A. Brataas, Phys. Rev. B 101, 184411 (2020).
- [4] R. Khymyn, et al., Sci. Rep. 8, 15727 (2018).
- [5] O. Sulymenko, et al., Phys. Rev. Appl. 8, 064007 (2017).
- [6] J. Slonczewski, Phys. Rev. B 39, 6995-7002 (1989).

GEOMERTY-GOVERNED CHIRAL EFFECTS IN CURVILINEAR MAGNETISM (INVITED)

D. D. Sheka

¹Taras Shevchenko National University of Kyiv, 01601 Kyiv, Ukraine

The nanotechnology rush extended conventional flat architectures to curved space, showcasing the fundamental importance of the mutual interplay between geometry, topology and the order parameter. In the case of magnetism, a mutual interplay of material properties such as magnetization texture and geometrical properties, such as curvature, thickness, topology becomes a playground for curvilinear magnetism [1]. By tailoring geometric properties of the conventional magnetic materials, a variety of possibilities emerge to control material response, leading to modification or even launching new functionalities [2].

This talk focuses on the peculiarities emerging from geometrically curved magnetic objects, including 3D bent and twisted curved wires and films. We discuss family of novel geometry-governed effects emerge, which include magnetochiral effects and topological patterning, resulting in theoretically predicted domain wall automotion, unlimited domain wall velocities, chirality symmetry breaking, mesoscale Dzyaloshinskii-Moriya interaction etc. Our special focus is chiral effects, which can be local driven by exchange and stemming from local curvature and torsion [1,3] or stemming from the varying cross-section [4-5], but also can be nonlocal driven by magnetostatics and supported by topology [6]. We discuss the nonlocal symmetry breaking effect is validated experimentally in the vortex state magnetic cap [7]: due to the symmetry break the vortex string becomes deformed into a helix. Moreover, the geometric chirality of the vortex string is determined by the magnetic helicity of the vortex texture, constituting coupling of two chiral parameters within the same texture.

- [1] D. Makarov, D. Sheka. Topics in Applied Physics. (Springer, Cham, 2022)
- [2] G. Gubbiotti et al, J. Phys: Cond Matt (2025);
- [3] K. Yershov, D. Sheka, S. Kondovych, Phys. Rev B 111 (2025) 184419;
- [4] K. Yershov, D. Sheka, Phys. Rev B 107 (2023) L100415;
- [5] D. Karakuts, K. Yershov, D. Sheka, in Functional Magnetic and Spintronic Nanomaterials (2024),
- [6] D. Sheka, O. Pylypovskyi, P. Landeros, Y. Gaididei, A. Kákay, D. Makarov, "Nonlocal chiral symmetry breaking in curvilinear magnetic shells", Comm. Phys. 3 (2020) 128,
- [7] O. Volkov, D. Wolf, O. Pylypovskyi, A. Kákay, D. Sheka, B. Büchner, J. Fassbender, A. Lubk, D. Makarov, "Chirality coupling in topological magnetic textures with multiple magnetochiral parameters", Nature Comms, 14 (2023) 1491,

CURVILINEAR MAGNETISM: FUNDAMENTALS AND APPLICATIONS (INVITED)

D. Makarov ¹

¹Helmholtz-Zentrum Dresden-Rossendorf e.V., Dresden, 01328, Germany

Curvilinear magnetism is a framework, which helps understanding the impact of geometric curvature on complex magnetic responses of curved 1D wires and 2D shells [1-4]. This approach provides means to modify conventional or to launch novel functionalities by tailoring curvature and 3D shape of magnetic thin films and nanowires [3]. In this talk, we will address fundamentals of curvature-induced effects in magnetism and review the envisioned application scenarios.

In particular, benefiting from theoretical predictions of the Ukrainian magnetism community [5,6], we demonstrated experimentally that curvature allows tailoring fundamental anisotropic and chiral magnetic interactions [7,8] and enables fundamentally new nonlocal chiral symmetry breaking effect [9,10]. The topology of the geometry of 3D shaped magnetic objects allows stabilizing multiple solitons within a confined nanoarchitecture [11]. These curvilinear magnetic architectures are relevant for numerous research and technology fields ranging from non-conventional computing, spin-wave splitters for low-energy magnonics, as well as memory devices [12].

The application potential of geometrically curved magnetic architectures is being explored as mechanically reshapeable magnetic field sensors for automotive applications, magnetic soft robots [13] as well as on-skin interactive electronics relying on mechanically flexible thin film [14-18] and printed [19,20] magnetic field sensors with appealing self-healing performance [21] and recyclability [22]. This opens perspectives for magnetoelectronics in smart wearables [23], interactive printed electronics [24] and motivates further explorations towards the realization of eco-sustainable magnetic field sensing relying on biocompatible and biodegradable materials [25,26].

- [1] D. Makarov et al., Advanced Materials (Review) 34, 2101758 (2022).
- [2] P. Gentile et al., Nature Electronics (Review) 5, 551 (2022).
- [3] G. Gubbiotti et al., J. Phys.: Condens. Matter. (Roadmap) 37, 143502 (2025).
- [4] P. Makushko et al., Nature Electronics 7, 207 (2024).
- [5] Y. Gaididei, V. P Kravchuk, and D. D. Sheka, Phys. Rev. Lett. 112, 257203 (2014).
- [6] D. D. Sheka et al., Communications Physics 3, 128 (2020).
- [7] O. Volkov et al., Phys. Rev. Lett. 123, 077201 (2019).
- [8] D. Raftey et al., ACS Nano (2025), https://pubs.acs.org/doi/10.1021/acsnano.5c08926

128 | Modern problems of solid state physics & magnetism

- [9] O. M. Volkov et al., Nature Communications 14, 1491 (2023).
- [10] O. Bezsmertna et al., Nano Letters 24, 15774 (2024).
- [11] O. Volkov et al., Nature Communications 15, 2193 (2024).
- [12] A. M. A. Farinha et al., Nature 639, 67 (2025).
- [13] M. Ha et al., Advanced Materials 33, 2008751 (2021).
- [14] G. S. Canon Bermudez and D. Makarov, Advanced Functional Materials (Review) 31, 2007788 (2021).
- [15] J. Ge et al., Nature Communications 10, 4405 (2019).
- [16] G. S. Canon Bermudez et al., Nature Electronics 1, 589 (2018).
- [17] P. Makushko et al., Nature Communications 16, 1647 (2025).
- [18] O. Bezsmertna et al., Adv. Funct. Mater. 2502947 (2025).
- [19] M. Ha et al., Advanced Materials 33, 2005521 (2021).
- [20] E. S. Oliveros Mata et al., Advanced Materials Technologies 7, 2200227 (2022).
- [21] R. Xu et al., Nature Communications 13, 6587 (2022).
- [22] X. Wang et al., J. Mater. Chem. A 12, 24906 (2024).
- [23] P. Lugoda et al., Communications Engineering 4, 33 (2025).
- [24] R. Xu et al., ACS Nano 19, 21891 (2025).
- [25] E. S. Oliveros Mata, R. Xu, L. Guo, and D. Makarov, Phys. Rev. Appl. (Review) **20**, 060501 (2023).
- [26] L. Guo, R. Xu, and D. Makarov, Chinese Journal of Structural Chemistry (Review) 44, 100428 (2025).

SPIN DYNAMICS IN FERRO-/ANTIFERROMAGNETIC MULTILAYERS (INVITED)

O. Busel, D. Polishchuk, A. Kravets, and V. Korenivski Royal Institute of Technology, Stockholm, 10691 Sweden

Antiferromagnets (AFs) are of growing interest for applications in spinthermionic devices [1,2] operating in the technologically attractive temperature range around the AF's Néel temperature, *T*_N, typically just above room temperature (RT). Although AF-based devices operating at sub-THz frequencies are still far from widespread use [2], a combination of ferromagnetic (F) and AF materials has the potential to close the so-called GHz-THz gap [3]. Standing spin waves (SSW) are higher-order resonance modes found in ferromagnets at higher frequencies than the uniform ferromagnetic resonance (FMR) and can reach the antiferromagnetic resonance (AFMR) frequency range of 0.1-1 THz. Furthermore, employing AF spacers as mediators of ferromagnetic interlayer exchange in multilayers [4] can extend the material's functionality with thermal control.

We recently demonstrated [5] thermal gating of AF-mediated interlayer exchange in F/AF/F trilayers, which can be used for thermally assisted parallel-toantiparallel switching in spin-valve devices. A combination of the AF finite-size, F-proximity, and AF-exchange-bias effects was used. The three layers, and especially the thin AF spacer, were designed to achieve ferromagnetic F-F coupling by magnon exchange via the AF spacer when the AF order is soft enough near its T_N for magnons in the system to F-AF hybridize. In this report we discuss our results on F/AF multilayers with up to eight F layers that can, in a specific thermal regime, show pronounced standing spin wave (SSW) modes in addition to uniform FMR [6].

The layout of the studied F/AF multilayers is shown in Fig. 1(a) and has the stack of N=2 to 8 F layers (Py or Fe₈₁Ni₁₉) spaced by (N-1) AF layers (FeMn or Fe₅₀Mn₅₀). The broadband FMR setup illustrated in Fig. 1(b) was used to measure the in-plane FMR spectra - the field-derivative of the microwave absorption dP/dH versus the in-plane DC magnetic field H, at different temperatures T, at fixed frequency *f*, such as shown in Fig. 2 for *N*=7 and 9 GHz.

We observe strongly nonlinear spin dynamics in such F/AF multilayers, controlled by the number of bilayers in the system, layer thicknesses, as well as temperature, peaking in magnitude near the Néel point of the AF layers just above room temperature. Well above the Néel transition, the individual ferromagnetic layers are exchange-decoupled and resonate independently.

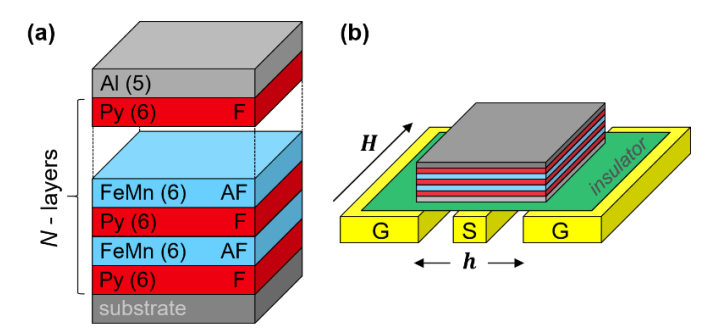


Fig. 1. Layout of studied F/AF multilayers, with alternating F and AF layers and total number of F layers of N=2-8; individual layer thicknesses are given in parentheses in nm. (b) Schematic of broadband FMR setup based on coplanar waveguide, with signal (S) and ground (G) lines as well as magnetic field geometry shown, operated in PPMS system at temperatures 2 to 400 K, magnetic fields up to 9 T, and frequencies up to 13 GHz.

As the temperature is lowered toward the Néel point, the ferromagnetic proximity effect through the thin AF spacers transforms the system into a weakly coupled macrospin chain along the film normal, which exhibits pronounced standing spin-wave resonance modes, comparable in intensity to the uniform resonance in the ferromagnetic layers. These findings, shown by the data in Fig. 2 (the inset shows the intensity of the SSW mode versus temperature), are supported by our micromagnetic simulations showing clear spin-wave profiles with precessional phase lag along the macrospin chain. Well below the Néel transition, the FeMn layers order strongly antiferromagnetically and exchange-pin the ferromagnetic layers to effectively make the multilayer one macrospin with high anisotropy. The appearance and intensity of the high-frequency spin-wave modes can thus be conveniently controlled by thermal gating the multilayer. The nonlinearity in the microwave response of the demonstrated material can approach 100%, giant compared to nonlinear materials used in e.g. optics, with second-harmonic generation often at the single percentage level.

The highly nonlinear material properties demonstrated in this work should be interesting for spin-thermionic and thermo-magnonic applications, where additional functionality can be achieved using thermal control in a narrow range near room temperature.

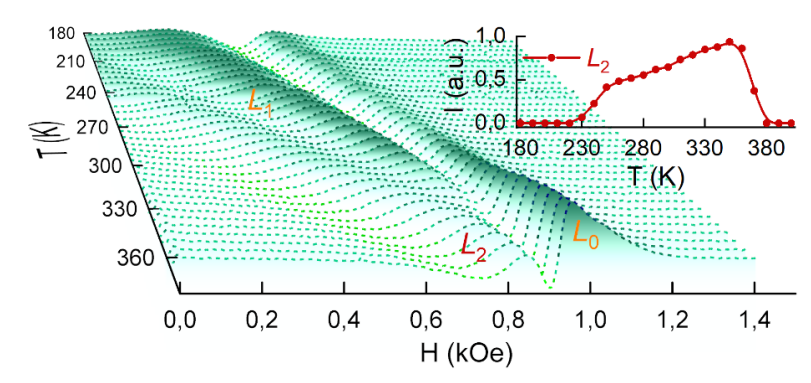


Fig. 2. FMR spectra as field-temperature map for F/AF with N=7, f=9 GHz. Inset shows novel SSW mode versus temperature across Néel transition.

Fig. 3 graphically illustrates the physics of the perpendicular SSW (standing spin wave perpendicular to film plane, PSSW) consistent with our measurements, micromagnetic simulations, and SW analytics mentioned above. The outer surfaces of the outer Py layers face nonmagnetic SiO2 and Al and, hence, are free from anisotropy, which corresponds to the no-surface pinning case for PSSW excitation. The leftmost panel in Fig. 2(a) shows the uniform mode (p=0, for visual clarity no distinction is made between L_0 and L_1 here, inner vs. outer Py); the rightmost panel is the p=3 mode corresponding to three half-wavelengths. Our micromagnetic results indicate most pronounced SSW's in the N = 7 sample and specifically this p=3 mode [6]. Well above T_N , at 400 K, the spacers are fully paramagnetic, hence the F layers are fully exchange-decoupled and precess independently under FMR, showing a single peak on the experiment (L₀). Well below *T*_N, below about 200 K, the AF order in the spacers becomes strong (AF magnon gap grows correspondingly wide), so the F layers become fully decoupled again but exchange-pinned individually and, as a result, precess individually under the higher anisotropy condition (illustrated using a smaller precession cone for low T). Near the AF phase transition (AF magnon gap is small and hybridized by F proximity), the finite ferromagnetic exchange-coupling between the F layers in the stack leads to an effective macrospin-chain along the normal to the film plane, which exhibits PSSW. This AF-mediated interlayer exchange is a sensitive function of

132 | Modern problems of solid state physics & magnetism

temperature, which offers a convenient thermal-control mechanism for microwave applications of the material.

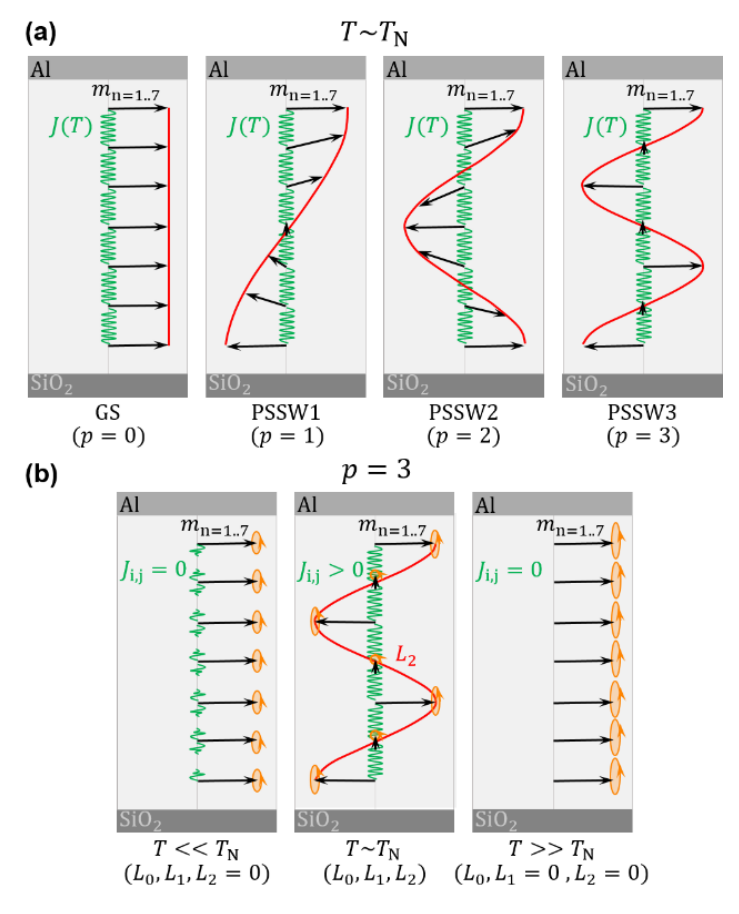


Fig. 3. (a) Possible PSSW modes in studied system near AF transition. (b) p=3 mode at temperature well below (left), about (middle), and well above T_N (right).

- [1] V. Baltz, et al., Rev. Mod. Phys. 90, 015005 (2018).
- [2] T. Jungwirth, et al., Nature Physics 14, 200 (2018).
- [3] Y. Saito, et al., Phys. Rev. Appl. 19, 064040 (2023).
- [4] R. Cheng, D. Xiao, J.-G. Zhu, Phys. Rev. Lett. 121, 207202 (2018).
- [5] D. Polishchuk, et al., Phys. Rev. Lett. 126, 227203 (2021); PRB 107, 224432 (2023).
- [6] O. Busel, D. Polishchuk, A. Kravets, V. Korenivski, APL Materials 13, 071121 (2025).

CURRENT-DRIVEN DYNAMICS OF CHIRAL DOMAIN WALLS IN A **OUASI-ONE-DIMENSIONAL HELIMAGNET**

R. R. Teslia, O. K. Kolezhuk

V.G. Baryakhtar Institute of Magnetism of the National Academy of Sciences of Ukraine, Kyiv, 03142, Ukraine

Effects of spontaneous symmetry breaking can naturally lead to the formation of domain walls connecting regions with different values of the order parameter. Domain walls in ferro- and antiferromagnetic materials can be driven by the electric current and are of practical interest for their applications in spintronics [1].

Recent progress in antiferromagnetic spintronics has also drawn attention to helimagnets, which combine the advantages of ferro- and antiferromagnets. The compensated (helical) magnetic structure of these materials can be manipulated by the (spin-polarized) electric current and magnetic field [2].

Modern experiments and micromagnetic calculations demonstrate the possibility of effective control and detection of chirality (the direction of rotation of magnetization in a helix) in helimagnetic thin film samples in the lowtemperature regime [3] as well as at room temperature [4], using the magnetic field and current. This robust degree of freedom is stable under temperature fluctuations and can be used in future spintronic memory devices. At the same time, the microscopic picture of the chirality switching remains unclear. One of the possible mechanisms that may contribute to this process is the motion of a "chiral" domain wall (see Fig. 1) connecting regions with opposite chiralities.

We have theoretically investigated the dynamics of a one-dimensional magnetic texture of the type shown in Fig.1 under the action of a spin-polarized current, in the continuum model of a frustrated conducting helimagnet. We reproduce the known effects of the out-of-plane angle tilt and the sliding motion of magnetization profile under the action of the dissipative spin-transfer torque analytically and numerically.



Fig. 1. Schematic depiction of a helical magnetic texture with a chiral domain wall (underlined with a dashed line). The sense of rotation of magnetization changes from clockwise (on the left) to counterclockwise (on the right).

Moreover, using the collective coordinates approach, we show that under the influence of the adiabatic ("gauge field") contribution of the current, an isolated

134 | Modern problems of solid state physics & magnetism

chiral domain wall experiences a force that is inversely proportional to the length of the system. The latter originates as a boundary effect and cannot (directly) be taken into account via the bulk Landau-Lifshitz equations. We show that due to the adiabatic spin transfer, a chiral domain wall can achieve the stationary velocity

$$V=Pj\cdot v_0 L_H/(2\pi\alpha_G\cdot L\cdot eS)$$
,

where L_H is the spatial period of the helix, L is the system length, α_G is the Gilbert damping, S is the underlying spin of magnetic atoms in the material, v_0 is the elementary cell volume, j is the current density and P its polarization, and e is the elementary charge.

This should be compared to the velocity V_{β} of a steady-state motion of the chiral domain wall that would result purely under the influence of the dissipative torque. The ratio of those velocities is given by $V_{\beta}/V = \pi \beta L/L_H$. For a rough estimate, assuming $\beta = 0.01$, and taking the helix period to be $L_H \approx 30$ nm, the above ratio drops below one for L smaller than approximately 1μ m. Therefore, this effect can become observable/important in sufficiently small samples.

- [1] S. W. Cheong and M. Mostovov, Nat. Mater. **6**, 13–20 (2007).
- [2] J.i. Ohe and Y. Onose, Appl. Phys. Lett., 118, 042407 (2021).
- [3] N. Jiang, et al., Nat Commun 11, 1601 (2020).
- [4] H. Masuda, et al., Nat Commun 15, 1999 (2024).

PROGRAMMABLE ARTIFICIAL "NEURON" BASED ON ANTIFERROMAGNETIC SPIN HALL OSCILLATOR

I. O. Sotnyk¹, O. V. Prokopenko¹

¹Taras Shevchenko National University of Kyiv, Kyiv, 01601, Ukraine

Modern computing systems are significantly inferior to the human brain in terms of efficiency in performing various tasks, such as image recognition, signal classification, and decision-making in uncertain conditions. This had led to increased interest in neuromorphic electronics, a technology that mimics the principles of biological neural networks. Artificial "neurons", implemented as nonlinear oscillators, are capable of generating impulses in response to external stimuli, similar to neurons in the brain, while operating with minimal energy consumption [1-4]. Examples of practical implementations of such systems are Intel's *Loihi* microchips and IBM's *TrueNorth* processor [4].

Currently, artificial "neurons" based on magnetic materials, in which antiferromagnets (AFMs) are used as magnetic materials, are considered promising. Such systems are capable of operating at terahertz frequencies, providing high speed and energy efficiency [5, 6]. However, existing AFM-"neurons" typically have only one input, which limits their functionality and application possibilities. To overcome this limitation, an approach is proposed for the implementation of a multi-input programmable artificial neuron ("P-neuron") by combining several single-input AFM-"neurons" into a two-level system (see [7] for details). This approach opens up new opportunities for the development and optimization of ultra-fast neural networks based on antiferromagnetic materials.

A typical artificial "neuron" is a spin Hall oscillator (SHO) based on AFM material, capable of generating controlled sequences of ultrashort delta-like pulses (spikes) lasting several picoseconds, under the action of input DC and AC signals when the total DC + AC current exceeds a certain threshold, see Fig. 1a [5]. In general, such a system is formed as a layered structure consisting of a layer of nonmagnetic metal (Pt) and an AFM layer (NiO) [8]. Accordingly, the spin current generated by the spin Hall effect in platinum goes into the AFM layer and creates a spin pumping effect [9, 10]. This effect acts on the magnetization of the AFM sublattices of the material, causing them to switch rapidly. Such switching creates a short output pulse of spin current, which returns to the Pt layer, where it can be converted into an electrical signal using the inverse spin Hall effect [5, 8, 9].

A programmable artificial "neuron" ("P-neuron") is a two-layer neural network in which each conventional AFM-based "neuron" in the first input layer

136 | Modern problems of solid state physics & magnetism

has only one independent input. The state of each "neuron" in the first layer can be changed by applying a specific DC density value, which independently affects the operating point of each "neuron". All outputs of the "neurons" of the first layer are connected to one AFM-"neuron" with multiple inputs, which forms the second layer of the considered "P-neuron", see Fig. 1b. Auxiliary "neurons" in the first layer control the inputs signals received by the main "neuron" in the second layer. Depending on their operating point, the applied DC current densities are selected, these "neurons" can generate 0, 1, 2 or more pulses for the same or different variable signals applied to their inputs [7].

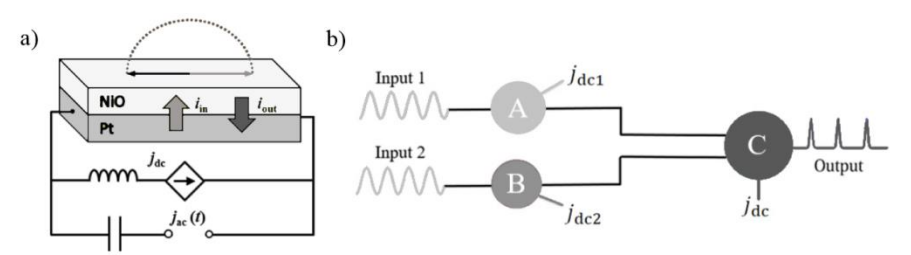


Fig. 1. Schematic representation of the systems: a) a conventional artificial "neuron" based on an antiferromagnetic spin Hall oscillator; b) a programmable artificial "neuron" consisting of AFM-"neurons".

This system can be described by the equation for the Neel vector angle [7, 8]:

$$\frac{1}{\omega_{ex}}\ddot{\varphi} + \alpha_{eff}\dot{\varphi} + \frac{\omega_{e}}{2}sin2\varphi = \sigma(j_{dc} + j_{out\ 1,2}(t))$$

Here ω_{ex} – exchange angular frequency, ω_e – easy-plain frequency, α_{eff} – effective Gilbert damping coefficient, σ – spin-transfer torque coefficient, j_{dc} – DC current density for main "neuron", $j_{out\ 1,2}(t)$ – output electric current for the "neurons" of the first layer. Typical parameters of the NiO/Pt spin Hall oscillator and input signals were used for the simulation [7, 8, 11]: the exchange field is $H_{ex}\sim 9.8$ MOe and the exchange frequency is $\omega_{ex}=2\pi\cdot 27.5$ THz, the easy-plain field is $H_e=628$ Oe and the easy-plain frequency is $\omega_e=2\pi\cdot 1.75$ GHz, and the spin-transfer torque coefficient is $\sigma=2\pi\cdot 4.32\cdot 10^{-4}$ Hz · m² / A.

In general, a conventional artificial "neuron" can have several modes of work, which are determined by the parameters of the control current. Such a system can work in the following modes: "no spike", "one spike", "bursting" [5, 6]. If we consider a programmable artificial "neuron", depending on the working point of the neurons in the first input layer, which is set using the input signal parameters (DC, AC current density and frequency), they can generate no pulses or generate

one or more spikes of equal duration, which then act on the main "neuron". In turn, all spikes arriving at the inputs of the "neuron" of the second layer, together with the DC current applied to it, determine its output signal. Accordingly, depending on the values of the "neuron" parameters, the main "neuron" generates one, two, or several spikes that correspond to the modes of work of the artificial "neuron".

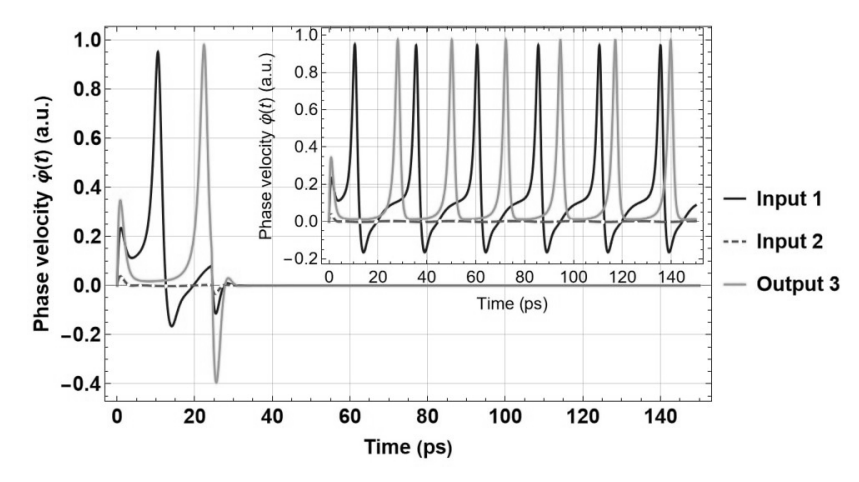


Fig. 2. Typical time dependence of the phase velocity of the Neel vector at input 1 (generated by "neuron A"), input 2 (generated by "neuron B") and output 3 of a second-layer AFM-based "neuron C". Main "neuron C" generates an output signal. The inset shows $\dot{\phi}(t)$ for the case of input AC signals acting on "neuron A" and "neuron B" over the entire simulation time of 150 ps.

From Fig. 2, it can be seen that by selecting the value of the constant component of the current supplied to the "neurons" of the first layer, it is possible to significantly change the "sensitivity" of each "neuron" for the same input harmonic signal, or for different AC signals. The smaller the value of the DC current the lower the sensitivity of the "neuron" will be. For example, the behavior of the "P-neuron" in Fig. 2 can be in the case of a "sensitive" $(j_{dc1} \neq 0)$ "neuron" A" and an "insensitive" ($j_{dc2} \approx 0$) "neuron B". When such an alternating signal acts on "neuron A" for one period, it generates one output pulse (line Input 1, Fig. 2). At the same time, when there is no alternating signal for "neuron B", the reaction of "neuron C" is determined by the output of the "neuron A", resulting in the generation of one output pulse (line Output 3, Fig.2a). At high DC values, the "sensitivity" of the system to the alternating signal increases.

138 | Modern problems of solid state physics & magnetism

A special case occurs when all "neurons" are in "sensitive" states, in which case the system generates many spikes, i.e., it is in "bursting" mode.

Due to their properties, artificial "neurons" based on antiferromagnetic materials are promising functional material for use in spintronics, contributing to the development of various fields of science and technology, ranging from terahertz technologies to artificial neural networks.

Accordingly, we have theoretically proposed a programmable artificial "neuron" ("P-neuron") based on AFM in the form a two-layer neural network consisting of several spin Hall oscillators that function as an artificial "neurons". The input DC currents independently determine the operating states of the "neurons" of the first layer, which generate output signals that are sent to the "neuron" of the second level with several inputs. By selecting the values of the constant component of the current, it is possible to change the "sensitivity" of the "neurons" and the state of the "P-neuron", which is characterized by the number of pulses generated by the "neuron" of the second layer. Based on the results, we can say that the proposed neural network can be controlled by means of constant currents and thus can function as a programmable artificial "neuron". We believe that the proposed approach may be suitable for the development of ultra-fast neural networks based on antiferromagnetic spintronic oscillator, as well as for image recognition.

- [1] Y. LeCun, Y. Bengio, and G. Hiton, "Deep learning," Nature, vol. 521, p. 436-444, May 2015.
- [2] J.D. Kendall and S. Kumar, "The building blocks of a brain-inspired computer," Appl. Phys. Rev., vol. 7, p. 011305, January 2020.
- [3] J. Grollier, et al., Nat. Electron., vol. 3, p. 360-370, March 2020.
- [4] H. Bradley, et al., AIP Adv., vol. 13, p. 015206, January 2023.
- [5] R. Khymyn, et al., Sci. Rep., vol. 8, p. 15727, October 2018.
- [6] O. Sulymenko, et al., J. Appl. Phys., vol. 124, p. 152115, September 2017.
- [7] I. Sotnyk, O. Prokopenko, "Multi-Input Programmable Artificial "Neuron" Based on Antiferromagnetic Spintronic Nanostructures", 2024 IEEE 14th International Conference on Nanomaterials: Applications & Properties (NAP). IEEE, 2024. C. 1-5.
- [8] R. Khymyn et al., Sci. Rep., vol. 7, p. 43705, March 2017.
- [9] J. Sinova et al., Rev. Mod. Phys., vol. 87, no. 4, p. 1213, October 2015.
- [10] R. Cheng, J. Xiao, Q. Niu, and A. Brataas, "Spin Pumping and Spin-Transfer Torques in Antiferromagnets," Phys. Rev. Lett., vol. 113, p. 057601, August 2014.
- [11] D. Slobodianiuk, O. Shtanko and O. Prokopenko, "Antiferromagnetic Spintronic Oscillators: Fundamentals and Applications," in Nanocomposite and Nanocrystalline Materials and Coatings. Advanced Structured Material, vol. 214, A.D. Pogrebnjak, Y. Bing, M. Sahul, Eds. Singapore: Springer, 2024, pp. 91-128.

DOMAIN WALL DIODE AND TRAP BY CROSS SECTION TAILORING IN FERROMAGNETIC NANOSTRIPES

D. Karakuts¹, K. V. Yershov^{2,3}, D. D. Sheka¹

¹ Taras Shevchenko National University of Kyiv, Kyiv, 01601, Ukraine ² Leibniz-Institut für Festkörper- und Werkstoffforschung, IFW Dresden, Dresden, 01171, Germany

³ Bogolyubov Institute for Theoretical Physics of the National Academy of Sciences of Ukraine, Kyiv, 03143, Ukraine

In this work, we theoretically and numerically study the domain wall dynamics in a ferromagnetic nanostripes with varying cross section under the effect of an external magnetic field. Recently, the cross-section gradient has been shown to induce a driving force for a domain wall motion in a ferromagnetic nanostripes [1]. However, previous studies were lacking the description of the external field's influence on the system, which is necessary for both experimental confirmation and practical implementation.

To illustrate the magnetic properties of a ferromagnetic nanostripe with varying cross section, we apply the recently introduced framework [2], with the domain wall motion being described by a collective variable approach. To explain the domain wall dynamics, we derive the equations of motion utilizing the Lagrange-Rayleigh formalism, while accounting for the spatial variation of the cross-sectional area.

Although our approach is general and applicable to a wide range of geometries, in this work we focus on two distinct nanostripe geometries, namely nanostripe with a localized constriction and a wedge-shaped nanostripe. We demonstrate that the cross-section gradient creates an internal driving force, which, under certain conditions, counteracts the external magnetic field's influence on the domain wall. The point of balance between these effects results in the formation of a domain wall pinning position, whose value was obtained for both geometries.

Additionally, we establish that for the sufficiently large applied fields the domain wall depinning occurs, with the critical depinning field value h_d being derived for both geometries. This effect can be used for the fabrication of domain wall diodes and traps by modifying nanostripe cross section.

All analytical predictions are validated by the full-scale micromagnetic simulations [2]. This research was supported by DFG via Grant No. MC 9/22–1.

[1] D. Karakuts, K. V. Yershov, and D. D. Sheka, Functional Magnetic and Spintronic Nanomaterials, P. 133-145, (Springer, 2024).

[2] K. V. Yershov, D. D. Sheka, Phys. Rev. B 107, L100415 (2023).

ANTIFERROMAGNETIC SPINTRONIC OSCILLATORS AND SIGNAL DETECTORS (INVITED)

O. V. Prokopenko

Educational and Scientific Institute of High Technologies, Taras Shevchenko National University of Kyiv, Kyiv, 01601, Ukraine

Antiferromagnetic (AFM) spintronics is an emerging field of science and technology that focuses on the study and utilization of static and dynamical magnetic states in antiferromagnets for the development and creation of various spintronic devices [1-19]. "Pure" AFM devices, consisting only AFM layers, can demonstrate ultra-fast magnetization dynamics at (sub-) terahertz (THz) frequencies in the absence of a bias DC magnetic field and therefore have great potential for applications in medicine, communications, security systems, bioelectronics, astronomy, material science [1-4].

Two base elements of AFM spintronics are an AFM spin Hall oscillator and an AFM signal detector, also known as an AFM spin diode. Both utilize the spin Hall effect [5]; this paper reviews their properties.

The simplest AFM spin Hall oscillator consists of at least of two neighboring layers: an AFM layer and a heavy metal layer [6-10], although oscillators with two heavy metal layers and more complex structures, such as an antiferromagnetic tunnel junction [11], are also known. Under the action of a bias DC / AC current flowing through the heavy metal layer, a THz-frequency dynamics of magnetic sublattices in the adjacent AFM layer could be excited due to the spin Hall effect [5]. These oscillations are then is converted into an output AC signal for the entire device using different possible physical mechanisms, including the spin pumping and the inverse spin Hall effects [6-8, 10], the dipole generation mechanism [9], the magnetoresistance and the spin-torque diode effects [11], etc. To date, there are a lot of theoretical proposals for diverse "pure" AFM devices, including the sources of harmonic [7-9] and chaotic [12] signals, artificial neurons [8] and neuron-based logic [10]. The features and limitations of different types of AFM spin Hall oscillators are discussed in the talk. Also, the talk briefly explores the possibility of creating THz signal sources based on several AFM oscillators, both independent and synchronized with each other [13].

Another topic of discussion is the fundamentals and applications of AFM signal detectors that are nanoscale devices capable of generating a low frequency or DC output voltage under the action of a (sub-) terahertz frequency input AC signal [14-17]. In a general case, an input AC signal current applied to the detector

excites the current-driven (sub-) terahertz dynamics of the magnetic sublattices in the detector's AFM layer, which then leads to the generation of the detector output voltage across the entire structure due to several possible mechanisms. In particular, they include voltage generation due to the spin pumping and the inverse spin Hall effects [15], the tunneling anisotropic magnetoresistance and the spin-torque diode effect [16, 17], and recently studied the giant or tunneling magnetoresistance effect and the spin-torque diode effect in a junction with two canted AFM layer [18]. In my talk, I will briefly discuss the key features of AFM signal detectors compared to the conventional ferromagnet-based detectors, and also discuss the recent advances, trends, and problems in the physics and applications of antiferromagnetic spintronic detectors [19].

The author would like to thank all the brave defenders of Ukraine who made the finalization of this publication possible.

- [1] V. Baltz, et al., Rev. Mod. Phys. 90, 015005 (2018).
- [2] J. Han, et al., Nat. Mater. 22, 684 (2023).
- [3] A. Dal Din, O.J. Amin, P. Wadley and K.W. Edmonds, npj Spintronics 2, 25 (2024).
- [4] B.H. Rimmler, B. Pal, and S.S.P. Parkin, Nat. Rev. Mater. 10, 109 (2025).
- [5] J. Sinova, et al., Rev. Mod. Phys. 87, 1213 (2015).
- [6] R. Cheng, D. Xiao, and A. Brataas, Phys. Rev. Lett. 116, 207603 (2016).
- [7] R. Khymyn, et al., Sci. Rep. 7, 43705 (2017).
- [8] R. Khymyn, et al., Sci. Rep. 8, 15727 (2018).
- [9] O. Sulymenko, et al., Phys. Rev. Appl. **8**, 064007 (2017).
- [10] O. Sulymenko, et al., J. Appl. Phys. **124**, 152115 (2018).
- [11] O.R. Sulymenko, et al., IEEE Magn. Lett. 9, 3104605 (2018).
- [12] D.V. Slobodianiuk and O.V. Prokopenko, J. Appl. Phys. 134, 153903 (2023).
- [13] D. Slobodianiuk, O. Shtanko, and O. Prokopenko, in Nanocomposite and Nanocrystalline Materials and Coatings – Microstructure, Properties and Applications, Advanced Structured Materials (Vol. 214), Eds. A.D. Pogrebnjak, Y. Bing, M. Sahul (Springer, Singapore, 2024), P. 91-128.
- [14] G. Finocchio, et al., Appl. Phys. Lett. 118, 160502 (2021).
- [15] R. Khymyn, V. Tiberkevich, and A. Slavin, AIP Adv. 7, 055931 (2017).
- [16] P. Y. Artemchuk et al., J. Appl. Phys. **127**, 063905 (2020).
- [17] V.O. Prokopenko, E.N. Bankowski, O.V. Prokopenko, A.N. Slavin, IEEE Trans. Magn. 60, 4000707 (2024).
- [18] O. Shtanko, O. Prokopenko, 2024 IEEE 42st International Conference on Electronics Nanotechnology (ELNANO-2024), P. 156-160 (2024).DOI: https://doi.org/10.1109/ELNANO63394.2024.10756929.
- [19] I. Fantych, V. Prokopenko, O. Prokopenko, Spin diodes with magnetic anisotropy for signal detection and energy harvesting applications (Springer, Singapore, 2025, in press).

L1₀-BASED SPIN DIODES AS NON-RESONANT SIGNAL DETECTORS AND ENERGY HARVESTERS

I. Fantych, O. V. Prokopenko

Educational and Scientific Institute of High Technologies Taras Shevchenko National University of Kyiv, Kyiv, 01601, Ukraine

Spin diodes (SDs) are nanoscale spintronic devices that generate an output dc voltage $U_{\rm dc}$ under the action of an input ac signal current $I_{ac}(t) = I_{ac} \sin(2\pi ft)$ of power $P_{ac} \sim I_{ac}^2$ and frequency f [1-8]. In this work, we develop a simplified theoretical model of an SD with an L10-based free magnetic layer (FL) which is characterized by weak uniaxial magnetocrystalline anisotropy. We calculate the frequency and current dependencies of the output dc voltage of an SD, $U_{dc}(f)$ and $U_{dc}(I_{ac})$, and demonstrate that the diode can operate as a non-resonant threshold detector of low-frequency microwave signals. To improve the power conversion efficiency ζ of a passive SD, we propose to use an SD whose FL is made of L10 material [9]. We presume that the L10-based FL has a uniaxial magnetocrystalline anisotropy, which is described by the field induction \boldsymbol{B}_a directed perpendicular to the FL's plane and has a sufficient magnitude.

The considered SD is a three-layer magnetic nanostructure with a circular cross-section consisting of a free magnetic layer and a pinned magnetic layer (PL), with a non-magnetic dielectric spacer situated between them. We consider the FL magnetization $M \equiv M(t)$ in the scope of the macrospin approximation and PL magnetization lies along the x axis. The input microwave current in the FL excites the magnetization oscillations which leads to oscillation of the magnetoresistance. The last can be describe as $R(t) \equiv R = R_{\perp}/(1+\eta^2\cos\beta)$ [3, 10]. Also, we rewrite unit magnetization vector $m = M/M_s$ in spherical coordinates as $m = \{\sin\theta\cos\phi, \sin\theta\sin\phi, \cos\theta\}$ and substitute it into the Landau-Lifshitz-Gilbert-Slonczewski (LLGS) equation to describe the magnetization precession [3, 11]:

$$\frac{d\mathbf{m}}{dt} = \gamma [\mathbf{B}_{\text{eff}} \times \mathbf{m}] + \alpha \left[\mathbf{m} \times \frac{d\mathbf{m}}{dt} \right] + \sigma I_{\text{ac}}(t) [\mathbf{m} \times [\mathbf{m} \times \mathbf{p}]] .$$
(1)

Here $B_{eff}=B_0+B_{dem}+B_a$ is the effective magnetic field, which has contributions from the external magnetic field B_0 , demagnetization field B_{dem} and uniaxial anisotropy field B_a , p is the unit vector along the x-axis which describes the magnetization direction in the pinned layer, γ is the modulus of the gyromagnetic ratio, α is the Gilbert damping constant, $\sigma=\eta\gamma\hbar/2eM_sV$ is the spin-torque coefficient, η is the spin-current polarization of current, \hbar is the

reduced Planck constant, e in the modulus of the electron charge, $V = \pi r^2 l$ is the volume of the free magnetic layer with radius r and height l.

The solution of the LLGS is a characteristic equation from which we obtain the threshold current, which depends on the anisotropy field.

The output dc voltage of an SD can be written as follows:

$$U_{dc} = \langle I_{ac}(t)R(t)\rangle = wI_{ac}R_{\perp}\sin\psi = wI_{th}R_{\perp}, \qquad (2)$$

where R_{\perp} is the device resistance for $\beta=\pi/2$, and $w{\sim}0.1$ is the dimensional coefficient (see [2, 3] for details).

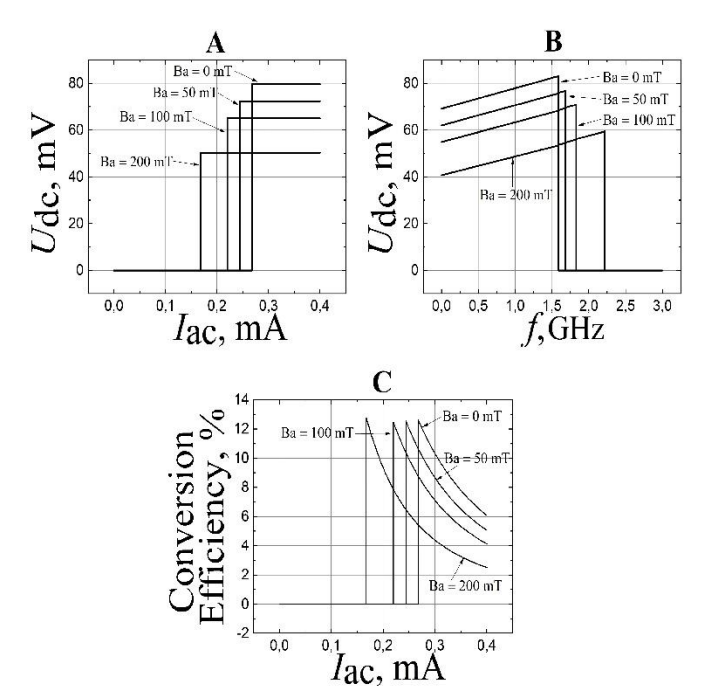


Fig.1. A - Dependence of the output dc voltage $U_{\rm dc}$ on the amplitude of the input signal current I_{ac} with frequency f = 1.2 GHz calculated for different values of the anisotropy field B_a ; **B** - Dependence of the output dc voltage U_{dc} on the frequency f of the input signal current with magnitude $I_{ac} = 0.2$ mA calculated for different values of the anisotropy field B_a ; C - Dependence of the power conversion efficiency ζ on the input signal current magnitude $I_{\rm ac}$ calculated for different values of the anisotropic field B_a

The output dc power of the diode can be estimated as $P_{dc} = U_{dc}^2 / \langle R(t) \rangle$,

where $\langle R(t) \rangle$ is the average value of the oscillating magnetoresistance R(t). Input ac signal power P_{dc} of an SD can be expressed as $P_{ac} = \langle I_{ac}^2(t)R(t) \rangle$, so one can calculate the device power conversion efficiency ζ as

$$\zeta = \frac{P_{\rm dc}}{P_{\rm ac}} = \frac{U_{\rm dc}^2}{\langle R(t)\rangle \langle I_{\rm ac}^2(t)R(t)\rangle}.$$
 (3)

As can be seen from Fig. 1, an SD with an L1₀-based FL that is characterized by weak uniaxial magnetocrystalline anisotropy can operate as a non-resonant threshold detector of low-frequency microwave signals. We have shown that the presence of uniaxial magnetic anisotropy in the FL can significantly reduce the threshold current required for proper diode operation and increase the device's power conversion efficiency ζ . Our theoretical estimations indicate that choosing an optimal anisotropy field value can achieve a conversion efficiency ζ of about 12%, which greatly exceeds that of conventional passive SDs with isotropic FLs. We believe that the obtained results can be important for the development and optimization of various microwave spintronic devices based on SDs with anisotropic FLs.

The authors would like to thank all the brave defenders of Ukraine who made the finalization of this publication possible.

- [1] A. A. Tulapurkar, et al., Nature, 438, 339-342 (2005).
- [2] O.V. Prokopenko, et al., J. Appl. Phys., 111, 123904 (2012).
- [3] O. V. Prokopenko, I. N. Krivorotov, T. J. Meitzler, E. Bankowski, V. S. Tiberkevich, and A. N. Slavin, Magnonics: From Fundamentals to Applications (Berlin/Heidelberg: Springer, 2013).
- [4] B. Fang, et al., Nat. Commun., 7, 11259 (2016).
- [5] L. Zhang, et al., Appl. Phys. Lett., 113, 102401 (2018).
- [6] B. Fang, et al., Phys. Rev. Appl., 11, 014022 (2019).
- [7] R. Tomasello, et al., Phys. Rev. Applied, 14, 024043 (2020).
- [8] G. Finocchio, et al., Appl. Phys. Lett., 118, 160502 (2021).
- [9] A. Hafarov, O. Prokopenko, S. Sidorenko, D. Makarov, and I. Vladymyrskyi, NATO Science for Peace and Security Series B: Physics and Biophysics. Dordrecht: Springer, 2020.
- [10] I. Fantych, V. Prokopenko, and O. Prokopenko, NATO Science for Peace and Security Series B: Physics and Biophysics, Eds. Dodrecht: Springer, 2024.
- [11] A. Slavin and V. Tiberkevich, IEEE Trans. Magn., 45, 1875–1918 (2009).

CURRENT-INDUCED SWITCHING OF INTERLAYER EXCHANGE IN SPIN VALVES AT ROOM TEMPERATURE

O. Kozlov¹, S.Reshetniak¹, A.Kravets^{2,3}, V. Korenivski^{2,3} and V. Kalita¹

¹National Technical University of Ukraine "Igor Sikorsky Kyiv Polytechnic Institute", Kyiv, 03056, Ukraine

² Institute of Magnetism, NASU and MESU, Kyiv, 03142, Ukraine ³ Nanostructure Physics, Royal Institute of Technology, Stockholm, 10691, Sweden

We have demonstrated current-induced switching between a low-resistance state and a high-resistance state in Fe/Cr/Fe_{17.5}Cr_{82.5}/Cr/Fe multilayer structures, where the switching mechanism is driven by Joule heating. The Fe concentration in the FeCr alloy was carefully optimized at 17.5% [1], setting its Curie temperature near 325 K, so that minimal Joule heating from a low current is sufficient to induce switching]. Additionally, the layer thicknesses were configured ($d_{Fe} = 2$ nm, $d_{Cr} =$ 0.4 nm, $d_{FeCr} = 0.9 \text{ nm}$) to enable direct exchange ferromagnetic coupling between the outer Fe layers when FeCr is in its ferromagnetic state, while producing an RKKY-mediated antiferromagnetic coupling when FeCr transitions to the paramagnetic state.

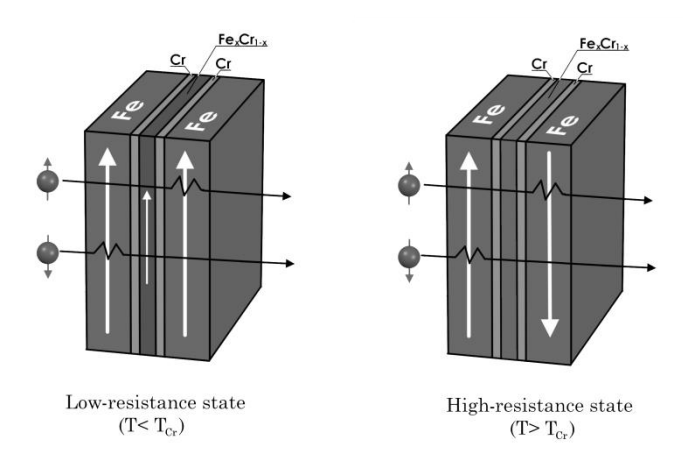


Fig.1. Schematics of the spin-dependent electron transport through Fe/Cr/Fe_{17.5}Cr_{82.5}/Cr/Fe

These findings provide a pathway towards tunable, current-controlled, zero-bias-field coupling between magnetic layers, which could be instrumental in enhancing thermally assisted magnetic memories or expanding the dynamic range of spintronic oscillators and detectors.

An analytical model was also developed based on the minimization of the structure's energy, allowing certain system parameters, such as magnetic anisotropy of the layers or exchange constants between layers, to be determined from magnetization loops.

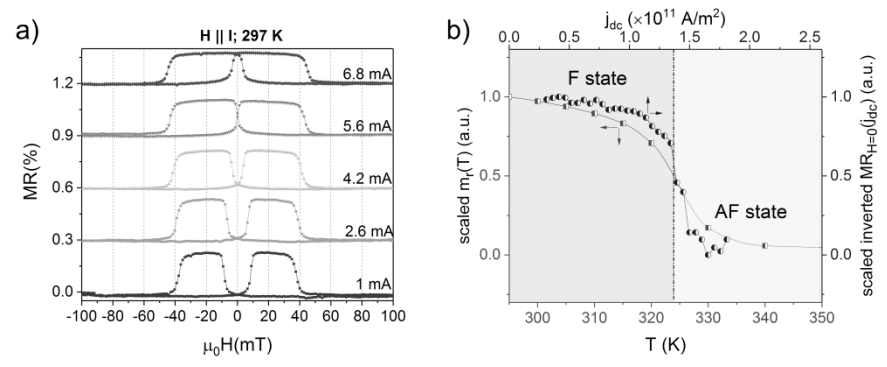


Fig 2. (a) Typical magnetoresistance loops measured on the 8 μ m wide stripe for H \parallel Idc and for the different values of the bias current injected into the device. The loops are vertically offset by 0.3%. (b) Remanent magnetic moment vs. temperature superimposed onto the inverted zero-field magnetoresistance vs. current density for 8 μ m wide stripe. Both quantities are scaled to the [0;1] range for better visualization

^[1] Polishchuk, D.M. et al. (2017) 'Thermally induced antiferromagnetic exchange in magnetic multilayers', Physical Review B, 96(10).

^[2] Iurchuk, V. et al. (2023) 'All-electrical operation of a Curie switch at room temperature', Physical Review Applied, 20(2).

^[3] Sorokin, S. et al. (2020) 'Magnetization dynamics in synthetic antiferromagnets: Role of Dynamical Energy and mutual spin pumping', Physical Review B, 101(14). doi:10.1103/physrevb.101.144410.

EIGENOSCILLATIONS OF THE NON-UNIFORM SPIN TEXTURE IN A TWO-SUBLATTICE ANTIFERROMAGNET WITH THE DZYALOSHINSKII-MORIYA INTERACTION

V. S. Gerasimchuk¹, <u>I. V. Gerasimchuk^{2,1}</u>

¹National Technical University of Ukraine "Igor Sikorsky Kyiv Polytechnic Institute", Kyiv, 03056, Ukraine

²V.G. Baryakhtar Institute of Magnetism of the NAS of Ukraine, Kyiv, 03142, Ukraine

Topological spin textures, which are variations of magnetization, confined and interrelated in a magnetic volume, are of considerable fundamental and applied interest. They hold great promise as information carriers for magnonics and spintronics (and skyrmion-electronics) devices [1,2]. There are reasons to believe that the best chances for this are antiferromagnets (AFM) with perpendicular magnetic anisotropy, in which spin textures are realized even at room temperature and zero external magnetic fields [3,4]. A special role is played by the exchangerelativistic Dzyaloshinskii-Moriya interaction (DMI), which can induce longperiod spiral textures in magnets devoid of inversion symmetry, forming chiral structures [5] and magnetic skyrmions [1,2,6].

AFMs with uniaxial magnetic anisotropy and DMI demonstrate a great variety of topological structures. Thus, the analytical model [7] describes a variety of skyrmion-like topological objects in nanorings and cylindrical nanoshells. In this regard, axisymmetric target skyrmions, spin configurations with a multi-ring structure and continuous rotation of the z-component of the magnetization, attract attention [8,9]. Spin textures, and primarily target skyrmions, usually represented as 2D topological solitons, in real systems, have a 3D spatial configuration, which are nanoscale cylinders [10,11].

Skyrmions exhibit several well-known dynamic regimes, among them are breathing modes when the skyrmion radius changes, and rotational modes when the position of the skyrmion core fluctuates. Various combinations of these modes and transitions between them, as well as inertial dynamics [12], can take place. In a collinear uniaxial AFM, the AFM skyrmion has a discrete spectrum of bound eigenstates. The spectrum can have several branches [13], including radially symmetrical mode. In thin AFM disks, the skyrmion exhibits oscillatory dynamics with well-defined amplitude and frequency, which can be controlled by a spinpolarized current if necessary. We emphasize the problems related to the determination of the effective mass of the skyrmion [14,15].

Oscillations of the localized ring configuration of magnetization in AFM with perpendicular magnetic anisotropy, in the absence of DMI and external fields, were studied by the authors of [16]. The main characteristics of the oscillatory process and the mass of the spin texture were determined. It should be recognized that the real oscillations of non-uniform spin textures, which take into account the inhomogeneous distribution of the density of inertial masses of solitons, have not been sufficiently studied in the literature. The oscillations of spin textures as a physical process have not practically been discussed before.

In the present work, we analytically study eigenoscillations of the topological spin texture in a two-sublattice AFM with DMI [17]. Using the solution of the Landau-Lifshitz equations, we calculate the surface energy density and surface mass density of the 3D topological spin texture as functions of the spin isosurface radius. Considering the inhomogeneity of the magnetization distribution, we derive the equation of free oscillations of the topological spin texture magnetization, which describes the natural physical process of oscillations, excited in a spin texture in one way or another. The analytical study of the spin texture dynamics for 3D solutions of the Landau–Lifshitz equations turns out to be possible to reduce to an equation of the wave equation type with variable coefficients. A boundary value problem of eigenexcitations of the thin axisymmetric circular nanoscale spin configuration is formulated, the solution of which allows us to determine the main dynamical characteristics, including the total oscillation energy, frequency and relative amplitude of oscillations. The topological and inertial masses of such axisymmetric circular spin configuration are determined. We convincingly show that the AFM spin texture of the target skyrmion type supports its own spin excitation modes, in which it can be by virtue of its inherent intrinsic nature.

Comparing the axisymmetric radial oscillations of the spin texture analytically studied by us with the magnetization configuration in a skyrmion tube studied through micromagnetic simulations [18], we find a close match, since both in our case and in a skyrmion tube preserves the radial symmetry, the excitation of the rotational modes is prohibited and only the breathing mode is permitted. In this case, our solution as well as the spin-wave propagation patterns exhibit the character of standing waves [18].

Note that if we consider the spatial profile of the spin texture in the direction of its symmetry axis, the oscillation process looks exactly like radial pulsations of the texture. Perhaps it is this process, i.e., the behavior of the breathing mode (its natural frequency of oscillations) that the authors of [19] consider as a consequence of the change in the skyrmion radius. In addition, they found [19] that the

oscillation frequency is directly related to the total energy of the system that also takes place in our case.

Our results can be useful for understanding the fundamental principles of the physics of magnetism, in particular, for understanding the nature of non-uniform spatial distributions of magnetization and their physical properties.

- [1] F. Büttner, I. Lemesh and G. S. D. Beach, Sci. Rep. **8**, 4464 (2018).
- [2] X. Zhang et al., J. Phys.: Condens. Matter **32**, 143001 (2020).
- [3] P. Ho et al., Phys. Rev. Applied **11**, 024064 (2019).
- [4] V. S. Gerasimchuk, Zh. Eksp. Teor. Fiz. 101, 1360 (1992).
- [5] V. G. Bar'yakhtar, E. P. Stefanovskii, D. A. Yablonskii, Fiz. Nizk. Temp. 1, 919 (1975).
- [6] S. Jaiswal et al., Appl. Phys. Lett. 111, 022409 (2017).
- [7] O. Yu. Gorobets, Yu. I. Gorobets, J. Magn. Magn. Mater. 507, 166800 (2020).
- [8] F. Zheng et al., Phys. Rev. Lett. 119, 197205 (2017).
- [9] Y. Zhang et al., Nano Lett. 23, 10205 (2023).
- [10] S. Seki et al., Nat. Commun. 11, 256 (2020).
- [11] F. Zheng at al., Nature **623**, 718 (2023).
- [12] F. Büttner et al., Nat. Phys. 11, 225 (2015).
- [13] V. P. Kravchuk et al., Phys. Rev. B 99, 184429 (2019).
- [14] V. P. Kravchuk et al., Phys. Rev. B 97, 064403 (2018).
- [15] X. Wu and O. Tchernyshyov, SciPost Phys. 12, 159 (2022).
- [16] V. S. Gerasimchuk, Yu. I. Gorobets, O. Yu. Gorobets and I. V. Gerasimchuk, Sci. Rep. **13**, 6613 (2023).
- [17] V. S. Gerasimchuk and I. V. Gerasimchuk, Low Temp. Phys. 51, 1023 (2025).
- [18] X. Xing, Y. Zhou, and H. B. Braun, Phys. Rev. Applied 13, 034051 (2020).
- [19] F. Tejo, F. Velozo, R. G. Elías and J. Escrig, Sci. Rep. 10, 16517 (2020).

RADIAL MAGNETIC VORTICES IN MULTILAYERED NANOPILLARS (INVITED)

M. Moalic 1 , R.V. Verba 2 , S.A. Bunyaev 3 , K.Y. Guslienko 4,5 , M. Krawczyk 1 , G.N.Kakazei 3

¹Institute of Spintronics and Quantum Information, Faculty of Physics, Adam Mickiewicz University in Poznan, Poznan, Poland

²V. G. Baryakhtar Institute of Magnetism of the National Academy of Science of Ukraine, Kyiv, Ukraine

³IFIMUP/Department of Physics and Astronomy, Faculty of Sciences, University of Porto, Porto, Portugal

⁴Departamento de Polímeros y Materiales Avanzados, Universidad del País Vasco, UPV/EHU, San Sebastián, Spain

⁵IKERBASQUE, the Basque Foundation for Science, Bilbao, Spain

Magnetic vortices, renowned for their topologically nontrivial states, hold potential in applications such as spin-transfer torque oscillators (STTO) and magnetic memory. Most studies focus on Bloch magnetic vortices in sub-micron ferromagnetic disks with thicknesses above 10 nm. Recently we have demonstrated the possibility to obtain a vortex state in a hybrid structure (see Fig. 1) where a soft (SL) magnetic nanodisk ($t_d \le 5$ nm) was placed inside a hole in a hard magnetic layer (HL) with perpendicular magnetization [1-3]. The diameter of soft disk d_d is slightly smaller than the one of hole d_{ad} , providing purely dipolar coupling between subsystems. Micromagnetic simulations and analytical calculations revealed that the ground magnetic state of soft nanodisk could be either a radial (Neel) vortex or a mixture of Neel and Bloch vortices - depending on the strength of dipolar field from HL, that is proportional to its magnetization $M_{\rm HL}$ and thickness (typically 20 nm $\le t_{\rm HL} \le 40$ nm).

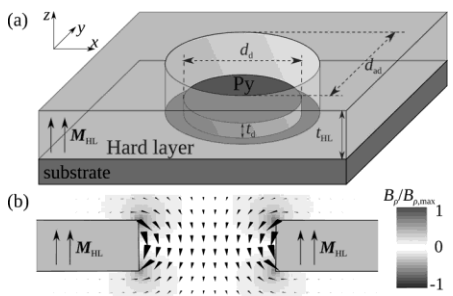


Fig. 1. (a) Sketch of hybrid structure; (b) - Distribution of stray fields in the hole; arrow length corresponds to the field magnitude.

Here we propose much more practical structure for creating a radial vortex: a three-layered circular nanopillar, consisted of SL, non-magnetic spacer (NMS), and HL (see Fig. 2). The spacer goal is to prevents direct exchange coupling between SL and HL, so it can be as thin as 1 nm, which allows to use this structure as STTO. Micromagnetic simulations using MuMax3 (with 0.5 nm cell discretization) revealed that radial vortex states can appear in significantly smaller disks compared to single layer soft ferromagnetic disks. With $M_{\rm HL}$ = 1000 emu/cm³ (typical value for FePt) and $M_{\rm SL} = 810 \, {\rm emu/cm^3}$ (typical value for Permalloy), radial vortices were formed in 0.5 nm thick SL with diameter as small as 30 nm, significantly surpassing the limitations of Bloch vortices in isolated circular disks.

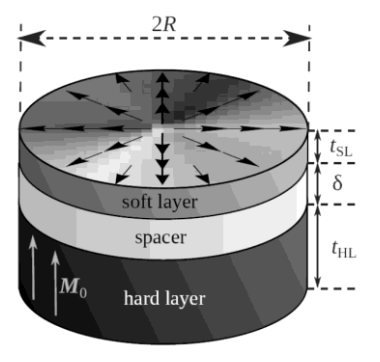


Fig. 1. Sketch of the proposed structure. Arrows demonstrate magnetization directions in soft and hard layers. In the absence of external magnetic field.

The magnetization dynamics was excited applying an in-plane microwave magnetic field with a sinc temporal profile on the SL, revealing a single intense peak corresponding to vortex core precession. The frequency is varying nonmonotonically with diameter (with a clear maximum around 2R = 50 nm for $Ni_{80}Fe_{20}$) and increasing with decrease of SL thickness, reaching 15 GHz for t_{SL} = 1 nm (if taking into account surface anisotropy of soft layer $K_{SL} = 3 \times 10^5$ erg/cm²). These findings align well with analytical predictions and allow to consider threelayered nanopillars HL/NMS/SL as next generation spin-torque nano-oscillators.

^[1] R.V. Verba, et al., Phys. Rev. Appl. 10, 031002 (2018).

^[2] R.V. Verba, et al., Phys. Rev. B 101, 064429 (2020)

^[3] S.A. Bunyaev, et al., Low Temp. Phys. **51**, 1017 (2025).

HYBRIDIZED EXCITATIONS IN A FERROMAGNETIC WIRE

O. V. Malyshev¹, V. Y. Malyshev¹, O. V. Prokopenko¹, G. A. Melkov¹
¹Taras Shevchenko National University of Kyiv, Kyiv, 01601, Ukraine

In contemporary physics, there is growing interest in hybridized excitations that emerge as a result of strong coupling between various types of collective modes. One such example is magnon-plasmon-polaritons – complex quasiparticles that combine magnonic, plasmonic, and electromagnetic components. Surface plasmon polaritons have been extensively studied in the optical and terahertz frequency ranges, where they have found widespread applications in nanophotonics, sensing, and spectroscopy [1-3]. However, the realization of analogous hybrid phenomena in the microwave regime remains a significant scientific challenge.

This work focuses on the formation of hybridized excitations in a ferromagnetic wire composed of an iron-nickel alloy with a predominant iron content. This material combines good electrical conductivity with pronounced ferromagnetic properties, making it suitable for the excitation and control of both magnonic and plasmonic modes. Under the application of an external magnetic field, such a structure allows for the observation of hybrid resonance effects arising from the interaction between surface electromagnetic waves and spin excitations [4].

The aim of this study is to investigate the conditions necessary for the formation of hybridized excitations in an FeNi-based ferromagnetic wire with dominant iron content, and to analyze the influence of external parameters on their resonant behavior. The obtained results may serve as a foundation for the development of novel functional components in magnonics and microwave electronics.

The studies were conducted in the X-band on an experimental setup, based on a standard scalar network analyzer R2-61 (Fig. 1). The electrodynamic system is based on a ferromagnetic surface electromagnetic wave resonator (FSEWR) made of ferromagnetic wire, located in a standard metal rectangular waveguide at a distance of 1 mm, parallel to its wide wall to achieve maximum interaction of hybridized oscillations [5] and equidistant from narrow walls, to maintain a significant Q-factor. The position inside the waveguide was provided by polystyrene foam, the presence of which inside the waveguide does not affect the distribution of the electromagnetic field. The sample section is located in a below-cutoff waveguide, which was formed as a result of rotating the standard waveguide

around its axis by an angle of 90 degrees. The electromagnetic wave of the fundamental mode H₁₀ of a regular waveguide cannot propagate in a below-cutoff waveguide, but the electric field can penetrate into its interior and excite the SEWR [6]. By changing the distance from the resonator to the waveguide junction, it is possible to regulate its coupling with the wave of the regular waveguide. This distance was chosen as optimal to ensure a subcritical coupling with a value close to the critical one. The sample section is located in the gap of the electromagnet, which provides a uniform constant magnetic field; the induction magnitude was determined by a pre-calibrated magnetic induction meter based on the Hall effect (SH1-8). The direction of the dc magnetic field coincides with the axis of the resonator to ensure maximum interaction and the emergence of hybridized oscillations [4]. The amplitude-frequency characteristics determined by a scalar network analyzer were digitized, accumulated, and averaged using a digital oscilloscope and transferred to a computer via cloud storage.

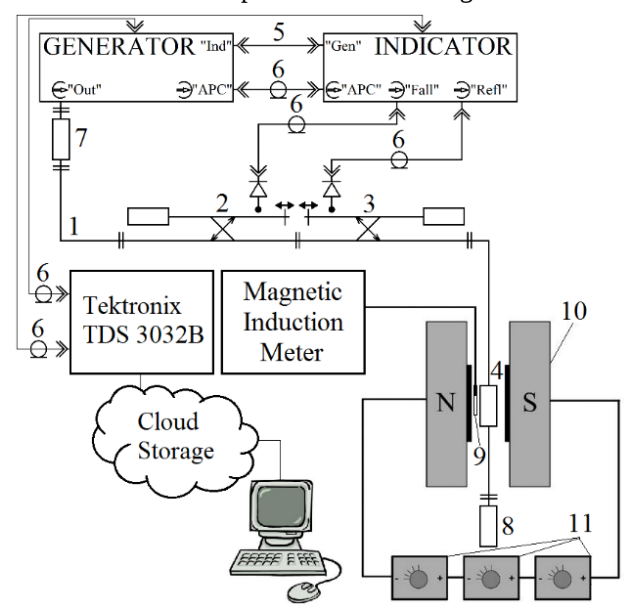


Fig. 1. Experimental setup based on network analyzer R2-61: coaxialwaveguide transition (1); directional coupler "Incident" (2); directional coupler "Reflected" (3); sample (4); bidirectional control cable (5); connecting coaxial cable HF (6); microwave coaxial cable (7); terminated load (8); Hall effect magnetic field sensor (9); electromagnet (10); electromagnet power supplies (11).

We experimentally investigate the excitation of hybridized oscillations in a ferromagnetic wire made of an iron-dominated FeNi alloy. We measure the dependence of the frequency shift and the change in the standing wave ratio (SWR) caused by the interaction of oscillations of different nature on the bias magnetic field. The wire is a natural resonant surface plasmon-polariton system, the so-called surface electromagnetic wave resonator [7]. In the absence of a bias magnetic field, the frequency of this resonance mainly depends on the length and diameter of the wire. However, in the presence of a bias magnetic field, magnons in the FeNi ferromagnetic wire are excited, and complex hybridized oscillations can be formed if the frequency of the magnons coincides with the frequency of the surface plasmon-polariton oscillations.

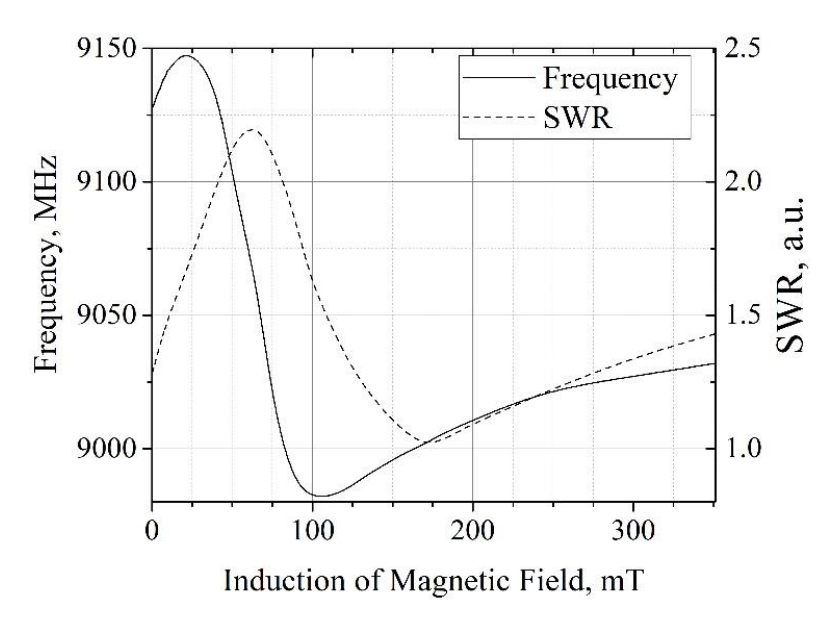


Fig. 2. Dependence of the frequency shift (solid line) and the change in the standing wave ratio (SWR) (dashed line) of the FSEWR under the action of an external induction of a constant magnetic field.

Figure 2 shows the experimental dependences of the resonant frequency and the standing wave coefficient in resonance under the action of an external uniform magnetic field. As can be seen from Figure 2, we observe a significant frequency shift of more than 160 MHz, which is more than 2 times higher than the frequency

shift on a ferromagnetic plate [6]. It is obvious that the efficiency of the interaction of surface waves with magnetization oscillations on a wire-shaped SEWR is much more effective than the similar interaction based on a ferromagnetic plate [5]. The most effective occurrence of hybridized oscillations is observed in a field with an induction value of 63 mT, which corresponds to the fastest change in the resonant frequency of the system and the maximum of the standing wave coefficient of 2.195, which corresponds to the minimum of the system's Q-factor, due to the most effective interaction, due to the absorption of the electromagnetic power of the system by the ferromagnetic medium of the resonator, effective excitation of magnetization oscillations. In a constant magnetic field with an induction value of about 172 mT, a minimum of the SWR is observed. This minimum is not a special point on the experimental dependence, but is the point of change in the type of coupling of the resonator with the electromagnetic wave from subcritical to supercritical coupling. The change in the coupling coefficient is observed due to a decrease in the inherent Q-factor of the SEWR due to a change in the efficiency of excitation of magnetization oscillations, and hence the formation of hybridized oscillations.

In conclusion, a wire-based FSEWR can have better frequency tuning than a plate-based resonator, which allows one to significantly expand the operating range of magnetically controlled filters and resonant devices. The large tuning of a wirebased FSEWR provides an ability to cover a wide spectrum of signals, quickly adapt to signals with altering frequencies and maintain a high selectivity. This can be especially useful for spectrum analyzers and broadband receivers, multi-channel radio terminals, tunable signal generators and tracking filters.

The work has been partly supported by the grant No. 25DF07-03 from the Ministry of Education and Science of Ukraine. The authors would like to thank all the brave defenders of Ukraine who made the finalization of this publication possible.

- [1] X. Zhang, et al., Adv. Photon. 2, 014001 (2020).
- [2] R.S. Anwar, H. Ning, L. Mao. Digit. Commun. Netw. 4, 244 (2018).
- [3] A.Korotun, Y.Karandas, V.Reva, Ukrainian Journal of Physics, 67(12), 849 (2023).
- [4] V.Yu. Malyshev, et al., Ukr. J. Phys., vol. 65, p. 939 (2020).
- [5] O.V. Malyshev, V.Yu. Malyshev, O.V. Prokopenko, IEEE 13th International Conference Nanomaterials: Applications & Properties (NAP). IEEE, p. 07nmm-22 (2023).
- [6] O.V. Malyshev, V.Yu. Malyshev, O.V. Prokopenko, IEEE 10th International Conference Nanomaterials: Applications & Properties (NAP). IEEE, p. 03NMM13-1 (2020).
- [7] G.A. Melkov, et al., J. Supercond. 13, 95 (2000).

QUANTUM MAGNONICS WITH PROPAGATING MAGNONS

A. V. Chumak¹

¹Faculty of Physics, University of Vienna, 1090 Austria

Quantum magnonics, a field that harnesses magnons (spin-wave quanta) for quantum technologies, holds great promise for the realisation of solid-state quantum technologies at the nanoscale. Yttrium iron garnet (YIG) is the material of choice due to its low magnon damping and efficient spin-wave propagation [1]. While ferromagnetic resonance (FMR) magnons have already been used for quantum magnonics studies [2,3], the transition from standing to propagating magnons is crucial for realising devices with spatially separated magnon sources and detectors [4]. Achieving this requires YIG films with long magnon lifetimes, usually grown on paramagnetic gadolinium gallium garnet (GGG) substrates [4-8].

In a series of experimental studies of magnon transport in YIG/GGG systems at temperatures down to tens of mK, we reveal a significant role of a stray field effect formed by the partially magnetised paramagnetic GGG substrate - see Fig. 1. This stray field opposes the applied biasing field, shifting the FMR frequency to lower frequencies [5], and could reach up to 40 mT in our studies. The determination of the GGG field allowed us to quantify the temperature dependent magnetic anisotropy in YIG/GGG, which increases threefold with decreasing temperature. Subsequent investigations of the FMR linewidth revealed an approximately tenfold increase in the Gilbert damping in YIG films on GGG with decreasing temperature. We show that the dominant physical mechanism (about 7 times) responsible for the FMR broadening in the non-uniform GGG field [6]. An approach to partially overcome the disturbance induced by the non-uniform GGG field, namely the etching of a smaller YIG structure in the central part of the GGG substrate, has been developed and tested [7]. Furthermore, at low temperatures and frequencies above 18 GHz, the FMR linewidth deviates from the viscous Gilbert model [6,7].

In order to understand the magnetic losses of propagating magnons in YIG/GGG, we have performed propagating spin wave spectroscopy (PSWS) measurements for temperatures between 4 K and 26 mK [8]. We show an increase in the dissipation rate with wavenumber at cryogenic temperatures, caused by dipolar coupling to the partially magnetised GGG substrate. In addition, we observe a temperature-dependent decrease in spin-wave transmission due to rare-earth ion relaxation mechanisms.

To isolate the intrinsic magnon properties of YIG without the influence of GGG, we studied YIG spheres with different impurity levels. Magnon lifetimes were

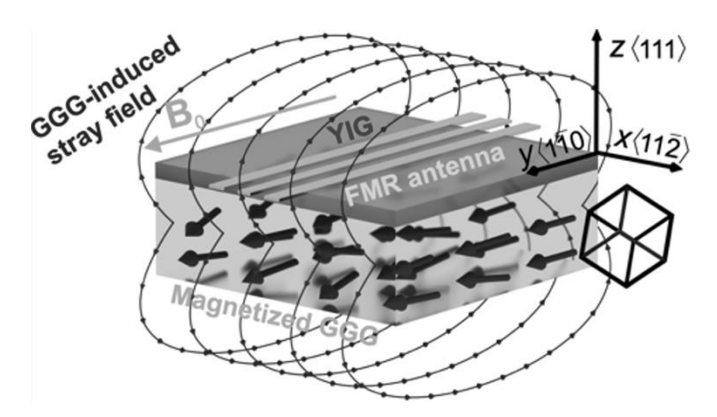


Fig. 1. Schematics of the stray field created by the Gadolinium Gallium Garnet (GGG) substrate at low temperature in the presence of an applied magnetic field.

measured, correlating with k=0 magnon modes and showing lifetimes on the order of up to 1 µs at mK temperatures. An intriguing result was obtained using a dedicated three-magnon splitting experiment at mK temperatures, which allowed us to measure the lifetimes of short-wavelength dipolar-exchange spin waves. Lifetimes reached values of up to 18 µs at a frequency of 1.7 GHz.

These results not only elucidate the factors influencing the magnon lifetimes in YIG and YIG/GGG systems, but also open new avenues towards the quantum devices with long-lived propagating magnons.

- [1] A. V. Chumak, et al., IEEE Trans. Magn. 58, 1 (2022).
- [2] D. Lachance-Quirion, et al., Science **367**, 425 (2020).
- [3] D. Xu, et al., Phys. Rev. Lett. **130**, 193603 (2023).
- [4] S. Knauer, et al., J. Appl. Phys. 133, 143905 (2023).
- [5] R. O. Serha, et al., npj Spintronics 2, 29 (2024).
- [6] R. O. Serha, et al., Mater. Today Quantum 5, 100025 (2025).
- [7] D. Schmoll, et al., Low Temp. Phys. **51**, 724 (2025).
- [8] D. Schmoll, et al., Phys. Rev. B 111, 134428 (2025).
- [9] R. O. Serha, et al., arXiv 2505.22773 (2025).

MAGNETIC TUNNEL JUNCTIONS: FERROMAGNETIC, SUPERPARAMAGNETIC, AND ANTIFERROMAGNETIC (INVITED)

S. A. Majetich¹

¹Carnegie Mellon University, Pittsburgh 15213, USA

Magnetic tunnel junctions (MTJs) are versatile devices that can be used for non-volatile information storage, due to their magnetically ordered layers, but can also be switched electrically and can be interfaced with existing silicon electronics.

After describing magnetic field switching of MTJs with ferromagnetic fixed and free layers, the three methods of electrical control are described. Voltage controlled magnetic anisotropy (VCMA) is used to reduce the perpendicular anisotropy, but switching is unidirectional [1] unless complex multilayers are used [2]. Spin transfer torque (STT) works for MTJs with either in-plane or perpendicular anisotropy, but requires high current densities (10⁶ A/cm²), making it difficult for single transistors to supply the power needed to switch individual MTJs. Spin orbit torque (SOT) is a lower power alternative, and has been used to switch MTJs as small as 20 nm in diameter [3]. However, this requires a three terminal device structure, more complex than a simple cross-bar geometry. Magnetic random access memory (MRAM) is a commercial product for niche applications, but adoption on a large scale for storage and logic requires low power consumption, magnetic field-free switching, and simple geometry.

For logic applications, one way to reduce power consumption is to use superparamagnetic tunnel junctions (SP-MTJs). Interacting nanomagnets with low thermal stability have been proposed for probabilistic computing, which has potential uses in low power sensing and logic, encryption and decryption, and integer factorization. The similarities and differences between superparamagnetic nanoparticles and electronically controlled superparamagnetic tunnel junctions will be reviewed, including a comparison of the Stoner-Wohlfarth asteroid and its tunnel junction equivalent. Next the differences between deterministic and probabilistic logic will be discussed. Boltzmann machines based on interacting spins, and how they achieve the lowest energy states with greatest statistical probability are described. By controlling the interaction strengths, probabilistic logic gates can be realized. Superparamagnetic tunnel junctions (SP-MTJs) are an ideal type of nanomagnet because their time-averaged magnetization of the free layer can be programmed with a voltage or current [4, 5]. Fabrication of hardwired magnetic tunnel junctions (MTJs) and incorporation in hybrid CMOS circuits are described. Experimental results for two example logic gates will be

discussed: first the simple NOT gate formed from two coupled MTJs, and then a more complex AND gate made from three coupled MTJs. The feedback for the NOT gate leads to very high anti-correlations (~95%) and is nearly deterministic in behavior. With the AND gate, we start with a theoretical discussion of the feedback weightings, and corresponding Boltzmann factors for the probabilities of different microstates. The effect of pinning the output on invertibility of the logic gates is shown in terms of energy levels and probabilities. While this approach is promising, there are significant challenges due to the need to prepare arrays of SP-MTJs with identical feedback behavior. In addition, the need to wire each one individually makes the two-terminal approach of STT much easier than the lower power SOT control. Possibilities to get around these barrriers using reservoir computing are discussed.

Finally, the possible use of antiferromagnets in tunnel junctions (AFTJs) is described. Here there are potential advantages in achieving higher density and faster switching than with MTJs, but readout is difficult. The anomalous Hall effect and spin Hall effect can be used to determine the direction of the Néel vector in an antiferromagnet, but the signals are very weak. Preliminary results using tunnel magnetoresistance indicate a larger signal is feasible, but the development of antiferromagnetic spintronic devices is still at an early stage.

- [1] S. K. Piotrowski, et al., Phys. Rev. B 94, 014404 (2016).
- [2] D. Zhang, et al., Nano Letters 22, 622 (2022).
- [3] M. Bapna, et al., Phys. Rev. Applied 10, 024013 (2018).
- [4] M. Bapna and S. A. Majetich, Applied Physics Letters 111, 243107 (2017).
- [5] B. Parks, et al., Phys. Rev. Applied 13, 014063 (2020).

SECTION VI. FUNCTIONAL MAGNETIC MATERIALS

MAGNETIC ANISOTROPY AND TEMPERATURE-DEPENDENT PROPERTIES OF AL-DOPED YIG CERAMICS

V. Borvnskyi¹, D. Popadiuk², A. Kravets², Y. Shlapa³, S. Solopan³, V. Korenivski², A. Belous³, A. Tovstolytkin¹

- ¹ V.G. Baryakhtar Institute of Magnetism of the NAS of Ukraine. Akad. Vernadskogo blvd. 36-b, Kyiv-03142, Ukraine.
- ² Nanostructure physics, Royal Institute of Technology. Hannes Alfvénsväg 12, Stockholm-10691, Sweden.
 - ³ V.I. Vernadsky Institute of General and Inorganic Chemistry of the NAS of Ukraine. Palladina ave. 32/34, Kyiv-03142, Ukraine.

Since the mid-20th century, yttrium iron garnet (YIG) has stood out as a foundational material in the advancement of different technologies. Its unique combination of superior physical properties - low magnetic damping, excellent dielectric behavior, good magneto-optical activity, and robust chemical stability make it indispensable for applications in telecommunications, microwave circuits, magneto-optics and magnonics [1]. The complex crystal structure of a garnet offers a convenient path for further adjusting garnet's magnetic and microwave performance via cation substitution.

As emerging technologies impose more rigorous requirements on functional materials, the demand for modified garnet systems is growing. Cation substitution with various dopants, such as Ni, Mn, Co, Sm, Gd, allows for optimization of key parameters, namely permittivity, saturation magnetization, and coercivity. Among these materials, aluminum-doped yttrium iron garnet (Y3AlFe4O12; YAIG) has received increasing attention for its potential to exceed limitations of conventional YIG. Recent studies suggest the need for higher dielectric constant and ultralow coercive fields, less than 10 Oe. While YAIG shows promise in meeting the former demand, its magnetic anisotropy remains insufficiently studied. We address this gap by analyzing a series of YAIG ceramic samples, synthesized via coprecipitation and sintering, as elaborated in [2].

Magnetic hysteresis loops revealed soft coercive behavior, typical for ferrimagnets materials with cubic symmetry. At low temperatures, the coercive field peaked at 57 Oe, which is higher than that of a typical undoped YIG (~40 Oe). However, room temperature values of coercivity are reduced to approximately 3 Oe. To separate the effective anisotropy term from other contributions, we employed the Law of Approach to Saturation (LAS), fitting the saturation region of the hysteresis loops, Fig. 1(a).

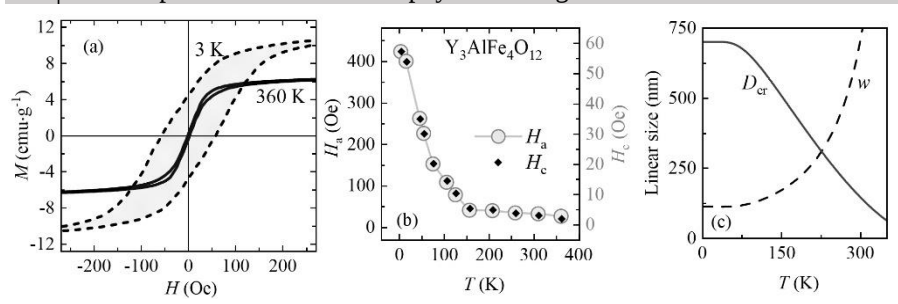


Fig. 1. (a) Hysteresis loops of YAIG ceramic sample at 360 K and 3 K. (b) Comparison between coercivity and anisotropy field, extracted using LAS. (c) Critical single-domain size and domain wall width for YAIG ceramics.

Extracted in this way effective anisotropy constant $K_{\rm eff}$ and its corresponding field $H_{\rm a}$, shown in Panel (b), exhibit a steep temperature trend with an exponential-like decay, resembling that of the coercive field. At room temperature, the anisotropy field $H_{\rm a}$ is about 33 Oe in YAIG as opposed to 87 Oe of a pure YIG. These observations indicate that the effective anisotropy – tunable through doping and arising from the averaged contributions of individual crystal grains – plays a key role in governing the coercive behavior of the fabricated ceramics. Consequently, incorporating non-magnetic dopants like Al is a promising strategy for minimizing hysteresis in low-field switching applications.

Using the Brillouin-Weiss model adapted for doped garnet systems [3], the temperature changes in the magnetization, associated with a non-uniform substitution of Al ions between tetrahedral and octahedral sites in YIG, were successfully captured. Furthermore, we determined the characteristic sizes for the fabricated ceramics, Panel (c). As can be seen, the critical single-domain size drops at room temperature to about 150 nm, which is comparable to the typical size observed in YIG nanoparticles. Knowledge on temperature variation of these parameters is crucial for integration of substituted garnets in nanoscale technology.

Our study provides a detailed characterization of temperature-dependent magnetic properties in YAIG, relevant for design and tuning of substituted garnets in novel magnonic or microwave devices. These findings open avenues for engineering magnetic ceramics with improved switching performance to meet evolving technological demands.

^[1] V. Harris, Modern Ferrites: Emerging Technologies and Applications (Wiley, 2022).

^[2] V. Borynskyi, et al., J. Alloys Compd. **1010**, 178320 (2024).

^[3] G. F. Dionne, J. Appl. Phys. 41, 4874 (1970).

CONTROLLABLE SYNTHESIS AND CHARACTERIZATION OF Fe₃O₄/Au COMPOSITES FOR MAGNETO-PLASMONIC APPLICATIONS

O. Kapush¹, B. Shanina¹, A. Konchits¹, N. Mazur ¹, V. Dzhagan¹, I. Vorona¹, L. Mikoliunaite², G. Zambzickaite², M. Talaikis², M. Skoryk³, Yukhymchuk V.¹

¹V. Lashkaryov Institute of Semiconductors Physics, NAS of Ukraine, Kyiv, 03028, Ukraine.

² Faculty of Chemistry and Geosciences, Vilnius University and Center for Physical Sciences and Technology, Vilnius, LT-01513 Lithuania

The Fe₃O₄ and Fe₃O₄/Au nanoparticles synthesized by means of colloidal chemistry have been intensively investigated in the past decade for numerous applications. In particular, it is a powerful tool in the Surface-Enhanced Raman spectroscopy (SERS) [1], catalysis [2], hyperthermia-based treatment of tumors [3], and targeted delivery of drugs [4]. Due to the biocompatibility of Fe₃O₄ and Au, they are considered for both therapeutic and diagnostic applications, which is not only beneficial for precise early diagnosis of diseases but also makes it easier to monitor the drug fate and evaluate treatment effect.

Synthesis of Fe₃O₄ magnetic nanoparticles was performed by co-precipitation of ferric and ferrous salts without the presence of N2 gas. The experimental apparatus for performing the chemical synthesis is shown in Fig. 1a.

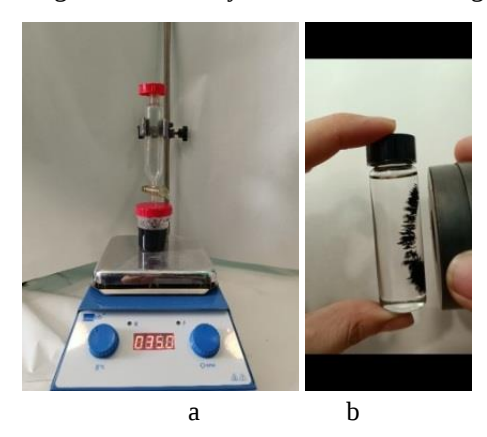


Figure 1. Apparatus for reaction (a) and the prepared Fe₃O₄ nanoparticles (b).

At high concentration, the Fe₃O₄ nanoparticles could form a magnetic fluid as shown in Figure 1b. The magnetic fluid remained stable after being stored in the air for a long time, providing the basis for its further use in the next preparation of

core-shell structure composites. Gold nanoparticles on the surface of Fe₃O₄ NPs were synthesized by citrate reduction of hydrogen tetrachloroaurate (III) trihydrate solution mixed with trisodium citrate in the presence of previously synthesized Fe₃O₄ NPs.

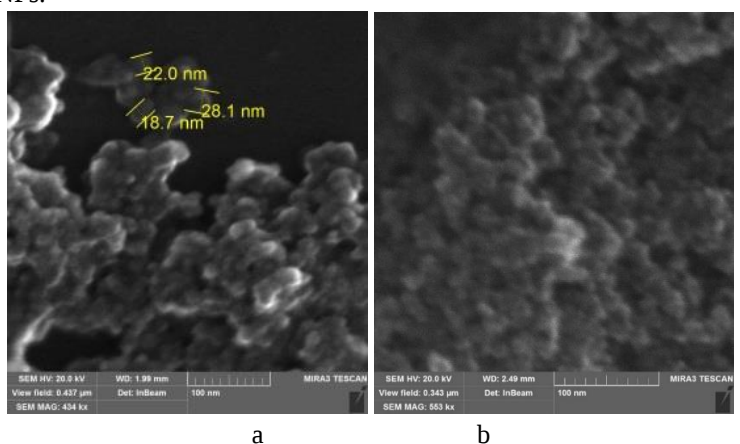


Figure 2. SEM images of the Fe₃O₄ NPs (a) and Fe₃O₄/Au NPs (b).

Figure 2 shows the SEM image of the Fe₃O₄ NPs (a) and Fe₃O₄/Au NPs (b), from which we can conclude that the material is obtained in the form of nanoparticles with an average size of about 20-30 nm. The strong aggregation of the NPs may be an inherent consequence of the magnetic properties; however, it can also be related to the surface passivation resulting from the synthesis. The optical absorption spectra of Fe₃O₄/Au NPs do not exhibit characteristic absorption bands related to localized surface plasmon resonance (LSPR), which is observed for Au NPs synthesized separately, presumably due to the influence of the magnetic oxide part. Raman spectroscopy study proves that the obtained material is magnetite (Fe₃O₄) without noticeable admixture of another stable iron oxide form, hematite (Fe₂O₃). The NPs also revealed very good oxidation resistance during long-term storage (about for 4 months), as well as identical Raman spectra were measured (not shown) on the NP solution, and the dry NP film prepared from it. The established good stability of Fe₃O₄ nanoparticles obtained using a simple and scalable wet chemistry approach is a strong argument in favor of their practical application.

The magnetic properties of Fe_3O_4 NPs and Fe_3O_4/Au NPs in this work were studied by Electron Paramagnetic Resonance (EPR) method. Here, the case of the high concentration of Fe_3O_4 in aqueous solution, and the spectrum changes caused

by the addition of Au NPs to aqueous solution or the process of Fe₃O₄ NPs formation are considered. Figures 3a and 3b show the EPR spectra of Fe₃O₄ and Fe₃O₄/Au nanoparticles in aqueous solution and their simulation.

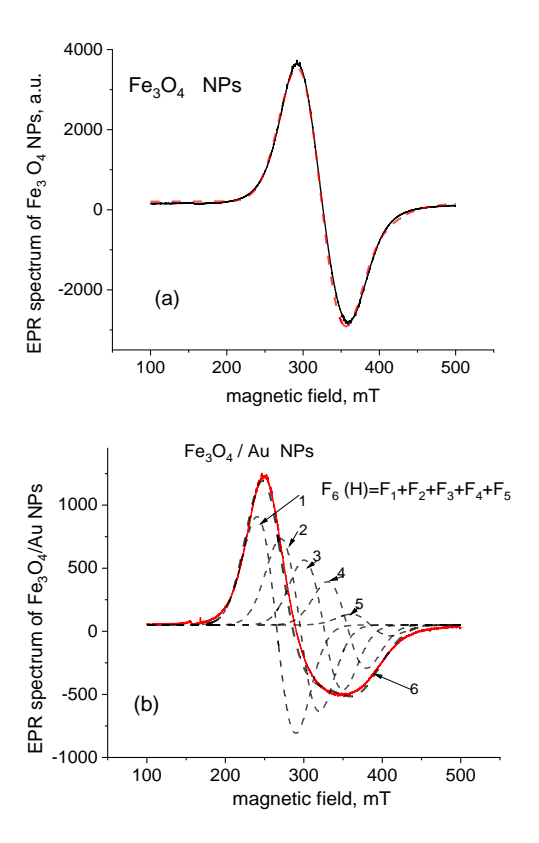


Figure 3. Spectra of the derivative of absorption of the microwave power by the system of Fe₃O₄ NPs produced in different conditions: (a) NP of Fe₃O₄ in aqueous solution, homogeneous system; solid black line is the experimental curve; dashed red line is the theoretical function. (b) Fe₃O₄/Au NPs in aqueous solution; the solid line is the experimental curve; the black dashed line is the calculated spectrum. The numbered dashed lines are five components of the spectrum.

The EPR spectra of the Fe₃O₄ NPs can be fit with a single component, while the line shape of the Fe₃O₄/Au NPs is significantly different and requires up to five components. Based on the developed theoretical model, we relate these components to the contribution of NPs with different sizes.

The results obtained indicate the presence of five sub-ensembles of the Fe₃O₄/Au NPs, which have different volumes and the magnetic moments of the Fe₃O₄ part. The maximum shift of the resonance field is characterized by the value $<\!H_A\!> + <\!H_{dem}\!> = 265$ mT and H_T =kT/ μ =15 mT. Here $<\!H_A\!>$ and $<\!H_{dem}\!>$ are the magnetic anisotropy field and the demagnetizing field, respectively. From value H_T follows $\mu = 3\times 10^4~\mu_B$, and the volume of nanoparticles in this group is equal to the volume of 540 cells. The size of NPs in this group is equal to 9.4 nm.

Such a pronounced difference between the EPR spectra of Fe_3O_4 and Fe_3O_4/Au NPs can be due to the effect of Au on the free charge carriers in the Fe_3O_4 part. This effect is size-dependent because it leads to size-dependent EPR spectra, which are not observed for bare Fe_3O_4 NPs (without Au part).

This project was supported by Research Council of Lithuania and Ministry of Education and Science of Ukraine, agreement no. S-LU-24-9 "Exploring magnetoplasmonic interactions in Fe $_3$ O $_4$ /Au (Ag) nanoparticles for multifunctional SERS applications".

- [1] S.-Y. Han et al., J. Colloid and Interface Sci. 378 51–57 (2012).
- [2] E.K. Fodjo et al., Chemistry Central Journal. 11, 58 (2017).
- [3] E. Cazares-Cortes et al., Advanced Drug Delivery Reviews. 138, 233-246 (2019).
- [4] N.S. Elbialy, M.M. Fathy, W.M. Khalil, Int. J. Pharm. 490 (1-2) 190-199 (2015).

NOVEL PRESS-FREE NANOCRYSTALLINE SOFT MAGNETIC COMPOSITES WITH A PORTLAND CEMENT BINDER FOR HIGH-TEMPERATURE APPLICATIONS

B. S. Baitaliuk, I. K. Yevlash, A. V. Nosenko, O. M. Semyrga, V. K. Nosenko G. V. Kurdyumov Institute for Metal Physics of the N.A.S. of Ukraine, Kviv, 03142, Ukraine

The continuous advancement of power electronics, particularly in mediumfrequency applications (10–200 kHz), demands soft magnetic composites (SMCs) with superior performance characteristics, including low core losses, stable permeability, and high thermal stability [1]. While modern SMCs based on amorphous and nanocrystalline alloy powders offer significant potential, their widespread adoption is hindered by fundamental manufacturing challenges [2]. These advanced powders exhibit exceptionally high yield strength and hardness, making them notoriously difficult to compact [3]. Achieving a high magnetic filling factor (MFF) necessitates the application of extreme pressures, often exceeding 1 GPa, which complicates the manufacturing technology, dramatically increases equipment costs, and limits the geometric complexity of the final components.

A second critical limitation of conventional SMCs is the poor thermal stability of the organic binders typically used to insulate the magnetic particles and provide mechanical strength [4]. Binders such as epoxy resins and silicone-organic varnishes generally restrict the maximum operating temperature of the cores to 100–120°C [5]. Exceeding this limit leads to binder degradation, which adversely affects magnetic properties, increases core losses, and compromises the long-term reliability of the device. These thermal constraints significantly limit the use of SMCs in high-power-density converters and other applications operating in harsh thermal environments.

This work introduces a novel approach that overcomes both of these longstanding challenges by fundamentally altering the manufacturing paradigm. We report the successful fabrication of toroidal SMCs using a powder of the nanocrystalline Fe73Si16B7Nb3Cu1 alloy (Finemet type) with an inorganic Portland cement binder. Crucially, the entire fabrication process is conducted without any high-pressure compaction. This press-free method represents a significant departure from traditional powder metallurgy, shifting from a capital-intensive, high-energy compaction route to a simple, low-energy, castable process. This simplification not only reduces manufacturing costs but also enables a far greater

diversification of core shapes and sizes, which is unachievable with conventional die pressing.

The nanocrystalline powder was produced by mechanical milling of a previously annealed amorphous ribbon of the nanocrystalline alloy in a ball mill. The resulting powder is polydisperse, with approximately 90% of the particles having a size less than 315 µm, and exhibits a characteristic shard-like morphology. The composite cores were fabricated through a remarkably simple procedure: 80 wt.% of the nanocrystalline powder was mixed with 20 wt.% of Portland cement ("CEM I" grade), after which water was added to initiate hydration. The resulting slurry was poured into silicone molds and allowed to harden at room temperature for 24 hours. This process yields mechanically robust cores with a ferromagnetic filling factor of approximately 0.31–0.33.

The magnetic properties of the resulting cement-bonded composites were comprehensively characterized and compared against several high-performance industrial cores based on Sendust, Molybdenum Permalloy Powder (MPP), Hi-FluxTM, and FluxSanTM alloys [6]. In a direct current (DC) magnetic field, the new composites exhibit highly linear magnetization curves and a stable relative magnetic permeability of approximately 28–29, which is comparable to the industrial Sendust-based core and establishes a baseline of excellent performance.

However, the most significant advantages of the novel material become apparent in its alternating current (AC) characteristics, particularly regarding core losses, which are a critical parameter for power applications. At a frequency of 10 kHz and a magnetic induction of 0.1 T, the cement-bonded cores exhibit total core losses of only $64.7–67.6~\text{mW/cm}^3$. This performance is not merely competitive but represents a substantial improvement over existing technologies. A direct comparison reveals that the core losses of the new composites are 30% to 80% lower than those of the benchmarked industrial materials under identical measurement conditions. The FluxSanTM core, for instance, exhibits losses of 175.5 mW/cm³, nearly three times higher than our cement-bonded sample.

This dramatic reduction in core losses, achieved despite a relatively modest MFF, points to the unique nature of the composite's internal structure. In conventional high-pressure manufacturing, the compaction process can damage the thin insulating layers surrounding the magnetic particles and induce significant internal mechanical stresses. Damaged insulation creates pathways for eddy currents, while internal stress increases hysteresis losses. The press-free, cement-based method avoids these issues entirely. The Portland cement does not merely act as a glue; it forms a continuous, robust, and relatively thick inorganic insulating matrix that completely encapsulates each magnetic particle. Because no pressure is

applied, this insulating network remains pristine and undamaged, effectively suppressing eddy currents. Furthermore, the absence of compaction results in a final composite that is almost entirely free of the internal mechanical stresses that plague pressed cores, leading to a significant reduction in hysteresis losses. This combination of superior particle insulation and a stress-free state is the primary reason for the observed low core losses.

Beyond its superior magnetic performance at room temperature, the most transformative property of the cement-bonded composite is its exceptional thermal stability, which far exceeds that of any SMC utilizing organic binders [7]. The temperature dependence of the effective magnetic permeability was investigated during continuous heating up to 300°C. As shown in Fig. 1, the permeability of the cement-bonded cores remains remarkably stable, exhibiting its maximum stability in the range of 20-200°C. Even at 300°C, a temperature at which all organic binders would have completely failed, the permeability decreases by only 3.5% from its room temperature value.

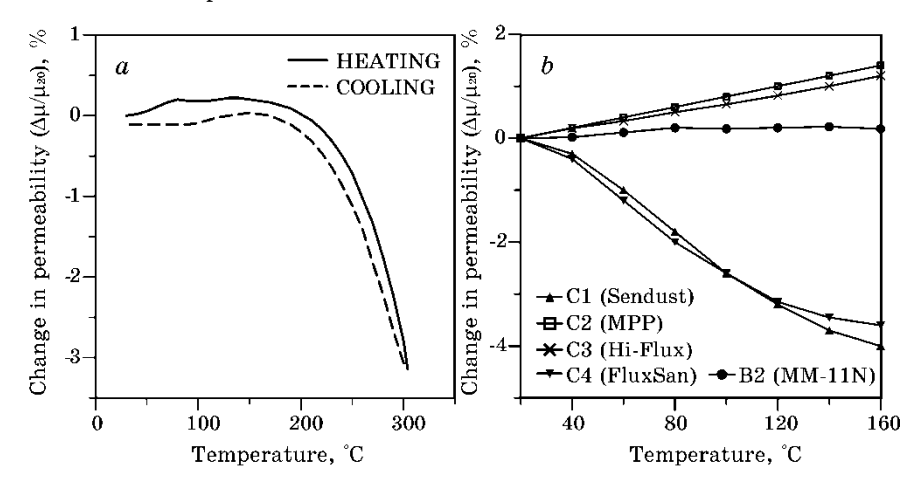


Fig. 1. Dependence of $\Delta \mu/\mu 20$ on temperature for nanocrystalline cores with cement binder.

To further assess their high-temperature resilience, the cores were subjected to sequential heat treatments at 300°C and 500°C for 30 minutes each. After cooling to room temperature, the cores retained their full mechanical integrity and their magnetic properties remained stable. Core losses after the 500°C anneal were nearly unchanged from their initial values. In stark contrast, the permeability of the industrial cores changed by approximately 20% after annealing at just 300°C. This instability is attributed to the relief of internal stresses induced during the high-

pressure manufacturing stage — stresses that are inherently absent in our press-free composites. This unprecedented thermal performance does not just represent an incremental improvement; it enables the design of magnetic components for entirely new application frontiers, such as power electronics for harsh automotive or aerospace environments, downhole drilling equipment, and magnetic flux concentrators for induction furnaces, where operating temperatures render conventional materials unusable.

In addition to their magnetic and thermal advantages, the new composites offer significant practical benefits in terms of weight and cost-effectiveness. The density of the cement-bonded cores is approximately 2.8–3.0 g/cm³, which is significantly lower than the 5.6–6.7 g/cm³ densities of the industrial materials. Calculations show that for the same standard core dimensions, the cement-bonded cores are approximately half the weight of their industrial counterparts. While the inductance per unit mass is moderately lower, the massive reduction in weight, combined with a manufacturing process that eliminates the need for expensive high-pressure equipment and uses inexpensive, widely available raw materials (substandard amorphous ribbon waste and Portland cement), presents a compelling case for the overall cost-effectiveness of this new technology, especially in weight-sensitive applications.

In conclusion, this work demonstrates a novel class of nanocrystalline soft magnetic composites fabricated via a simple, press-free casting method using a Portland cement binder. These composites exhibit core losses that are 30–80% lower than leading industrial materials, exceptional thermal stability with reliable operation up to 300°C and structural integrity after annealing at 500°C, and a 50% reduction in weight for equivalent-sized cores. These combined properties make the new material a highly promising candidate for next-generation power electronics, particularly for high-temperature and weight-sensitive applications where conventional SMCs are inadequate.

- [1] A. Talaat, et al., J. Alloys Compd. 870, 159500 (2021).
- [2] S. Lu, M. Wang, and Z. Zhao, J. Non-Cryst. Solids 616, 122440 (2023).
- [3] H. Sun, et al., J. Magn. Magn. Mater. 502, 166548 (2020).
- [4] G. L. Zhao, C. Wu, and M. Yan, J. Alloys Compd. 685, 231 (2016).
- [5] H. Shokrollahi and K. Janghorban, J. Mater. Process. Technol. 189, 1 (2007).
- [6] M. A. Swihart, New and Modified Alloy Powder Core Materials, Proc. PSMA Magnetics Workshop, 17 pp. (2020)
- [7] Micrometals, 2021 Alloy Powders Product Catalog [online]. Available https://s3.amazonaws.com/micrometals-production/filer_public/2f/ed/2fedd6eb-44d0-4834-a442-8222486f0b77/micrometals_alloy-en-2021.pdf

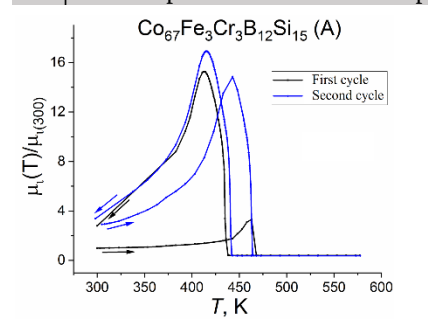
MAGNETIC BEHAVIOR AND STRUCTURAL RELAXATION OF Co-Si-B AMORPHOUS ALLOYS DOPED BY Fe AND Cr

V. K. Nosenko, A. V. Nosenko, V. V. Kyrylchuk, O. I. Boshko, I. V. Zagorulko G. V. Kurdyumov Institute for Metal Physics, N.A.S. of Ukraine, Kyiv, 03142, Ukraine

Amorphous cobalt-based alloys Co-Si-B, doped with transition metals, exhibit near-zero magnetostriction and are characterized by extremely low magnetic hysteresis losses. This determines their wide application in radio electronics and instrumentation. Alloying these materials with Fe and Cr increases their glassforming ability and affects the thermal stability of their amorphous state. For the study, three alloys were selected: A - Co₆₇Fe₃Cr₃B₁₂Si₁₅, B - Co₆₆Fe₃Cr₆B₁₅Si₁₀, and C - Co6Fe3Cr9B14Si8.

It was established that for the specified alloys, in the vicinity of the Curie temperature $T_{\rm C}$, the curve of the relative initial magnetic permeability $\mu_{\rm i}(T)/\mu_{\rm i(300)}$ exhibits a hysteresis behavior. The Curie temperature T_C was taken as the temperature at which, during cooling, a sharp increase in $\mu_i(T)/\mu_{i(300)}$ from zero to a certain value was observed. For alloy A, in the first heating cycle from room temperature to 573 K and subsequent cooling to 300 K, T_C = 438 K, which increases to 442 K after the second identical heating-cooling cycle. For the most Cr-enriched alloy C, no change in T_C = 437 K occurs after two similar heating cooling cycles. Overall, the temperature dependences $\mu_i(T)$ during the first and second heating cycles differ significantly for alloys with different contents of alloying elements. At the same time, it was shown that the cooling curves of $\mu_i(T)$ after the first and second heating cycles are very close to each other (Fig. 1).

At the same time, it was shown that the cooling curves of $\mu_i(T)$ after the first and second heating cycles are very close to each other. This indicates that the first low-temperature stage of structural relaxation in the alloys is nearly completed already after the first heating to the relatively low temperature of 573 K and subsequent slow cooling to 300 K. It is likely that, as a result of the release of the excess component of free volume and the relaxation of quenching stresses, substantial homogenization of the amorphous phase occurs during heating to the temperature of the ductile-brittle transition. The threefold increase in μ_i after heating to 573 K is associated with structural relaxation accompanied by the release of free volume.



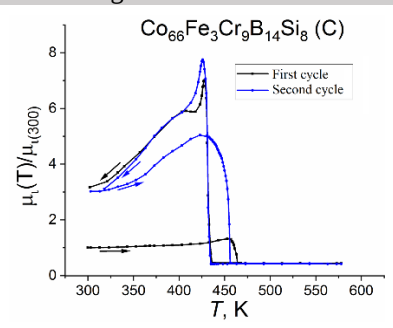


Fig. 1. Dependencies $\mu_i(T)/\mu_{i(300)}$ of toroidal strip cores made of alloys A and C in two heating-cooling cycles.

The increase in μ_i during heating (up to T_C) is due to the facilitation of domain wall motion and the rotation of the magnetization vector. The stabilization of domain walls, which is accompanied by a decrease in $\mu_i(T)$ during cooling, occurs as a result of atomic composition-directed ordering stimulated by the gain in the magnetic component of the free energy.

Thus, it was shown that during heating at a constant rate or under isothermal pre-crystallization annealing, the annihilation of excess free volume, relaxation of quenching stresses, and compositional and topological ordering lead to improved magnetic properties of the studied alloys. An example of the influence of structural relaxation processes on the magnetic properties is the change in the shape of the hysteresis loop of amorphous ribbons of alloys Co₆₆-₆₇Fe₃Cr₃-₉(Si,B)₂₂-₂₇ after relaxation annealing (Fig. 2).

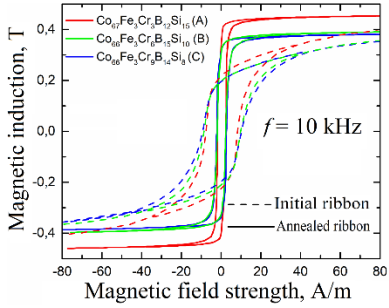


Fig. 2. Change in the shape of the magnetization reversal loop of investigated alloys after relaxation annealing.

The squareness ratio B_r/B_s increases (from 0.5 to 0.8), the saturation induction B_s rises, and the dynamic coercive force H_C decreases by a factor of 4–5 (for example, from 9.2 A/m to 2.1 A/m for alloy B).

TENSILE STRESSES IN NIMNGA LAMINATE COMPOSITE FRAMED BY SOFT MAGNETIC FOILS

- J. Kharlan ^{1,2}, O. Salyuk¹, H. Marinchenko³, V. Golub¹
- ¹ V. G. Baryakhtar Institute of Magnetism of the National Academy of Sciences of Ukraine, Kyiv 03142, Ukraine
- ² Faculty of Physics, Adam Mickiewicz University in Poznan, Poznan 61– 614, Poland
- ³Faculty of General and Applied Physics, State University "Kyiv Aviation Institute", Kyiv 03058, Ukraine

Today, an urgent task is to obtain effective materials used in modern types of actuators, sensors, and mechanical energy harvesters. One of the possible solutions to this issue is the use of composites, such as ferromagnetic shape memory alloy (usually Ni-Mn-Ga) particles incorporated into a polymer [6] or layered metal foil-ferromagnetic shape memory alloy particles-metal foil [1] magnetostrain active materials. However, during the production of such materials, a problem arises related to the constraints of twin reorientation by adjacent grain boundaries [2], leading to low values of magnetic field-induced strains.

Recently, to eliminate the influence of grain boundaries, it was suggested to disintegrate polycrystals of Ni-Mn-Ga into individual grains and use them to produce composite magnetostrain active materials [3]. However, it was found that due to the constraints from neighboring particles, some particles did not show a shape deformation, and the inhomogeneous distribution of stress concentration was discerned in these composite materials [4].

To avoid the inter-particle constraints, laminate composites "Cu foil/Ni-Mn-Ga particles/Cu foil" were designed [5], where 16 particles (with an average particle size of 250 μ m) were mounted between two Cu foils (3 × 3 × 0.125 mm) and fixed by thin layers of silicone rubber serving as an adhesive.

During preparation, the composites were cured under an external magnetic field of 1 T applied along the particle layer, aligning the easy-magnetization short c-axis of the tetragonal unit cells of the particles in the layer plane direction. Then the initial deformed state of the composite was set by 10 MPa compression perpendicular to the plane of the composite, which caused the short c-axes reorientation perpendicular to the plane. These composites showed magnetic fieldinduced strains values around 3.5% under the action of a magnetic field in the range 0.7-0.9 T applied in the film plane. A gradual increase in magnetic fieldinduced strains during an incremental change in the magnetic field was observed. The high value of the saturation field and the gradual behavior were attributed to the influence of the polymer.

Recent experiments [6] have shown that this problem can be overcome if Fe foils are used instead of Cu ones. In this case, a steep-wise dependence of magnetic field induced strains is observed, and the saturation field drops to 0.14 T, which was ascribed by the action of an additional magnetic force acting on the element.

The results of the calculations for the repulsive force acting between the 3×3 mm Fe foils of different thicknesses h and various separation distances are shown in Fig. 1. In the case of laminate composite used in [6], this results in a tensile stress of about 0.12 MPa, which is close to the value obtained from the analysis of experimental data. The calculated value should be considered as a rough estimation. For the real system, a deformation of the silicon adhesive layer should be taken into account, which gives rise into a decrease of the stress in NiMnGa particles, while the irregular shape of the particles can result in local stresses that can substantially exceed the obtained value.

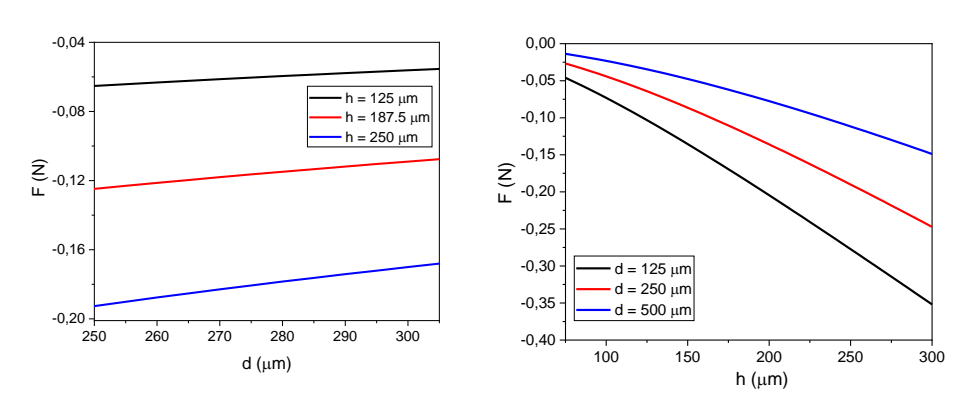


Fig. 1. (a) Repulsive force between Fe foils as a function of the distance d, shown for three different foil thicknesses. (b) Repulsive force as a function of the foil thickness h for three different separation distances.

- [1] D. K. Han, W.-T. Chiu, M. Tahara, V. Chernenko, S. Lanceros-Mendez, and H. Hosoda, Acta. Mater. 277, 120158 (2024).
- [2] M. Chmielus, X. X. Zhang, C. Witherspoon, D. C. Dunand, and P. Müllner, Nat. Mater. 8, 863 (2009).
- [3] P. Sratong-on, V. A. Chernenko, J. Feuchtwanger, and H. Hosoda, Sci. Rep. 9, 1 (2019).
- [4] P. Sratong-on, V. A. Chernenko, and H. Hosoda, Results Mater. 2, 100037 (2019).
- [5] D. K. Han, W.-T. Chiu, M. Tahara, V. Chernenko, S. Lanceros-Mendez, and H. Hosoda, Acta. Mater. 277, 120158 (2024).
- [6] D. K. Han, W.-T. Chiu, M. Tahara, N. Nohira, V. Chernenko, S. Lanceros-Mendez, and H. Hosoda, Scripta Mater. 261, 116624 (2025).

INFLUENCE OF A CONSTANT MAGNETIC FIELD ON THE STRUCTURE FORMATION OF A Cu-Fe ALLOY IN ITS CASTING AND **SOLIDIFYING**

O. V. Nogovitsyn, V. O. Seredenko¹, O. V. Seredenko¹, D. O. Derecha² ¹ Physico-Technological Institute of Metals and Alloys NAS of Ukraine, Kyiv, 03680. Ukraine

² V. G. Baryakhtar Institute of Magnetism NAS of Ukraine, Kyiv, 03142. Ukraine

Alloys of the Cu-Fe system are promising highly thermally and electrically conductive strengthened materials with significant magnetic resistance for use, in particular, in the latest devices for electromagnetic shielding, high-speed transport, aerospace engineering, mechanical engineering, etc.

Alloys under certain cooling conditions tend to have immiscible liquid phases, which allows the formation of emulsified strengthening inclusions based on iron in the copper base. The formation of small emulsified inclusions in the structure is associated with high cooling rates of the melt during its transformation into a solid state. Therefore, currently scientific and technological developments are aimed at the formation of a strengthening phase in the form of fragmented dendrites. Among the technologies used to obtain alloys of the Cu-Fe system, the cheapest are foundries using external influences, in particular, permanent magnetic fields. But such technologies need improvement due to the complexity of controlling structure formation in the liquid state and the transition to the solid state.

The aim of the work was to study the changes in the shape and structure of iron dendrites in a Cu-20% Fe alloy that was poured, cooled, and solidified at rates typical of conventional casting methods (<1·10² K/s) under the influence of a constant magnetic field (with induction B $\leq 5 \cdot 10^{-1}$ T).

To prepare a melt weighing 1.0 kg, high-purity Cu (99.99%) and 3 ps steel (Fe 98.78%; C 0.20%; remaining impurities) were used. The alloy was melted in an induction crucible furnace with an electric current frequency in the inductor of 44 kHz. To prevent uncontrolled saturation of iron with carbon and erosion of the crucible, an alundum crucible was used, which was located in the middle of the graphite crucible. The liquid alloy with a temperature of 1723 K was poured into non-magnetic steel casting molds with a jet directed towards the center of the mold. During casting, cooling and solidification of the alloy in the molds, a horizontal permanent magnetic field (B≤2.5·10⁻¹ T) was applied to it, which was created by a permanent magnet. Control castings were obtained without the action

of a magnetic field. The castings had a diameter of 35 and a height of 40 μm . The structure was studied on sections of vertically cut castings.

The structure of the castings contained two zones that differed significantly in the size and shape of iron-based inclusions – central and surface (Fig. 1).

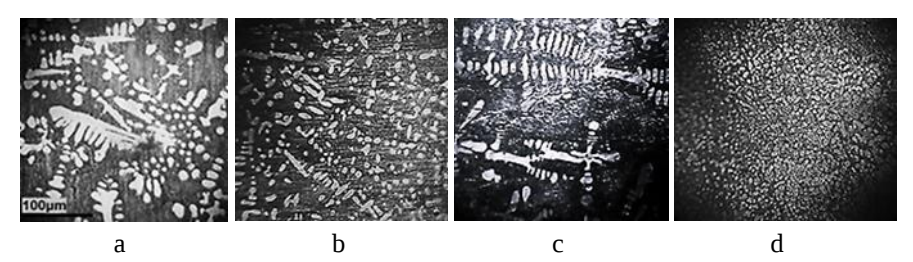


Fig. 1. Structure of castings from Cu-20%Fe alloy: control metal - a) central zone, b) surface zone; metal treated with a permanent magnetic field - c) central zone, d) surface zone.

The central zone of the control alloy was formed under cooling conditions at a rate of ~ 1 K/s and occupied the majority of the casting and was 10.6 times longer than the surface zone.

The central zone of these castings contained iron-based inclusions up to 250 μ m in the form of dendrites, ~56% of which were fragmented into rounded parts (Fig. a). The surface zone cooled and solidified 20 times faster than the central zone. As a result, these inclusions were up to 10 times smaller and up to 90% fragmented (Fig. b).

Under the influence of a magnetic field in the central zone of the castings, the fragmentation of the inclusions increased - up to 90% with a threefold increase in the distance between the fragments (Fig. c). The surface zone expanded twice as much as in the control castings, the size of the inclusions decreased by up to 5 times and they were all fragmented. This occurred due to an increase in heat transfer from the casting to the mold wall and, as a result, an increase in the cooling rate by 1.5 times due to the redistribution of the energy of the melt's motion during casting the melt into the mold in a magnetic field. Under such conditions, the velocity in the boundary layer accompanying the crystallization front as it moved during the formation of the surface zone increased (Hartmann effect).

Thus, to obtain dispersed inclusions in the structure, an optimal regime of hydrodynamics, heat dissipation, and magnetic field action is necessary, which is effectively implemented during continuous casting of thin billets.

MODIFYING MLCs OF PST FOR IMPROVED PERFORMANCE (INVITED)

M. Guo¹, V. Farenkov¹, X. Chen¹, A. Mohanathan³, A. Z. K. Goh³, Y. Tang¹, J. Zhang¹, M. Vickers¹, S. M. Fairclough¹, C. Ducati¹, X. Moya¹, S. Hirose², N. D. Mathur¹

¹Department of Materials Science, University of Cambridge, Cambridge, UK ²Murata Manufacturing Co., Ltd, Kyoto, Japan ³Department of Physics, University of Cambridge, Cambridge, UK

Electrocaloric effects are voltage driven thermal changes that arise due to changes in the magnitude of the local electrical polarization. Large electrocaloric effects are observed in ferroelectric materials above the Curie temperature when first-order phase transitions are driven by the applied electric field, e.g. above 295 K in ceramic PbSc_{0.5}Ta_{0.5}O₃ (PST), whose B-site scandium and tantalum cations are well ordered in the perovskite crystal lattice.

Electrocaloric effects are large in thin films because thin films can support large electric fields without breakdown, and electrocaloric effects in assemblies of thin films (multilayer capacitors, MLCs) can be exploited in prototype heat pumps for cooling and heating.

MLCs of PbSc_{0.5}Ta_{0.5}O₃ (PST) [1] show large electrocaloric effects that arise over a wide range of temperatures when driven by supercritical electric fields, and such MLCs have been exploited in prototype coolers during the last years.

I will present MLCs of PST whose performance has been improved by changes to the B-site cations, for use in future prototype coolers.

[1] Nair et al., Nature 575 (2019) 468

HIGH-PRESSURE STABILIZED Bi(FeSc)O₃ MULTIFERROICS: MAGNETIC BEHAVIOUR (INVITED)

O. L. Fertman¹, O. V. Fedorchenko¹, D. D. Khalyavin², E. Cižmár³, A. N. Salak⁴

¹B. Verkin Inst. for Low Temp. Physics & Eng. NASU, Kharkiv, 61103, Ukraine ²ISIS Facility, Rutherford Appleton Laboratory, OX11 0QX, UK

³Faculty of Sciences, Institute of Physics, P. J. Šafárik University, 041 54 Košice, Slovakia

⁴Department of Materials and Ceramics Engineering/CICECO-Aveiro Institute of Materials, University of Aveiro, 3810-193, Portugal

Until now, bismuth ferrite BiFeO₃ and materials based on it remain the only ones that is both magnetic and a strong ferroelectric at room temperature, and a strong coupling between magnetism and ferroelectricity exists. Due to this unique combination of properties, bismuth ferrite is of significant interest for spintronics, magnetoelectronic. energy harvesting, memory devices and other areas of functional materials [1].

Bismuth ferrite possesses a highly distorted perovskite crystal structure, with *R*3*c* crystal symmetry. Fe³⁺ cations are octahedrally coordinated by oxygen ions. Bi³⁺ cations are excentrically located in the cavities formed by FeO₆ octahedra. BiFeO3 is a G-type antiferromagnet with a long period cycloidal spin structure, demonstrates a high magnetic order temperature, $T_N \sim 640$ K, and the ferroelectric one at $T_C \sim 1100$ K, and possess a weak ferromagnetism due to the spin canting. Each Fe³⁺ spin is surrounded by the six nearest antiparallel Fe neighbors (G-type antiferromagnetic structure). The main mechanism of exchange interaction in BiFeO3 is superexchange between Fe³⁺ ions through the oxygen. The spins are not perfectly antiparallel due to the coupling to the polarization (Dzyaloshinskii-Moriya antisymmetric exchange interaction), and an incommensurate spin cycloid with period about 62-64 nm appears [2]. The net weak ferromagnetic moment is averaged out to zero due to the cycloidal rotation, but a non-zero macroscopic magnetization can be stabilized if the spin-cycloid is destroyed. The suppression of the modulated spin structure is the necessary condition for the appearance of the spontaneous magnetization and linear magnetoelectric effect in BiFeO₃. One of the possible ways to destroy the magnetic cycloidal structure is to combine chemical doping and creation of mechanical stresses. Substitutions in the Fe-sublattice are enough difficult because of a limited solubility even in the case of cations which are close to octahedrally coordinated Fe³⁺ in terms of ionic size. High-pressure synthesis technique makes it possible to extend the solubility and thereby the perovskite phase existence ranges. In many cases, metastable perovskite phases can be stabilized by quenching under pressure.

We have studied magnetic properties of the high-pressure (6 GPa) stabilized perovskite BiFe_{1-y}Sc_yO₃ phases $(0.1 \le y \le 0.9)$ by means of magnetization measurements and neutron diffraction [3]. The perovskites in the range of $0.20 \le y$ ≤ 0.60 demonstrate a weak ferromagnetic contribution to the AFM state. Recently found phenomenon of annealing-stimulated irreversible structural transformations of high-pressure stabilized oxide perovskites (conversion polymorphism) appeared to be a powerful tool to produce novel phases, which cannot be prepared using any conventional routes [4]. In our case, the phenomenon resulted in the formation of several perovskite polymorphs with unique combinations of structural distortions and magnetic orders. Magnetic phase diagram for the BiFe_{1-y}ScyO₃ perovskites synthesized under high-pressure was constructed (Fig. 1). One of the most interesting new magnetic structures found is a collinear G-type AFM phase with the spins polarized along the threefold axis, which appears as a result of reversible phase transition at $Tm < T_N$ (T_N represents the Néel temperature) for compositions with y < 0.4.

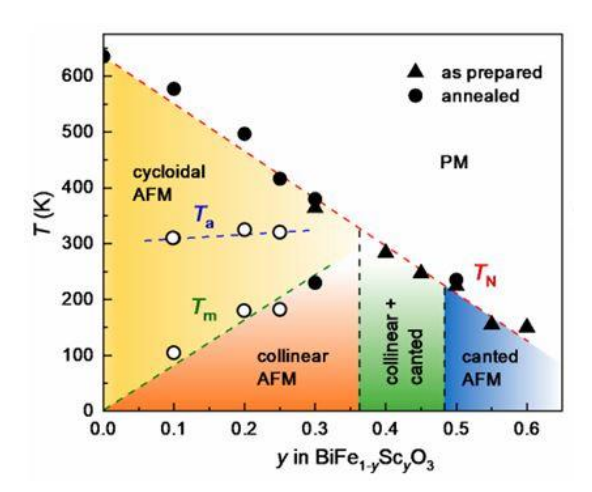


Fig. 1. Magnetic phase diagram of the magnetic structures observed in the BiFe_{1-v}Sc_vO₃ perovskites synthesized under high-pressure followed by annealing.

- [1] G. Catalan, J.F. Scott, Adv. Mater. 21, 2463 (2009).
- [2] D. Lebeugle, et al., Phys. Rev. Lett. 100, 227602 (2008).
- [3] E.L. Fertman, et al., Crystals 10, 950 (2020).
- [4] D.D. Khalyavin, et al., Chem. Commun., 55 4683 (2019).

SECTION VII. INTERDISCIPLINARY RESEARCH

GRAPH NEURAL NETWORKS FOR PREDICTING PROPERTIES OF **OUASI-ONE-DIMENSIONAL ISING SYSTEMS**

O. O. Kryvchikov, D. V. Laptev, V. V. Slavin

B. Verkin Institute for Low Temperature Physics and Engineering of the National Academy of Sciences of Ukraine

Our work presents a graph-based deep learning framework for predicting magnetization curves in quasi-one-dimensional antiferromagnetic Ising spin systems. The lattice geometry is encoded as a graph, where nodes represent spins and edges denote pairwise interactions corresponding to non-zero coupling constants. The system Hamiltonian, reformulated to emphasize repeated structural units and local connectivity, is mapped onto a graph representation that serves as input to a graph neural network (GNN).

This representation preserves the physical equivalence of different unit cell layouts by relying on graph isomorphism, allowing the model to treat structurally identical but visually distinct configurations as the same. The reformulated Hamiltonian is decomposed into repeating blocks, each described by intra- and inter-block coupling matrices, which fully determine the corresponding interaction graph.

To ensure consistent predictions for systems with different sizes and structures, the model processes each input graph in a way that allows comparison across configurations. This enables the prediction of magnetization behavior for a wide range of lattice geometries, including those with complex or irregular unit cells. As a result, magnetization curves can be obtained for a broad class of quasione-dimensional lattices without modifying the model architecture or retraining for specific cases.

The model is trained on data generated by classical Monte Carlo simulations for a diverse set of interaction graphs characterized by varying degrees of frustration and symmetry. The GNN processes the interaction graph and outputs the predicted magnetization curve as a function of the external magnetic field.

Quantitative evaluation against unseen graph topologies shows that the model accurately reproduces key features of the magnetization curve, including plateaus, transition points, and the effects of geometric frustration. The mean error in favorable cases is as low as 0.045, with the largest discrepancies occurring in highly regular geometries such as two-leg ladders. The model demonstrates sensitivity to local motifs and global symmetries, suggesting that GNNs can extract physically relevant information directly from structural connectivity.

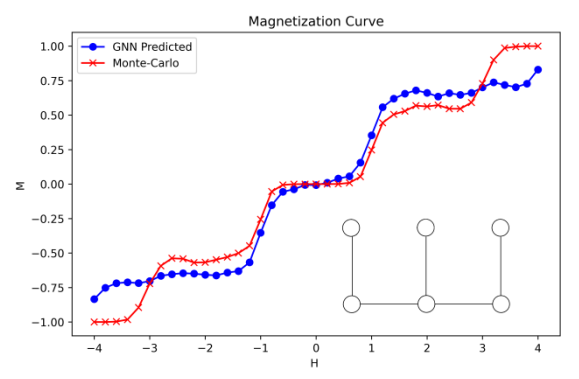


Fig.1. The dependence of the magnetization on the external field. Tested Monte Carlo (red) and predicted (blue). The corresponding graph is in the corner.

By eliminating the need for repeated Monte Carlo simulations, the proposed approach offers a computationally efficient alternative for estimating magnetic response functions in low-dimensional systems. The results support the broader applicability of graph-based models in statistical physics and indicate potential extensions to higher-dimensional systems and other spin models such as the Potts or Heisenberg variants.

In addition to predictive accuracy, the model provides insight into the structural organization of spin systems. By projecting learned graph embeddings into a low-dimensional space using t-distributed Stochastic Neighbor Embedding method (t-SNE), distinct clusters emerge that broadly correspond to different classes of lattice geometries—such as chain-like, ladder-like, and frustrated configurations. This suggests that the GNN not only captures quantitative magnetization behavior but also encodes meaningful structural distinctions.

- [1] M. Withnall, et al., *J. Cheminform.* **12**, 1 (2020).
- [2] L. A. Pastur and V. Y. Slavin, arXiv preprint arXiv:2302.14382 (2023).
- [3] D. V. Laptiev, et al., *Low Temp. Phys.* **50**, 158 (2024). Originally published in *Fiz. Nizk. Temp.*, pp. 158–166.

HALBACH MATRIX APPROACH AS A PROMISING METHOD TO ADVANCE MAGNETOMECHANICAL ACTION ON BIOLOGICAL **TISSUES**

Oleksandra S. Ostapenko¹, Serhii O. Mamilov¹, Valerii B. Orel^{2,3}, Valerii E. Orel^{2,3}, Alexandr I. Tovstolytkin¹

- ¹ V.G. Baryakhtar Institute of Magnetism of the National Academy of Sciences of Ukraine, 36-b Akad. Vernadskogo Blvd., 03142 Kyiv, Ukraine;
 - ² National Cancer Institute, 33/43 Zdanovska Str., 03022 Kyiv, Ukraine;
- ³ National Technical University of Ukraine "Igor Sikorsky Kyiv Polytechnic Institute", 37 Prospect Beresteiskyi, 03056 Kyiv, Ukraine;

Cancer is one of the leading causes of death worldwide. Breast cancer accounts for 15% of all cancer deaths in women [1]. According to clinical study results, patients who undergo combined treatment using chemotherapy and regional inductive moderate hyperthermia (IMH) (≤42 °C) have higher survival rates than those who undergo chemotherapy alone [2,3].

In most cases, hyperthermia treatment involves increasing the power until the tumor's internal temperature reaches a maximum that is tolerable yet sufficient to destroy cancer cells. However, the limitations of this approach are related to the inherent heterogeneity of malignant tumors and the significant increase in temperature of surrounding tissues [5].

One method involves combining IMH with magnetic nanoparticles (MNPs), which allows for localized heating. MNPs can be directed remotely to the tumor site using a non-uniform stationary magnetic field (SMF). This field penetrates the human body with minimal attenuation [6, 7] and can organize NPs into userdefined cluster patterns [8].

Furthermore, MNPs transmit mechanical forces to biological media in response to non-uniform SMFs, a phenomenon known as the magneto-mechanical effect.

To promote targeted MNP localization and effectively exploit the magnetomechanical effect, it is important to create SMFs with controlled induction distribution, i.e., with controlled gradients. One way to achieve this is to use the Halbach matrix approach [9,10]. In this study, neodymium magnets 5x5x5 mm in size with a magnetic induction of B = 250 Gs were employed. Three configurations of nine or eight magnets were considered. Each configuration was placed in a special plastic holder, and wooden plugs were used to fix the ends if necessary.

The first configuration consists of nine cubic magnets with magnetic moments oriented as follows: $\rightarrow \rightarrow \rightarrow \downarrow \downarrow \downarrow \downarrow \leftarrow \leftarrow \leftarrow \leftarrow$. Figure 1 shows the field distribution along the long edge of the parallelepiped. Measurements were taken 3 mm from the magnets surface.

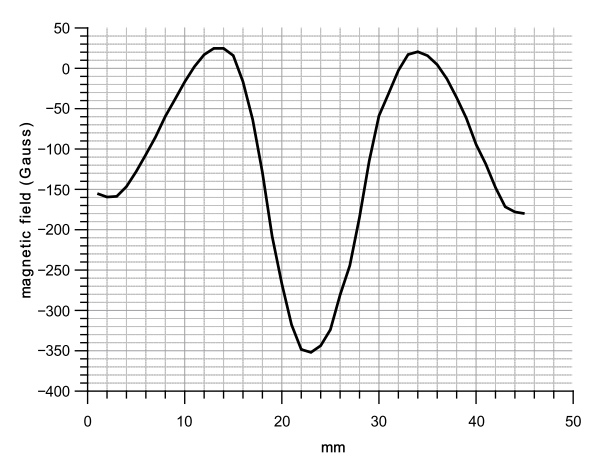


Fig. 1. Spatial distribution of the field configuration 1 at a distance of 3 mm.

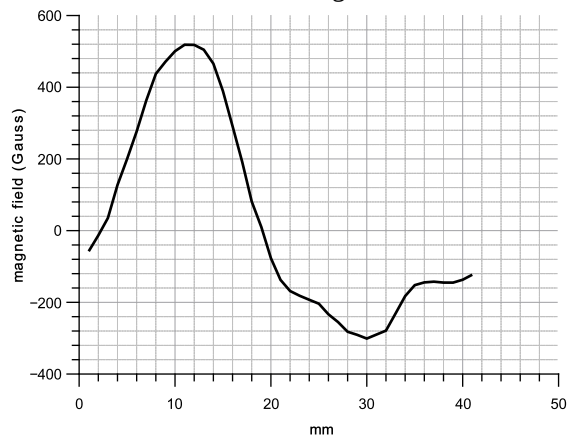


Fig. 2. Spatial distribution of the field configuration 2 at a distance of 3 mm.

The second configuration consists of eight cubic magnets whose magnetic moments were oriented as follows: $\rightarrow \uparrow \uparrow \leftarrow \rightarrow \downarrow \downarrow \leftarrow$. Figure 2 shows the corresponding field distribution measured at 3 mm from the magnets surface.

The third configuration also consists of eight cubic magnets, with magnetic moments oriented as follows: $\downarrow \leftarrow \leftarrow \uparrow \uparrow \uparrow \rightarrow \rightarrow \downarrow$. Figure 3 shows the corresponding field distribution at a distance of 3 mm from the surface of the magnets.

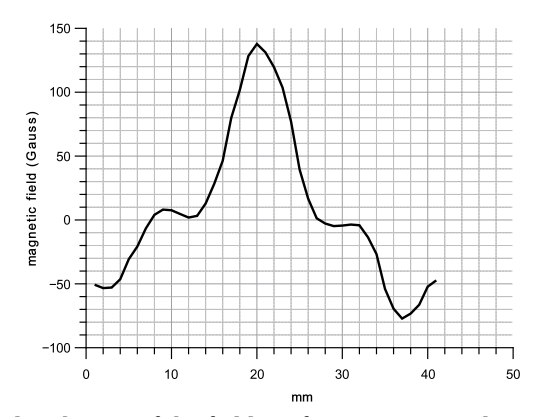


Fig. 3. Spatial distribution of the field configuration 3 at a distance of 3 mm.

Thus, the Halbach matrix approach allows obtaining different configurations of the gradient magnetic field. By changing the size of the elements, their magnetic moment and configuration, the spatial distribution of the field can be easily controlled.

The work is partially supported by the IEEE Magnetics Society Program "Magnetism for Ukraine - 2025" (STCU Project No. 9918) and the Ministry of Health of Ukraine "To develop a method of antitumor therapy of primary malignant bone tumors based on magnetochemical technology nanocomplexes", code BH.14.01.07.204-23, registration number 0123U100711.

- [1] Siegel RL, Miller KD, Fuchs HE, Jemal A. A Cancer Journal for Clinicians. 72(1):7–33. (2022).
- [2] Klimanov MY, et al. Technology in Cancer Research & Treatment. Jan 1;17. (2018).
- [3] Loboda A, et al. Technology in Cancer Research & Treatment. Jan 1;19. (2020).
- [4] Oleson JR. IEEE Transactions on Biomedical Engineering. BME-31(1):91–7. (1984).
- [5] Dewhirst MW, Lee CT, Ashcraft KA. International Journal of Hyperthermia. 32(1):4-13. (2016).
- [6] Fatima H, Charinpanitkul T, Kim KS. Nanomaterials. May 1;11(5):1203. (2021)
- [7] Gavilán H, et al. Chemical Society Reviews. **50**(20):11614–67. (2021).
- [8] Tracy JB, Crawford TM. MRS Bulletin. **38**(11):915–20. (2013).
- [9] Kang JH, et al. Applied Physics Letters. 108(21): 213702-5. (2016).
- [10] O'Reilly T, et al. Magnetic Resonance in Medicine. **85**(1): 495–505. (2021).

EFFECT OF A CONSTANT MANGITIC FIELD ON THE MAGNITUDE OF LASER PHOTODISSOCIATION OF OXYHEMOGLOBIN IN ARTERIAL BLOOD

O. Yu. Salyuk^{1,2}, O. S. Ostapenko¹, Yu.B. Skirta^{1,2}, D.V. Velyhotskyi^{1,2}, S. O. Mamilov¹.

- ¹ V.G. Baryakhtar Institute of Magnetism of the National Academy of Sciences of Ukraine, 36-b Akad. Vernadskogo Blvd., 03142 Kyiv, Ukraine;
- ² National Technical University of Ukraine "Igor Sikorsky Kyiv Polytechnic Institute", 37 Prospect Beresteiskyi, 03056 Kyiv, Ukraine.

Low-intensity laser therapy is widely used in many areas of medicine [1]. It is believed that the process of oxyhemoglobin photodissociation is one of the most important in the therapeutic effect of laser radiation. This process involves the interfractional transition of oxyhemoglobin - deoxyhemoglobin, which releases oxygen, which is an effective means of combating anaerobic infections, in particular, in the area of burn and wound injuries [2]. However, modern approaches to physiotherapy are increasingly focused on the development of methods for the combined effects of various physical factors. One example is magnetolaser therapy, an example of complex therapy where a laser and a magnetic field are simultaneously exposed. Doctors have gained some experimental experience in the use of magnetic laser therapy in vertebrology, traumatology, gynecology, urology; for the elimination of pain syndromes and inflammatory processes. [3-5].

There are several hypotheses regarding the mechanisms of action. Some authors believe that under the simultaneous influence of laser radiation and magnetic field, other physical phenomena occur in addition to the simple summation of energies. Other authors believe that under the influence of low-intensity laser radiation, freely charged ions (Na⁺, K⁺, Ca²⁺, etc.) are formed in tissues, which leads to an increase in metabolism due to the activation of membrane processes. [6,7].

The purpose of our work is to study the effect of a magnetic field on the phenomenon of photo-stimulated photodissociation of hemoglobins, i.e., the transformation of hemoglobin forms in peripheral tissues.

To conduct the experiments, we used a pulse oximeter-spectrophotometer developed by the authors [8]. The pulse oximeter sensor realized the scheme of light passing through the biotissue. The sensor was assembled on the basis of a standard pulse oximetry pair of LEDs with emission wavelengths of 940 and 660

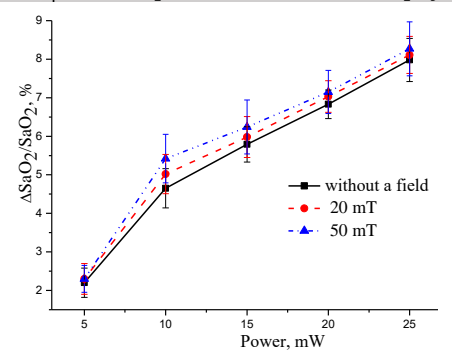
nm and a BPW34 silicon photodiode (OSRAM). The optical pulses had a duration of t=160 μs and a frequency of fopr=348 Hz. To prevent the signal received by the photodiode from one LED from affecting the signal of another, we used time separation of the signals. The sensor operation, data collection, and transmission are controlled by the measuring unit. It is connected to a personal computer, which processes the data, displays information on the monitor screen and stores the signal trend on the hard disk.

The sensor was placed between the poles of the electromagnet so that the irradiation zone was at the same distance from the magnet poles. The direction of the laser beam coincided with the line connecting the poles of the magnet; no dependence on the direction of the magnetic field was observed. The wavelength of the external laser irradiation was chosen from the condition of a large effect of oxyhemoglobin photodissociation, it was 605 nm.

The experiment was conducted as follows: 30 seconds without radiation, 30 seconds with radiation on, and 30 seconds without radiation for each value of laser external irradiation power and magnetic field magnitude of 10 mT, 20 mT, and 50 mT to measure 15 to 20 signal recordings. The magnitude of the magnetic field corresponds to the values used in magnetic laser therapy devices [7].

The study involved 8 volunteers aged 25 to 54 years. The wavelength of the external laser irradiation was chosen based on the condition of a large effect of oxyhemoglobin photodissociation. For these reasons, wavelengths of 525 nm and 605 nm were chosen. The power level of the irradiation used corresponded to that used in low-intensity laser therapy and is safe for humans, and the irradiation was performed noninvasively. Measurements were performed at magnetic field strengths of 10 mT, 20 mT, and 50 mT.

Fig. 1 shows the relative change in the value of arterial blood oxygen saturation under irradiation with a wavelength of 525 nm in the absence of a magnetic field and with a field of 20 mT and 50 mT. Fig. 2 shows, respectively, under irradiation with a wavelength of 605 nm. At a magnetic field of 10 mT, the obtained values of changes in arterial blood oxygen saturation were almost the same as those obtained in the absence of a field, so they are not shown in the figures.



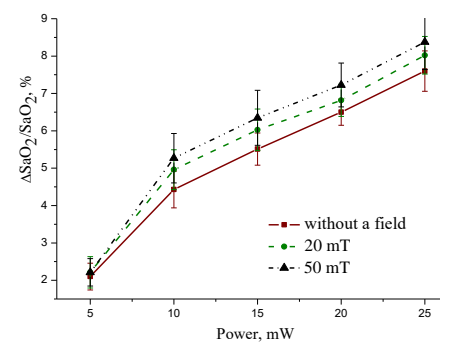


Fig. 1. Relative change in arterial blood oxygen saturation under irradiation with a wavelength of 525 nm in the absence of a magnetic field and with a field of 20 mT and 50 mT.

Fig. 2. Relative change in arterial blood oxygen saturation under irradiation with a wavelength of 605 nm in the absence of a magnetic field and with a field of 20 mT and 50 mT.

It is shown that a separate effect of a magnetic field in the range of 0-100 mT does not lead to photodissociation of hemoglobin fractions. It is shown that simultaneous exposure to low-intensity laser radiation and a constant magnetic field of more than 20 mT increases the efficiency of oxyhemoglobin photodissociation, which allows to increase the range of control over the intermolecular rearrangement of hemoglobin complexes without increasing the irradiation load on the surface of a biological object.

- 1. Abdildin, Y., Tapinova, K., Jyeniskhan, N., & Viderman, D. (2023). Lasers in Medical Science, 38(1), 166.
- 2. Mamilov, S., Bezuglyi, M. (2025). Photodissociation of Hemoglobin Molecules in Vivo Under External Irradiation. In: Bezuglyi, M., Bouraou, N., Mykytenko, V., Tymchyk, G., Zaporozhets, A. (eds) Advanced System Development Technologies II. Studies in Systems, Decision and Control, vol 581. Springer, Cham.
- 3. Kubsik A, Klimkiewicz R, Janczewska K, Klimkiewicz P, Jankowska A, Woldańska-Okońska M. NeuroRehabilitation. 2016;38(2):183-190.
- 4. Pasek, Jarosław, Sebastian Szajkowski, and Grzegorz Cieślar. Electromagnetic Biology and Medicine 43.1-2 (2024): 95-106.
- 5. Arede, Daniele Pedrosa, et al. MedNEXT Journal of Medical and Health Sciences 4.S2 (2023).
- 6. Lewandoski, L. T., Grymuza de Souza, V., Cannan Kiekiss, G., Soares, F., Buzanello, M. R., & Bertolini, G. R. F. (2025). Electromagnetic Biology and Medicine, 44(1), 107–118.
- 7. Терещенко, М. Ф., Тимчик, Г. С., Рудик, В. Ю., Чухраєв, М. В., & Рудик, Т. О. (2020). Автоматизовані магнітотерапевтичні апарати. Політехніка. 272 с.
- 8. M.M. Asimov, R.M. Asimov, A.N. Rubinov, S.A. Mamilov, Yu.S. Plaksiy.. Proceeding of SPIE, 2006, Vol. 6251, p. 147-154.

APPLICATION OF MAGNETIC NANOCOMPOSITE FOR CANCER IMAGING AND TREATMENT IN AN EXPERIMENTAL TUMOR MODEL (INVITED)

V. B. Orel^{1,2}, O. Y. Dasyukevich¹, O. Yu. Rykhalskyi¹, A. G. Diedkov¹,
 S. O. Mamilov³, O. S. Ostapenko³, Yu. A. Kurapov⁴, S. Ye. Lytvyn⁴, V. E. Orel^{1,2},
 A. I. Tovstolytkin³

¹National Cancer Institute, Kyiv, 03022, Ukraine ²National Technical University of Ukraine "Igor Sikorsky Kyiv Polytechnic Institute", Kyiv, 03056, Ukraine

³V.G. Baryakhtar Institute of Magnetism of the National Academy of Sciences of Ukraine, Kyiv, 03142, Ukraine

⁴E.O. Paton Electric Welding Institute, Kyiv, 03150, Ukraine

Introduction. Magnetic nanocomposites (MNCs) represent versatile theranostic agents for drug delivery and imaging, with tunable physicochemical properties that enhance antitumor efficacy and tumor contrast on magnetic resonance imaging (MRI). Fe₃O₄-Au MNCs show promise for medical translation, as they feature a magnetic core responsive to the action of constant magnetic fields (CMFs) and electromagnetic fields (EMFs), as well as a gold-covered surface that reduces aggregation and improves optical properties [1,2].

Purpose. This study aimed to synthesize MNC loaded with an antitumor drug doxorubicin (DOX) and to evaluate its effects on tumor growth kinetics, redox state and MRI features.

Materials and methods. DOX-loaded Fe₃O₄-Au MNC was produced using deposition electron beam physical vapor combined with magneto-mechanochemical synthesis [3]. MNC morphology and structure were analyzed using transmission and scanning electron microscopy. Magnetic properties were assessed using vibrating sample magnetometry (VSM). Walker-256 carcinosarcoma-bearing animals were randomly divided into four groups (n = 5 in each): (1) control (no treatment), (2) conventional DOX, (3) DOX-MNC, and (4) DOX-MNC + CMF + EMF. Tumor-bearing animals received intravenous DOX (1.5 mg/kg) or DOX-MNC (3 mg/kg loaded with 1.5 mg/kg DOX) and were exposed for 15 minutes to a 42 MHz electromagnetic field generated by the MagTherm prototype (Radmir, Ukraine). A magnetic dipole applicator with an NdFeB magnet (30 mT) was placed beneath the tumor, guiding DOX-MNC delivery to the tumor site. Changes in tumor growth kinetics were assessed based using the growth factor φ and breaking ratio κ [4]. Tumor response

was visualized with T_2 -weighted MRI scans. Texture parameters (intensity, skewness, kurtosis) were computed using ImageJ 1.53a (National Institutes of Health, USA) and Horos v. 4.0 (Horos Project, Switzerland) software. Electron spin resonance (ESR) spectroscopy detected changes in ubisemiquinone, superoxide radical and nitric oxide levels in tissue samples. Statistical analysis was carried out using SPSS Statistics v. 25.0 (IBM, Inc., Armonk, USA) software.

Results. TEM and SEM confirmed spherical Fe₃O₄ cores with discontinuous Au coating. A 22% decrease in Moran's spatial autocorrelation index (p < 0.05) calculated in TEM images following DOX loading reflected an increase in heterogeneity of MNC distribution. VSM showed ferromagnetic properties post-coating. DOX-MNC combined with CMF and EMF led to a 14% and 16% greater inhibition of tumor growth kinetics than DOX and DOX-MNC, respectively (p < 0.05). Untreated control animals exhibited the greatest increase in total body weight over the study period, whereas animals treated with DOX or DOX-MNC showed ~25% less weight gain, as compared with the control group (p < 0.05). Quantitative analysis of T₂-weighted MRI scans indicated a significant increase in tumor intensity after DOX-MNC + CMF + EMF treatment, when compared with the control group (1.4-fold), DOX (1.6-fold), and DOX-MNC alone (1.8-fold) (p < 0.05), alongside the lowest skewness value. On average, treatment with DOX, DOX-MNC or DOX-MNC combined with CMF and EMF reduced tumor levels of ubisemiquinone, superoxide radicals, and nitric oxide by 47% relative to the control group. Nitric oxide levels were the lowest in the group receiving DOX-MNC + CMF + EMF (p < 0.05).

Conclusion. DOX-loaded Fe₃O₄-Au MNC synthesized by EB-PVD and magneto-mechanochemical synthesis demonstrated enhanced antitumor efficacy and imaging contrast when combined with CMF and EMF. The combined treatment resulted in tumor growth inhibition, an increase in tumor intensity and more pronounced necrotic changes on MRI and changes in tumor redox state, as measured by ubisemiquinone, superoxide and nitric oxide levels.

^[1] C. Li, et al., Adv. Funct. Mater. **24**, 1772–80 (2014).

^{[2].} A. Tovstolytkin, et al., Nanoscale Heat Mediators for Magnetic Hyperthermia: Materials, Problems, and Prospects (Springer, Cham, 2021).

^[3] V. B. Orel, et al., RCS Adv. 14, 14126-38 (2024).

^[4] N. Emanuel, *Kinetics of Experimental Tumor Processes* (Pergamon Press, Oxford, 1982).

ELECTRONIC HYDRODYNAMICS IN GRAPHENE, INCOHERENT METALS AND OTHER STRONGLY CORRELATED SYSTEMS (INVITED)

K. E. Schalm

Leiden Institute of Physics, Faculty of Science, Leiden University, 2300 RA Leiden, Netherlands

Transport in almost all metallic systems can be understood microscopically from the Boltzmann equation. The recent decade has seen a surge of interest into strongly correlated systems where this may not work. One can only understand transport in an effective macroscopic hydrodynamic description. We review some of the progress in this field and the remarkable role black holes have played in this.

MAGNETIC FIELD INFLUENCE ON INTRACELLULAR CA2+ **DYNAMICS**

S. Gorobets¹, O. Gorobets¹, D. Sverdlichenko¹ ¹National Technical University of Ukraine "Igor Sikorsky Kyiv Polytechnic Institute", Kyiv, 03056, Ukraine

Calcium ions (Ca²⁺) function as ubiquitous second messengers in cellular orchestrating diverse physiological processes including muscle contraction, neuronal signaling, gene expression, and apoptosis [1]. The spatiotemporal regulation of intracellular Ca2+ dynamics involves a sophisticated network of ion channels, pumps, and Ca2+-binding proteins (CaBPs) that ensure precise signaling specificity [2] [3]. With 720 proteins currently annotated as Ca²⁺binding entities in the human proteome [4], calcium emerges as a master regulator in both physiological homeostasis and pathological states.

The multifaceted role of calcium signaling encompasses critical cellular processes: muscle contraction through troponin-mediated actin-myosin interactions [5] [6], synaptic neurotransmitter release essential for learning and memory [7], cell motility and division [8] [9] [10], oocyte maturation and fertilization [11], hormonal secretion [12], cell proliferation and differentiation [13] [14] [15] [16], enzymatic regulation [17], ion channel modulation [18] [19] [20], transcriptional

control [21] [22] [23] [24], immune cell development [25], and apoptotic regulation [26].

Recent theoretical advances in Ca²⁺ dynamics modeling have evolved from early descriptions of IP₃ receptor kinetics with cooperative binding and cytosolic calcium feedback [27] to comprehensive frameworks incorporating calcium-induced calcium release (CICR), mitochondrial buffering, and store-operated calcium entry (SOCE) [28]. Spatially-resolved models utilizing reaction-diffusion equations and stochastic channel gating have provided insights into cardiac myocyte calcium dynamics [29]. Building upon the empirical model of Ca²⁺ concentration dynamics in endothelial cells proposed by Plank et al. [30], Gorobets et al. [31] developed a theoretical framework describing magnetic field modulation of intracellular Ca²⁺ concentrations in the presence of biogenic and/or artificial magnetic nanoparticles (MNPs).

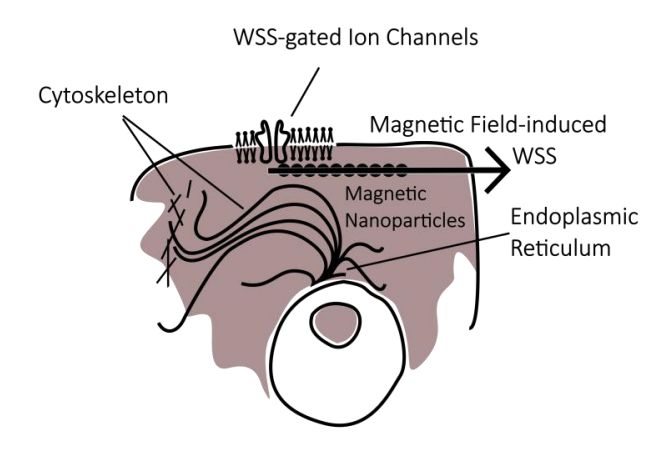


Fig. 2. Empirical modeling framework modified with MNPs chain.

This magnetomechanical approach leverages mechanosensitive Ca²⁺ channels as bioelectronic transducers, enabling external magnetic stimuli applied to membrane-bound MNPs to modulate ion flux and downstream calcium signaling cascades [31]. The method offers spatially targeted, non-invasive control over Ca²⁺ oscillation patterns that regulate cellular proliferation, differentiation, and apoptosis. By adjusting magnetic field parameters—including frequency, magnetic induction, and vector orientation relative to MNP chain alignment—precise

modulation of pathological tissues becomes feasible while minimizing off-target effects.

The cross-disciplinary integration of magnetism and cellular biology presents significant opportunities for neuromodulation, cardiac electrophysiology, tissue engineering, and cancer therapeutics. The consistency of experimental observations validates the modified Plank model [31] as a robust framework for investigating tunable Ca²⁺ signaling modulation via magnetic stimulation.

References

- [1] M. S. Jafri and A. Ullah, Editorial on Special Issue: Computational Insights into Calcium Signaling, Biomolecules 15, 485 (2025).
- F. Speelman-Rooms, M. Vanmunster, A. Coughlan, M. Hinrichs, I. Pontisso, S. [2] Barbeau, T. Parpaite, G. Bultynck, and M. Brohus, 10th European Calcium Society Symposium: The Ca2+-Signaling Toolkit in Cell Function, Health and Disease, Biol. Open 13, (2024).
- V. S. Morris, E. M. B. Richards, R. Morris, C. Dart, and N. Helassa, Structure-[3] Function Diversity of Calcium-Binding Proteins (CaBPs): Key Roles in Cell Signalling and Disease, Cells 14, 152 (2025).
- [4] T. M. Locke, R. Fields, H. Gizinski, G. M. Otto, D. M. Shechner, M. D. Berg, J. Villen, Y. Sancak, and D. Schweppe, High-Throughput Identification of Calcium Regulated Proteins Across Diverse Proteomes.
- [5] M. Dong and A. D. Maturana, Effects of Aging on Calcium Channels in Skeletal Muscle, Front. Mol. Biosci. 12, (2025).
- S. S. and B. P. S. J. -, RYR2 and Calcium Signalling: A Review, Int. J. Multidiscip. [6] Res. 7, (2025).
- J. Rupert and D. Milovanovic, At the Crossroads of Calcium Signaling, Protein [7] Synthesis and Neuropeptide Release, Elife 14, (2025).
- A. D. PERRIS, J. F. WHITFIELD, and P. K. TÖLG, Role of Calcium in the [8] Control of Growth and Cell Division, Nature 219, 527 (1968).
- [9] C. DerMardirossian, The Role of Calcium in Actin-Dependent Cell Migration and Invasion in Cancer, in (2024).
- [10] A. S. Hammad and K. Machaca, Store Operated Calcium Entry in Cell Migration and Cancer Metastasis, Cells 10, 1246 (2021).
- [11] C. Chen, Z. Huang, S. Dong, M. Ding, J. Li, M. Wang, X. Zeng, X. Zhang, and X. Sun, Calcium Signaling in Oocyte Quality and Functionality and Its Application, Front. Endocrinol. (Lausanne). 15, (2024).
- [12] M. S. Islam, Ryanodine Receptors in Islet Cell Function: Calcium Signaling, Hormone Secretion, and Diabetes, Cells 14, 690 (2025).
- [13] D. A. Díaz-Piña, N. Rivera-Ramírez, G. García-López, N. F. Díaz, and A. Molina-Hernández, Calcium and Neural Stem Cell Proliferation, Int. J. Mol. Sci. 25, 4073 (2024).
- [14] M. C. X. Pinto, A. H. Kihara, V. A. M. Goulart, F. M. P. Tonelli, K. N. Gomes, H. Ulrich, and R. R. Resende, Calcium Signaling and Cell Proliferation, Cell. Signal. 27, 2139 (2015).
- F. M. P. Tonelli, A. K. Santos, D. A. Gomes, S. L. da Silva, K. N. Gomes, L. O. [15]

- Ladeira, and R. R. Resende, *Stem Cells and Calcium Signaling*, in (2012), pp. 891–916.
- [16] I. Eidhof, B. Ulfenborg, M. Kele, M. Shahsavani, D. Winn, P. Uhlén, and A. Falk, Defined Culture Conditions Robustly Maintain Human Stem Cell Pluripotency, Highlighting a Role for Ca2+ Signaling, Commun. Biol. 8, 255 (2025).
- [17] T. Vygodina, A. Kirichenko, and A. A. Konstantinov, *Direct Regulation of Cytochrome c Oxidase by Calcium Ions*, PLoS One **8**, e74436 (2013).
- [18] C. M. Armstrong and G. Cota, *Calcium Ion as a Cofactor in Na Channel Gating.*, Proc. Natl. Acad. Sci. **88**, 6528 (1991).
- [19] M. M. Freitas and E. Gouaux, *BPS2025 Structural Basis for Calcium-Dependent Gating of the Bile Acid-Sensitive Ion Channel*, Biophys. J. **124**, 199a (2025).
- [20] Z. Ma, U. Paudel, M. Wang, and J. K. Foskett, A Mechanism of CALHM1 Ion Channel Gating, Am. J. Physiol. Physiol. 328, C1109 (2025).
- [21] A. E. West, W. G. Chen, M. B. Dalva, R. E. Dolmetsch, J. M. Kornhauser, A. J. Shaywitz, M. A. Takasu, X. Tao, and M. E. Greenberg, *Calcium Regulation of Neuronal Gene Expression*, Proc. Natl. Acad. Sci. 98, 11024 (2001).
- [22] F. G. Campos, D. P. Seixas, G. R. Barzotto, L. G. Jorge, K. R. Ducatti, G. Ferreira, T. M. Rodrigues, E. A. A. da Silva, and C. S. F. Boaro, Roles of Calcium Signaling in Gene Expression and Photosynthetic Acclimatization of Solanum Lycopersicum Micro-Tom (MT) after Mechanical Damage, Int. J. Mol. Sci. 23, 13571 (2022).
- [23] D. Duarte-Delgado, I. Vogt, S. Dadshani, J. Léon, and A. Ballvora, Expression Interplay of Genes Coding for Calcium-Binding Proteins and Transcription Factors during the Osmotic Phase Provides Insights on Salt Stress Response Mechanisms in Bread Wheat, Plant Mol. Biol. 114, 119 (2024).
- [24] V. Zablotskii, O. Gorobets, S. Gorobets, and T. Polyakova, *Effects of Static and Low-Frequency Magnetic Fields on Gene Expression*, J. Magn. Reson. Imaging (2025).
- [25] W. Song, T. J. Kim, and W. Liu, Editorial: Community Series in BCR Signaling and B Cell Activation, Volume 2, Front. Immunol. 16, (2025).
- [26] D.-O. Moon, Calcium's Role in Orchestrating Cancer Apoptosis: Mitochondrial-Centric Perspective, Int. J. Mol. Sci. 24, 8982 (2023).
- [27] G. W. De Young and J. Keizer, A Single-Pool Inositol 1,4,5-Trisphosphate-Receptor-Based Model for Agonist-Stimulated Oscillations in Ca2+ Concentration., Proc. Natl. Acad. Sci. 89, 9895 (1992).
- [28] M. Falcke, Reading the Patterns in Living Cells —the Physics of ca 2+ Signaling, Adv. Phys. 53, 255 (2004).
- [29] M. A. Colman, C. Pinali, A. W. Trafford, H. Zhang, and A. Kitmitto, A Computational Model of Spatio-Temporal Cardiac Intracellular Calcium Handling with Realistic Structure and Spatial Flux Distribution from Sarcoplasmic Reticulum and t-Tubule Reconstructions, PLOS Comput. Biol. 13, e1005714 (2017).
- [30] M. J. Plank, D. J. N. Wall, and T. David, Atherosclerosis and Calcium Signalling in Endothelial Cells, Prog. Biophys. Mol. Biol. 91, 287 (2006).
- [31] O. Gorobets, S. Gorobets, T. Polyakova, and V. Zablotskii, *Modulation of Calcium Signaling and Metabolic Pathways in Endothelial Cells with Magnetic Fields*, Nanoscale Adv. **6**, 1163 (2024).

MAGNETIC FIELD CONTROL OF CALCIUM SIGNAL IN CANCER CELLS

Ye. A. Salatskyi¹, S. V. Gorobets¹

¹ Department of Bioenergy, Bioinformatics and Environmental Biotechnology, Igor Sikorsky Kyiv Polytechnic Institute Kyiv, 03056, Ukraine

Problem statement

Calcium homeostasis dysregulation characterizes malignant neoplasms, affecting proliferation, apoptosis, and metastasis [1]. Calcium channels represent promising anticancer targets due to their oncogenic role, with this dysfunction classified as oncochannelopathy [2].

Drug development faces major limits. While making up 18% of smallmolecule drug targets, only 8% gain approval due to similar pore structures and calcium's widespread signaling role, causing targeting problems [3]. Antibody drugs are limited by their size and conserved extracellular loops (the only binding sites they can reach), which lowers binding ability and specificity [3,4].

The complexity of ion channels targeting restricts their application. Only the polyclonal antibody BIL010t (Biosceptre), which targets the inactive form of the P2X7 channel [5], has finished early-stage human testing as a skin ointment against basal cell carcinoma [6].

Solution approach

Magnetomechanical transduction modulates calcium signalling via nonbiogenic [7] and biogenic [8] magnetic nanoparticles on cell membranes under magnetic field action [9]. This is confirmed by reduced therapeutic effects with channel blockers [10] and mathematical models [11], though no consensus mechanism exists.

Mechanosensitive calcium channels are controllable through magnetic fields and biocompatible magnetic nanoparticles for selective tumor effects via targeted delivery systems [12] and specialized magnetic field localization [13], making them promising oncology targets [14]. Fig. 1 demonstrates that expressions of mechanosentitive calcium channels are disperse within the same cancer type.

Functionalized magnetic particles on cell membranes can be used for remote cellular control through magnetic field-induced mechanical forces [15–17]. This enables precise receptor activity control such as endocytosis and ion channel gating via mechanical transduction signalling pathways [17], with scalable simultaneous stimulation of thousands of cells [18].

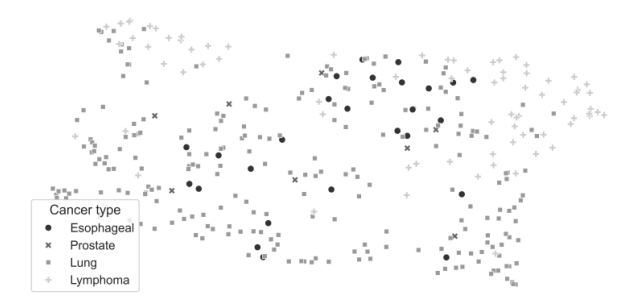


Fig. 1. UMAP visualization for expressions of PIEZO1, TRPC1, TRPV2, PKD1, and PKD2 from Human Protein Atlas

Calcium influx consequences

Tumor apoptosis occurs under magnetic fields (MFs) via calcium-mediated p53/caspase activation at 10–350 Hz (0.0012–80 mT) [19]. Effects show non-linear frequency dependence: 10 mT at 50 Hz stimulates proliferation while 100 Hz inhibits glioblastoma cells [20]. Weak MFs (0.1 mT) achieve maximum cytotoxicity at 45–55 Hz [21], while ultra-low frequency (1.6 mHz) with high induction (5.5–8.5 T) proves effective [22].

Calcium dynamics can be desynchronized from membrane potential with MFs (20 Hz, 5 mT), increasing intracellular pH and suppressing proliferation [23]. They activate VGCCs, specifically L/T-type channels [24]. Thomas fields (25–6 Hz, 0.002–0.010 mT) selectively elevate [Ca²⁺] in tumor cells while sparing normal cells [25], exploiting reduced VGCC expression in carcinomas [26]. Such effect produces 60% viability reduction in MDA-MB-231 (7.83 Hz, 1 mT) [27].

Additional mechanisms include membrane blebbing (20 Hz, 10 mT as optimal MF parameters) [28], nanoparticle-mediated lysosomal destabilization [29], and cytoskeletal changes affecting mechanosensitive channels [19]. Mathematical modeling enables personalized magnetotherapy targeting oncogene pathways [19].

Ca²⁺-binding proteins shape cell-specific responses [30], with major mechanosensitive pathways incorporating YAP/TAZ, NF- κ B, and SRF [31]. The 720 Ca²⁺-binding proteins in human proteome [32] suggest broad therapeutic potential for low-frequency magnetic fields with membrane-bound nanoparticles.

Mathematical modelling approaches

Current intracellular $[Ca^{2+}]$ dynamics modeling encompasses both physiologically normal [33–35] and tumor cells [36–38].

The Goldbeter model [34] established modern calcium dynamics modelling by incorporating cytoplasmic and ER [Ca²⁺] considering inositol-1,4,5-triphosphate

(IP3) influence. Subsequent enhancements included the Plank model's reversible calcium buffering in endothelial cells [35] and the Debir model's alternative approach describing IP3-receptor activity without explicit ER [Ca²⁺] accounting [33].

The Chang model can be viewed as an extension of Goldbeter model with IP3-receptor opening probability assessment, though it lacks calcium leak channel representation [36]. The Langthaler models demonstrate progressive improvement: the initial model focused exclusively on extracellular-cytoplasmic ionic exchange [37], while the subsequent version incorporated ER states and a specialized junction compartment between ER and plasma membrane [38].

Goldbeter-based models generate self-oscillations with stable periodic orbits, rendering calcium dynamics insensitive to wide ranges of initial conditions.

Conclusions

We demonstrated that calcium signalling can be affected by magnetic fields, so it can be an explanation of magnetotherapy efficacy for specific malignancies. One of possible mechanisms uses magnetic nanoparticles (both biogenic and artificial) for mechanotransduction to mechanosensitive calcium channels. Magnetotherapies exhibit selective effects on some tumor tissues, which can be explained by differences in biogenic magnetic nanoparticles amounts or mechanosensitive channels expressed in malignancies.

Such calcium influx affects variety of pathways such as caspase cascades activations, which leads to apoptosis. Other mechanisms involve membrane blebbing and lysosomal destabilization.

Currently present calcium oscillation models could be extended by considering magnetic nanoparticles action on mechanosensitive calcium channels. Consequently, it is theoretically possible to use mathematical models for magnetic field parametrization *in cilico*, because its effects are frequency-dependent. Such modifications could potentially reduce the efforts for experimental parameters findings for magnetogenetic therapies. That is important to consider mechanosensitive channels expressions (as in Fig. 1) for personalized treatment.

References

- [1] S. Marchi, C. Giorgi, L. Galluzzi, and P. Pinton, Molecular Cell 78, 1055 (2020).
- [2] N. Prevarskaya, R. Skryma, and Y. Shuba, Physiological Reviews 98, 559 (2018).
- [3] C. J. Hutchings, P. Colussi, and T. G. Clark, mAbs 11, 265 (2018).
- [4] J. Garcia, et al., Nature 626, 626 (2024).
- [5] R. Lara, et al., Frontiers in Pharmacology **11**, (2020).
- [6] D. Matyśniak, M. Oslislok, and P. Pomorski, Acta Biochimica Polonica (2022).
- [7] B. Govindan, et al., Pharmaceutics 15, 868 (2023).

- [8] S. Gorobets, O. Gorobets, Y. Gorobets, and M. Bulaievska, Bioelectromagnetics 43, 119
- [9] M. O. Çakıt, et al., Anatolian Current Medical Journal 5, 102 (2023).
- [10] S. Sharma, et al., eBioMedicine 44, 194 (2019).
- [11] O. Gorobets, S. Gorobets, T. Polyakova, and V. Zablotskii, Nanoscale Advances 6, 1163 (2024).
- [12] M. Sabzini, et al., in Functionalized Nanomaterials for Cancer Research (Elsevier, 2024), pp. 435–457.
- [13] M. Ahmed and M. Douek, BioMed Research International 2013, 1 (2013).
- [14] M. Xu, et al., Cell & Bioscience 8, (2018).
- [15] C. Monzel, et al., Chemical Science 8, 7330 (2017).
- [16] M. Puig-De-Morales, M. Grabulosa, J. Alcaraz, J. Mullol, G. N. Maksym, J. J. Fredberg, and D. Navajas, Journal of Applied Physiology **91**, 1152 (2001).
- [17] M. Rotherham, et al., Current Opinion in Biomedical Engineering 24, 100410 (2022).
- [18] P. Tseng, J. W. Judy, and D. Di Carlo, Nature Methods 9, 1113 (2012).
- [19] Y. Liu, et al., Journal of Advanced Research **69**, 531 (2025).
- [20] Z. Akbarnejad, et al., Electromagnetic Biology and Medicine 36, 238 (2016).
- [21] I. López de Mingo, M. X. Rivera González, M. Ramos Gómez, and C. Maestú Unturbe, Biomolecules 15, 503 (2025).
- [22] O. Lunov, et al., Cancers 11, 1873 (2019).
- [23] J. Sun, et al., Scientific Reports 13, (2023).
- [24] M.-H. Wang, et al., Electromagnetic Biology and Medicine 40, 150 (2020).
- [25] C. A. Buckner, et al., PLOS ONE **10**, e0124136 (2015).
- [26] N. N. Phan, et al., Oncology Letters **14**, 2059 (2017).
- [27] M.-H. Wang, et al., Electromagnetic Biology and Medicine **40**, 384 (2021).
- [28] O. Gorobets, et al., Bioelectrochemistry 151, 108390 (2023).
- [29] S. Lopez, et al., Nanoscale Advances 4, 421 (2022).
- [30] V. S. Morris, et al., Cells 14, 152 (2025).
- [31] V. Zablotskii, O. Gorobets, S. Gorobets, and T. Polyakova, Journal of Magnetic Resonance Imaging (2025).
- [32] T. M. Locke, et al., Cell Reports 43, 114879 (2024).
- [33] B. Debir, C. Meaney, M. Kohandel, and M. B. Unlu, Scientific Reports 11, (2021).
- [34] A. Goldbeter, G. Dupont, and M. J. Berridge, Proceedings of the National Academy of Sciences 87, 1461 (1990).
- [35] M. J. Plank, D. J. N. Wall, and T. David, Progress in Biophysics and Molecular Biology **91**, 287 (2006).
- [36] Y. Chang, et al., International Journal of Molecular Sciences **23**, 1763 (2022).[36] S. Langthaler, et al., PLOS Computational Biology **17**, e1009091 (2021).
- [37] S. Langthaler, et al., Frontiers in Molecular Biosciences 11, (2024).
- [38] S. Langthaler, et al., PLOS Computational Biology 17, e1009091 (2021).



SPONTANEOUS EMERGENCE OF PHASE COHERENCE IN A ROOM-TEMPERATURE MAGNON BOSE-EINSTEIN CONDENSATE

A. A. Serga¹

¹RPTU University Kaiserslautern-Landau, Kaiserslautern, 67663, Germany

The field of magnonics is regarded as a promising route toward advanced information processing technologies [1]. The central idea is to use magnons, the quanta of spin waves, as information carriers. Magnons can be excited in magnetic materials by various methods, including ferromagnetic resonance driven by external microwave fields, parametric pumping, and spintronic injection. Of particular interest is the spontaneous formation of highly populated, partially or fully coherent magnon states due to nonlinear scattering of initially injected magnons—the so-called magnon accumulation. Among the underlying phenomena, one of the most remarkable is magnon Bose–Einstein condensation (BEC) [2–8].

My talk will focus on the coherence of these accumulated quasiparticles and our recent results on determining the correlation characteristics of magnon condensates formed by parametric pumping in single-crystal yttrium iron garnet (YIG) films.

BEC is the spontaneous accumulation of bosonic particles or quasiparticles at the minimum of their frequency spectrum. It can be achieved either by lowering the temperature or by increasing the particle density. The latter route is particularly relevant for systems with temperature-dependent populations, such as magnons, photons, polaritons, and excitons [2]. In an artificially overpopulated magnon gas in YIG, condensation can occur even at room temperature [3–8]. A defining property of the BEC state is coherence [2], expressed by the spontaneous emergence of a well-defined global phase shared by all particles condensed at the spectral minimum. Until recently, this phase was revealed only indirectly, through phenomena dependent on spatial phase differences, such as interference [5], as well as macroscopic condensate dynamics including supercurrents [6], superfluidity, and Josephson oscillations [7].

Here, I present our recent progress in directly probing the temporal and phase coherence of magnon BECs. Using time-domain detection of microwave radiation emitted from a parametrically pumped, perpendicularly magnetized YIG film (Fig. 1), we observe the spontaneous condensation of magnons into a uniform precession state (Kittel mode) with minimal energy and a well-defined phase [8]. In particular, we detected the spontaneous narrowing of the spectral line and

showed that a randomly coherent condensate phase appears in every individual realization.

These findings confirm the fundamental properties long postulated for quasiparticle condensates, open direct access to the coherence degree of freedom in magnon systems, and suggest new opportunities for information processing based on microwave-frequency magnon BECs.

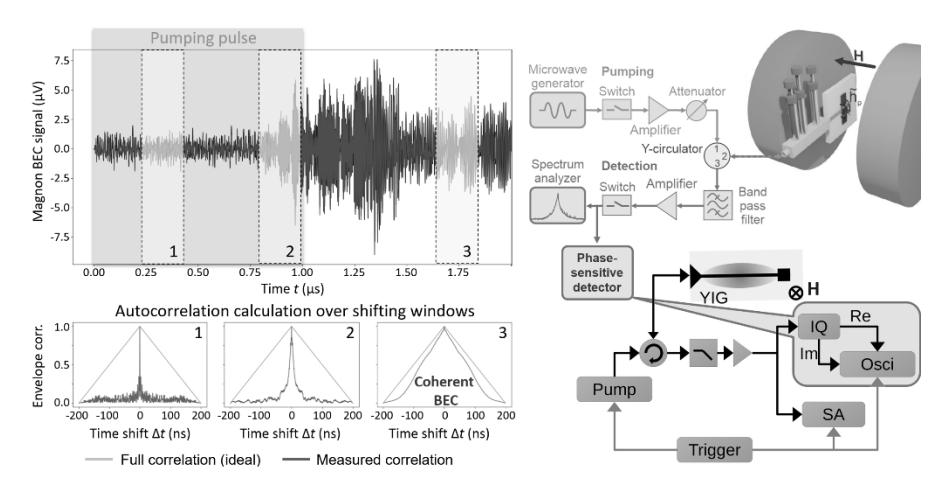


Fig. 1. Phase-sensitive detection of a magnon Bose-Einstein condensate (BEC) in a perpendicularly magnetized YIG film. The coherence was quantified as the integral of the normalized autocorrelation of the detected signal over a 200 ns window, shifted across the entire measurement interval.

This research was funded by the Deutsche Forschungsgemeinschaft (DFG, German Research Foundation) in the framework of TRR 173 - Grant No. 268565370 Spin+X (Projects B04 and B13), as well as by grant DMR-2338060 from the National Science Foundation of the United States.

- [1] P. Pirro, V. I. Vasyuchka, A. A. Serga, B. Hillebrands, Nat. Rev. Mater. 6, 1114 (2021).
- [2] D. Snoke, Nature 443, 403-404 (2006).
- [3] S. O. Demokritov et al., Nature **443**, 430-433 (2006).
- [4] T. B. Noack et al., Phys. Rev. B 104, L100410 (2021).
- [5] Nowik-Boltyk et al., Sci. Rep. 2, 482 (2012).
- [6] M. R. Schweizer et al., App. Phys. Lett. **124**, 092402 (2024).
- [7] A. J. E. Kreil et al., Phys. Rev. B **104**, 144414 (2021).
- [8] M. Koster et al., arXiv:2507.16862 (2025).

НАУКОВЕ ВИДАННЯ

Матеріали конференції

СУЧАСНІ ПРОБЛЕМИ ФІЗИКИ ТВЕРДОГО ТІЛА ТА МАГНЕТИЗМУ

Київ, Україна 24 – 26 вересня 2025 р.

Праці конференції надруковані в авторській редакції

Голова конференції – Олександр Товстолиткін Комп'ютерна верстка – Сергій Мамілов, Роман Верба

Підписано до друку 15.09.2025. Формат 60х90/16. Папір офсетний. Гарнітура Liberation Serif. Ум. друк. арк. 12,2. Обл.-вид. арк. 10,5. Наклад 60 прим.

Надруковано в друкарні «БУЛАЙН» 61000, м. Харків, вул. Катерининська, 46. Тел. (099) 604-49-45 www.bookline.online

